Universität Zürich

PHYSIK - INSTITUT

www.physik.unizh.ch

Wissenschaftlicher Jahresbericht

April 2002 - März 2003

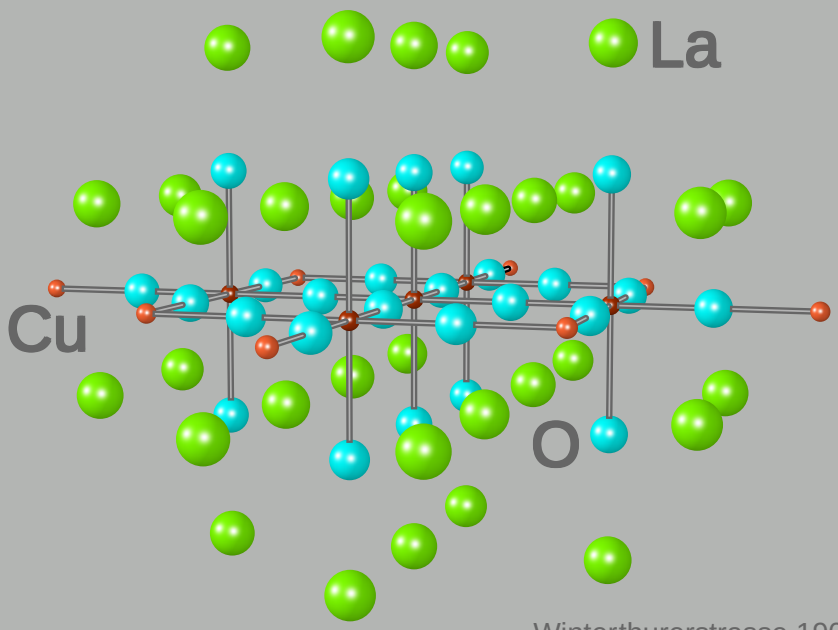

Winterthurerstrasse 190, CH-8057 Zürich/Schweiz

Universität Zürich

PHYSIK - INSTITUT

Wissenschaftlicher Jahresbericht

April 2002 - März 2003

Winterthurerstrasse 190, CH-8057 Zürich/Schweiz www.physik.unizh.ch

The picture on the cover shows a cluster comprising 13 copper, 26 oxygen, and 34 lanthanum atoms which has been used to calculate the local electronic structure of the substance La_2CuO_4. This insulator becomes superconducting when some La^{3+} ions are substituted by Ba^{2+} or Sr^{2+} (see Sec.15).

Sekretariat	01 635 5721	secret@physik.unizh.ch
Prof. C. Amsler	01 635 5784 022 767 2914	amsler@cern.ch
Prof. H.-W. Fink	01 635 5801	fink@physik.unizh.ch
Prof. H. Keller	01 635 5748	keller@physik.unizh.ch
Prof. P.F. Meier	01 635 4016	pfmeier@physik.unizh.ch
Prof. J. Osterwalder	01 635 5827	osterwal@physik.unizh.ch
Prof. U.D. Straumann	01 635 5768	strauman@physik.unizh.ch
Prof. P. Truöl	01 635 5777	truoel@physik.unizh.ch

Die Jahresberichte sind im Internet einsehbar: http://www.physik.unizh.ch/reports.html.

Begleitwort

In den beiden Hauptforschungsbereichen des Physik-Institut, der Physik der kondensierten Materie und der Physik fundamentaler Systeme, finden sich sieben Gruppen in der Bio-, der Oberflächen-, der Festkörper- und der Elementarteilchenphysik. Diese Forschungsgruppen stellen in zehn vom Schweizerischen Nationalsfonds unterstützten Forschungsgesuchen den Hauptgesuchsteller. Zwei Gruppen bilden dabei Teil nationaler Forschungskompetenzzentren (NCCR), i.e. *MaNEP* (Materials with novel electronic properties, H. Keller) und *Nanoscale Science* (Impact on life sciences, sustainability, information and communication technology, H.W. Fink). Die mit dem Rücktritt von Roland Engfer im Februar 2001 freigewordene Professur in Kern- und Teilchenphysik wurde am 1.4.2003 durch Andreas Schilling im Bereich Physik der kondensierten Materie besetzt.

Fundamentale magnetische und elektronische Eigenschaften von Supraleitern und verwandten Systemen werden in der Gruppe von H. Keller untersucht mit dem Ziel den noch immer unverstandenen Mechanismus der Hochtemperatur-Supraleitung zu klären. Dank detaillierter experimenteller Untersuchungen von Isotopeneffekten, die zeigen, dass neben der Elektron-Elektron-Korrelation auch die Wechselwirkung zwischen den supraleitenden Ladungsträgern und den Gitterschwingungen (Phononen) eine wichtige Rolle spielt, ist man der Lösung dieser grundlegenden Frage näher gekommen.

Nanostrukturen in Form von ultradünnen Schichten, Quantendrähten und Quantenpunkten sind von grossem wissenschaftlichem und technologischem Interesse, weil sich damit gezielt elektronische und magnetische Eigenschaften erzeugen lassen, welche durch Quanteneffekte dominiert werden. Da die geometrische Ausdehnung dieser Objekte in mindestens einer Richtung nur wenige Atomdurchmesser beträgt, bestehen sie im wesentlichen aus Grenzflächen und Oberflächen. In der Gruppe von J. Osterwalder und T. Greber werden solche Strukturen kontrolliert hergestellt und die entsprechenden Grenzschichten mit atomarer Auflösung auf ihre Güte getestet. Mit einem neuartigen spinpolarisierten Photoemissionsexperiment ist im letzten Jahr eine wichtige apparative Neuentwicklung erfolgreich eingesetzt worden. So konnte z.B. beobachtet werden, wie sich die elektronischen Bänder und der Magnetismus dünner Nickelfilme entwickeln, wenn mono-Atomare Lagen auf eine Kupferoberfläche aufgedampft werden.

Die Biophysik-Gruppe von H.-W. Fink war seit Bezug ihres neuen Labors im Februar 2002 vollauf beschäftigt mit der Inbetriebnahme ihrer Apparaturen, darunter die selbstentwickelten LEEPS-Mikroskope (Low energy electron point source), mit denen die Abbildung einzelner Biomoleküle mit hoher Auflösung möglich ist. Eine neu konstruierte Variante dieses Mikroskops arbeitet bei tiefen Temperaturen (2.5 K). Ausserdem stehen ein Feldionenmikroskop zur Herstellung und Charakterisierung von Elektronenpunktquellen und ein Rasterelektronenmikroskop mit Temperaturregelung zur Beobachtung von Flüssigkeiten zur Verfügung. Erste Messungen betreffen die Relaxationszeiten einzelner DNS Moleküle unter Einfluss äusserer elektrischer Felder.

Die Gruppe Computerassistierte Physik von P.F. Meier untersucht mit der Methode der Dichtefunktionale die elektronische Struktur von Materialien, die Hochtemperatur-Supraleitung aufzeigen. Die berechneten Grössen wie z.B. elektrische Feldgradienten, Hyperfeinfelder und chemische Verschiebungen ermöglichen die Interpretation der mit Kernresonanzspektroskopie gemessenen Daten.

Die Messung der Gravitationskonstanten konnte erfolgreich abgeschlossen werden. Das vielbeachtete Resultat hilft den immer noch grossen Unsicherheitsbereich dieser *ältesten* Naturkonstanten entscheidend einzuschränken.

Dank immer höherer Strahlenergie und -intensität der Teilchenbeschleuniger können die Bausteine der Materie und ihre Wechselwirkungen mit zunehmender räumlicher Auflösung untersucht werden. So lassen sich einerseits die Vorhersagen des Standard Models der Elementarteilchen immer

genauer überprüfen, andererseits lässt sich die Entwicklung des Universums zu immer früheren Zeiten zurückverfolgen. Diese Entwicklung bedingt allerdings auch eine ständig wachsende Komplexität der Instrumente, deren Anforderungen bezüglich mechanischer Konstruktion, Integrationsdichte der elektronischen Komponenten, Geschwindigkeit der Datenaufnahme, etc. jene kommerziell erhältlicher Systeme in der Regel weit überschreiten, und deren Herstellung und Betrieb somit Pioniercharakter aufweisen. Die an den europäischen Beschleunigerzentren CERN, Genf und DESY, Hamburg arbeitenden Teilchenphysikgruppen werden bei diesen Aufgaben durch den hohen technischen Standard unserer Werkstätten unterstützt. So waren die in Zürich entwickelten Detektoren von zentraler Bedeutung für die erstmalige Erzeugung von Antiwasserstoffatomen und deren Nachweis (Gruppe C. Amsler) und für den kürzlich erfolgten *Upgrade* des H1-Detektors am DESY (U. Straumann und P. Truöl). Zunehmend verstärken die Teilchenphysikgruppen auch ihre Expertise im Bau grossflächiger Siliziumstreifen- (U. Straumann) und Siliziumpixel-Detektoren (C. Amsler).

Alle Forschungsgruppen können sich auf die zuverlässige Mitarbeit der mechanischen und elektronischen Werkstätten, des sonstigen technischen Personals des Instituts und des Sekretariats verlassen. In unserer mechanischen Werkstatt hat Kurt Bösiger die Leitung von Bernhard Schmid übernommen. Bernhard Schmid stand der Werkstatt seit 28 Jahren vor. Er hat den Umzug auf den Irchel mit der damit verbundenen Erneuerung und Kapazitätserweiterung geplant und realisiert. Unter seiner Leitung ist die Werkstatt ein wichtiger Erfolgsfaktor für alle Forschungsgruppen geworden, um den uns auswärtige Kollegen beneiden. Zum Glück wird Bernhard Schmid uns bis zu seiner Pensionierung in ein paar Jahren für anspruchvolle Spezialprojekte und Kurt Bösigers Stellvertretung weiterhin zur Verfügung stehen.

Ausserhalb des Forschungsbereichs führten die doppelte Maturitätsjahrgänge zu steigenden Zahlen der Studierenden, darunter überdurchschnittlich viele, die sich für das Hauptfach Physik entschieden haben. Über letzteres freuen wir uns selbstverständlich sehr. Andererseits sind die steigende Zahlen an Medizin- und Biologiestudierenden in den Grundvorlesungen, Praktika und Übungen ohne zusätzliche Personalmittel zu betreuen. Die Situation wurde zusätzlich erschwert durch eine nicht besetzte Professur. Zunehmende administrative Belastung durch Evaluationsprozeduren, administrative Jahresberichte neben den gewohnten Rechenschaftsberichten (*sic*) für die forschungsfördernden Institutionen und schliesslich eine ständig wachsende Flut von Umfragen und Vernehmlassungen lassen immer weniger Zeit für die Forschung, unser wichtigstes Kerngeschäft, über das hier berichtet wird. Es ist dem grossen Einsatz und der Belastbarkeit aller Mitarbeiter zu verdanken, dass trotzdem die hohe Qualität in der Forschung erhalten werden konnte, wie es die starke internationale und nationale Vernetzung und die beachtlich lange Liste von wissenschaftlichen Publikationen belegen. Dass die Qualität sich ohne die erwähnten, sich zunehmend verschlechternden Randbedingungen noch wesentlich steigern liesse, ist allerdings anzunehmen.

Zürich, im April 2003

Prof. Dr. Peter Truöl

Contents

1 Measurement of the Gravitational Constant G

W. Kündig, R. E. Pixley, St. Schlamminger and U. Straumann

The Newtonian gravitational constant G is determined by means of a beam-balance experiment, with an accuracy comparable to that of the best Cavendish-like precise torsion-balance experiments. The gravitational force of two stainless steel tanks filled with $13\,521$ kg mercury on two 1.1 kg test masses has been measured using a commercial mass comparator. The experiment was located at the Paul Scherrer Institute (Villigen, Switzerland) in a 4.5 m deep pit. The pit has thick concrete walls, which provided the thermal and mechanical stability which is essential for the experiment.

The by far largest uncertainty in the determination of G reported earlier from this experiment was due to the assumed nonlinearity of the balance. Since we compare the amplitude of the signal ($784\,\mu$g) to the much larger mass of the calibration weights (both $100\,$mg), any nonlinearity of the balance can produce a systematic error. A rough estimate of this nonlinearity based on information given by the producer *Mettler-Toledo* gave an upper limit of 200 ppm. In order to reduce this large error, we developed a new measurement method which allows to average out the nonlinearity in situ. The amplitude of the signal was measured at many different working points of the balance within the calibration interval. By averaging the different readings, the influence of a possible nonlinearity of the balance is considerably reduced.

The final measurements were done in three different periods with two different test masses made of Copper and Tantalum respectively. Various other systematic effects were investigated, such as sorption effects at the test masses, small temperature dependences and influence of magnetic forces. As a result the final value of G was found [1] to be

$$G = 6.674\,07(22) \times 10^{-11}\ \ \mathrm{m^3\,kg^{-1}\,s^{-2}}.$$

This value is in agreement with other recently published experiments, most of them using a Cavendish type torsion balance (Fig.1.1). The different experimental approaches give rise to completely different systematics. Therefore we can conclude, that most likely there are no significant unknown systematic effects. The experiment, which was originally initiated by W. Kündig, was completed in Summer 2002 and dismantled by the end of 2002. The presently published systematic uncertainties of our experiment are dominated by the nonlinearity of the balance readings and the calculations of the field mass distributions. Walter Kündig and Ralph E. Pixley (both retired) continue to work on the data analysis and try to improve the understanding of all these systematic uncertainties.

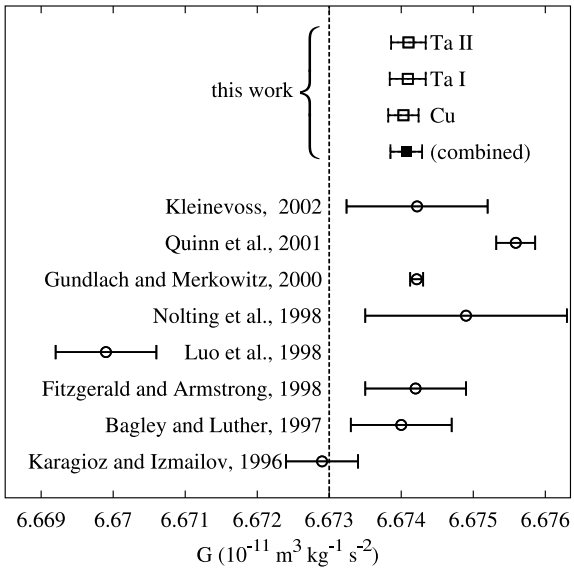

Figure 1.1: *A comparison of recently published values of the Gravitational constant. The dashed line represents the CODATA recommendation of 1998.*

[1] *Determination of the Gravitational Constant with a Beam Balance*
St. Schlamminger, E. Holzschuh, W. Kündig, Phys.Rev.Lett.**89** (2002) Nr. 16, p. 161102.

[2] *Determination of the Gravitational Constant Using a Beam Balance*
Stephan Schlamminger, Dissertation, Zürich, 2002.

2 Measurement of the Neutrino Magnetic Moment at the Bugey Nuclear Reactor

C. Amsler, O. Link and H. Pruys

in collaboration with:
Institut des Sciences Nucléaires (Grenoble), Université de Neuchâtel, Università di Padova

(MUNU Collaboration)

The MUNU experiment measures the magnetic moment of antineutrinos $\overline{\nu}_e$ from a nuclear reactor, using the elastic scattering reaction $\overline{\nu}_e e^- \rightarrow \overline{\nu}_e e^-$. This process is very sensitive to the magnetic moment of the $\overline{\nu}_e$ (especially at low neutrino and low electron recoil energies) because it is a pure leptonic and theoretically well understood weak process.

In the standard model the magnetic moment vanishes for massless neutrinos. Even for massive ν_e with masses in the range observed recently, the standard model predicts magnetic moments much below $10^{-20}\ \mu_B$, which are not accessible experimentally. The experimental evidence for a large magnetic moment would mean new physics beyond the standard model. With a finite magnetic moment the spin of a lefthanded neutrino may flip due to the electromagnetic interaction, and the neutrino become a "sterile" righthanded state which does not interact, and hence is experimentally invisible. The precession of a magnetic moment in the range $\mu_\nu \sim 10^{-10} - 10^{-12}\ \mu_B$ in the solar magnetic field offers an alternative explanation to the MSW effect for the observed deficit of solar neutrinos.

A detailed description of the apparatus can be found in ref. [1; 2] and in previous annual reports. MUNU uses a 1 m^3 time projection chamber (TPC, gaseous CF_4 at 3 bar) to measure the scattering angle and the kinetic energy of the recoil electron. The energy threshold for detecting electrons is typically 300 keV. Since the cross section for neutrino reactions is very low, background measurements are important. To reject background events due to cosmic muons and Compton scattering of low energy γ's, the TPC is surrounded by a tank filled with liquid scintillator. The electrons are scattered into the forward hemisphere. To subtract the background, electrons are also measured in the backward hemisphere. Measurements during reactor shutdown were done to check that equal amounts of background electrons are emitted in the forward and backward hemispheres.

Data taking was completed in 2002. We collected neutrino data during 111 days, corresponding to a livetime of 66.3 days after deadtime subtraction. We also collected reactor off data during 37 days (19.3 days after deadtime subtraction). In addition, calibration data were recorded periodically for various triggers.

A first quick analysis was done by "visual" tracking: every potential neutrino event was examined by eye and the scattering angle and recoil energy were determined. This method, applied by the Neuchâtel group, was restricted to the analysis of recoil electrons with an energy above 700 keV.

A systematic data analysis was performed by the University of Zürich group using a pattern recognition program ("automatic tracking"). With the automatic reconstruction program we were able to analyze larger datasets, e.g. neutrino data with lower electron recoil energies. The software was carefully tested and compared to Monte Carlo simulation [3]. The angular resolution and acceptance were determined from Monte Carlo generated events (see fig. 2.1). The resolution and acceptance become worse at lower energies, mainly due to multiple scattering and electronic noise.

The final analysis is done by comparing the electron rates in the forward hemisphere (neutrino scattering events and background events) with those in the backward hemisphere (background events

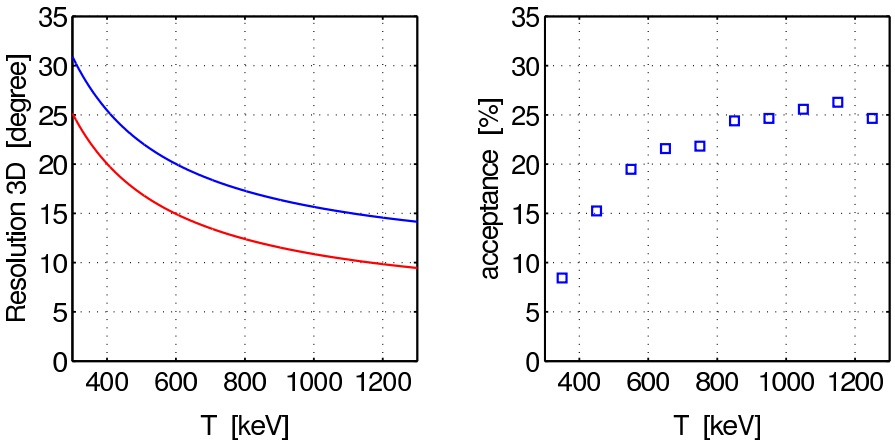

Figure 2.1: *Left: Angular resolution on the direction of the recoil electron as a function of electron energy. Red curve: 3d angular fit with true vertex; blue curve: fit with reconstructed vertex. Right: Acceptance as function of electron energy.*

only).

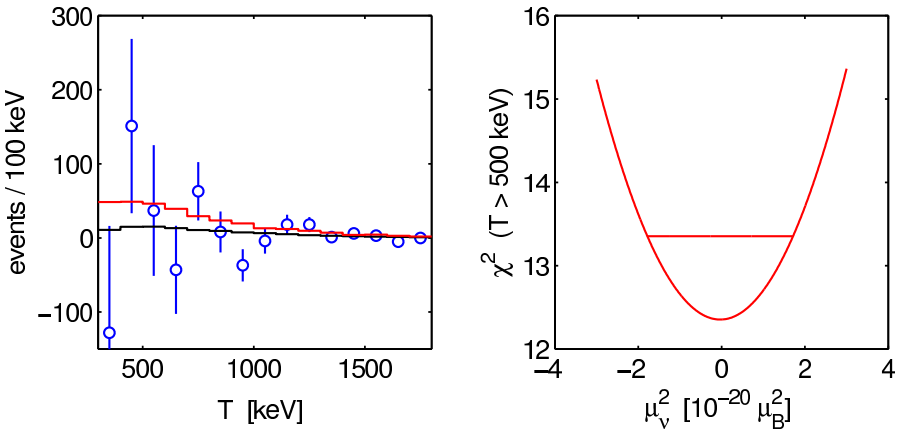

Figure 2.2: *Left: Energy spectrum of forward minus backward events. The data points are compared with Monte Carlo spectra without magnetic moment (black curve) and with a magnetic moment of* $1.7 \times 10^{-10}\mu_B$ *(red curve). Right:* χ^2 *as function of* μ_ν^2 *(fit parameter).*

Figure 2.2 (left) shows the measured forward minus backward intensity as a function of electron energy. The curves show Monte Carlo simulations based on the electroweak theory with no contribution from the neutrino magnetic moment (black) and with a magnetic moment of $1.7 \times 10^{-10}\mu_B$ (red). The Monte Carlo simulation gives the expected number of events per 100 keV as a function of recoil electron energy T

$$MC(T) = W(T) + \mu_\nu^2\, M(T),$$

where the part $W(T)$ is independent of the magnetic moment and the part involving $M(T)$ depends on the square of the magnetic moment. Fitting this expression to the data and using μ_ν^2 as free parameter gives $\mu_\nu^2 = (-0.04 \pm 1.74) \times 10^{-20}\mu_B^2$ (fig. 2.2, right). Thus there is no indication of a finite magnetic moment. A 90% confidence level upper limit of

$$\mu_\nu < 1.7 \times 10^{-10}\, \mu_B \tag{2.1}$$

is obtained using the unified approach of ref. [4] to obtain an upper limit from gaussian data close to a physical boundary. This upper limit is somewhat smaller than the preliminary limit $2.3 \times 10^{-10}\mu_B$ published by the MUNU collaboration [5] and somewhat larger than the limit $1.4\times10^{-10}\mu_B$ obtained by a visual scan above 700 keV. However, our upper limit, eqn. (2.1), is independent of the applied energy threshold (see fig. 2.3). The larger background compensates for the increased sensitivity to μ_ν at lower recoil energies.

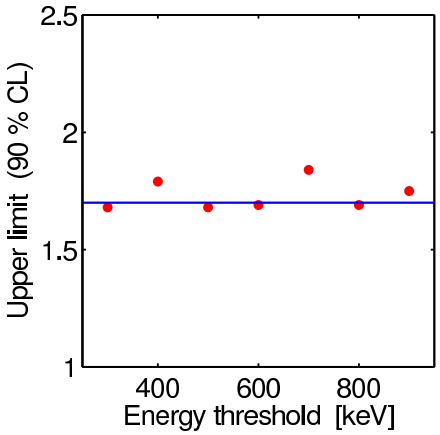

Figure 2.3: *Upper limits on μ_ν (in units of $10^{-10}\mu_B$) as a function of recoil energy threshold.*

Previous laboratory experiments led to upper limits of $\mu_\nu < 1.9 \times 10^{-10}\ \mu_B$ [6] and 1.5×10^{-10} μ_B [7]. The astrophysical upper limits, e.g. from SN1987A, are lower by two orders of magnitude but make assumptions, in particular that the neutrino is a Dirac particle. On the other hand, it is interesting to note that a reanalysis of Reines' Savannah data [8] led to a magnetic moment of the size of our upper limit, when taking into account today's improved knowledge of reactor spectra [9].

The present work is part of a PhD thesis [3]. The apparatus is being dismantled in 2003. This report is therefore the last one on our contribution to the MUNU experiment.

[1] C. Amsler *et al.* (MUNU Collaboration), Nucl.Instr.Meth.**A 396** (1997) 115.
[2] M. Avenier *et al.* (MUNU Collaboration), Nucl.Instr.Meth.**A 482** (2002) 408.
[3] O. Link, PhD thesis, Universität Zürich, in preparation.
[4] G.J. Feldman and R.R. Cousins, Phys.Rev.**D 57** (1998) 3873.
[5] C. Amsler *et al.* (MUNU Collaboration), Phys.Lett.**B 545** (2002) 57.
[6] A. I. Derbin *et al.*, JETP Lett. **57** (1993) 768.
[7] J .F. Beacom and P. Vogel, Phys. Rev. Lett. **83** (1999) 5222.
[8] F. Reines, H. S. Gurr and H. W. Sobel, Phys.Rev.Lett.**37** (1976) 315.
[9] P. Vogel and J. Engel, Phys.Rev.**D 39** (1989) 3378.

3 A New Upper Limit on the Branching Ratio for μe Conversion on Gold

Andries van der Schaaf

in collaboration with: Willi Bertl, PSI, Villigen

the measurements discussed here were performed in the year 2000 by:
W. Bertl, F. Rosenbaum and N.M. Ryskulov, Paul Scherrer Institute, R. Engfer, E.A. Hermes, G. Kurz, A. van der Schaaf and P. Wintz, Physik-Institut der Universität Zürich, J. Kuth and G. Otter, RWTH Aachen, and T. Kozlowski and I. Zychor, IPJ Swierk

(SINDRUM II)

Lepton flavour violation as observed in neutrino oscillations[1] automatically leads to charged lepton flavour violation (CLFV), i.e.

$$B(\mu \to e\gamma) = \frac{3\alpha}{32\pi} \sum_i |V^*_{\mu i} V_{ei} \frac{m^2_{\nu_i}}{M^2_W}|^2.$$

Since neutrino masses are so small this leads to a branching ratio of $O(10^{-50})$ which is out of reach of any experiment. The same mechanism in the quark sector gives $B(b \to s\gamma) \approx 10^{-4}$ due to the large top mass. The observation of CLFV would thus be an unambiguous sign of physics beyond the Standard Model and indeed, numerous extensions can be probed [1]. Neutrino-less μe conversion of μ^- bound in muonic atoms is a very sensitive probe of CLFV. The process results in mono-energetic electrons at the kinematic endpoint of normal muon decay $\mu^- \to e^- \overline{\nu_e} \nu_\mu$ which constitutes the only intrinsic background. Other potential background results from pions contaminating the beam or cosmic rays.

In the year 2000 SINDRUM II raised the sensitivity to neutrino-less μe conversion on heavy targets by two orders of magnitude. See [2] for a description of the setup and [3] for a discussion of the data below 90 MeV which are dominated by muon decay in orbit. Recently we finished the analysis and we present the resulting upper limit for the first time.

Muon stops were monitored with a germanium X-ray detector. The detection efficiency was measured with calibrated ^{137}Cs and ^{60}Co sources at three positions along the target. $4.37 \pm 0.32 \times 10^{13}$ muonic gold atoms were formed during the 81 days of data taking. Given the overall detection efficiency (including the 97% capture probability) of 7.0% this leads to a single event sensitivity of $3.26 \pm 0.22 \times 10^{-13}$.

Events were selected with electron trajectories originating in the target. Cosmic ray background was recognised by the occurence of additional prompt detector signals. Figure 3.2 shows the distibution of the decay time w.r.t. the 50 MHz cyclotron rf signal v.s. longitudinal momentum.

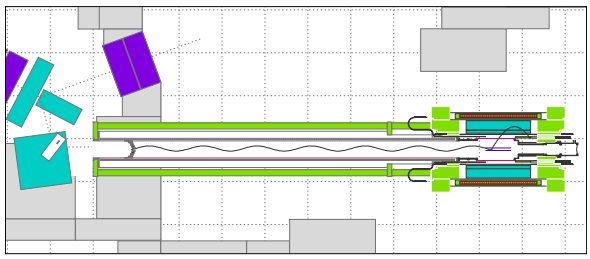

Figure 3.1: *Plan view of the experiment. The 53 MeV/c μ^- beam entering from the left is focused on a degrader situated inside a collimator at the entrance of the 9 m long transport solenoid. Whereas most muons cross the degrader only very few pions enter the solenoid. Shown is a background event in which a high-momentum e^- emitted from the degrader reaches the gold target from where it scatters into the acceptance of the SINDRUM II spectrometer.*

[1] Raymond Davis and Masotoshi Koshiba received the 2002 Nobel prize in physics for their contributions to these results.

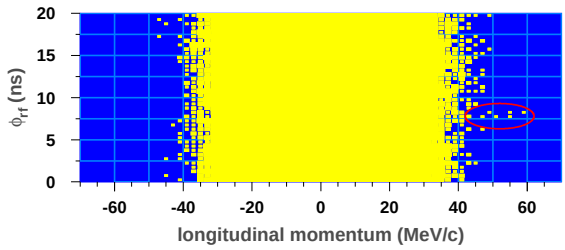

Figure 3.2: *Distribution of the phase of the track time w.r.t. cyclotron r.f. signal v.s. longitudinal momentum. The bulk of the events have a flat phase distribution as expected for muon decay in orbit which has a decay time of* ≈ 70 *ns. The red contour indicates events induced by radiative* π^- *capture in the moderator (see also Fig.3.1 and the discussion in the text).*

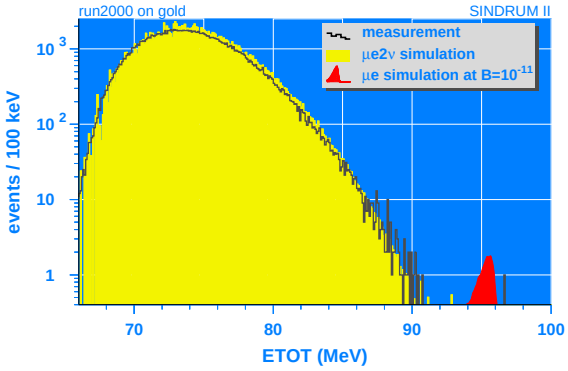

Figure 3.3: *The measured energy distribution is compared with simulated distributions for muon decay in orbit and* μe *conversion. No events are found above 100 MeV.*

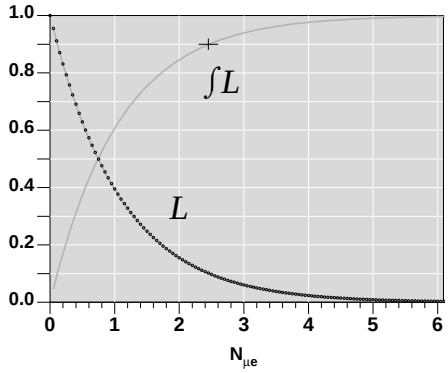

Figure 3.4: $\mathcal{L}(N_{\mu e})$ *and* $\int_0^{N_{\mu e}^{\max}} \mathcal{L}(N_{\mu e}) dN_{\mu e}$.

Indicated are some events from radiative π^- capture in the moderator followed by asymmetric $\gamma \rightarrow e^+e^-$ conversion and large-angle e^- scattering in the gold target, a process that keeps memory of the 50 MHz time structure of the proton beam. The observed rate for this background process is in rough agreement with the predictions from the GEANT simulation. Figure 3.3 shows e^- energy distribution after removal of the events in the indicated region. The steep drop below 74 MeV reflects the requirement that the electron moves at least 46 cm from the spectrometer axis.

The measured spectrum is in reasonable agreement with the prediction for decay in orbit. One event is observed around 96.4 MeV which is marginally compatible with the energy distribution expected for μe conversion. We performed a likelihood analysis of the energy distribution including a flat background from cosmic rays and radiative pion capture in addition to the distributions shown in Fig. 3.3

Figure 3.4 shows the resulting likelihood function $\mathcal{L}(N_{\mu e})$ for the expectation value of the number of μe conversion events. The 90% C.L. upper limit deduced from $\int_0^{2.45} \mathcal{L}(N_{\mu e}) / \int_0^{\infty} \mathcal{L}(N_{\mu e})$ =90% is $N_{\mu e}^{\max}(90\%\ \text{C.L.}) = 2.45$. Combined with the single event sensitivity quoted above this leads to:

$$B_{\mu e}^{\text{gold}} < 8 \times 10^{-13} \quad 90\%\ \text{C.L.}$$

This final SINDRUM II result lowers the best previous limit on μe conversion on a heavy target[4] by two orders of magnitude.

[1] Y. Kuno and Y. Okada, Rev. Mod. Phys. **73** (2001) 151.
J. Ellis, PSI Summer School, Zuoz, 2002, hep-ph/0211168.

[2] SINDRUM II Collab., Annual Report 2000-2001, Physik-Institut, Zurich University, p.8.

[3] SINDRUM II Collab., Annual Report 2001-2002, Physik-Institut, Zurich University, p.7.

[4] SINDRUM II Collab., W. Honecker *et al.*, Phys.Rev.Lett.**76** (1996) 200.

4 The Scalar Glueball

C. Amsler

The Crystal Barrel experiment which ran at CERN's Low Energy Antiproton Ring until 1996 discovered several new mesons, among them the $J^{PC} = 0^{++}$ isoscalar meson $f_0(1500)$ and the 0^{++} isovector $a_0(1450)$ (for a review see ref. [1]). We have shown several years ago that the $f_0(1500)$ was an excellent candidate for the ground state glueball expected by lattice gauge theories around this mass [2]. In the present report we argue that recent results from LEP indicate that $f_0(1500)$ couples only weakly to photons. This strengthens the evidence that $f_0(1500)$ contains a large fraction of glue. On the other hand, a reasonable $q\overline{q}$ nonet for the scalar mesons can be built with the other known mesons, among them the $f_0(1710)$ which appears to be the $s\overline{s}$ state in the nonet [3].

The $f_0(1370)$ and $f_0(1500)$ mesons were established by Crystal Barrel, first in their $\eta\eta$ and $\pi^0\pi^0$ decay modes [4]. The $f_0(1370)$ is broad ($\sim$ 400 MeV) while the $f_0(1500)$ is rather narrow ($\sim$ 100 MeV). Their $K\bar{K}$ decay rates were measured by Crystal Barrel [5]. They are small compared to $\pi\pi$, indicating that neither state can have a large $s\overline{s}$ component [3].

The WA102 Collaboration at CERN observed the f_0(1370), $f_0(1500)$ and $f_0(1710)$ decaying to $K\bar{K}$ and $\pi\pi$ in pp central production at 450 GeV [6]. For f_0(1370) and $f_0(1500)$, the $\pi\pi$ decay mode was favoured over $K\overline{K}$. Hence both $f_0(1370)$ and $f_0(1500)$ do not have large $s\bar{s}$ components, in agreement with Crystal Barrel results. However, for $f_0(1710)$, $K\bar{K}$ decay dominates $\pi\pi$ by a large factor, suggesting that this state must be dominantly $s\overline{s}$.

The $f_0(1710)$ was also searched for in $\overline{p}p$ annihilation into three pseudoscalar mesons with 900 MeV/c antiprotons [7]. For example, in $\overline{p}p \to \pi^0\eta\eta$ the $f_0(1710) \to \eta\eta$ is not observed, while $f_0(1500)$ is clearly seen. This is prima facie evidence that $f_0(1710)$ cannot have a large $u\overline{u} + d\overline{d}$ component.

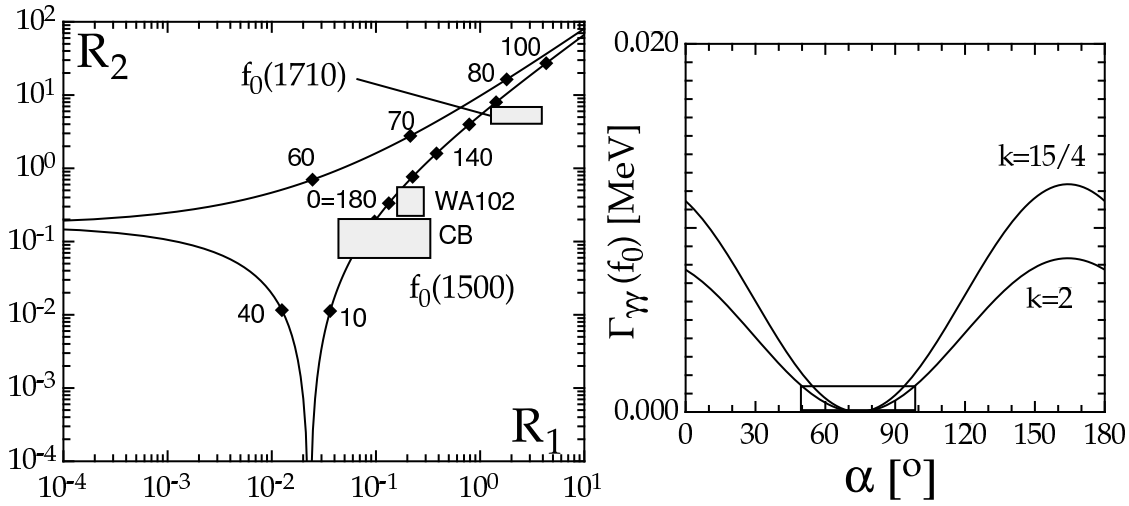

Figure 4.1: *Left: relative decay branching ratio* $R_2 = B(K\overline{K})/B(\pi\pi)$ *vs.* $R_1 = B(\eta\eta)/B(\pi\pi)$ *as a function of mixing angle* α *(in deg.); right: predicted* $\gamma\gamma$*-width for the* $f_0(1500)$*. The experimental upper limit is shown by the box (from ref.[3]).*

For a more quantitative statement, look at fig. 4.1 (left) which shows the ratio of branching ratios R_2 = $B(K\overline{K})/B(\pi\pi)$ vs. R_1 = $B(\eta\eta)/B(\pi\pi)$ for scalar mesons, apart from phase space factors. Data from Crystal Barrel and WA102 (2σ boundaries) on the $f_0(1500)$ and $f_0(1710)$ are compared with

predictions from SU(3). The angle α describes the mixing of the two nonet isoscalar mesons,

$$|f_0\rangle = \cos\alpha\,|n\overline{n}\rangle - \sin\alpha\,|s\overline{s}\rangle \quad \text{with} \quad |n\overline{n}\rangle \equiv \frac{u\overline{u}+d\overline{d}}{\sqrt{2}}\,. \tag{4.2}$$

Hence for α = 0, f_0 is pure $n\overline{n}$ and for α = 90°, pure $s\overline{s}$. Assuming that $f_0(1500)$ and $f_0(1710)$ are $q\overline{q}$ states, we conclude from fig. 4.1 (left) that the former is mainly $n\overline{n}$ (-10° $\leq \alpha \leq$ 5°) and the latter mainly $s\overline{s}$ ($\alpha \simeq 117°$).

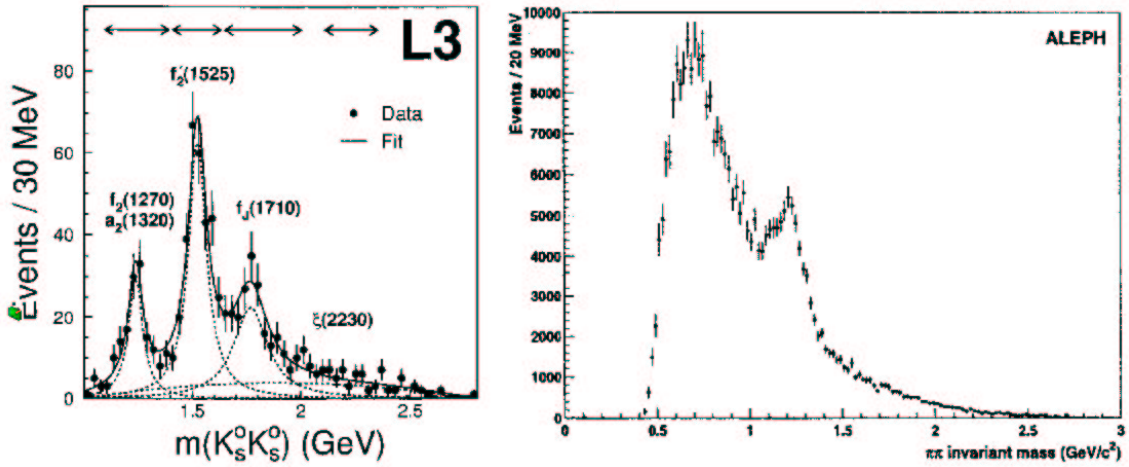

Figure 4.2: *Left: K_SK_S mass distribution in $\gamma\gamma$-collisions at LEP/L3 (from ref. [8]); right: $\pi^+\pi^-$ mass distribution from LEP/ALEPH showing only the $f_2(1270)$ (from ref.[9]).*

Let us now deal with two-photon processes which are useful to probe the charge content of mesons through their electromagnetic couplings. Glueballs do not couple directly to photons and their production should therefore be suppressed in $\gamma\gamma$-processes. New data in $\gamma\gamma$-collisions have been presented by the LEP collaborations. L3 observes three peaks below 2 GeV in the K_SK_S mass distribution [8] (fig. 4.2, left), but the spin 0 $f_0(1500)$ is not seen. Since $f_0(1500)$ does not couple strongly to $K\bar{K}$, this is perhaps not surprising. However, ALEPH studying the reaction $\gamma\gamma \to \pi^+\pi^-$, does not observe $f_0(1500)$ either [9] (see fig. 4.2, right). An upper limit of 1.4 keV (95 % CL) can be derived for its $\gamma\gamma$-width from the ALEPH result [9], using the known $\pi\pi$ decay branching ratio of the $f_0(1500)$.

The $\gamma\gamma$-width of a $q\overline{q}$ state can be predicted from SU(3). Apart from an unknown nonet constant C and for a meson of mass m:

$$\Gamma_{\gamma\gamma} = C(5\cos\alpha - \sqrt{2}\sin\alpha)^2 m^3\,. \tag{4.3}$$

The $\gamma\gamma$-width of a scalar meson is related to that of the corresponding tensor by

$$\Gamma_{\gamma\gamma}(0^{++}) = k\left(\frac{m_0}{m_2}\right)^3 \Gamma_{\gamma\gamma}(2^{++})\,, \tag{4.4}$$

with obvious notations. Here the factor $k = 15/4$ arises from spin multiplicities in a non-relativistic calculation, while relativistically $k \simeq 2$. Figure 4.1 (right) shows the prediction for the $\gamma\gamma$ partial width of the $f_0(1500)$ as a function of α, together with the ALEPH upper limit [3]. Assuming a $q\overline{q}$ structure, one concludes that $f_0(1500)$ is dominantly $s\overline{s}$ (50° $\leq \alpha \leq$ 100°), at variance with the hadronic results discussed above.

This contradiction indicates that $f_0(1500)$ is not $q\overline{q}$ and the lack of $\gamma\gamma$-coupling points to a large gluonic content. Obviously, some mixing with nearby $q\overline{q}$ states is possible [2] but more accurate

Table 4.1: *Classification of the low-mass scalar mesons showing the scattering resonances below 1 GeV and the ground state $q\overline{q}$ nonet (1^3P_0).*

State	Γ [MeV]	Isospin	Nature
$a_0(980)$	~ 50	1	$K\overline{K}, qq\bar{q}\bar{q}$
$f_0(980)$	~ 50	0	$K\overline{K}, qq\bar{q}\bar{q}$
$f_0(600)$	~ 800	0	meson-meson
$\kappa(800)$?	~ 600	1/2	resonances
$a_0(1450)$	265	1	$u\bar{d}, d\bar{u}, d\bar{d} - u\bar{u}$
$f_0(1370)$	~ 400	0	$d\bar{d} + u\bar{u}$
$f_0(1710)$	125	0	$s\bar{s}$
$K_0^*(1430)$	294	1/2	$u\bar{s}, d\bar{s}, s\bar{u}, s\bar{d}$

data in $\gamma\gamma$-collisions and theoretical guidance on the strength of $\gamma\gamma$-couplings to glueballs are needed for a more quantitative statement on mixing. Table 4.1 shows an increasingly popular classification scheme for the low lying scalar nonets [10]. The lower mass nonet is made of four-quark states and/or meson-meson resonances. The ground state (1^3P_0 or 0^{++}) $q\overline{q}$ nonet lies in the 1400 MeV region. The supernumerary $f_0(1500)$ (not shown) is dominantly glue.

[1] For a review see C. Amsler, Rev. Mod. Phys. **70** (1998) 1293.

[2] C. Amsler and F.E. Close, Phys. Rev. **D 53** (1996) 295
see also F.E. Close and A. Kirk, Eur. Phys. J **C 21** (2001) 531.

[3] C. Amsler, Phys. Lett. **B 541** (2002) 22.

[4] C. Amsler et al., Phys. Lett. **B 353** (1995) 571; **B 342** (1995) 433.

[5] A. Abele et al., Phys. Lett. **B 385** (1996) 425.

[6] D. Barberis et al., Phys. Lett. **B 479** (2000) 59.

[7] C. Amsler et al., Eur. Phys. J. **C 23** (2002) 29.

[8] M. Acciarri et al., Phys. Lett. **B 501** (2001) 173.

[9] R. Barate et al., Phys. Lett. **B 472** (2000) 189.

[10] C. Amsler and N. Törnqvist, Physics Reports (in preparation).

5 Production and Spectroscopy of Antihydrogen

C. Amsler, A. Glauser, O. Iannarelli, D. Lindelöf, N. Madsen, H. Pruys, and C. Regenfus

in collaboration with:
CERN, University of Aarhus, Brescia, Genoa, Pavia, Rio de Janeiro, Swansea, Tokyo

(ATHENA Collaboration)

The final goal of the ATHENA experiment is a test of the CPT symmetry in the baryon and lepton sectors by comparing the energy levels of antihydrogen and hydrogen atoms. The long lifetime (122 ms) of the metastable (anti-) hydrogen 2s level is associated with a relative natural line width of 5×10^{-16} for the 1s-2s transition, which can be exploited by two-photon laser spectroscopy. Such high precision measurements would also give valuable experimental information on the gravitational interaction of antihydrogen, because a change in the 1s-2s transition frequency could also originate from a different redshift of antihydrogen and hydrogen atoms in the gravitational field of the earth.

Antihydrogen forms when antiprotons are mixed with cold positrons. In 2001-2002 we demonstrated trapping, cooling and transfer of $\sim 10^4$ cold antiprotons into the mixing trap. In the positron accumulator 150 million positrons were routinely accumulated within 5 minutes. Excellent vacuum conditions could be maintained during and after the transfer process, with a lifetime of antiprotons and positrons exceeding several hours. In 2002 we demonstrated for the first time the production of cold antihydrogen atoms in large quantities [1]. The observation of antihydrogen through its annihilation was achieved with the high granularity detector built in our institute. These results were obtained following improvements to the apparatus, in particular a more efficient positron transfer, the implementation of non-destructive plasma diagnostics, and better signal-to-noise ratio for 511 keV photon detection.

Antihydrogen was produced with $\bar{p}e^+$ mixing cycles of about 3 minutes duration which could be repeated every 500 seconds thanks to our fast positron accumulator. At the beginning of each mixing cycle about 10'000 $\bar{p}$ with kinetic energy of $\sim$ 50 eV entered a large and dense positron plasma of typically 70 million e^+. Rapid cooling of the antiprotons in less than 100 msec was observed and the antihydrogen detector registered a rapid increase in the annihilation rate. From the analysis of several hundred cycles a clear signal was identified from unconfined neutral antihydrogen atoms hitting the trap wall. The antihydrogen signal disappeared when the positron plasma was heated to 3500 K.

We refer to previous annual reports and to the experimental proposal [2] for details on the apparatus.

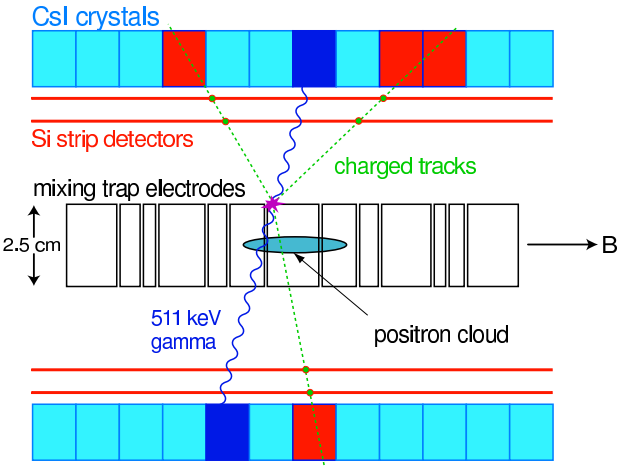

Figure 5.1: *Principle of antihydrogen detection (see text).*

5.1 Development of the antihydrogen detector

The detector (fig. 5.1) features two cylindrical layers of double-sided silicon microstrips (8192 channels) and 16 rows of 12 pure CsI crystals ($17 \times 13 \times 17.5$ mm^3) read out by avalanche photodiodes. It is located in the small space between the (37 mm diameter) UHV vessel of the combination trap and the (70 mm diameter) cold bore of the 3 T superconducting magnet, where vacuum conditions of 10^{-7} mbar and a temperature of 140 K prevail.

The antiproton and positron cease to be confined in the combination trap once bound to antihydrogen. The antiatom therefore collides after less than 1 μs with the surface of the trap electrode. On average three charged pions and three high energy (50-500 MeV) photons are produced by the annihilation of the antiproton, while the positron annihilates with an electron, generating two back-to-back 511 keV photons. The unique identification of antihydrogen is based on the 180° opening angle between the two 511 keV photons, as seen from the antiproton annihilation vertex. A 5μs timing coincidence between the detection of the pions and two 511 keV photons is also required.

Pure CsI was chosen because of the excellent light yield at low temperature (50'000 photons/MeV at 80 K [3]), together with a total absorption probability of 20% for 511 keV photons. Initially, the crystals were coupled to pn photodiodes, but the quantum efficiency decreased dramatically below 450 nm, especially at low temperatures. A systematic study of this effect was undertaken by building an optical spectrometer based on an Echelette grating (fig. 5.2) [4]. The selected light (resolution of

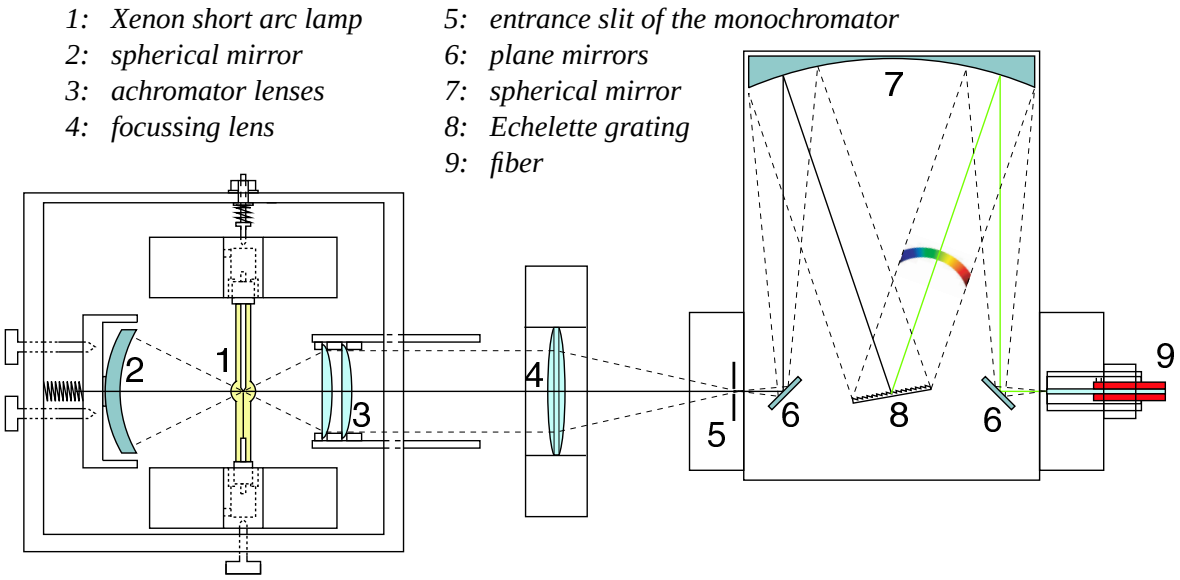

Figure 5.2: *Optical spectrometer (after [4]).*

2 nm FWHM) exiting the spectrometer was transferred by an optical fiber to a liquid nitrogen cell containing the test photodiodes. Figure 5.3 shows the relative quantum efficieny as a function of temperature and wavelength (a unit relative efficiency corresponds to an absolute efficiency of 62%, obtained by comparison with a commercially calibrated photodiode). One observes a fast drop in the detection efficiency of blue light with decreasing temperature. The reason for this behaviour is not quite understood. In addition, the performance of our photodiodes deteriorated with time (apparently due to corrosion from the iodine in CsI). In 2002 we therefore replaced all photodiodes by avalanche photodiodes (APD) which have the advantage of a large gain and hence a much better signal-over-noise ratio. Figure 5.4 shows a photograph of one of the 300 APD's purchased from CMS (a small batch from their 160'000 supply!). The gain of the APD as a function of bias voltage was measured

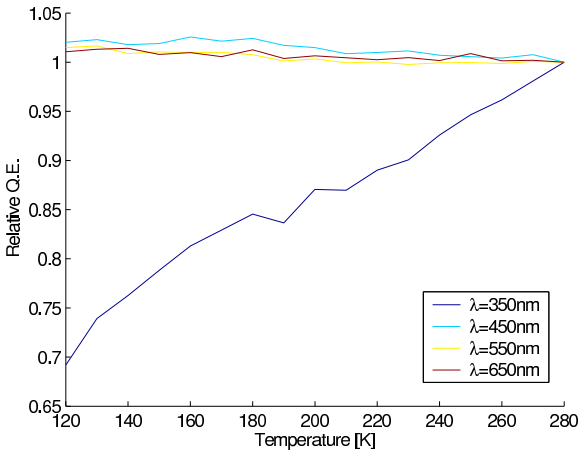

Figure 5.3: *Relative quantum efficiency of a photodiode as a function of temperature and wavelength.*

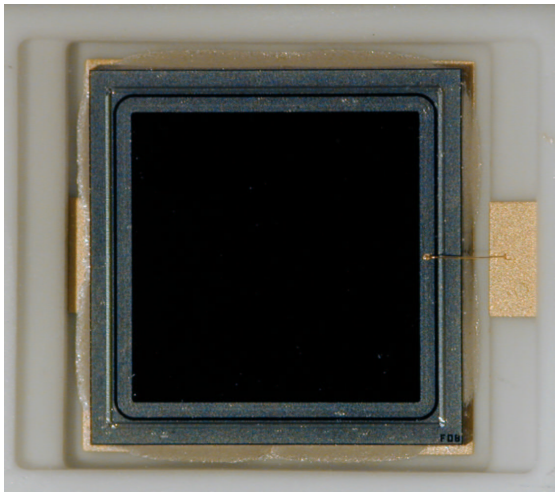

Figure 5.4: *Avalanche photodiode (5×5 mm^2) purchased from the CMS experiment. The epoxy window was removed with sulfuric acid.*

with a pulsed light emitting photodiode (fig. 5.5). The plateau at low voltage corresponds to unit gain, the rise is due to the generated avalanche in the diode. The voltage at which multiplication starts depends on temperature, due to mobility which is a function of temperature. The advantage of APD's for ATHENA is the very low dark current at low temperature, so that the signal can be amplified to very high values. We settled for a gain of 20 corresponding to a signal-over-noise ratio of about 100.

The detector is now working to our full satisfaction. Figure 5.6 shows the measured photon energy spectrum with APDs from positron annihilation in the combination trap, summed over all crystals. The peak at 511 keV has a resolution of 18% FWHM and is well separated from the Compton plateau and the noise.

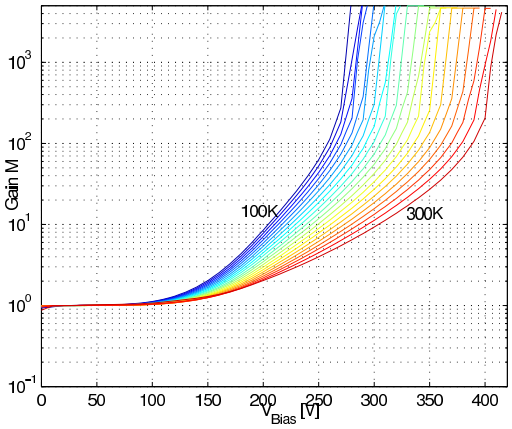

Figure 5.5: *Gain of an avalanche photodiode as a function of bias voltage V for different temperatures. The curves are fits with exponential functions of the form* $a + b\exp(cV)$.

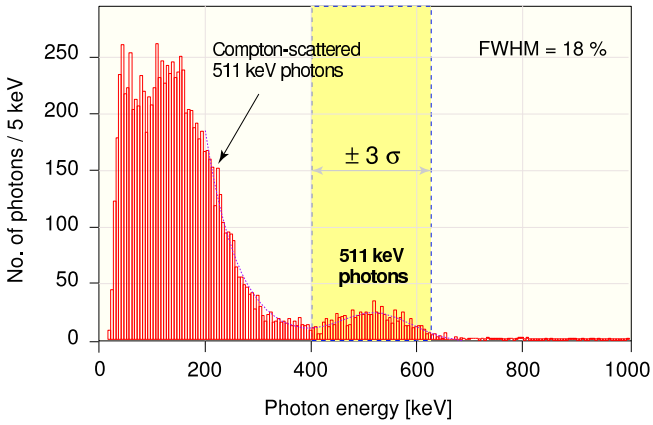

Figure 5.6: *Measured photon energy distribution for positron annihilation in the combination trap (sum over all 192 crystals).*

5.2 Positron heating

Characteristics of the positron plasma such as shape, dimension, density and temperature, are important parameters for the antiproton-positron interaction. For instance, the temperature dependence of antihydrogen formation depends crucially on the formation mechanism, spontaneous radiative transitions (which populates the lower energy levels) or three-body combination (which populates the higher energy states).

The positron plasma is confined in the central part of the mixing trap by the harmonic axial potential. The positrons cool to the ambient temperature of the surrounding trap walls ($\simeq$ 15 K) through synchrotron radiation in the 3 T magnetic field, with a typical time constant of 400 msec. The shape of the plasma is a prolate ellipsoid, 3 cm long and 4 mm in diameter, with a density of $2.5\times\ 10^8$ cm^{-3}. We use a non-destructive diagnostic to control and monitor the positron plasma parameters. It is based on the excitation of the first two axial resonant plasma oscillation modes (dipole, quadrupole) by applying a sinusoidal perturbation to one electrode, and then observing the induced current in a pick-up electrode [5]. The plasma density and shape of the plasma is extracted from the measured frequencies of the dipole and quadrupole modes [6]. By applying an RF signal to one of the trap electrodes that sweeps a frequency band near the dipole frequency (21 MHz), the plasma can be heated in a controlled way, depending on the heating amplitude of typically a few mV. Antihydrogen formation can therefore be controlled and even quenched by controlling the positron plasma temperature. The dependence of the plasma temperature shift ΔT on the excitation voltage V_d was measured and is shown in fig. 5.7.

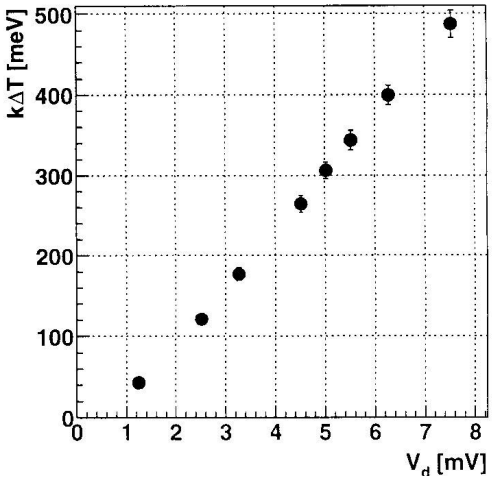

Figure 5.7: *Plasma temperature variation ΔT vs. RF heating amplitude V_d.*

5.3 Antihydrogen production

A positron-antiproton mixing cycle lasts for 500 s and starts with the transfer of about $7\ \times\ 10^7$ positrons into the combination trap, where they cool to $\simeq$ 15 K. A W-shaped potential (nested trap) is then formed around the positron plasma. Positrons are confined in the central part of the potential. Simultaneously, 10'000 antiprotons are captured, cooled by electrons in the capture trap and then launched into the combination trap. The antiproton and the positron plasma mix for about 3 minutes, after which all particles are dumped and the process is repeated.

Positron cooling of antiprotons was reported earlier by the ATRAP collaboration [7]. In ATHENA, we studied this process with 10'000 antiprotons crossing a much larger and denser positron plasma. Antiprotons were stored in a side potential well and then launched into the mixing region with a kinetic energy of $\simeq$ 50 eV. Antiprotons traversing the positron plasma loose energy through collisions. Evidence for positron cooling was obtained by lowering the potentials of the side wells in the nested trap and measuring the number of annihilating antiprotons as a function of voltage. The results show that, after a short initial cooling time of $\simeq$ 500 ms, the two plasmas separate both in longitudinal and radial direction, leading to a decreasing overlap and hence interaction between the two antiparticle species.

Annihilation events trigger the silicon detector. In the offline analysis antiproton annihilation vertices are reconstructed from the silicon detector data. For each reconstructed vertex, we search for two well separated 511 keV photon hits in the crystal data. To search for antihydrogen events we calculate the opening angle $\Theta_{\gamma\gamma}$, between the γ-directions. For an antihydrogen event, this angle should be 180°.

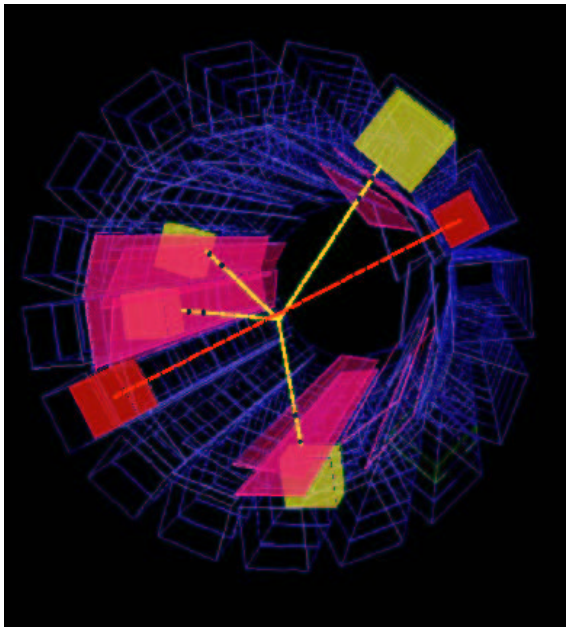

Figure 5.8: *Reconstructed antihydrogen annihilation event with four charged particles from a common vertex, and two isolated 511 keV photons that appear back-to-back when looking from the vertex.*

Figure 5.8 shows an event compatible with antihydrogen annihilation.The spatial resolution on the annihilation vertex is mainly determined by the unknown track curvature in the 3 T magnetic field. The charged particle vertex resolution in radial direction was measured experimentally by letting antiprotons annihilate on the trap electrodes (radius 12.5 mm). The measured distribution agrees well with the Monte Carlo prediction and the radial resolution is $\sigma \simeq 4$ mm. The simulation gives a probability of 50 % for vertex reconstruction, in agreement with measurement. This probability is determined by the solid angle of the outer silicon layer and the trigger and detector efficiencies. The interaction probability of 511 keV photons in a crystal is about 20 %. Taking into account the solid angle of the CsI calorimeter, crystal inefficiencies and all cuts, the detection efficiency for both photons is about 1 %, leading to a total efficiency for event reconstruction of about 0.5 %.

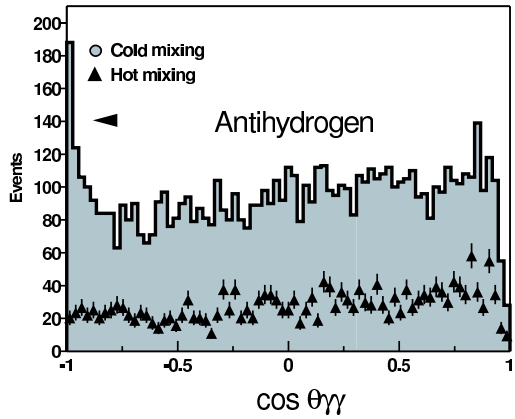

The histogram shows cold mixing data (7'125 events). The triangles represent hot mixing data, scaled by 1.6 to the same number of mixing cycles (from ref. [1]).

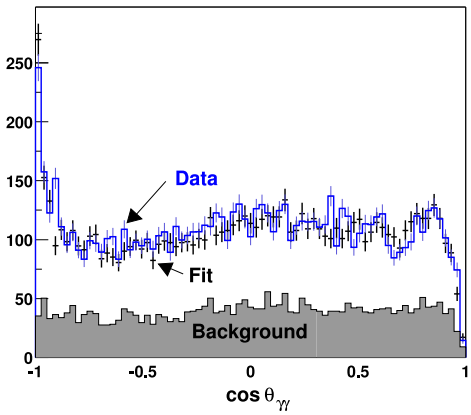

Fit to the opening angle distribution for cold mixing using simulated data for antihydrogen annihilation and antiproton background from hot mixing (for a slightly larger data sample).

Figure 5.9: *Distributions of the opening angle* $\Theta_{\gamma\gamma}$.

Figure 5.9 shows the opening angle distribution from 165 mixing cycles of antiprotons with cold positrons. The peak at cos $\Theta_{\gamma\gamma}$ = -1 is clearly observed. It contains 131 $\pm$ 22 events, corresponding

to a statistical significance of more than 5σ. The triangles in fig. 5.9 (left) represent hot mixing data in which no antihydrogen formation is expected. The flat background from spatially uncorrelated two-photon events is due to high-energy photons from antiproton annihilations on the wall, producing electromagnetic showers with secondary positrons. This process does not produce a peak at 180 °.

We have studied the relative contribution of antihydrogen and antiproton annihilations. Antihydrogen atoms annihilate on a trap electrode. On the other hand, antiprotons are confined by the fields and oscillate in the centre of the trap, where they may annihilate with rest gas or with positive ions trapped with the positron plasma. We have measured the $(x - y)$ vertex distribution (fig. 5.10) for antiproton mixing with cold and hot positron plasma. For cold mixing, a clear image of the trap electrodes is obtained, consistent with antihydrogen annihilations on the wall. The distribution for hot mixing, also shown in fig. 5.10, has a very different shape. Antihydrogen production is suppressed, and stored antiprotons annihilate with trapped ions (or with rest gas) in the centre of the trap. The relative contribution of antihydrogen versus antiproton background in the cold mixing data was determined by fitting the $x - y$ distribution with a simple model consisting of two contributions, (i) antihydrogen annihilation on the trap wall (from Monte Carlo simulation) and (ii) antiproton-ion annihilation inside the trap volume (from the hot mixing measurement). The fit gave a relative contribution of 35 $\pm$ 10% background in fig. 5.9. The same result is obtained by fitting the $\Theta_{\gamma\gamma}$ distributions for hot and cold mixing. The result is shown in fig. 5.9 (right). Hence about 65 % of the events in the $\Theta_{\gamma\gamma}$ distribution are actually due to antihydrogen formation, where at least one of the two 511 keV γ's stems from background. The data collected in 2002 correspond to the production of about 10^6 antihydrogen atoms in the ATHENA apparatus. Figure 5.11 shows the number of reconstructed vertices as a function of time during a typical mixing cycle. Immediately after antiproton injection a sharp increase in the number of annihilations is observed by the detector. The event rate is above 100 Hz during the first second. The annihilation rate then decreases slowly to 1 Hz after 3 minutes. Fast cooling antiprotons within the positron cloud lead to a high initial antihydrogen rate. As most of their kinetic energy is lost the remaining antiprotons are located in the side wells or are radially separated from the positron plasma, thus reducing the probability of antihydrogen formation.

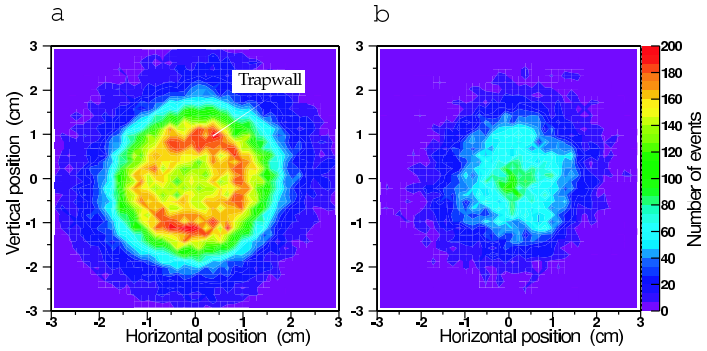

Figure 5.10: *Transverse vertex positions for mixing with cold positrons (left) and hot positrons (right) (from ref. [1]).*

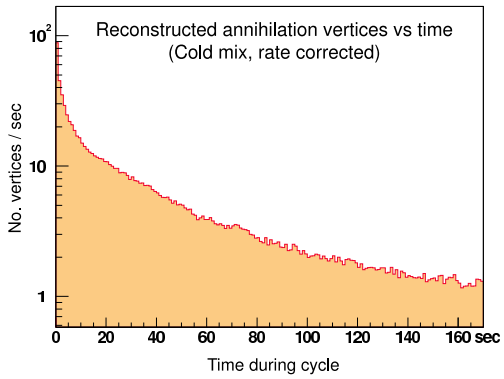

Figure 5.11: *Number of reconstructed annihilation vertices as a function of time after injection of the antiprotons into the positron plasma.*

We studied also the temperature dependence of antihydrogen production. The distributions show that for increasing plasma temperature, the relative size of the back-to-back peak decreases and there is clear evidence that antihydrogen production takes place even at room temperature (30 meV). This speaks in favour of radiative combination as the dominant formation mechanism, since three-body combination is only expected to occur at very low temperatures (much below 10 meV). Furthermore the temperature dependence of antihydrogen production seems to follow the simple $1/T$ dependence consistent with radiative combination. These are very good news for atomic level spectroscopy, since we will require antihydrogen to be in the 1s state.

The dependence on temperature can be used for pulsed antihydrogen production. By switching on the RF heating of positrons, antihydrogen production can be switched off within $\sim$ 100 ms. The positron plasma then cools down by synchrotron radiation after switching the RF heating off, and antihydrogen production resumes within less than 1 second (fig. 5.12).

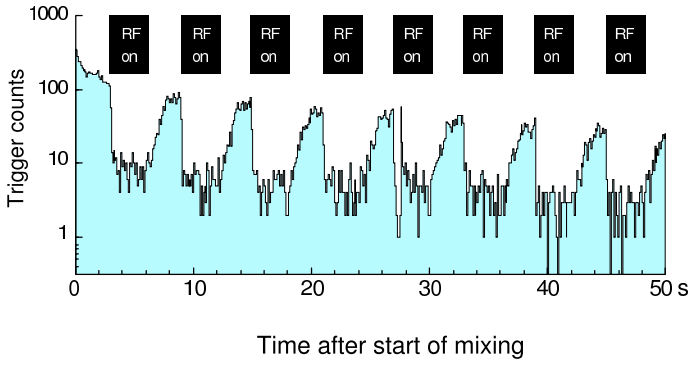

Figure 5.12: *Annihilation trigger rate with and without RF heating of the plasma during 3s intervals.*

5.4 R & D for laser spectroscopy

Until the one year accelerator shutdown in 2005 we will study antihydrogen production and its dependence on parameters such as the number, density and temperature of antiprotons and positrons. Currently roughly 15-20 % of all antiprotons in the mixing trap form antihydrogen, and we are studying ways to increase this number. Stimulated combination by irradiation with laser light is also being investigated.

In 2002 the Zurich group initiated the first part of the spectroscopy phase, the construction of a laser system to generate the 243 nm light for 1s-2s two-photon spectroscopy in antihydrogen [8]. No laser-sources are available in the ultra-violet region. We therefore use a non-linear technique to generate the 243 nm light from a laser source of longer wavelength. Figure 5.13 shows schematically the laser system that is currently being implemented [8]. Most of the equipment was provided by the University of Aarhus. The system consists first of a Coherent Innova Sabre - Kr^+ ion laser that emits 4 W in the range 406 nm to 415 nm. The Kr^+ ion laser pumps a Coherent 899-21 Ring Dye laser that circulates Coumarin 102 dye which emits in the range 460 nm to 516 nm. The dye laser is necessary to introduce tunability in the system, as an ion laser emits only at specific wavelengths. The dye laser is tuned to a wavelength of 486.2 nm which is twice the wavelength of the two-photon 1s-2s transition in antihydrogen. About 500 mW of light is emitted at 486.2 nm.

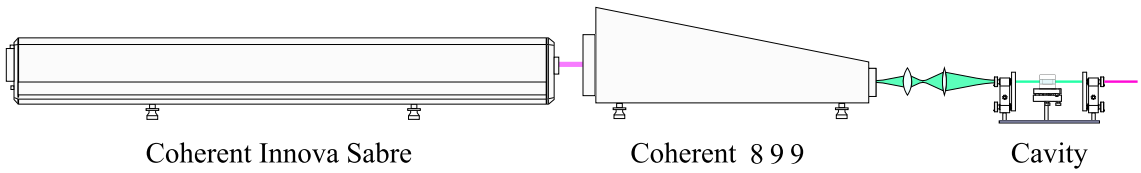

Figure 5.13: *Sketch of the laser chain to generate the 243 nm light for 1s-2s two-photon spectroscopy.*

The light from the dye laser is sent into an external frequency doubling cavity containing a nonlinear crystal. The second harmonic generation power in the crystal is maximum when the refractive indices n for the fundamental and the second harmonics are equal. Since the refractive index depends on frequency, a birefringent crystal with a suitably oriented optical axis is used, in which the ordinary ray is chosen for the fundamental frequency and the extraordinary ray for the second harmonic, i.e. $n_o(\omega) = n_e(2\omega)$. Losses are reduced by using a crystal cut such that the light with fundamental frequency traversing the crystal penetrates the crystal under the Brewster angle. Under this angle the polarisation parallel to the plane formed by the incident beam and the normal to the crystal surface is not reflected but transmitted into the crystal. The cavity that was chosen is shown in fig. 5.14 (for details see ref. [8]). It consists of a Brewster cut rhomb shaped beta barium borate (BBO) crystal with a side length of 8 mm. The light from the dye laser enters from the right. The convex mirrors have a reflection coefficient of 100% for the first harmonic and a transmission coefficient of 95 % for the second harmonic. The locking beam is sent to a photodiode for frequency locking. The external cavity is expected to deliver about 50 mW of laser light at 243.1 nm. In 2002 we installed the clean room and most of the laser system. The various components such as mirrors and the BBO crystal have been purchased. The cavity assembly is close to completion. The setting up of the dye laser was complicated by technical problems. Its operation is now stable but only at about half the nominal power. This is sufficient for the first tests of the frequency doubling, which we expect to commence shortly.

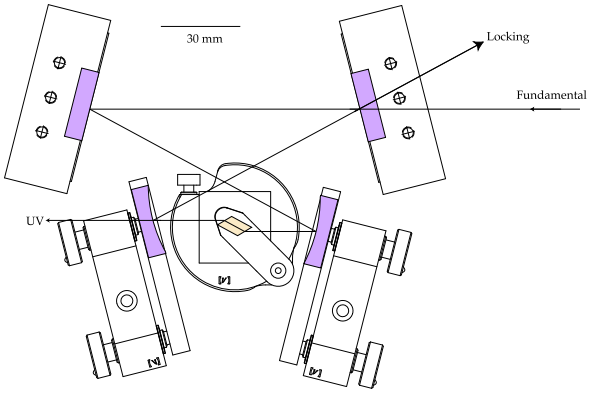

Figure 5.14: *External cavity with BBO crystal (yellow) for second harmonic generation (see text).*

[1] M. Amoretti *et al.*, Nature **419** (2002) 456.

[2] ATHENA proposal, M.H. Holzscheiter et al., CERN-SPSLC/P302, October 1996, see also http://www.cern.ch/athena/.

[3] C. Amsler *et al.*, Nucl. Instr. Meth. in Phys. Res. **A 480** (2002) 494.

[4] A. Glauser, Diplomarbeit, Universität Zürich, 2003.

[5] M. Amoretti *et al.*, submitted to Phys. Rev. Lett.

[6] D. H. E. Dubin, Phys. Rev. Lett. **66** (1991) 2076.

[7] G. Gabrielse *et al.*, Phys. Lett. **B 507** (2001) 1.

[8] O. Iannarelli, Diplomarbeit, Universität Zürich, in preparation.

6 Rare Kaon Decays at Brookhaven AGS

H. Kaspar (visiting scientist), P. Robmann, A. van der Schaaf,
S. Scheu, A. Sher and P. Truöl

The two projects E-865 and KOPIO discussed below have used or will use the unique low-momentum neutral and charged kaon beams available at Brookhaven National Laboratory's Alternating Gradient Synchrotron (AGS). Although BNL E-865 finished data-taking four years ago a small part of the analysis is still in progress. KOPIO on the other hand is still in its planning phase. The experimental proposal has been reviewed and approved for funding by the U.S. National Science Foundation.

6.1 BNL E-865: a search for lepton flavor violation in K^+ decay

in collaboration with:
Paul–Scherrer–Institut, CH-5234 Villigen; Brookhaven National Laboratory, Upton, NY-11973, USA; University of New Mexico, Albuquerque, NM-87131, USA; University of Pittsburgh, Pittsburgh, PA-15260, USA; Yale University, New Haven, CT-06511, USA; Institute for Nuclear Research, Academy of Sciences 117 312 Moscow, Russia

While the analysis of the data for the lepton flavor violating decay $K^+ \to \pi^+\mu^+e^-$ ($K_{\pi\mu e}$) [1], the primary goal of experiment E-865 at the Brookhaven AGS [2], is still in progress, the analysis of the $K^+ \to \pi^0 e^+\nu_e$ (K^+_{e3}) decay channel has been concluded last year [3; 4]. Furthermore the definitive publication on the $K^+ \to \pi^+\pi^-e^+\nu_e$ (K^+_{e4}) results has been submitted [5].

6.1.1 $K^+ \to \pi^0 e^+\nu_e$ (K^+_{e3})

During the last two weeks of data taking around Christmas 1998 we collected 70,000 events from the decay with the purpose to measure the branching ratio for this decay mode as accurately as possible. This branching ratio and that of the analogous decay of the neutral kaon $K^0_L \to \pi^\pm e^\mp \overline{\nu_e}(\nu_e)$ (K^0_{Le3}) are the primary sources for the determination of the Cabbibo-Kobayashi-Maskawa (CKM) matrix element V_{us}, linking the first and the second quark generation. One of several relations resulting from the unitarity of the CKM-matrix relates the elements of the first row as

$$\sum_i |V_{ui}|^2 = |V_{ud}|^2 + |V_{us}|^2 + |V_{ub}|^2 = 1$$

With $V_{ud} = 0.9740 \pm 0.0005$ determined from nuclear superallowed Fermi β-decays or with $V_{ud} = 0.9745 \pm 0.0016$ from neutron β-decay [6], $V_{us} = 0.2196 \pm 0.0023$ and $V_{ub} = 0.0036 \pm 0.0010$ [7] one obtains

$$\begin{aligned} \textstyle\sum_i |V_{ui}|^2 &= 0.9968 \pm 0.0014 \qquad \text{(nuclear)} \\ &= 0.9978 \pm 0.0033 \qquad \text{(neutron)}\,. \end{aligned}$$

The deviation from unitarity at two standard deviation level has been discussed for quite some time, and e.g. lead to considerable experimental activity remeasuring decay asymmetries and correlations in neutron decay, where the data [8] are still somewhat inconsistent.

On the other hand the value for V_{us} quoted above stems from pre-1984 K_{e3} measurements with fairly low statistics. The second source for V_{us}, hyperon decay suffers from larger uncertainties arising from the axial-vector couplings. K_{e3} is a pure Fermi transition

$$\langle \pi^0(p)|V_\mu|K^+(k)\rangle = \frac{1}{\sqrt{2}}\left((k+p)_\mu f_+(q^2) + (k-p)_\mu f_-(q^2)\right)\ ,\ q^2 = (k-p)^2\ ,$$

leading to the transition rate

$$d\Gamma(K^+_{e3}) = \frac{G_F^2 M_K^5}{64\pi^3}|V_{us}|^2|f_+(0)|^2\left(1+\lambda_+\frac{q^2}{m_\pi^2}\right)dq^2\ .$$

The contribution from $f_-(t)$ has been neglected because it enters multiplied with m_e^2/m_K^2. In order to determine V_{us} one needs to measure the K_{e3} branching ratio and the slope factor λ_+, evaluate the radiative corrections and calculate $f_+(0)$. The latter is done in the frame of chiral perturbation theory pioneered for K_{e3} by Leutwyler and Roos [10], which leads to the value of V_{us} quoted above. In the SU(3)-limit $f_+(0) = 1$ holds (Adamollo-Gatto theorem). The latest $\mathcal{O}(p^4)$ calculation including an estimate of the $\mathcal{O}(p^6)$ corrections yields $f_+(0) = 0.9874 \pm 0.0084$ [9], leading to $V_{us} = 0.2207 \pm 0.0024$. The nuclear value for V_{ud} combined with unitarity would require $V_{us} = 0.2265 \pm 0.0034$ and hence a K^+_{e3} branching ratio 5% larger than the measured one.

In our experiment [3] the π^0 is detected via its Dalitz decay $\pi^0 \to e^+e^-\gamma$ and the K^+_{e3} branching ratio (B) is measured relative to the sum of all other decays involving π^0: $K^+ \to \pi^0\mu^+\nu_e$ ($K^+_{\mu 3}$), $K^+ \to \pi^0\pi^+$ ($K^+_{\pi 2}$) and $K^+ \to \pi^0\pi^0\pi^+$ ($K^+_{\pi 3}$). We measured

$$\frac{\mathrm{B}(K^+_{e3})}{0.990\ \mathrm{B}(K^+_{\mu 3}) + 0.990\ \mathrm{B}(K^+_{\pi 2}) + 0.995\ \mathrm{B}(K^+_{\pi 3})} = 0.1998 \pm 0.0008\ \text{stat.}\ \pm 0.0036\ \text{syst.}\ ,$$

which using the Particle Data Group values [7] in the denominator leads to

$$\mathrm{B}(K^+_{e3}) = (5.16 \pm 0.02\ \text{stat.}\ \pm 0.09\ \text{syst.} \pm 0.04\ \text{norm.})\%$$

This value is higher than the Particle Data Group value $\mathrm{B}(K^+_{e3}) = (4.82 \pm 0.06)\%$ [7] by $(7.1 \pm 2.5)\%$ and would hence solve the unitarity problem.

The data were taken at a beam intensity reduced by a factor of ten compared to the $K_{\pi\mu e}$ runs to reduce the chamber occupancy in the charged particle spectrometer, which followed a magnet separating the K decay products by charge. The K_{e3} trigger required the identification of a low mass e^+e^- pair ($M_{ee} < 50$ MeV, characteristic of π^0 Dalitz-decay) through a signal from the two CH_4 filled threshold Čerenkov counters located inside the spectrometer on both sides. A prescaled version of the same trigger requiring only three out of the four Čerenkov counters was used to measure their efficiency. For the second e^+ the information of the electromagnetic calorimeter was used in those cases, where one of the Čerenkov counters did not deliver a signal. In one third of the event sample the photon from the π^0 Dalitz-decay was detected too. This allowed checks of the reconstruction methods, but in the final sample the photon was not required. The 1.8% relative systematic error quoted above was determined from the stability under the variation of the reconstruction procedure, selection criteria, detector efficiencies applied to the Monte Carlo simulation and subdivision of data and monitor samples. It includes uncertainties in the magnetic field (0.3%), vertex finding and quality cut (0.6%), Čerenkov counter efficiency and ambiguity cut (0.4%), proportional chamber and trigger counter efficiencies (0.25%), background contamination from $\pi^0 \to e^+e^-e^+e^-$ and misidentified π^+/μ^+ (0.3%) and small, but significant discrepancies between the observed and Monte Carlo simulated e^+/e^- momentum (1.3%) and vertical decay angle (0.8 %) distributions, adding quadratically

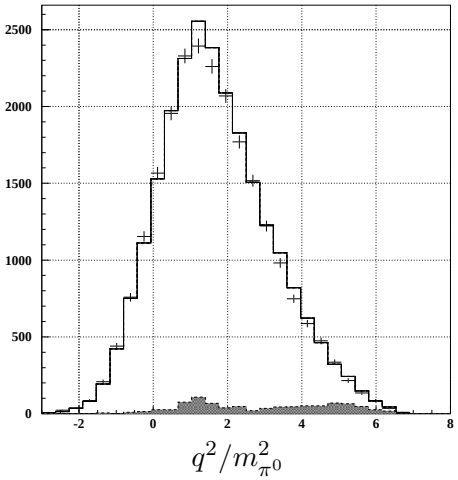

Figure 6.1: *Momentum transfer $q^2/m^2_{\pi^0}$ distribution in K^+_{e3} decay. The open (shaded) histogram shows the Monte Carlo simulated signal (background) distributions. The points with error bars are measured data.*

to 1.8%. The Monte Carlo simulation includes radiative corrections [9]. The detector efficiencies were all determined from data. Figure 6.1 demonstrates the good agreement between simulation and data using the momentum transfer q^2 distribution as an example. From this distribution the slope parameter λ_+ could be extracted with the result $\lambda_+ = 0.0324 \pm 0.0044$, which is in good agreement with the PDG value $\lambda_+ = 0.0282 \pm 0.0027$ [7]. As a further check the $K^+ \to \pi^+\pi^-\pi^+$ (K_τ) branching ratio was determined relative to the same normalisation channels used for K^+_{e3}, and found to agree with the PDG value within a factor 1.01 ± 0.02.

6.1.2 $K^+ \to \pi^+\mu^\pm e^\mp$

The analysis of the final $K_{\pi\mu e}$ run dating from 1998, which is the thesis project of Aleksey Sher, is almost completed. In order to quote a limit on the branching ratio the Monte Carlo simulation had to be retuned for the running conditions of 1998, i.e. measured efficiencies had to be implemented. The acceptance for $K_{\pi\mu e}$ events and the two monitor samples $K_{\pi 2}$, K_τ was calculated, with consistent results. In view of the *blind* analysis philosophy, which is followed here, the possible signal region has been excluded from the analysis so far. The statistical analysis tools, the ingredients of the maximum likelihood analysis and the cuts, which reduce the backgrounds in the signal region have been all been optimized and prepared, such that the final answer can be expected in the immediate future.

[1] R. Appel *et al.*, Phys.Rev.Lett.**85** (2000), 2450.

[2] R. Appel *et al.*, Nucl.Instr.Meth.**A479** (2002), 340.

[3] *Positive kaon decay into neutral pion, positron, and neutrino: relative branching ratio measurement in the E865 experiment at the Brookhaven National Laboratory*, Alexander Sher, PhD. Thesis, University of Pittsburgh, 2002; available at http://www.scipp.ucsb.edu/sher/thesis.ps.

[4] *A New, High Statistics Measurement of the $K^+ \to \pi^0 e^+ \nu_e$ (K^+_{e3}) Branching Ratio*, A. Sher *et al.*, in preparation, to be submitted to Phys.Rev.Lett.

[5] *A High Statistics Measurement of K^+_{e4} Decay*, S. Pislak *et al.*, Phys.Rev.**D67** (2003), in print.

[6] For a review see I.S. Towner and J.C. Hardy, J. Phys. G: Nucl. Part. Phys. **29** (2003), 197.

[7] K. Hagiwara *et al.*, Phys.Rev.**D66**, 010001.

[8] H. Abele *et al.* Phys.Rev.Lett.**88** (2002), 211801, and references therein.

[9] V. Cirigliano, M. Knecht, H. Neufeld, H. Rupertsberger, and P. Talavera, Eur.Phys.J.**C23** (2002), 121.

[10] H. Leutwyler and M. Roos, Z. Phys. **C25** (1984), 25.

6.2 KOPIO: a study of the CP-violating rare decay $K_L^0 \to \pi^0\nu\overline{\nu}$

in collaboration with:
Brookhaven National Laboratory, University of Cincinatti, INR Moscow, KEK, Kyoto University of Education, Kyoto University, University of New Mexico, INFN University of Perugia, Stony Brook University, Thomas Jefferson National Accelerator Facility, TRIUMF/UBC, University of Virginia, Virginia Polytechnic Institute & State University, and Yale University.

Enormous efforts are made to study CP violation in the B meson sector. One of the most important measurements is, however, still to be done in the K meson sector, where CP violation was originally discovered, namely that of the $K_L^0 \to \pi^0\nu\overline{\nu}$ branching ratio, which has a Standard Model (SM) prediction in the range $(3.1 \pm 1.3) \times 10^{-11}$. The KOPIO experiment plans to measure the branching ratio with a single-event sensitivity around 6×10^{-13} corresponding to $\approx 50 \pm 20$ observed events for the SM value.

The combined MECO/KOPIO proposal[2] was submitted to the US National Science Foundations (NSF) Major Research Equipment (MRE) program in 1999. Meanwhile the project has been approved and is part of the budget proposal to the US Congress for the fiscal year 2004. The plan includes funding of pre-construction r&d as well as substantial operating funds required for AGS operation.

The KOPIO experiment plans to use an intense low momentum, time structured K_L^0 beam available only at the AGS. The planned detection system will allow a fully constrained reconstruction of the π^0 mass, momentum and energy in the K_L^0 center-of-mass system. Kinematical cuts and an elaborate veto counter system are designed to nearly eliminate all background contributions from K_L^0 decays with more than one π^0 or from other photon sources. The goal of KOPIO is to obtain the ≈ 50 events with a signal to background ratio of 2:1, yielding a 10% uncertainty for the height of the CKM triangle.

The University of Zürich group has taken on the responsibility for the design and test of the charged particle veto counters, which are of crucial importance for a variety of background sources, e.g. from the radiative decay $K_L^0 \to \pi^- e^+ \gamma \nu_e$. The energy of the PSI $\pi^\pm$ beams is ideally suited for such measurements, which have started in 2000/1.

6.2.1 CP violation in the quark sector: Standard Model and beyond

Within the Standard Model CP violation in the quark sector arises from a single complex phase in the CKM mixing matrix [1]. In the Wolfenstein parametrisation (see last year's annual report) the violation results from a non-zero value of the parameter η which manifests itself in two CKM elements:

$$\begin{array}{rcccl} V_{ub} & = & |V_{ub}|e^{-i\beta} & = & A\lambda^3(\rho - i\eta) \\ V_{td} & = & |V_{td}|e^{-i\gamma} & = & A\lambda^3(1-(1-\lambda^2/2)(\rho+i\eta)) \;\approx\; A\lambda^3(1-\rho-i\eta) \end{array}$$

The decay $K_L^0 \to \pi^0\nu\overline{\nu}$ has major contributions from penguin and box diagrams with up-type quarks in the intermediate state. Since the transition amplitude scales with the quark mass the top contribution dominates by far and $A(K_L^0 \to \pi^0\nu\overline{\nu}) \propto V_{td}^* V_{ts} - V_{ts}^* V_{td} \propto i\eta$. As a result $B(K_L^0 \to \pi^0\nu\overline{\nu}) \propto \eta^2$. The branching ratio is thus a direct measure of η, i.e. the area (or height) of

[2] http://pubweb.bnl.gov/people/rsvp/proposal.ps

the CKM unitarity triangles.

The corresponding charged decay mode does not require CP violation but gives a circular constraint around $\rho = 1.3, \eta = 0$: $B(K^+ \to \pi^+ \nu\overline{\nu}) \propto (\rho - 1.3)^2 + \eta^2$. Until recently BNL E-787 found two event candidates [2]. An upgraded version of this experiment (E-949 [3]) which has started to take data last year hopes to increase the sensitivity by a next order of magnitude. Another experiment (Fermilab E921 [4]) which is still in the stage of preparation should observe some 95 events at the prefered SM branching ratio. Ultimately these two decay modes together will give a complete picture of CP violation in the K system with negligible theoretical uncertainties.

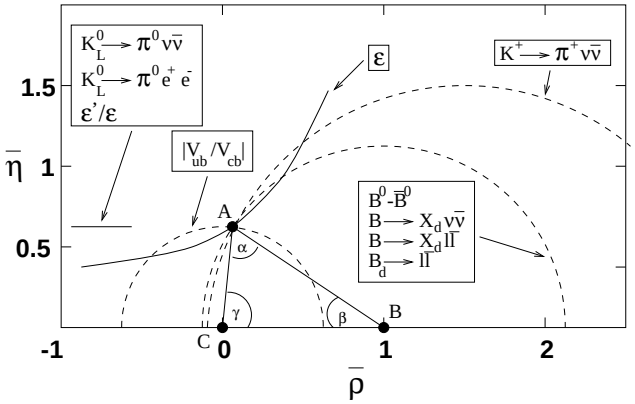

Figure 6.2: *The unitarity triangle and the constraints from various K and B decays.*

Figure 6.2 shows how various observables in K and B decays contribute to our knowledge of $\overline{\eta} \equiv (1 - \lambda^2)\eta$ and $\overline{\rho} \equiv (1 - \lambda^2)\rho$ which define point A in the figure.
Physics beyond the Standard Model generally allows additional CP-violating phases [5] and as a result the SM description with a universal set of Wolfenstein parameters for K and B would break down. It is very fortunate that we may expect significant improvements in the experimental constraints in both areas during the next decade so that meaningful tests can be made.

6.2.2 The charged particle veto system

In last years annual report the complete KOPIO detection system has been presented. The decay $K_L^0 \to \pi^0 \nu\overline{\nu}$ will be distinguished from other more likely decay modes on the basis of the following signature:

- Two photons are observed with a common vertex inside the decay region and an invariant mass equal to m_{π^0}.
- No simultaneous charged particles or additional photons are observed.
- The energy $E^*_{\pi^0}$ of the reconstructed π^0 in the K_L^0 rest frame (using the K^0 time of flight through the beam line) and the photon energy sharing do not coincide with the regions populated by the background of the decay $K^0 \to 2\pi^0$ remaining after test 2.

The Zürich group took over the responsibility for the main charged-particle veto system situated directly around the decay region. In the following we discuss the requirements to this system and some other considerations that should lead to a specific design.

The purpose of the charged-particle veto system is the efficient identification of background processes in which an apparent $\pi^0 \to 2\gamma$ decay inside the decay volume is accompanied by charged particle emission. Examples of such background processes are, (i) $K_L^0 \to \pi^+\pi^-\pi^0$, (ii) $K_L^0 \to e^+\pi^-\nu\gamma$ in which the positron creates a second photon through Bremsstrahlung or annihilation in flight, (iii)

$K_L^0 \to e^+\pi^-\nu$ again followed by $e^+ \to \gamma$ whereas the π^- creates a photon through $\pi^- p \to \pi^0 n$. In all cases two particles with opposite electrical charge emerge. The events may also produce signals in other detector elements, like the barrel veto system. Detection efficiencies of 99.99% or better are required to keep these backgrounds below a few events in the final sample.

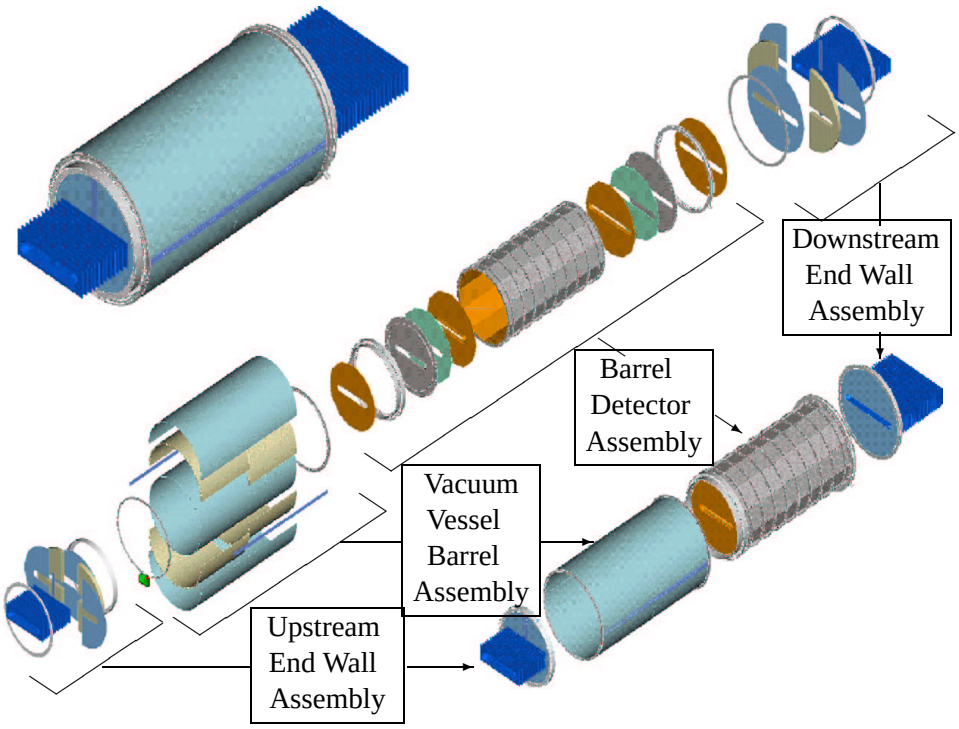

Figure 6.3: *The present concept of the charged particle veto system and surrounding vacuum tank. The latter has a length of 4 m and a diameter of 2.5 m.*

The charged-particle veto system will consist of one or two layers of plastic scintillator mounted inside the vacuum tank surrounding the decay volume. About 100 m^2 of plastic scintillator will be distributed over some 500 independent elements. Figure 6.3 shows an exploded view of the system. As discussed in last year's report the requirement of a veto efficiency for $e^{\pm}$, $\pi^{\pm}$ and $\mu^{\pm}$ of 99.99% or better can be met if the dead layer in front of the veto system (which may include a window separating the detector from the high-vacuum decay region) could be kept below 20 mg/cm^2 if a detection threshold of ≈ 75 keV (corresponding to ≈ 0.3 mm scintillator thickness) could be reached. Minimising dead material mainly helps to reduce the inefficiency for π^- caused by nuclear reactions.Tests by the PSI vacuum group indicate that it may be possible to leave out the vacuum window in which case only the scintillator wrapping would contribute. A low detection threshold translatesinto a high yield for the number of photo electrons per energy deposit which in turn demands a high efficiency for the collection of the scintillation light. The optimisation of the light yield is the central issue of our present r&d program. In the past year we compared the performance of various wrapping materials. Table 6.1 sum-

Table 6.1: *Mean amplitude of the signals produced by cosmic muons in the scintillator prototype with w.l.s. fibre readout for various wrapping materials.*

wrapping material	ADC peak position
black paper	860
nothing	900
aluminum	1350
white paper (Tyvek[a])	1580
teflon	1610

[a] Du Pont trademark

marises our findings for a prototype detector with w.l.s. fibre readout. Best results were obtained with teflon and Tyvek which both almost double the light yield. During a two weeks beam period at PSI in September 2002 various prototypes were studied. These tests were made with 550 MeV/c π^-. Two xy MWPC's were used to determine the impact position on the scintillator. Four alternative readout schemes were under investigation:

- Light extraction through wave-length-shifting fibres put in grooves inside the scintillator. The photon detectors would be situated at a few meters distance outside the vacuum tank. As reported last year $\approx$ 10 p.e./mm were observed in a first prototype using Kuraray Y-11(200)MS w.l.s. fibres coupled to Burle S83062E photo multipliers which have enhanced quantum efficiency for the green light emitted by the fibres. Meanwhile we achieved somewhat larger yields with Kuraray SCSF-81Y-11(200)MS fibres.
- Light extraction through wave-length-shifting bars. This scheme gives results which are similar to the fibre readout. It needs more photo cathode area but would be significantly cheaper otherwise.
- Photo-multipliers coupled directly to the scintillator slabs.

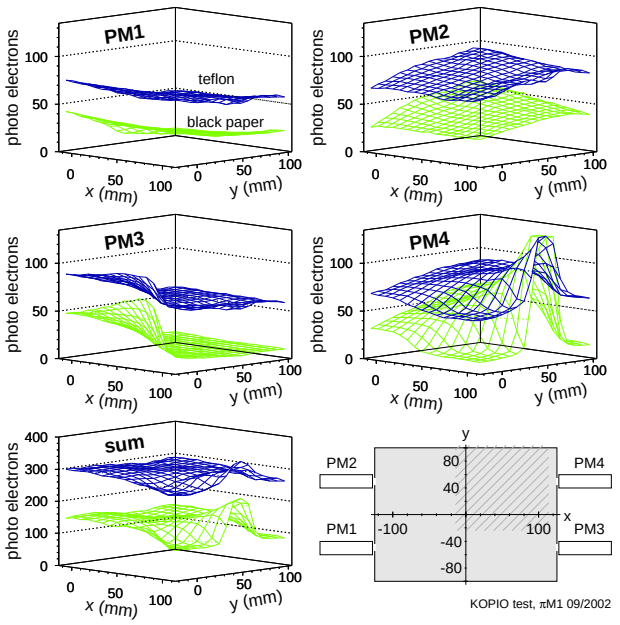

Figure 6.4: *Position dependence of the light yield with and without teflon wrapping. The* $250 \times 200 \times 6$ *mm*^{3} *scintillator was viewed by photo-multipliers through four 10 mm wide holes on opposite sides. The hatched area corresponds to the region studied.*

As a first result of these measurements Fig. 6.4 shows the position dependence of the light extracted through four windows on two opposite sides of a slab of scintillator with and without teflon wrapping. The mean yields for all geometries that were studied with and without reflective wrapping are compared in Fig. 6.5. As in Table 6.1 wrapping tends to double the light yield. In addition the reflecting material improves the uniformity of the detector response over the detector surface. From these results we conclude that scintillator elements of $\approx$ 500 $\times$ 500 mm^2 viewed from one side by a series of small photo-multipliers should give a yield of ≈ 50 photo electrons per millimetre which would result in inefficiencies below 3×10^{-5} for the various particles.

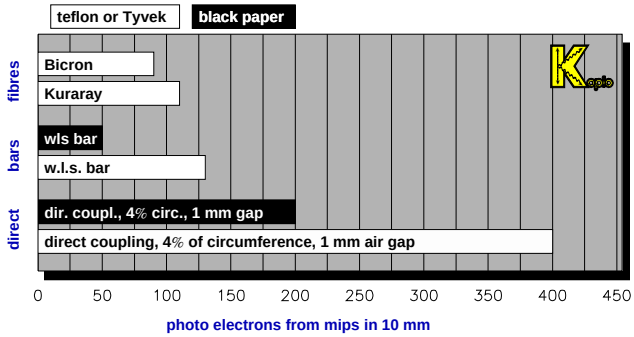

Figure 6.5: *Comparison of the photoelectron yield observed with various light-collection schemes with and without reflective wrapping.*

[1] A. Buras, *Flavour physics and CP violation in the SM*, Proceedings of KAON 2001, eds. F. Constantini, G. Isidori and M. Sozzi, (Frascati Physics Series Vol.XXVI), pp. 15-43.

[2] S. Adler *et al.*, E787 Collaboration, Phys. Rev. Lett. **88** (2002), 041803.

[3] BNL proposal E949, *An experiment to measure the branching ratio* $B(K^+ \to \pi^+ \nu\overline{\nu})$, D. Bryman, S. Kettell, S. Sugimoto spokesmen, http://www.phy.bnl.gov/e949.

[4] Fermilab proposal E921, *Charged Kaons at the Main Injector (CKM)*, P.S. Cooper spokesman, http://www.fnal.gov/projects/ckm/Welcome.html.

[5] A. Masiero, *Flavour physics and CP violation beyond the SM*, Proceedings of KAON 2001, eds. F. Constantini, G. Isidori and M. Sozzi, (Frascati Physics Series Vol.XXVI), pp. 45-58.

7 Particle Physics at DESY/HERA (H1)

J. Becker, Ilaria Foresti, M. Hildebrandt (until 9/02), N. Keller, J. Kroseberg, L. Lindfeld, Katharina Müller, P. Robmann, S. Schmitt, F. Sefkow (until 7/02)
U. Straumann, P. Truöl, M. Urban, Nicole Werner, and Stefania Xella Hansen

in collaboration with:
R. Baldinger, S. Baumgartner, N. Berger, W. Erdmann, C. Grab, M. Hilgers, B. List, S. Mangano, D. Meer, A. Schöning and R. Weber, Institut für Teilchenphysik der ETH, Zürich; S. Egli, R. Eichler, K. Gabathuler, and R. Horisberger, Paul–Scherrer–Institut, Villigen, and 34 institutes outside Switzerland

(**H1**–Collaboration)

7.1 Electron proton collisions at up to 320 GeV center of mass energy: overall status of the project

Since September 2000 only a limited amount of data has been collected by the H1-experiment, corresponding to an integrated luminosity of $\mathcal{L}_{\rm int} = 9.8$ pb^{-1}. Between the end of the long shutdown for the upgrade of the detector and the accelerator in July 2001 and March 2003, when the accelerator was shut down again, most of the beam time was dedicated to recommissioning the machine, tuning for luminosity, fighting background problems and identifying background sources, and polarisation studies. Even though it could be proven that a specific luminosity $\mathcal{L}_{\rm spec} = 1.80 \cdot 10^{30}$ cm^{-2}s^{-1}mA^{-2} and a beam polarisation of 50 % can be reached, the severe backgrounds and radiation levels limited the beam currents and number of colliding bunches to two thirds of the design values. Hence the peak luminosity has only reached about half of its design value of $\mathcal{L}_{\rm peak} = 4.8 \cdot 10^{31}$ cm^{2}s^{-1}. Even far below this level the tracking devices could not be operated most of the time. More details are given below (Sec.7.2). The analysis of the data taken in 1999/2000 ($\mathcal{L} = 91$ pb^{-1}), combined in some cases with the pre-1999 data ($\mathcal{L} = 50$ pb^{-1}) continued vigorously leading to 16 publications ([1]-[16]) and 30 papers contributed to the 2002 high-energy physics conferences [17] ([18]-[47]), adressing the following subjects:

- neutral and charged electroweak current cross sections, proton structure functions and parton densities (extensions into the lower and higher Q^2 regimes, use of radiative events) [16; 19; 20];
- search for states and interactions outside the standard model: compositeness [40; 48], squarks [40; 48], ν^* [2], e^* [13], leptoquarks [40; 46; 48], single top [45], instantons [9], odderons [12; 38], charged Higgs [42], anomalous lepton pair [41; 43] and W [14; 44] production, anomalous dimensions [40], magnetic monopoles [47];
- photo- and electroproduction of di- and multijets [3; 4; 5; 11; 15; 22; 24; 25];
- photo- and electroproduction of exclusive final states: π^0 [12; 21], ρ [6; 35; 36], J/Ψ [7; 8; 37], Ψ' [10];
- production of open charm and beauty [1; 26; 27; 49; 50];
- diffractively produced final states: inclusive [29; 30; 31; 32; 39], π^0, η [38], jets [33; 34], ρ [6; 35; 36], J/Ψ [37], Ψ' [10];

- photon structure [23].

We will give below an overview of all analyses dealing with physics beyond the standard model (Sec. 7.4.1), and also report on the progress of the analyses, in which University of Zürich group members are involved, namely beauty and prompt photon production, QED Compton scattering and high Q^2 charged current data (Sec. 7.4.2).

Besides the physics analysis the commissioning of our contributions to the upgrade program of the H1-detector occupied most group members (see Sec. 7.3).

7.2 Status of the HERA accelerator

Since the 2000/2001 shutdown, necessary to prepare the HERA II luminosity upgrade, the operation of HERA has been limited to moderate beam currents because of high backgrounds and difficult beam steering requirements. A severe synchrotron radiation background was observed in November and December 2001, limiting the positron current to less than 1 mA. Additional upstream collimators were installed in February and early March 2002, and aperture limitations for the direct synchrotron radiation were removed on the downstream side. Over the following months a positron orbit has been established, which allowed beam currents of up to 30 mA to be stored with tolerable backgrounds. It then became evident that the proton beam-gas background, enhanced by the dynamic pressure increase when raising the positron current, is limiting the tolerable beam currents to about $I_e \cdot I_p < 600\,\mathrm{mA}^2$. With these constraints the maximum integrated luminosity for a given run reached early September 2002 was 80 nb^{-1}, with a specific luminosity near the post upgrade expectation of $2 \cdot 10^{30}$ $\mathrm{cm}^{-2}\mathrm{s}^{-1}\mathrm{mA}^{-2}$. Extensive measurements with a variety of beam conditions have been performed to understand the background effects from synchrotron radiation and from beam-gas interactions. In addition, detailed simulations, especially of the proton background, have been performed. The results of these studies were presented in two reports [51] to the DESY directorate including an extrapolation to the high HERA II design beam currents, of $I_{e,max} = 55$ mA and $I_{p,max} = 135$ mA, and a quantitative evaluation of possible remedies. The limit for safe operation of the H1 detector given above is determined by the currents drawn in the central outer drift chamber (CJC2), which rise beyond the tolerable limit of 150 to 200 μA, and the rate in the silicon pad detector (radiation monitor), which should not exceed its safe limit of about 50kHz.

The behaviour of the CJC currents was studied in HERA runs with single positron and proton beams and during ep collisions. These currents were found to be primarily due to the effects of synchrotron radiation, positron beam-gas and proton beam-gas interactions. Extrapolation to the anticipated HERA-II beam currents leads to an estimated current of about 1 mA in the CJC2, nearly 90% of which is due to proton initiated background. Similarly, the radiation monitor rate, when extrapolated to the design beam currents, is about 400 kHz whereas a rate of 50 kHz is expected from the positron beam alone.

The backgrounds within the H1 detector decreased significantly in the last quarter of 2002 and the quality and quantity of the data taken by H1 has increased accordingly. Problems remained, however, due to a combination of continuous background levels and background spikes. A further reduction in the currents drawn in the CJC by a factor of about three is necessary if safe operation is to be possible with HERA design currents.

In order to optimize the luminosity at high beam currents while respecting the background set limits on the product $I_e \cdot I_p$ the number of filled bunches was reduced in February of 2003. This is useful

since the luminosity is given by

$$\mathcal{L} = \frac{I_e \cdot I_p}{4\pi q^2 N_B f_{\rm rev} \sigma_x \sigma_y} = \mathcal{L}_{\rm spec} \frac{I_e \cdot I_p}{N_B} \ .$$

The space charge limit at injection and the beam-beam effects limit the proton and electron currents to 0.6 mA/bunch and 0.3 mA/bunch, respectively. With a post-upgrade specific luminosity of $\mathcal{L}_{\rm spec} = 1.8 \cdot 10^{30} {\rm cm}^{-2}{\rm s}^{-1}{\rm mA}^{-2}$ one obtains the luminosity values listed in Table 7.1.

Table 7.1: *Luminosity parameters for HERA operation.*

N_B	$I_p^{\rm max}$ [mA]	$I_e^{\rm max}$ [mA]	$I_p \cdot I_e$ [mA^2]	$\mathcal{L}_{\rm peak}$ [10^{31}cm^{-2}s^{-1}]	
119	67	32	2144	2.7	measured 24. 2. 2003
119	72	37	2664	3.3	expected limits
174	108	56	6048	4.8	post-upgrade design
175	94	44	4136	1.4	typical for 2000 running

Further measurements near the end of 2002 and early 2003 and simulations have shown that the tighter acceptances and new magnet configuration following the luminosity upgrade imply that H1 is about 1.5 times more sensitive to backgrounds now than was the case during HERA I operation. The composition of the residual gas has not changed significantly as a consequence of the upgrade. The pressure in the interaction region is higher than prior to the upgrade and is more strongly dependent on the positron current. During the best running conditions achieved to date, the pressure was a factor of about 2 higher than that in 2000. The sensitivity of the H1 central detectors to the pressure in the HERA beam line has been determined as a function of the distance from the detector. Monte Carlo simulations and measurements are in reasonable agreement and imply that sensitivity extends to about 20 m along the proton beam line. Incidents in which the backgrounds are extremely high have caused damage to detectors close to the beam line, in particular to the backward silicon tracker, which according to the evaluation of the thermo-lumiscence dosimeters has received a dose of up to 32'000 Gy. The forward and central silicon trackers have typically doses 400 times less. Heating of elements of the beam line in and around H1 through higher order mode losses at injection energies has been observed and has led to modifications in the design of some elements of the beam line. Current extrapolations indicate that proton induced backgrounds will dominate at HERA II design currents. Improvements in the vacuum therefore remain the primary means of reducing these.

The following modifications are also foreseen: the installation of an ion getter pump at $z = 1.5$ m; improvement of the instrumentation of the vacuum system by installing a residual gas analyser at $z = 3.6$ m; coating of an absorber with molybdenum at 10.8 m to reduce the effects of backscattered synchrotron radiation; protection of the silicon detector and CJC electronics by installing 1 mm of lead shielding around the beam pipe in the region $-150 < z < -70$ cm; alteration of a collimator at $z = -150$ cm (C5B) to reduce scattering of secondaires and also higher order mode heating in this region.

7.3 Summary of group activities related to the H1-upgrade

To cope with the higher luminosity and the more complex background situation a set of five new cylindrical multiwire proportional chambers (CIP2k) was built in Zürich which provide the information which allows to distinguish between beam-gas induced background events and true ep-interactions within 2.3 μs at the first trigger level. Since the development and implementation of this system

binds most of our personal resources, we give some further deails below citing from our recent publications [52; 53; 54]. The project is led by U. Straumann and coordinated at DESY by S. Schmitt.

The five cylindrical chambers with a cathode pad readout have a 16-fold segmentation in azimuth ϕ and a 120-fold segmentation along the beam axis (z), leading to 9600 readout channels. Groups of 60 cathode pads are read out via striplines by a custom designed readout chip (CIPix). It contains an integrating preamplifier and pulse shaping stage for 64 channels. Signals are discriminated (two thresholds are possible) and synchronized to the 10.4 MHz HERA clock. The on-chamber electronics digitizes and multiplexes the data fourfold and sends them via optical links [55] to the trigger and data acquisition system at a rate of about 10 GBit/s. For one progammable channel it is possible to inspect the analog signal, too. Programming is afforded via a standard I^2C interface.

The trigger task is illustrated in Fig. 7.1. By reconstructing the origin of tracks passing through the CIP2k chambers beam gas events are discriminated against physics events from the interaction region. To decide whether an event is a physics or a background event the trigger adds up the number of tracks originating from the nominal interaction region (n_{phys}) and compares this number to the sum of the numbers of tracks originating from outside this region in the forward (n_{forw}) and the backward (n_{bac}) part of the detector with respect to the flight direction of the proton. Events with $n_{\mathrm{phys}} < n_{\mathrm{forw}} + n_{\mathrm{bac}}$ are identified as background, the others as physics events. The trigger algorithm

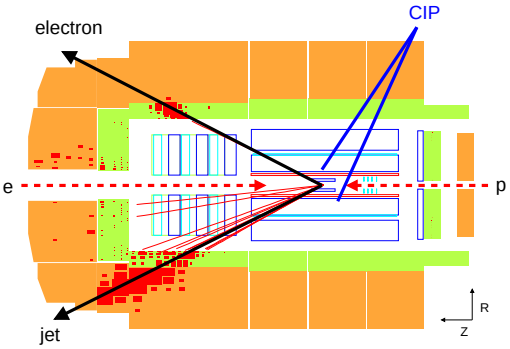

Typical neutral current deep-inelastic scattering event.

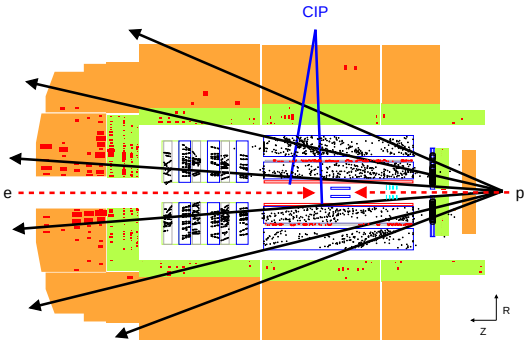

Typical beam-gas event. Most tracks originate outside the nominal interaction region surrounded by the inner tracker.

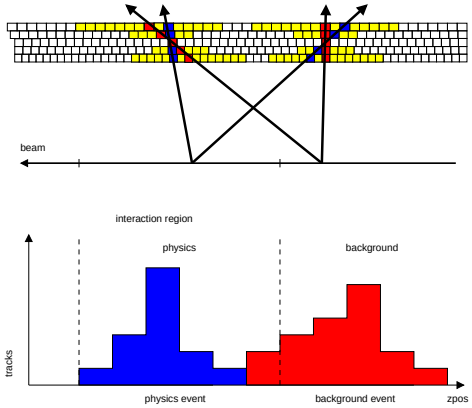

Vertex distribution along the beam axis of tracks crossing the chambers as calculated by the trigger system. From this histogram regions of background and physics tracks can be defined.

Figure 7.1: H1-vertex trigger.

chosen in the CIP2k system is also illustrated in Fig. 7.1. It is separated in three stages - track finding,

- building and - deriving the trigger information from the z-vertex histogram. The tracking algorithm is based on bit pattern comparison of pad data. Field-programmable gate arrays (FPGA) were chosen to accomplish this complex and highly parallelized task. In addition the FPGAs contain pipelines to store the chamber data making it possible to read out the information if a trigger occurs. The trigger, data acquisition and high voltage system are controlled and monitored by the experiment control system (ECS) based on commercial software called PVSSII.

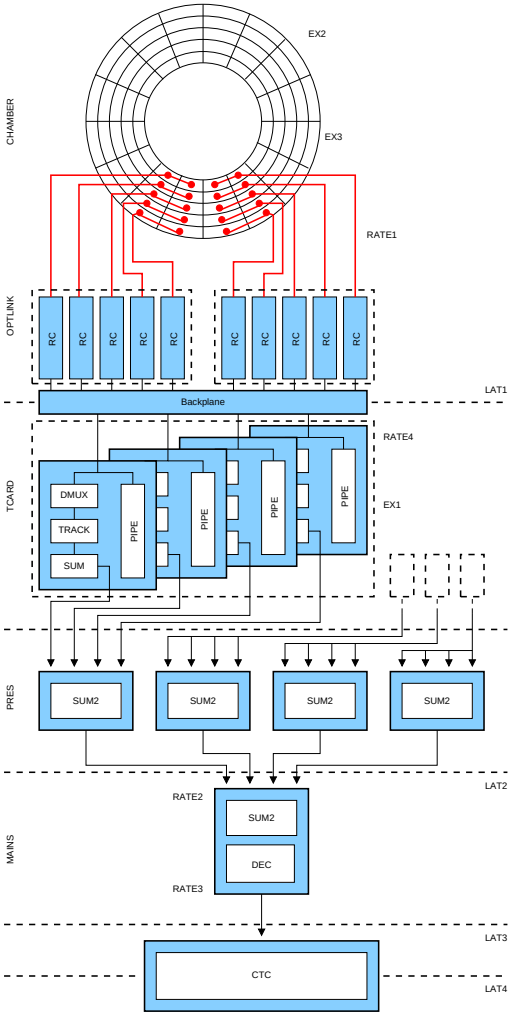

Signal path of the CIP2k trigger system.

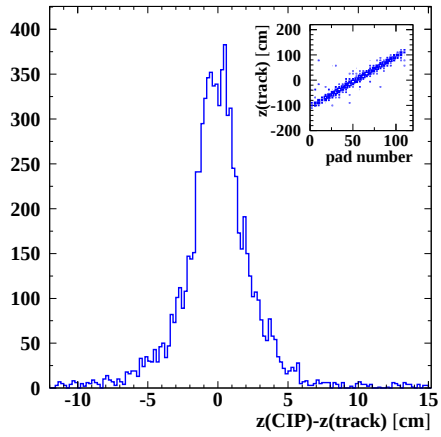

Difference between the CIP hit z-position and the z-coordinate of extrapolated drift chamber tracks. The insert shows the correlation of the CIP2k pad number and extrapolated drift chamber tracks.

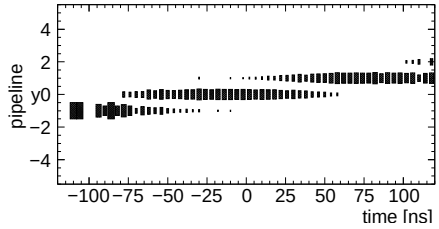

CIP2k trigger pipeline position of the trigger decision with respect to the event timing measured by drift chambers.

Figure 7.2: H1-vertex trigger electronics.

The core of the trigger system (see Fig. 7.2), which is the thesis project of Max Urban, are the custom designed trigger cards (see Fig. 7.3), which contain each two Altera APEX 20K400 FPGAs into which the complete trigger algorithm and the data acquisition pipelines are programmed. These FPGAs were chosen because of the large number of about 500 user I/O pins and the integrated memory pipeline. The trigger card has access to the VME (Versatile Module Europe) bus to read out the data pipeline and to steer the trigger algorithm. The 15 bin wide z-vertex histogram for each ϕ sector is sent via an LVDS link to a custom designed sum card. Each sum card sums up the histogram for four ϕ-sectors. The sum card is equipped with one FPGA (same as on the trigger card). Each sum card builds the z-vertex histogram for one ϕ-quadrant of the chamber. The resulting histograms are sent via an LVDS

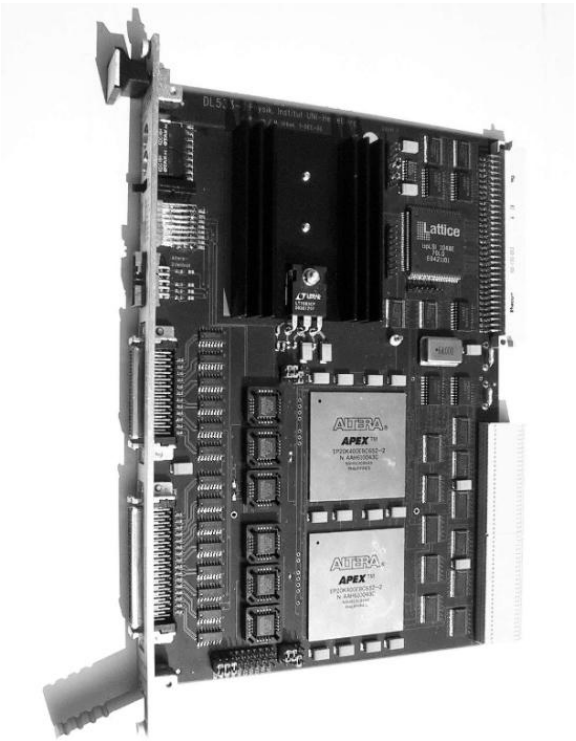

Figure 7.3:
The trigger card. The two FPGAs, the 250 pin input connector on the right side and the micro sub-D connectors on the left side can be seen.

link to the main sum card, which is built as the other sum cards and calculates the global z-vertex histogram for the whole chamber relevant for the 16-bit trigger information for the H1 central trigger system.

The data acquisition system, which is the thesis project of Jan Becker, is based on the VME and the pVIC (PCI Vertical Interconnect) bus system. CPU boards of the type RIO2 8062 with a PowerPC CPU 603 running the real-time operation system LynxOS installed in each trigger crate perform and control the readout of the data from the pipelines in the FPGAs until the arrival of the data at the H1 central data acquisition system. The synchronous part of the data acquisition system with a deadtime constraint of less than 1-2 ms begins with the arrival of a trigger decision starting the readout of the 32 bunch crossing deep pipelines in the FPGAs on the trigger cards. This is done via the VME bus using the single cycle D32/A24 mode with the possibility to switch to an implemented block mode which is not used at the moment. A window of five bunch crossings is read out and grouped into one readout block to study the timing behavior of the trigger system. The readout CPUs arrange the data of the four read out trigger cards in one data package and collect all the packages at one of the CPUs (main CPU) via the pVIC bus. The BMA (block mover accelerator) mode of the pVIC bus is used in this data transfer. The synchronization of the pVIC bus avoiding access conflicts is handled via a custom protocol using the pVIC bus in single cycle mode. With the arrival of the data packages at the main CPU the synchronous part of the readout is finished and the pipelines are ready to be released again. The asynchronous part of the readout starts with the data reduction process in the main CPU. First the chamber data stored as a bit pattern is translated into 16 bit wide pad numbers resulting in an e ective zero suppression if the occupancy of the chamber is less than 10%. Known noisy pads are removed from the data. The data are sent via a VIC link to MEB (Multi Event Buffer) units where they are stored until the H1 central DAQ collects the data from each event via an optical ring.

The system is operational since summer 2001. Early performance tests mainly made use of cosmic muon tracks because of their low rate and clean event signatures. The muon tracks are triggered by the central drift chamber, requiring two track halves opposite in azimuth. The clear correlation between the CIP2k hits and drift chamber tracks and difference between the calculated z-coordinates is

demonstrated in Fig. 7.2. The noise level is negligible, and the width of the distribution is compatible with the expectation from the pad size. This correlation serves as a global test of the chamber, the optical link, and the memory in the FPGAs and DAQ system. Also in Fig. 7.2 the clear correlation between the pipeline position at which the trigger is activated is displayed against the event timing derived from the drift chamber timing. The transition from one pipeline slot to the next slot has a width of about 25 ns which is sufficient to determine the bunch crossings of events from ep collisions. This was demonstrated during 2002/2003 by comparing CIP-timing signals in an offline analysis to event timing without using CIP. Using the CIP timing eliminates the large fraction of non ep events appearing between bunch crossings (see Fig. 7.4).

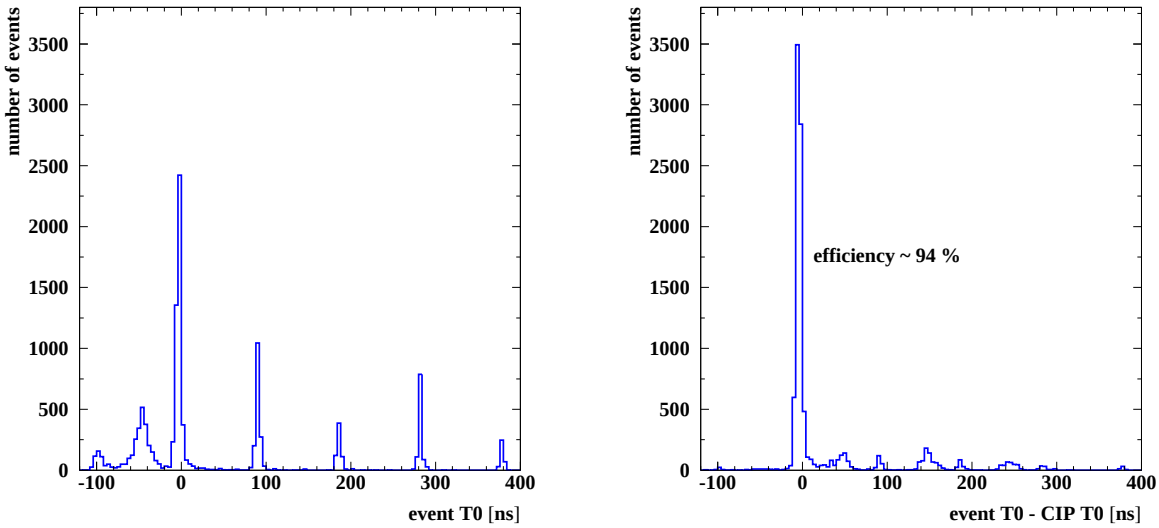

Figure 7.4: *Left: H1 event timing (t_0) at the input of trigger level 4. Bad trigger timing leads to a high rate of non ep events. Right: the same event sample with the CIP2k t_0 applied offline.*

The trigger algorithm has been studied by analysing the simulation of the algorithm on real readout chamber data from cosmic ray events. Due to the cooling problems discussed below only active pads from two out of three layers could be considered. Though the trigger efficiency was found to be high, the separation power for backward, central and forward tracks was yet limited [54], but according to simulations large improvements are expected by running all five layers of the system in the future.

After the initial tests of the chamber performance in 2001 a variety of problems related to insufficient cooling developed. The ambient temperature produced by the central jet chamber electronics is so high, that the CIPix reaches temperatures near 50°C with the normal cooling circuit running at 17°C. At these temperatures instabilities in the addressing of some CIPix chips occurred at first, and later a complete loss of their functionality was observed. A subsequent laboratory test confirmed that at these high temperatures wires bonded to the chips can break, which explains the loss of connection. As a counter measure a separate cooling circuit was installed with an operating temperature of 8°C, which kept the CIPix temperature below 40°C. However, out of the five chamber layers the outermost two were partly lost before the roots of the problem were discovered. The whole frontend electronics has now been rebuilt in such a way, that the bond breaking can no longer occur, and has been replaced during the ongoing shutdown. Additional cooling lines are being added to the chamber electronics, too.

Whenever the central drift chamber was switched on during HERA luminosity runs, the CIP was switched on, too. The design and implmentation of the CIP slow control (i.e. chamber HV and

current as well as temperature monitoring and control, on-line monitoring of the chamber efficiency) is part of the thesis project of N. Werner. The temperature monitoring e.g. is used to automatically switch off the supply voltages if a limit is exceeded. The CIPix chips have proven to be stable and the different programming options quite useful during HERA operation. Having the analog signal available allowed for optimisation of the timing as well as the signal to noise ratio. No sign of radiation damage has been observed. After replacement of the damaged boards on the chamber and on-chamber readout tests the CIP will be reinstalled in the H1 detector early May 2003.

7.4 Results from recent analyses

7.4.1 Search for physics outside the Standard Model

Contact interactions and leptoquarks

Many proposed extensions to the Standard Model (SM) would manifest themselves in the HERA ep data at large momentum transfer. Examples discussed below are composite models, leptoquarks, supersymmetry and extra dimensions. The most recent H1-analysis [40; 48] is based on three data sets comprising a total integrated luminosity $\mathcal{L}_{\rm int}$ 117.2 pb^{-1} (Tab. 7.2), and extends an earlier analysis based on the pre-1998 data [58].

Table 7.2: *Data sets used in the search for exotics analysis.*

Reaction	$\mathcal{L}_{\rm int}$ [pb^{-1}]	$\sqrt{s}$ [GeV]	Run period	Ref.
$e^-p \to e^-X$	16.4 ± 0.3	319	1998 - 1999	[57]
$e^+p \to e^+X$	65.2 ± 1.0	319	1999 - 2000	[16]
$e^+p \to e^+X$	35.6 ± 0.5	301	1994 - 1997	[56]

The new cross section data $d\sigma(e^-p \to e^-X)/dQ^2$ [57] and $d\sigma(e^+p \to e^+X)/dQ^2$ [16] are shown in Fig. 7.5. Over six orders of magnitude the data are well described by a next-to-leading order deep inelastic scattering calculation using the CTEQ5D parton distributions [59]. In order to compare the different models with the data the predicted cross sections are reweighted at each Q^2 by the ratio of the leading order cross section with and without inclusion of the contact interaction (CI) $\hat{\sigma}^{LO}(SM + CI)/\hat{\sigma}^{LO}(SM)$. For any particular model the most general form of the chiral invariant vector-like four-fermion contact interaction Lagrangian

$$\mathcal{L}_V = \sum_q \sum_{a,b=L,R} \eta^q_{ab} (\bar{e}_a \gamma_\mu e_a)(\bar{q}_b \gamma_\mu q_b) \; ,$$

with an appropiate choice of couplings $\eta^q_{ab} = \epsilon_{ab}(g/\Lambda^q_{ab})^2$ can be used. Here a and b indicate the left-handed (L) and right-handed (R) fermion helicities, g is the the overall coupling strength, Λ^q_{ab} is a scale parameter and ϵ_{ab} determines the sign of the interference term.

In general models allowing for compositeness or substructure it is convenient to choose a coupling strength of $g^2 = 4\pi$ and to assume a universal scale Λ for all quarks: $\eta^q_{ab} = \epsilon_{ab}(4\pi)/(\Lambda^2)$. Various chiral structures, pure left, right, vector or axial vector couplings are chosen by setting $e_{ab} = \pm 1$ and putting all other contributions to zero. Lower limits at 95 % CL on the scale parameters $\Lambda^\pm$ range between 1.6 and 5.5 TeV depending on the chiral structure.

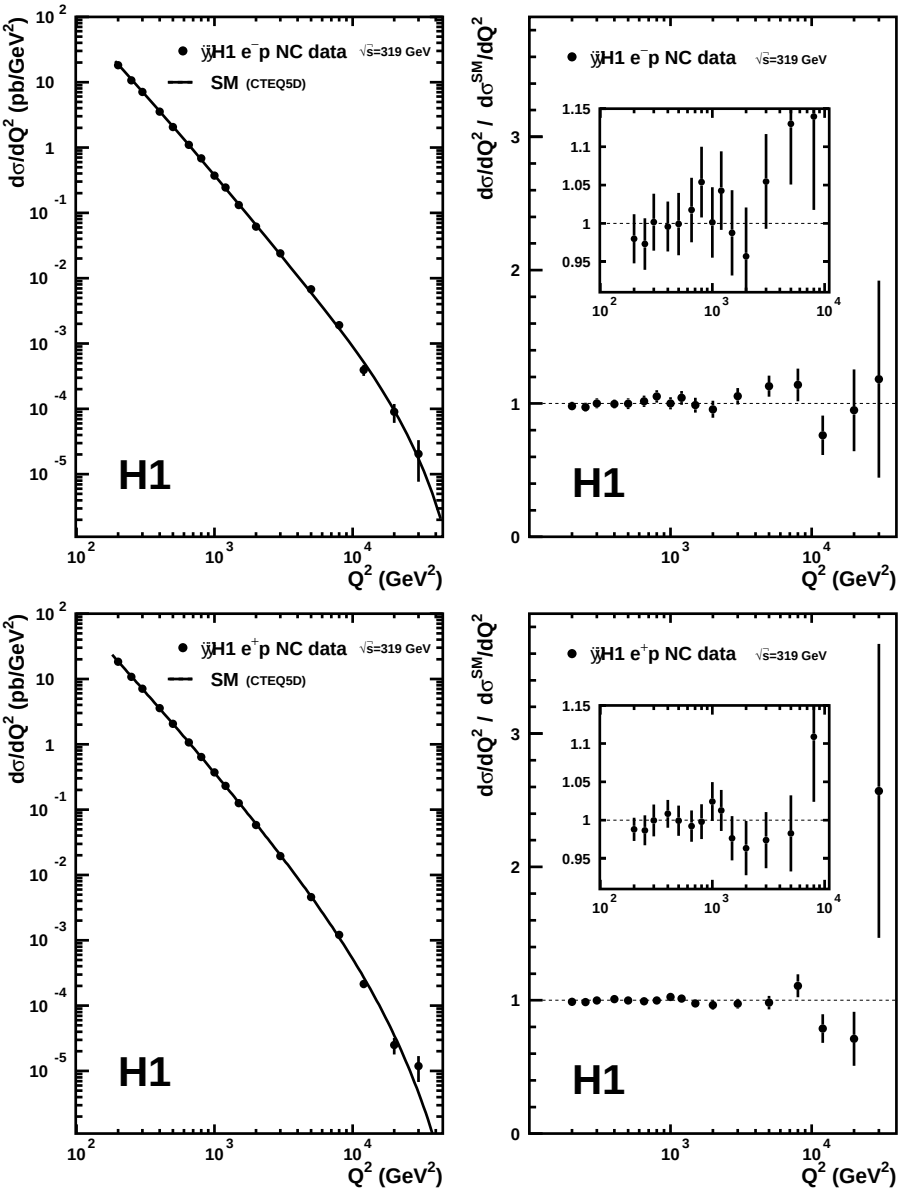

Figure 7.5: Differential cross sections $d\sigma/dQ^2$ at $\sqrt{s} = 319$ GeV for $e^-p \to e^-X$ scattering (top) and $e^+p \to e^+X$ scattering (bottom), compared to SM expectations using the CTEQ5D parton distributions. A preliminary version of these data was shown in the 2000/1 annualreport.

Leptoquarks couple to lepton-quark pairs and appear in extensions of the SM which connect the lepton and the quark sectors. They are colour triplet scalar or vector bosons, carrying lepton (L) and baryon (B) number and a fermion number $F = L + 3B$, with $F = 2$ for e^-q and $F = 0$ for e^+q states. For high enough scales the leptoquark mass M_{LQ} and its coupling are related to the contact interaction coefficients via $\eta^q_{ab} = \epsilon^q_{ab}(\lambda^2)/(M^2_{LQ})$. Lower limits on the ratio M_{LQ}/λ between 0.3 and 1.4 TeV are found.

A more detailed analysis [46] of the full 1994 - 2000 data sample with $Q^2 > 2500$ GeV^2 and $0 < Q^2/M^2 < 0.9$, requiring an identified electron with transverse momentum above 15 GeV/c (neutral current interactions) or a missing transverse momentum above 25 GeV/c (charged current

interactions), set limits on leptoquark production in the s-channel. Leptoquarks decaying to eq or νq in s-channel are produced at a mass $M = \sqrt{s_{ep}x}$, where x is the momentum fraction of the proton carried by the interacting quark. Masses below 300 GeV are accessible this way. In addition exchange of a leptoquark in the u-channel between the incoming lepton and a quark from the proton is possible. The amplitudes for these processes interfere with those from normal deep-inelastic scattering. The analysis updates an earlier one [60] and considers those mass domains, where the resonant s-channel dominates the leptoquark signal cross section. The analysis excludes leptoquarks with electromagnetic coupling strength and masses below 290 GeV, extending exclusion plots from Tevatron experiments into the mass range above 200 GeV.

In the most general formulation of supersymmetry there exist couplings between a lepton-quark pair and a squark, the scalar superpartner of a quark. Such couplings violate R-parity (via lepton number violation $\Delta L \neq 0$), defined as $R_p = (-1)^{3B+L+2S}$ with S being the spin. This interaction allows single squarks to be produced or exchanged in deep inelastic scattering via

$$e^+ d_R \to \tilde{u}_L,\, \tilde{c}_L,\, \tilde{t}_L \;:\; \text{coupling } \lambda'_{1j1}\,; \qquad e^+ \tilde{u}_L \to \bar{\tilde{d}}_R,\, \bar{\tilde{s}}_R,\, \bar{\tilde{b}}_R \;:\; \text{coupling } \lambda'_{11k}\,.$$

The subscripts ijk describe the generation indices of the left-handed leptons, left-handed quarks and right-handed down-type quarks of the superfields, respectively. Squarks with masses satisfying $M_{\tilde{u}}/\lambda'_{1j1} < 0.43$ TeV and $M_{\tilde{d}}/\lambda'_{11k} < 0.71$ TeV can be excluded.

It has been suggested that the gravitational scale M_S in $4+n$ dimensional string theory may be as low as the electroweak scale of order TeV [61]. The relation to the Planck scale $M_P \approx 10^{19}$ GeV and the size R of the n compactified extra dimensions is given by $M_P^2 = R^n M_S^{2+n}$. In some models with large extra dimensions the SM particles reside on a four-dimensional brane, while the spin 2 graviton propagates into the extra spatial dimensions and appears in the four-dimensional world as a tower of massive Kaluza-Klein states with a level spacing $\Delta m = 1/R$. Though the gravitons couple to the SM particles via the energy-momentum tensor with a tiny strength given by the Planck scale, the summation over the enormous number of Kaluza-Klein states up to the ultraviolet cut-off scale, taken as M_S leads to an effective contact-type interaction with coupling $\eta_G = \lambda/M_S^4$. The details of the calculation of the cross section have been given in [58]. The interference between the graviton

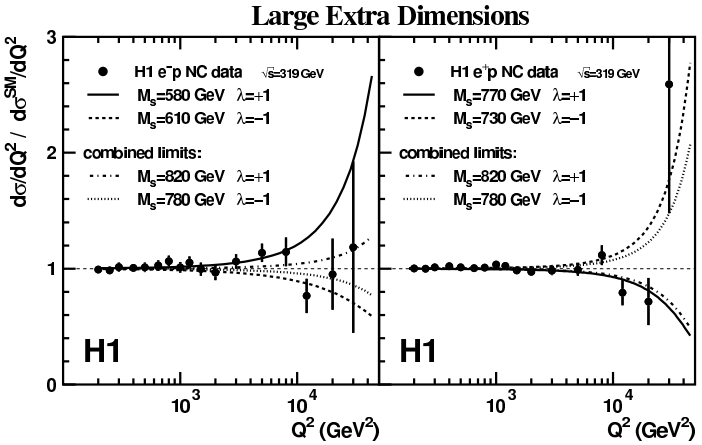

Figure 7.6: *Neutral current cross sections $d\sigma/dQ^2$ at $\sqrt{s}$ =319 GeV normalised to SM expectation. The data are compared to the 95 % CL exclusion limits obtained from each data set and the combined data for gravitational scales M_S assuming positive ($\lambda = +1$) or negative ($\lambda = -1$) coupling.*

and the photon has opposite sign for electron and positron scattering as illustrated in Fig. 7.6. Lower limits on the scale parameter are given in Table 7.3.

A fermion substructure can also be formulated by assigning a finite size to the electroweak charge distributions. It is convenient to introduce electron and quark form factors $f(Q^2)$ which reduce the

Table 7.3: *Lower limits (95 % CL) on the gravitational scale M_S assuming positive ($\lambda = +1$) and negative ($\lambda = -1$) coupling from the e^-p, e^+p and combined $e^-(e^+)p$ data (top part). Upper limits (95 % CL) on the quark radius assuming point-like leptons ($f_e \equiv 1$) or common form factors ($f_e = f_q$) from the e^-p, e^+p and combined $e^-(e^+)p$ data (bottom part).*

	e^-p (319 GeV)	e^+p (319 GeV)	all e^-p & e^+p
Coupling	M_S [TeV]	M_S [TeV]	M_S [TeV]
$\lambda = +1$	0.58	0.77	0.82
$\lambda = -1$	0.61	0.73	0.78
Form factor	$R[10^{-18}\mathrm{m}]$	$R[10^{-18}\mathrm{m}]$	$R[10^{-18}\mathrm{m}]$
$f_e \equiv 1$	1.1	1.1	1.0
$f_e = f_q$	0.8	0.8	0.7

SM cross section at high momentum transfer

$$f(Q^2) = 1 - \frac{\langle r^2 \rangle}{6} Q^2 \ , \quad \frac{d\sigma}{dQ^2} = \frac{d\sigma^{SM}}{dQ^2} f_e(Q^2) f_q(Q^2) \ .$$

Upper limits for $R = \sqrt{\langle r^2 \rangle}$ are given in Table 7.3, too. Analyses performed by other experiments at HERA, LEP and the TEVATRON are providing results similar to ours.

Higgs-, single top-, and W-production

The measurement of rare processes in ep interactions at HERA provides a unique method to search for new physics. Particularly suitable are those final states where high transverse momentum (p_T) leptons are produced. The H1 collaboration analysed quite a few different channels and compared the cross sections to SM model expectations. No statistically significant deviations have been found so far, but some anomalies appear, which need to be substantiated or refuted by HERA II data. In the following a summary of these results is given[3].

Multi-lepton production at high transverse momentum is dominated in the SM by the interactions of quasireal photons radiated by the incident electron and proton leading to a lepton pair ($\gamma\gamma \to \ell^+\ell^-$). For multi-electron final states data corresponding to $\mathcal{L}_{\mathrm{int}} = 115$ pb^{-1}have been analysed [41]. At least two electrons with $20^\circ < \theta_e < 150^\circ$ and $p_T(1) > 10, p_T(2) > 5$ GeV are required in the sample, which comprises 105 $2e$ events and 16 $3e$ events. Good overall agreement is found with the SM predictions, dominated by photon-photon interactions. Six events are observed with a di-electron mass above 100 GeV, where the SM prediction is 0.5. A subsample of 41 events is identified with the $\gamma\gamma$ process by requiring $2e = e^+e^-$ and $\sum E_i - P_{Li} < 45$ GeV (fractional incoming electron energy loss $y < 0.82$). The expected rate within the accepted kinematical region is 48 ± 6. This analysis is the first of its kind at HERA. A similar analysis for muon pair production [43] ($\mathcal{L}_{\mathrm{int}} = 71$ pb^{-1}, $M_{\mu\mu} > 5$ GeV, $p_{T\mu} > 2$ GeV) finds good agreement with the SM model predictions. In the data sample 1243 events were found, while 1253 ± 125 were expected. Figure 7.7 shows the di-muon mass distribution.

The search for the single production of doubly-charged Higgs bosons ($H^{\pm\pm}$) is motivated by the observation discussed above of a few multi-electron events with a large di-electron mass, in a domain

[3]If not explicetely mentioned otherwise the term *electron* describes generically electrons and positrons here

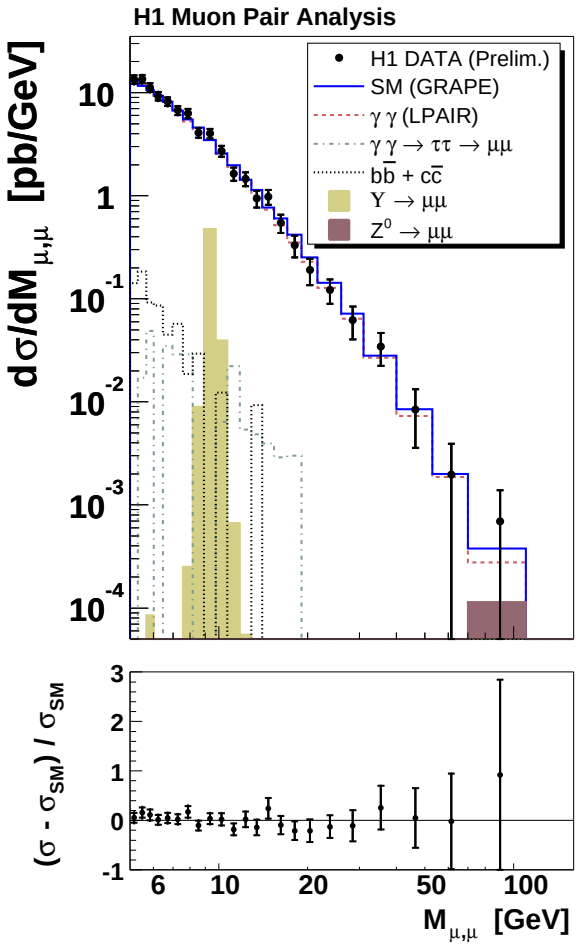

Figure 7.7: *Invariant di-muon mass distribution compared to electroweak SM predictions calculated with the Monte Carlo generator GRAPE [62]. The contributions for the most important processes are indicated separately.*

where the SM expectation is small. It is performed in the framework of models where a Higgs triplet is coupled to leptons of the i^{th} generation via Yukawa couplings h_{ii}. The signal is searched for in the decay modes $H^{\pm\pm} \rightarrow e^{\pm}e^{\pm}, \mu^{\pm}\mu^{\pm}$ using the H1-multi-lepton data sample [42]. Only one of the multi-electron events is found to be compatible with the hypothesis of the decay of a heavy Higgs boson. Assuming that the doubly-charged Higgs only decays to electrons, a lower limit of about 131 GeV can be set on the $H^{\pm\pm}$ mass for a value $h_{ee} = 0.3$ of the coupling, which corresponds to an interaction of electromagnetic strength. This is the first search for doubly-charged Higgs production at HERA.

The search for anomalous top quark production mediated by a flavour changing neutral current via a γut-coupling again the data from an integrated luminosity of $\mathcal{L}_{\rm int} = 115$ pb^{-1} [45]. The top decays into a b-quark jet and a W boson are considered in both the leptonic and the hadronic decay modes of the W. In the leptonic decay modes, five events are found to be compatible with the hypothesis of anomalous top quark production while 1.8 events are expected from the SM. No excess above the SM expectation is found in the hadronic decay channel. An upper limit on the anomalous γut-coupling of $\kappa_{\gamma,u} = 0.22$ is established in the framework of recent NLO calculations [63].

The H1 experiment has reported an excess of events with an isolated lepton, missing transverse momentum and a high E_T hadronic system [14]. We have reported on this in previous annual reports. The kinematics of these events are mostly compatible with a leptonic W decay. While in e^-p scattering ($\mathcal{L}_{\rm int} = 13.6$ pb^{-1}) no events were found consistent with the expectataion for this low luminosity sample, in e^+p ($\mathcal{L}_{\rm int} = 101.6$ pb^{-1}) 18 events were found compared to an expected 10.5 ± 2.5 dominated by W production (8.2 ± 2.5). The excess above the expectation is mainly due to events with transverse momentum of the hadronic system greater than 25 GeV where 10 events are found compared to 2.8 ± 0.7 expected. This prompted a new analysis looking for W production in the jet decay channel. Jets are selected using the inclusive k_T algorithm with a minimum transverse energy of 25 GeV. The phase space has been optimised to maximise the acceptance for W events and to reject other SM processes. No deviation from the SM is found up to highest values of p_T^X, the transverse momentum of the hadronic system. For $P_T^X > 40$ GeV, 25 events are found compared to 2.3 ± 0.7 expected from W-production and 25.9 ± 6.5 from other QCD processes.

7.4.2 Progress of Zürich analysis projects

Prompt photon production

ep collisions at HERA are dominated by electron scattering at small angles with a quasi real photon interacting with the proton (γp collisions). These interactions can also lead to the emission of photons - so called prompt photons - from the hard QCD process, which makes them sensitive both to the partonic structure of the proton and the photon. Events, in which a hard, prompt photon instead of a gluon is emitted depend much less on the fragmentation or hadronisation models since a direct observation of a particle from the hard subprocess is possible. This considerably reduces the systematic error in the determination of the momentum fraction of the partons of the scattering process, and is therefore a better method than the study of dijet-events, which so far has been used, because the full integrated luminosity from the years 96-00 was not available yet.

Prompt photons are identified in the H1 liquid argon calorimeter (LAR) by a compact electromagnetic cluster with transverse energy 5 GeV$< E_T^\gamma <$ 10 GeV in the pseudorapidity region $-1 < \eta^\gamma < 0.9$. No track is allowed to point to the candidate. The main experimental difficulty is the separation from hadronic background. The signal from neutral mesons (π^0 or η^0) at high energies is very similar to the signal of a photon since the decay photons cannot be resolved in the calorimeter. Most of these mesons are associated by a hadronic jet, therefore the photon candidate is required to be isolated. The range of y ($0.2 < y < 0.7$) corresponds to a γp center of mass energy of $142 < W < 266$ GeV.

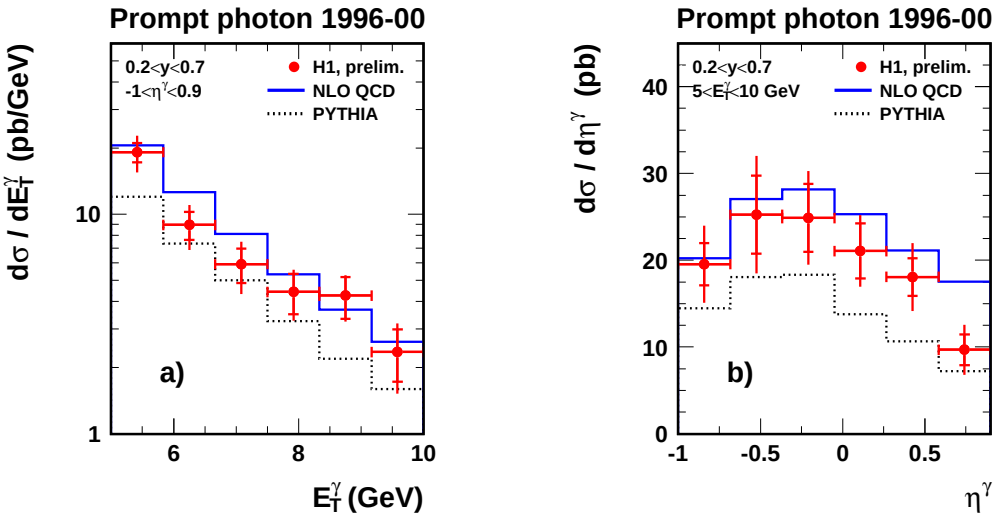

Figure 7.8: *Cross section for prompt photon events as a function of transverse momenta (a) and pseudorapidity η (b) of the photon. The result is compared to LO-Monte Carlo (black) and NLO(blue) calculation.*

First results of this analysis based on $\mathcal{L}_{\rm int} = 102$ pb^{-1} are now avalable [23]. Figure 7.8 shows the prompt photon cross section as a function of transverse energy (a) and pseudorapidity (b). The results are compared to the PYTHIA Monte-Carlo and a NLO-QCD calculation[64]. Both models describe the shape of the data quite well, but not the magnitude.

The measurement will be extended (K. Müller) into the region of high E_T photons as well as into the forward region of the detector to gain more sensitivity on the resolved component of the photon. This will require a detailed knowledge of both the detector response and the detector simulation. Furthermore events with a hadronic jet together with the isolated photon will be selected in order to reconstruct the parton momenta in the photon and the proton.

Beauty production

A strong focus of our physics analysis activities within the H1 collaboration in the past years has been the field of heavy quark production [49]. The interest is twofold: charm production accounts for a large proportion – about 25% – of the total deep inelastic scattering rate at HERA. Understanding the heavy quark production process thus forms a vital ingredient to the proton structure function analysis of inclusive DIS data. Since it is, in the theoretical framework of QCD, a mostly gluon induced reaction, it is particularly suited to enlighten the rôle of gluons in hadronic structure. On the other hand, the heavy quark mass induces a scale in the calculations which renders perturbative methods applicable, such that QCD is relatively predictive for heavy flavour production and allows meaningful tests of the concepts. The fact that the observable hadrons to a large extent inherit the kinematics of the primordially produced quarks provides direct insight into production dynamics at the level of the hard-interacting partons. In contrast to what may be expected on the basis of the large b quark mass, the predictions for beauty production do not well match the experimental data obtained in $\bar{p}p$ collision experiments, or recently from two photon interactions. The HERA data are in similar conflict with theoretical expectations which are based on common methods for these different production modes.

These results received considerable interest; they relate HERA to other environments and communities and demonstrate that there are still open issues in perturbative QCD, to which ep collisions provide particularly viable access. Experimentally, the subject relies strongly on track-based triggering and on precise track and vertex reconstruction, and it thus complements well the contributions to the detector construction made by our institute.

Five PhD thesis projects on heavy quark production have been performed in our group, under supervision of F. Sefkow, who is since last year also acting as convenor of the heavy flavour physics working group in H1. Three theses, on charm production in DIS, in photo-production, and in diffractive interactions, have been completed some time ago and all resulted in journal publications. The electroproduction analysis has recently been updated using a statistically larger data set ($\mathcal{L}_{\rm int} = 48$ pb^{-1} [27], making use of the separation of the D^* decay vertex from the ep-vertex. The thesis of J. Kroseberg on beauty production [50], which pioneered this use of the central silicon tracker information in the H1-analysis, presented the first measurement of b quark production in deep inelastic scattering [26].

In a new approach, explored in the thesis project of I. Foresti, heavy flavoured hadrons are tagged using secondary vertex techniques, which take advantge of the long life-time. The analysis is performed on a sample of μ tagged dijet events. To build up a b-tagging tool, the combined probability for a group of tracks to come from a common origin (the primary vertex of the event) is calculated, and used as a discriminating variable. With the same method used in the μ analysis, the quantities $P_{T,rel}$ (P_T of the track with respect to the jet axis it belongs to) and δ (signed impact parameter) are calculated for the muon. A fit on the distribution of $P_{T,rel}$ against δ gives the decomposition of the data sample (reference spectra from the Monte Carlo distributions of $b\bar{b}$, $c\bar{c}$ and light quark samples). Cutting on the combined probability, it is possible to reject non b events. This analysis has been interupted due to a motherhood leave, but is going to resume soon with the help of S. Xella and will be extended to include the 1999/2000 data, too.

High Q^2 charged current data

As part of the upgrade project the H1 collaboration also changes its software tools to object oriented programming. Within this new analysis frame charged current (CC) data at high Q^2 taken during the last pre-upgrade run 1999/2000 are being analysed by Nicole Werner for her thesis project. The goal of this analysis is a reevaluation of the CC cross section. The analysis has progressed to a point,

where satisfatory initial agreement between the old and the new analysis approach has been reached in all control variables and nearly all bins in Q^2 and x. Fine tuning is in progress.

QED Compton scattering

QED Compton scattering [65] in high energy ep collisions denotes the reaction $ep \to e\gamma X$. In the elastic case ($X = p$) the characteristic event signature is a nearly coplanar electron-photon pair with typically 10 GeV of energy, observed at a finite angle within the detector, with no other activity in the calorimeter, in contrast to Bethe-Heitler bremsstrahlung, where both e and γ escape under small angle, and are possibly detected by the luminosity system. The process was first observed at HERA by H1 [66], and can be used for a measurement of the luminosity (cross check), electromagnetic calibration of the detectors, search for excited electrons e^*, the photon content of the proton and the measurement of F_2 at small Q^2 and large x. For the latter two aspects the inelastic process ($X \neq p$) is used. The analysis, which is the basis of N. Keller thesis, deals with both the elastic and the inelastic channel and the data up to 1997, and is nearly completed.

[1] *Measurement of $D^{*\pm}$-Meson Production and F_2^c in Deep-Inelastic Scattering at HERA*, H1-Coll. C. Adloff *et al.*, DESY 01 – 100, hep-ex/0108039, Phys. Lett. **B528** (2002), 199 - 215

[2] *Search for Excited Neutrinos at HERA*, H1-Coll., C. Adloff *et al.*, DESY 01 – 145, hep-ex/0110037, Phys. Lett. **B525** (2002), 9 - 16.

[3] *Measurement of Dijet Electroproduction at Small Jet Separation*, H1-Coll., C. Adloff *et al.*, DESY 01 – 178, hep-ex/0111006, Eur. Phys. J. **C24** (2002), 33 - 41.

[4] *Measurement of Dijet Cross Sections in Photoproduction at HERA*, H1-Coll., C. Adloff *et al.*, DESY 01 – 225, hep-ex/0201006, Eur. Phys. J. **C25** (2002), 13 - 23.

[5] *Energy Flow and Rapidity Gaps between Jets in Photoproduction at HERA*, H1-Coll., C. Adloff *et al.*, DESY 02 – 023, hep-ex/0203011, Eur. Phys. J. **C24** (2002), 517 - 527.

[6] *A Measurement of the t Dependence of the Helicity Structure of Diffractive ρ Meson Electroproduction at HERA*, H1-Coll., C. Adloff *et al.*, DESY 02 – 027, hep-ex/0203022, Phys. Lett. **B539** (2002), 25 - 39.

[7] *Inelastic Photoproduction of J/Ψ Mesons at HERA*, H1-Coll., C. Adloff *et al.*, DESY 02 – 059, hep-ex/0205064, Eur. Phys. J. **C25** (2002), 25 - 39.

[8] *Inelastic Leptoproduction of J/Ψ Mesons at HERA*, H1-Coll., C. Adloff *et al.*, DESY 02 – 060, hep-ex/0205065, Eur. Phys. J. **C25** (2002), 41 - 53.

[9] *Search for QCD Instanton-Induced Processes in Deep-Inelastic Scattering at HERA*, H1-Coll., C. Adloff *et al.*, DESY 02 – 062, hep-ex/0205078, Eur. Phys. J. **C25** (2002), 495 - 509.

[10] *Diffractive Photoproduction of $\Psi(2S)$ Mesons at HERA*, H1-Coll., C. Adloff *et al.*, DESY 02 – 075, hep-ex/0205107, Phys. Lett. **B541** (2002), 251 - 264.

[11] *Measurement of Inclusive Jet Cross Sections in Deep-Inelastic ep Scattering at HERA*, H1-Coll., C. Adloff *et al.*, DESY 02 – 079, hep-ex/0206029, Phys. Lett. **B542** (2002), 193 - 206.

[12] *Search for Odderon-induced Contributions to Exclusive π^0 Photoproduction at HERA*, H1-Coll., C. Adloff *et al.*, DESY 02 – 087, hep-ex/0206073, Phys. Lett. **B544** (2002), 35 - 43.

[13] *Search for Excited Electrons at HERA*, H1-Coll., C. Adloff *et al.*, DESY 02 – 096, hep-ex/0207038, Phys. Lett. **B548** (2002), 35 - 44.

[14] *Isolated Electrons and Muons in Events with Missing Transverse Momentum at HERA*, H1-Coll., V. Andreev *et al.*, DESY 02 – 224, hep-ex/0301030, submitted to Phys. Lett. **B** (2003).

[15] *Measurement of Inclusive Jet Cross Sections in Photoproduction at HERA*, H1-Coll., C. Adloff *et al.*, DESY 02 – 225, hep-ex/0302034, submitted to Eur. Phys. J. **C** (2003).

[16] *Measurement and QCD Analysis of Neutral and Charged Current Cross Sections at HERA*, H1-Coll., C. Adloff *et al.*, DESY 03 – 038, hep-ex/0304003, submitted to Eur. Phys. J. **C** (2003).

[17] Contr. Papers of the H1-Coll., C. Adloff *et al.*, to the Int. Conf. on High Energy Physics, Amsterdam (July 2002).

[18] *Measurement of the Deep Inelastic Scattering Cross Section at $Q^2 \approx 1$ GeV^2 with the H1 Experiment*, (#975 [17]).

[19] *Measurement of the Proton Structure Function Using Radiative Events at HERA*, (#976 [17]).

[20] *Measurement and QCD Analysis of Inclusive Deep-Inelastic Scattering at High Q^2 and Large x*, (#978 [17]).

[21] *Forward π^0 Meson Production at HERA*, (#1000 [17]).

[22] *Forward Jet Production at HERA*, (#1001 [17]).

[23] *Prompt Photon Production at HERA*, (#1007 [17]).

[24] *Measurement of Dijet Cross Sections at low Q^2 at HERA*, (#1009 [17]).

[25] *Measurement of Single Inclusive High E_T Jet Cross Sections in Photoproduction at HERA*, (#1010 [17]).

[26] *Beauty Production in Deep Inelastic Scattering*, (#1013 [17]).

[27] *Inclusive D-meson Production in Deep Inelastic Scattering at HERA*, (#1015 [17]).

[28] *Measurement of D^* - Muon Correlations in Deep Inelastic Scattering*, (#1016 [17]).

[29] *Measurement and NLO DGLAP QCD Analysis of Inclusive Diffractive Deep Inelastic Scattering*, (#980 [17]).

[30] *Measurement of the Diffractive Structure Function at Low Q^2*, (#981 [17]).

[31] *Measurement of Semi-inclusive Diffractive Deep Inelastic Scattering with a Leading Proton*, (#984 [17]).

[32] *Diffractive Dissociation in Photoproduction at HERA*, (#985 [17]).

[33] *Diffractive Photoproduction of Jets at HERA*, (#987 [17]).

[34] *Measurement of Dijet Cross-Sections with Leading Neutrons in ep interactions at HERA*, (#988 [17]).

[35] *Elastic Electroproduction of ρ Mesons at High Q^2*, (#989 [17]).

[36] *Photoproduction of ρ Mesons with a Leading Proton*, (#991 [17]).

[37] *Diffractive J/Ψ Photoproduction at Large $|t|$ at HERA*, (#993 [17]).

[38] *Investigation of Pomeron- and Odderon Induced Photoproduction of Mesons Decaying to Pure Multiphoton Final States at HERA*, (#997 [17]).

[39] *The Photoproduction of Protons at HERA*, (#1002 [17]).

[40] *A Search for Contact Interactions at HERA*, (#979 [17]).

[41] *Electron Pair Production in ep Collisions at HERA*, (#1019 [17]).

[42] *Search for Doubly Charged Higgs Production at HERA*, (#1020 [17]).

[43] *Muon Pair Production in ep Collisions at HERA*, (#1021 [17]).

[44] *Search for W Production in the Hadronic Decay Channel at HERA*, (#1023 [17]).

[45] *A Search for Single Top Production at HERA*, (#1024 [17]).

[46] *A Search for Leptoquarks at HERA*, (#1027 [17]).

[47] *A Direct Search for Magnetic Monopoles*, H1-Coll., A. Aktas *et al.*, Contr. to 11^{th} Int. Workshop on Deep Inelastic Scattering (DIS2003), St. Petersburg RU (April 2003).

[48] *Searches for contact interactions at HERA*, S. Schmitt, Proc. 10^{th} Int. Workshop on Deep Inelastic Scattering (DIS2002), Cracow PL (May 2002), Acta Phys. Polon. **B33** (2002), 3923-3928.

[49] *Heavy Quark Physics at HERA*, F. Sefkow, Proc. XXX^{th} SLAC Summer Institute, Stanford CA, USA (July 2002).

[50] *A Measurement of Beauty Production in High-Energy Positron-Proton Scattering*, Jürgen Kroseberg, PhD-thesis, Zürich 2002.

[51] V. Andreev *et. al.*, Report H1-01/03-607; H1-10/02-606.

[52] *The CIP2k first level trigger system at the H1 experiment at HERA*, M. Urban, J. Becker, S. Schmitt, and U. Straumann, IEEE Trans. Nucl. Sci. **50**, 4 (2003), in print.

[53] *The CIP2k first level trigger system at the H1 experiment at HERA*, M. Urban, J. Becker, S. Schmitt, and U. Straumann, Proc. 2002 IEEE Nucl. Sci. Symp./Medical Imaging Conf., Norfolk VI, USA (November 2002).

[54] *A first level Trigger subsystem CIP2k for the H1 experiment at HERA*, J. Becker, H. Cramer, M. Hildebrandt, K. Müller, S. Schmitt, U. Straumann, M. Urban, and N. Werner, Proc. 8^{th} Topical Seminar on Innovative Particle and Radiation Detectors, Siena I (October 2002), Nucl. Instr. Methods **A**, in print.

[55] *Compact Frontend-Electronics and Bidirectional 3.3 Gbps Optical Datalink for Fast Proportional Chamber Readout*, S. Lüders *et al.*, hep-ex 0107064, Nucl.Instr.Meth.**A484** (2002) 515-527.

[56] H1-Coll., C. Adloff *et al.*, Eur. Phys. J. **C13** (2000) 609.

[57] H1-Coll., C. Adloff *et al.*, Eur. Phys. J. **C19** (2001) 269.

[58] H1-Coll., C. Adloff *et al.*, Phys. Lett. **B479** (2000) 358.

[59] H.L. Lai *et al.*, Eur. Phys. J. **C12** (2000) 375.

[60] H1-Coll., C. Adloff *et al.*, Eur. Phys. J. **C11** (1999) 447; erratum ibid. **C14** (1999) 553.

[61] N. Arkani-Hamed, S. Dimopoulos, and G.R. Dvali, Phys.Lett. **B429** (1998) 263; Phys. Rev. **D59** (1999) 086004.

[62] T. Abe, Comp. Phys. Comm. **136** (2001) 126.

[63] A. Belyaev and N. Kidonakis, preprint hep-ph/0102072.

[64] M. Fontannaz, J.P. Guillet, and G. Heinrich, Eur. Phys. J. **C21** (2001) 303.

[65] A. Courau, and P. Kessler, Phys. Rev. **46** (1992), 117.

[66] H1-coll., C. Adloff *et al.*, Phys. Lett. **B517**, 47 (2001).

8 Particle Physics at DESY/HERA (HERA-B)

P. Robmann and P. Truöl

in collaboration with:
the Universities of Heidelberg and Siegen and 31 further institutes from outside Switzerland

(HERA-B)

During the long HERA shutdown period that ended in 2002 many detector components were improved. These include the microstrip gas chamber system of the inner tracker in which we are involved (see also [1] and [2]). Now the experiment performs to full satisfaction and the number of recorded J/ψ decays, for example, has increased from ≈ 0.5 min^{-1} during the year 2000 to ≈ 20 min^{-1} in January 2003. Only a small fraction of theses events have been analyzed sofar. Figure 8.1 shows the invariant mass distributions of $\mu^+\mu^-$ and e^+e^- pairs. Clearly visible are the peaks from J/ψ and ψ' decays at 3.1 GeV/c^2 and 3.65 GeV/c^2, respectively.

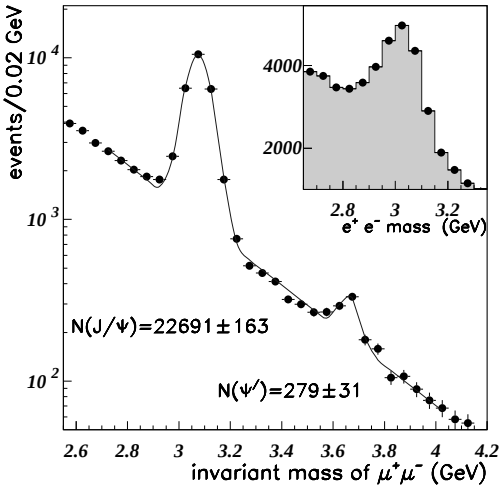

Figure 8.1: *Invariant mass spectrum of $\mu^+\mu^-$ pairs. Charmonium states are clearly seen on an exponentially falling background. The insert shows the coresponding electron distribution.*

As a consequence of the better noise performance of the electromagnetic calorimeter, the electron identification no longer has to rely on the existence of bremsstrahlung photons and J/ψ decays are clearly reconstructible in the channel $J/\psi \to e^+e^-$ (Fig. 8.1). Thanks to the increased DAQ bandwidth the event logging rate could be raised from about 40 Hz to more than 1000 Hz. This allowed to take a large sample of minimum bias data in a relatively short time using a simple trigger based on the multiplicities observed in the ring imaging Cerenkov counter (RICH) and the electromagnetic calorimeter (ECAL). These data will be used both for calibration and for physics analysis of inclusive proton-nucleus collisions.

Different target materials between carbon and tungsten can be used to study A-dependencies. These measurements give important input for the theoretical understanding of the creation of quark-gluon plasma in heavy-ion collisions and of heavy flavour production in hadronic interactions. To minimize systematic uncertainties several targets of different material can be operated simultaneously. HERA-B is an almost central detector in the proton-nucleon center of mass system. The accessible kinematic region therefore extends to the backward hemisphere with the Feynman's $x_F < 0$, which is barely covered by other experiments in this energy regime.

8.1 Charmonium production in 920 GeV proton-nucleus interactions

The production mechanism of heavy flavours in hadronic collisions is not well understood and rather different theoretical concepts are used for its description. The Color Singlet Model (CSM) assumes the $q\bar{q}$ pair to be produced in a color singlet state with the quantum numbers of the final meson. In the

non-relativistic QCD factorization approach (NRQCD) a color singlet or octet quark pair evolves towards the final bound state via exchange of soft gluons while in the Color Evaporation Model (CEM) the exchange of many soft gluons during the formation process of the bound state results in the loss of information about the production mechanism of the $q\bar{q}$ pair. Charmonium production is an attractive test case as the quarks are heavy enough for perturbative calculations, and the cross sections are large enough to be experimentally accessible. In particular, the dependence of the ratio of production cross sections of different charmonium states like $R_{\chi ci} = \sigma(\chi_{ci}) \,/\, \sigma(J/\psi)$ on center-of-mass energy $\sqrt{s}$ allows to differentiate between different models. Preferably, the radiative decay $\chi_{ci} \to J/\psi\gamma_i$ is measured using the subsequent decay $J/\psi \to \ell^+\ell^-$ for triggering. In most experiments the energy resolution is insufficient to resolve the individual χ_{ci} states, and one usually quotes the ratio $R_{\chi_c} = \sum_{i=1}^{2} \left(\sigma(\chi_{ci}) \cdot Br(\chi_{ci} \to J/\psi)\right) \,/\, \sigma(J/\psi)$ where $\sigma(J/\psi)$ is the sum of cross sections for direct J/ψ production and for J/ψ production from χ_{ci} and ψ' decays. Quite a few experimental data are available for values of $\sqrt{s}$ between 8.5 and 62 GeV but the situation is unclear since experimental errors are in general large. We determined a new value of $R_{\chi c}$ at $\sqrt{s} = 41.6$ GeV [3] based on data collected during a short commissioning run of the J/ψ trigger in 2000. About half of this data was taken with a single carbon wire target, the rest with carbon and titanium wires together. The detector acceptance for the J/ψ's covered a range of $-0.25 < x_F < 0.15$.

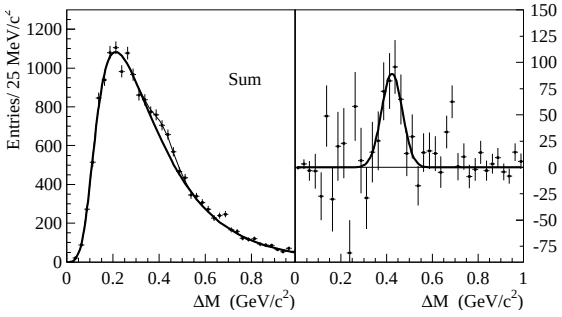

Figure 8.2: *ΔM distributions (see text). Left: experimental points and combinatorial background from event mixing (solid line). Right: χ_c signals after background subtraction.*

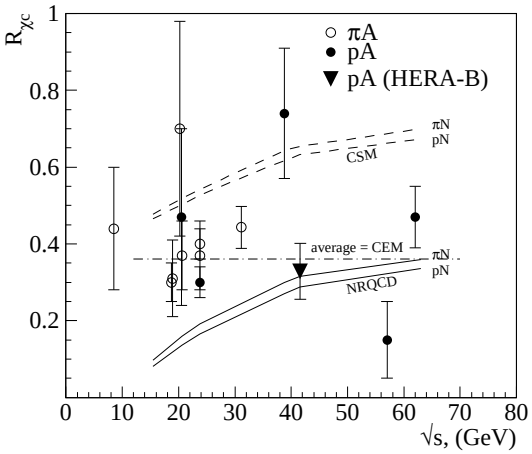

Figure 8.3: *Comparison of $R_{\chi c}$ values determined in pA and πA experiments at indicated center-of-mass energies $\sqrt{s}$. Error bars include statistical and systematic uncertainties. The dot-dashed line is the average of all measurements. Model predictions based on NRQCD and CSM (see text) are shown by solid and dashed lines, respectively. The CEM predicts a constant value.*

The χ_c is observed in the radiative χ_c decay using the difference ΔM between the invariant mass of the $(\ell^+\ell^-\gamma)$ system and the invariant mass of the lepton pair, $\Delta M = M(\ell^+\ell^-\gamma) - M(\ell^+\ell^-)$. Fig. 8.2 shows for all combinations of J/ψ and photon candidates the ΔM distribution for the entire data sample. The excess of events above the combinatorial background determines the number of χ_c candidates from which $R_{\chi c}$ is calculated. Within statistics the results obtained for carbon and titanium are consistent with each other; their average yields a value of $\langle R_{\chi c} \rangle = 0.32 \pm 0.06_{stat} \pm 0.04_{sys}$. Fig. 8.3 compares the HERA-B result with previous data and theoretical predictions; see [3] for a detailed list of references. The HERA-B result is compatible with most of the previous data.

Due to the large errors, a flat energy dependence, as predicted by CEM, cannot be ruled out. Similarly, the slope of the energy dependence as predicted by a Monte Carlo based on NRQCD is also compatible with the data. The absolute value, however, in general seems to be too low, indicating that the NRQCD long distance matrix elements for χ_c production are un-

derestimated. On the other hand, CSM predicts $R_{\chi c}$ to be larger than most of the experimental values. During the 2002 physics run the data sample increased by more than an order of magnitude which will reduce the statistical error of $R_{\chi c}$ significantly. It will also be possible to study the A-dependence.

8.2 Inclusive V^0 production cross sections from 920 GeV fixed target proton-nucleus collisions

One of the main goals of heavy-ion experiments is the observation of the quark-gluon plasma[5] and a possible signature for this state is the enhanced production of strange particles [6]. This led to a renewed interest in strangeness production. Observables of interest are ratios of antibaryons to baryons at mid-rapidity, which are important for net baryon density evaluations and which have been used recently to extract values of chemical potentials and temperatures [7; 8] for Au-Au collisions at RHIC. Also of interest is the transverse momentum distribution which contains information on the temperature of the system after reaching thermal equilibrium (see [9]). These investigations motivate a comprehensive measurement of strange-particle production properties in "ordinary" nucleon-nucleon (NN) and nucleon-nucleus (NA) collisions. The latter are expected to establish a valuable baseline for comparisons among AA results [7].

A sample of $\sim$2.4 million minimum bias events selected with a random trigger that uniformly sampled all HERA bunches, was taken in 2000 to allow for a precise measurement of strange-particle production cross sections. The inclusive cross sections for K^0_S, Λ, and $\bar{\Lambda}$ particles, collectively referred to as V^0 particles, were determined with various nuclear targets. Experimental details can be found in [4]. V^0 candidates were selected from events with track pairs of opposite charge with a vertex downstream of the primary vertex. The primary vertex was required to coincide with the center of a target wire to within three standard deviations. If no primary vertex could be reconstructed, the z-coordinate of the target was used to calculate the z-component of the particle's flight path. The requirement of a minimal flight path reduces the tracks combinatorial background. The invariant mass distributions for the selected candidates are shown in Fig. 8.4. Clear signals corresponding to K^0_S, Λ, and $\bar{\Lambda}$ decays are visible. Based on the Monte-Carlo simulation, the luminosity evaluation and the extrapolation by the Glauber formalism, the production cross section per nucleon was calculated. The result is in good agreement with previous measurements (see Fig. 8.5)

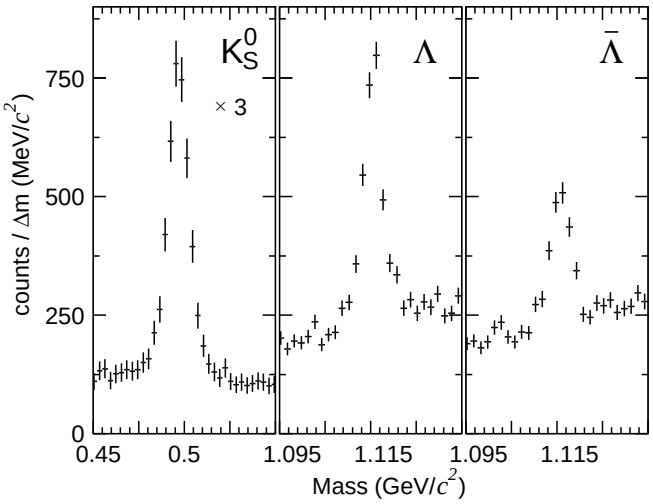

Figure 8.4: *Invariant mass distributions for K^0_S, Λ, and $\bar{\Lambda}$ particles summed over all runs with different targets. The bin width Δm is 3.0 MeV/c^2 for the K^0_S distribution and 1.5 MeV/c^2 otherwise.*

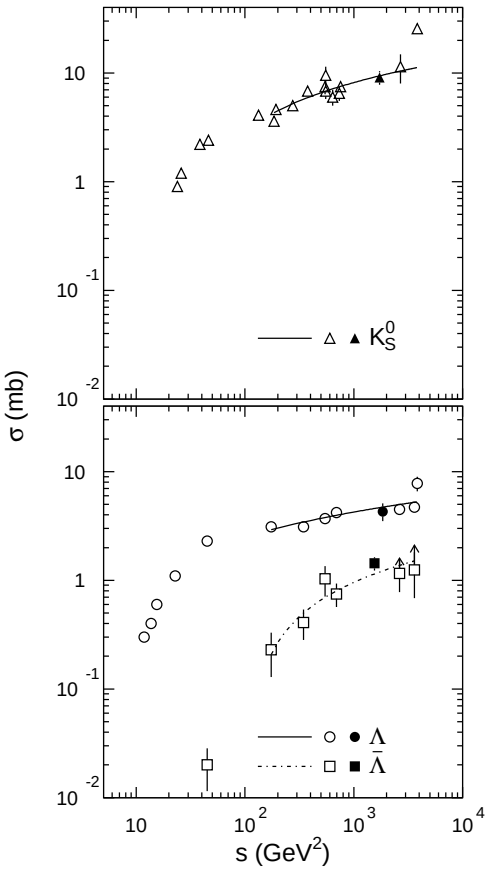

Figure 8.5: *The total cross section per nucleon σ_{pN} for the production of K^0_S, Λ and $\bar{\Lambda}$ as a function of the center-of-mass energy squared s. Full black symbols denote our own results. The curves are fit [12] to the data in the interval 180 - 800 GeV. See [4] for the full references.*

[1] Physik-Institut, Universität Zürich, Annual Report 2001/2, available at *http://www.physik.unizh.ch/jb/2002*.

[2] *Studies of Aging and HV Breakdown Problems during Development and Operation of MSGC and GEM Detectors for the Inner Tracking System of HERA-B* Y. Bagaturia, O. Baruth, H.B. Dreis, F. Eisele, I. Gorbunov, S. Gradl, W. Gradl, S. Hausmann, M. Hildebrandt, T. Hott, S. Keller, C. Krauss, B. Lomonosov, M. Negodaev, C. Richter, P. Robmann, B. Schmidt, U. Straumann, P. Truöl, S. Visbeck, T. Walter, C. Werner, U. Werthenbach, G. Zech, T. Zeuner, and M. Ziegler, hep-ex/0204011, Nucl.Instr.Meth.**A490** (2002), 223 - 242.

[3] *J/ψ Production via χ_c Decays in 920 GeV pA Interactions*, The HERA-B Collaboration, I. Abt *et al.*, DESY-02-187, hep-ex/0211033, submitted to Phys.Lett.**B**.

[4] *Inclusive V^0 Production Cross Sections from 920 GeV Fixed Target Proton-Nucleus Collisions*, The HERA-B Collaboration, I. Abt *et al.*, DESY-02-213, hep-ex/0212040, submitted to Eur.Phys.J.**C**.

[5] see, e.g., Proc. 15th Int. Conf. on Ultra-Relativistic Nucleus-Nucleus Collisions (QM2001), Nucl.Phys.**A698** (2002) Issue 1-4.

[6] S. A. Bass *et al.*, Nucl.Phys.**A661** (1999) 205c.

[7] J. Rafelski *et al.*, nucl-th/0104042.

[8] P. Braun-Munzinger *et al.* nucl-ph/0105229.

[9] L. V. Bravina *et al.*, Phys.Rev.**C60** (1999) 024904.

[10] V. Blobel *et al.*, Nucl.Phys.**B69** (1974) 454.

[11] M. Asai *et al.*, Z. Phys. **C27** (1985) 11.

[12] H. Kichimi *et al.*, Phys.Rev.**D20** (1979) 37.

9 High-precision CP-violation Physics at LHCb

R.Bernet, R.P.Bernhard, St.Heule, F.Lehner, C.Lois Gomez, M.Needham,
P.Sievers, O.Steinkamp, U.Straumann, A.Vollhardt

in collaboration with:
The silicon tracking group of LHCb: University of Lausanne; Max Planck Institute, Heidelberg, Germany; University of Santiago de Compostela, Spain; Budker Institute for Nuclear Physics (INP), Novosibirsk, Russia and Ukrainian Academy of Sciences, Kiev, Ukraine.

The full LHCb collaboration consists of 51 institutes from Brazil, China, Finland, France, Germany, Italy, The Netherlands, Poland, Romania, Russia, Spain, Switzerland, Ukraine, and the United Kingdom.

(LHCb)

The LHCb experiment [1] is designed to exploit the large $\mathrm{b\overline{b}}$ production cross section at the LHC in order to perform a wide range of precision studies of CP violating phenomena in the B meson systems. The experiment will use a moderate luminosity of $2 - 5 \times 10^{32}\mathrm{cm}^{-2}\mathrm{s}^{-1}$ and will be fully operational at the startup of the collider, which is foreseen for 2007.

The copious production of all flavours of B mesons and of b hadrons, combined with the unique particle-identification capabilities of the LHCb detector, will allow the experiment to perform sensitive measurements of CP violating asymmetries in a variety of decay channels that are beyond the reach of the current generation of CP-violation experiments. In particular, the possibility to investigate the decays of $\mathrm{B_s}$ mesons gives access to an important field of research that is not accessible to the successfully operating "B factories", BaBar and Belle. Both these experiments have recently presented first precision measurements of a CP violationg asymmetry in the decay $\mathrm{B_d} \rightarrow \mathrm{J}/\psi\mathrm{K_s}$. However, $\mathrm{B_s}$ mesons are not produced at the $\mathrm{e^+e^-}$ colliders at which these experiments operate.

Since the production of b quarks at LHC is strongly peaked towards small polar angles with respect to the beam axis, the LHCb detector is layed out as a single-arm forward spectrometer. Its acceptance extends out to 300 mrad in the horizontal bending plane of the 4 Tm dipole magnet and to 250 mrad in the vertical plane. The forward acceptance is limited by the LHC beam pipe which follows a 10 mrad cone.

In order to fully exploit its exciting physics potential, the LHCb apparatus must ensure high trigger and event reconstruction efficiencies for all interesting physics channels. An efficient and precise reconstruction of the trajectories of charged particles is a key ingredient towards achieving this aim, since many of the interesting B meson decay channels are characterised by final states that involve multiple charged particles. On the other hand, track reconstruction is one of the most challenging tasks in the high-rate environment of LHCb, where charged particle fluxes of up to $5 \times 10^5\,\mathrm{cm}^{-2}\mathrm{s}^{-1}$ are expected in the very forward region.

Our group has taken a major responsibility for the design and development of the silicon tracking system for LHCb.

9.1 Silicon tracker

In the original design of the LHCb detector, the tracking system consisted of nine planar tracking stations, each of which employed two different detector technologies: silicon microstrip detectors

covered the region of highest particle fluxes close to the beam pipe and straw drift tube detectors were employed for the remainder of the acceptance. Extensive simulation studies, in which M. Needham took a leading role, demonstrated that the required reconstruction efficiency and momentum resolution were reached in this setup.

Further investigations, to which M. Needham again contributed significantly, showed that a comparable tracking performance could be achieved [2] in a reduced setup using only one station (TT) upstream of the dipole magnet and three stations (T1-T3) downstream of the magnet. A smaller number of tracking stations is advantageous for several reasons, one of the most important being that the loss of particles due to nuclear interactions in the material of the detector is reduced significantly.

In addition, the reduction of the number of tracking stations liberated resources that permitted to envisage a layout of the relatively small TT station, in which the acceptance of this station is entirely covered by silicon microstrip detectors. This station is going to be used not only in the offline track reconstruction but also in the Level-1 trigger. Here, it is employed in order to assign transverse momentum information to high-impact parameter tracks reconstructed in the vertex detector. Simulation studies [3] have shown that an all-silicon layout for the TT station provided for a significantly better trigger performance than the original layout with silicon microstrips close to the beam pipe and straw drift tubes in the outer region of the station.

In the revised layout of the LHCb tracking system, silicon microstrip detectors thus cover the entire TT station and the innermost part of stations T1-T3 (Inner Tracker). TT and Inner Tracker together form the so-called Silicon Tracker system, which is led by U. Straumann (coordinator) and O. Steinkamp (deputy coordinator).

The design of the Inner Tracker is well advanced. The Techical Design Report (TDR) for this detector [4], written by O. Steinkamp, was submitted to the CERN LHCC on November 8, 2002. It was well received by the committee and has been recommended for general approval. The Inner Tracker TDR is based to a large extent on design and R&D efforts carried out in our group, as described below.

The design of the TT station is, by comparison, in an early stage. A conceptual layout for the all-silicon station has been proposed [5] by O. Steinkamp, but a significant R&D effort is still required in order to validate this layout and develop a technical design for the station. After the submission of the Inner Tracker TDR, our group has taken a leading role in this effort.

9.1.1 Inner tracker

The size and shape of the area covered by the Inner Tracker was determined from the requirement of acceptably low occupancies in the straw tracker [6], while keeping the area covered by the expensive silicon technology as small as possible. Optimisation studies lead to the layout illustrated in Figure 9.1.

Each Inner Tracker station consists of four independent detector boxes, above, below and to both sides of the beam pipe. A detector box contains four detection layers and each detection layer consists of seven staggered ladders of silicon sensors. Silicon ladders are two sensors (22 cm) long in the side boxes, and one sensor (11 cm) long in the top/bottom boxes. All silicon ladders within a detector box are mounted on a common cooling plate that removes the heat generated by the front-end readout chips and cools the silicon sensors. The detector box is housed in an enclosure that provides thermal, optical and electrical insulation. In total, the Inner Tracker employs 12 detector boxes and 504 silicon sensors arranged in 336 ladders. It covers a sensitive area of approximately 4.2 m^2 and

Figure 9.1: *The inner tracker.*

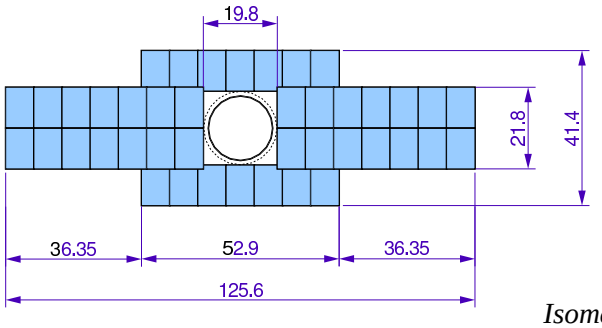

Layout of an Inner Tracker station. Dimensions are in cm.

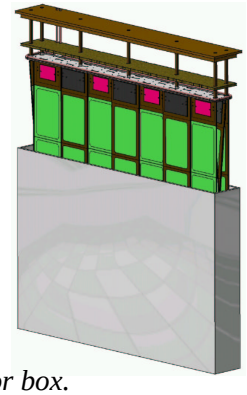

Isometric view of a detector box. The box enclosure is partially removed to show the silicon sensors and box mechanics.

has 130k readout channels.

R&D for the Inner Tracker is to a large extent driven by the effort to minimise detector material. Any active or passive material inside the acceptance of the experiment reduces the performance of the detector, due to multiple scattering and inelastic interactions of the particles. Minimising detector material implies on the one hand that silicon sensors should be as thin as possible, and on the other hand that light-weight materials have to be used for the mechanical support of the detectors.

The LHC bunch-crossing frequency of 40 MHz requires the use of fast front-end electronics with a shaping time of the order of 25 ns in order to avoid overlapping events from consecutive bunch crossings. The combined requirements of fast read-out electronics, thin sensors, and long read-out strips limit the attainable signal-to-noise performance of the detector. A detailed R&D program, involving laboratory tests and test beams at CERN has been carried out in order to optimise the detector geometry and demonstrate that a sufficiently high signal-to-noise ratio and full particle detection efficiency can be ensured. P. Sievers contributed significantly at all stages of these investigations and in January 2003 obtained his PhD degree for his excellent work [7].

First measurements [8], performend on prototype sensors produced at the company SPA Detector, Kiev, had demonstrated a significant reduction of charge collection efficiency in the central region in between readout strips. For a 22 cm long ladder at LHC-compatible shaping time, this signal loss would result in a sizeable loss of particle detection efficiency. However, these measurements were hampered by a relatively low breakdown voltage of the sensors. Subsequently, a second generation of prototype sensors were produced by HPK Hamamatsu from 320 μm thick 6" wafers, according to specifications by F. Lehner and O. Steinkamp. These sensors are 110 mm long and 78 mm wide, which are the dimensions foreseen for the final detectors. They contain 352 read-out strips with five different strip geometries, namely two strip pitches (198 μm and 237.5 μm) and different strip widths corresponding to w/p values between 0.25 and 0.35.

After an extensive characterisation of their electrical and mechanical properties [9], these sensors were assembled in one- and two-sensor long detector ladders and equipped with a prototype version of the LHCb readout chip, called Beetle 1.1. Measurements in a beam test at the CERN X7 facility in May/June 2002 confirmed [10] the occurance of a reduced charge collection efficiency in the central region in between readout strips. However, as illustrated in Figure 9.2, the observed signal loss was reduced to an acceptably low level for the smaller strip pitch of 198 μm and sufficiently high sensor bias voltages. Furthermore, the measurements demonstrated that a signal-to-noise level of eleven could be obtained for the 22 cm long silicon ladders, whereas a signal-to-noise level of ten was shown to be sufficient to ensure full particle detection efficiency. It was thus decided to adopt the proposed

layout of the Inner Tracker, using the smaller strip pitch of 198 μm.

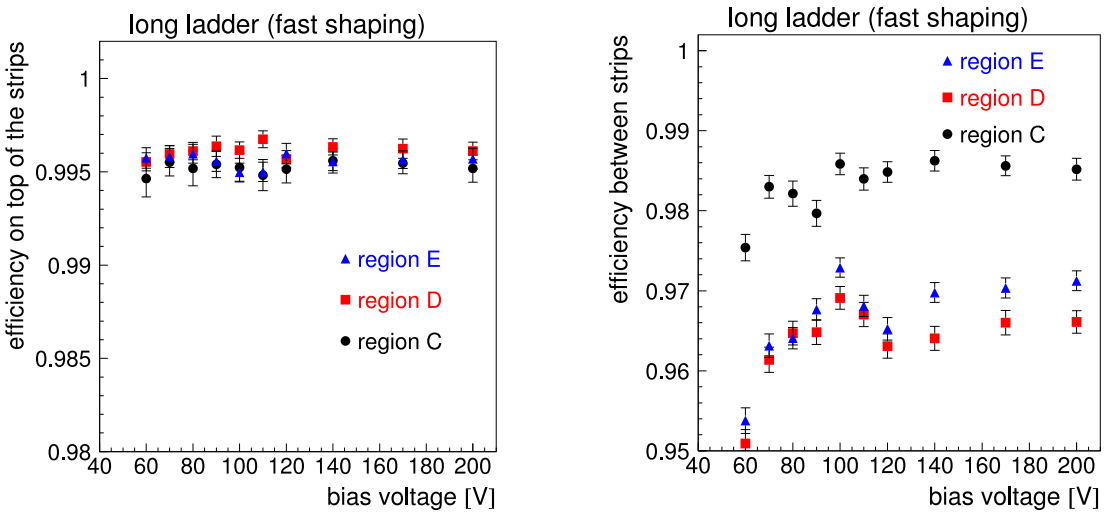

Figure 9.2: *Particle detection efficiency close to a readout strip (left) and in between two strips (right). Region "C" has a strip pitch of 198 μm, regions "D" and "E" have a strip pitch of 237 μm.*

In order to study the origin of the observed loss of charge collection efficiency in between readout strips, a dedicated simulation program was developed by St. Heule as part of his Diploma thesis. The simulation includes the charge transport and signal generation in silicon, as well as the response of the Beetle readout chip. In addition, a laboratory test stand that employs a focussed infra-red laser beam to generate charges at well-defined locations on the silicon sensors has been set up in our laboratory by P. Bernhard, St. Heule and A. Vollhardt.

In parallel to the studies on silicon sensors, an extensive R&D program was carried out [11] in order to identify suitable lightweight materials for the detector box mechanics. These materials must be precisely machinable, have to exhibit high thermal conductivity and should have as long as possible radiation length and nuclear interaction length. The R&D program was led by F. Lehner and carried out both in our laboratory and in collaboration with several outside institutes. In particular, a new type of metal matrix composite material, using high-tensile carbon fibres embedded in a Magnesium matrix, was developed and characterized in a joint effort with the EMPA/Thun. This material was shown to exhibit all properties required for the various pieces of the Inner Tracker mechanics.

9.1.2 TT station

The acceptance of the TT station covers an area of approximately 140 cm $\times$ 120 cm. The proposed layout [5] for this station is illustrated in Figure 9.3. It employs long silicon ladders that span the full height of the active area. All readout electronics and associated mechanics are located above and below the active area and outside of the acceptance of the experiment. Electronically, each ladder is split into five readout sectors, with the inner sectors being connected to their readout electronics via 33 cm and 55 cm long kapton interconnects, respectively. For four detection layers, the TT station employs 832 silicon sensors, arranged in 80 ladders and 376 readout sectors. It covers a sensitive area of approximately 6.8 m^2 and counts 144k readout channels.

Compared to the Inner Tracker detectors, the longer readout strips and the kapton interconnects employed in the TT station will give rise to higher load capacitances at the input of the front-end readout chips, resulting in larger noise. Thicker silicon sensors need thus to be employed here, in order

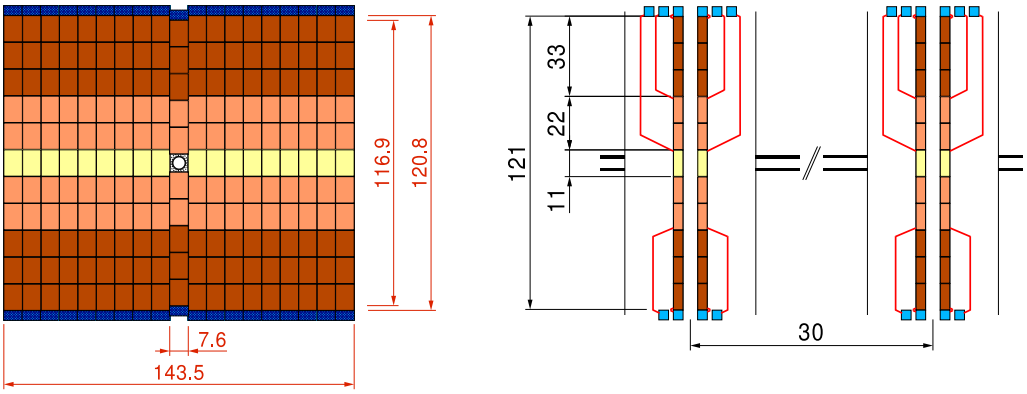

Figure 9.3: *Front (left) and side (right) views of the proposed layout for the TT station.*

to maintain sufficiently high signal-to-noise ratios. First estimates show that 500 μm thick sensors should provide large enough signals to ensure full particle detection efficiency. However, these estimates do not take into account ballistic deficits, which could become sizeable at the fast shaping times required for operation at LHC.

Our group has started an intensive R&D program in order to investigate signal collection in thick silicon sensors and particle detection efficiencies for long ladders using fast signal shaping times. Several, approx. 30 cm long test ladders have been assembled from sensors of different thicknesses between 320 μm and 500 μm. One test ladder is equipped with a 33 cm long kapton interconnect that has been produced in cooperation with the company Dyconex, Bassersdorf. All ladders are equipped with an improved version of the read-out chip, the Beetle 1.2. The ladders are being tested in the infra-red laser setup in our laboratory, while a beam test at CERN is under preparation. In addition, the simulation studies mentioned above are being extended to include thicker sensors and kapton interconnects.

In parallel, we have started to work on the mechanical design of the station.

9.2 Optical readout link

The front-end chip samples detector data at the LHC bunch crossing frequency of 40 MHz. At a Level-0 trigger accept, the analog data are read out, digitised, multiplexed and transmitted via 100 m long optical fibres to the LHCb electronics barrack. Here, the data are processed and transmitted to the higher-level triggers and the data acquisition system.

The L0 Trigger operating at a rate of 1.1 MHz, a total of 2.6 Tbit of digitised detector data have to be transmitted per second. A low-cost digital optical link, using commercially available components is being developed [12] for this purpose by Achim Vollhardt. A prototype link has been set up and is working in the laboratory. Bit error tests are under way and radiation tests for those components that are located close to the detector are being prepared. Expected radiation doses at the location of the readout link electronics do not exceed 10 krad after ten years of LHCb operation at nominal luminosity.

9.3 Summary and outlook

In the revised layout of the LHCb detector, the main tracking system consists of four stations. In three stations downstream of the magnet, silicon microstrip detectors cover the innermost region close to the beam pipe. A Technical Design Report for this detector, called Inner Tracker, has been submitted to the CERN LHCC committee, which has recommended it for approval. The fourth station, called TT, is covered entirely by silicon microstrip detectors. Work on the design of this station has started, including R&D on silicon detectors and readout, as well as a mechanical design of the station. Work on the TT station will be the major occupation of our group for the year 2003. A prototype digital optical readout link is operational in the laboratory, detailed tests are in progress.

The construction of the detector is estimated to require approximately 18 months and will be scheduled such that the detector can be installed and fully commissioned before the startup of LHC, foreseen for 2007.

[1] LHCb technical proposal, CERN/LHCC 998-4.
[2] M.Needham, LHCb-2002-043.
[3] H.Dijkstra et al., LHCb-2002-045.
[4] LHCb Inner Tracker Technical Design Report, CERN/LHCC 2002-029.
[5] O.Steinkamp, LHCb-2002-056.
[6] M.Needham, LHCb-2002-032.
[7] P.Sievers, A silicon inner tracker for the LHCb experiment, PhD thesis, Universität Zürich, 2002.
[8] C.Bauer et al., LHCb-2001-135.
[9] F.Lehner et al., LHCb-2002-038.
[10] M.Agari et al., LHCb-2002-058.
[11] K.Bösiger et al., LHCb-2002-061.
[12] A.Vollhardt, LHCb-2002-062, LHCb-2002-068.

10 The DØ experiment at the Tevatron $p\bar{p}$ Collider: Search for Rare Decays of B_s-Mesons and a New Silicon Detector for Run IIb

Ralf Bernhard and Frank Lehner

The DØ collaboration consists of 80 institutes from 18 countries: Argentina (1), Brazil (3), China (1), Czech Republic (3), Colombia (1), Ecuador (1), France (7), Germany (6), India (3), Ireland (1), Korea (1), Mexico (1), Netherlands (3), Russia (5), Sweden (4), United Kingdom (3), U.S.A. (35) and Vietnam (1)

(DØ Collaboration)

Until LHC at CERN starts its operation in 2007, the Tevatron at the Fermi National Accelerator Laboratory, Batavia, USA, is the world's highest energy accelerator with an available center of mass energy of 1.8 TeV. The so-called Run IIa phase of the $p\bar{p}$ collider has started in 2001 and addresses some of the most important questions in particle physics. The most recent physics results [1] involve direct searches for as yet unknown particles and forces, including those that are predicted or expected (like the Higgs boson and supersymmetry) and those that would come as a surprise. Other highlights of this programme will be the precise measurements of the top quark properties, new accurate determinations of the mass of the W boson and the couplings of the electroweak bosons. Moreover, numerous measurements of various B meson decay modes allow the investigation of CP-violating effects.

Because of the tantalising physics prospects a high integrated luminosity run will bring, a second phase of Tevatron running, the Run IIb which will cover the years 2005 and beyond, is presently being prepared. To optimise its physics capability for the future run, the existing silicon detector of the DØ experiment at Tevatron is being replaced [2]. This replacement is necessary, since the present silicon vertex detector will suffer from the harsh radiation environment at Run IIa.

After the DØ detector is now fully operational for Run IIa and $p\bar{p}$ collision data are being taken, Ralf Bernhard has started with his physics analysis programme of rare B_s decay searches. The study of the B_s meson is unique to hadron colliders since they can not be produced at the $\Upsilon(4S)$ resonance at which e^+e^- B-Factories like BaBar and Belle are running. We will focus in our searches on flavor-changing neutral currents, which are forbidden at tree level. Of particular interest is the decay $B_s \to \mu^+\mu^-$. This decay channel is very sensitive to new physics beyond the Standard Model (SM) since it has a very small SM branching ratio of $3.5 \cdot 10^{-9}$ and supersymmetric extension of the SM could enhance this branching ratio significantly [3]. Within the framework of the well-motivated minimal supergravity model mSUGRA, the search for $B_s \to \mu^+\mu^-$ is a powerful tool to probe the model in the region of high $\tan\beta$. We expect to improve the existing branching ratio limit for $B_s \to \mu^+\mu^-$ of $2.6 \cdot 10^{-6}$ at 95% C.L. [4] by a factor of almost 20 in Run IIa. This branching ratio limit will already start to constrain the allowed parameter space of mSUGRA models at high $\tan\beta$.

We are also involved in the design and construction of the new DØ silicon detector for Run IIb. We have worked on the sensor design and specifications and have defined the quality assurance procedures and methods for the more than 2200 silicon sensors which are being ordered now [5]. One of us (Frank Lehner) is the responsible coordinator at DØ for the silicon sensor procurement and testing program. In addition we have designed a long analog low-mass cable with a very fine pitch geometry to route the silicon analog signals in the innermost detector layer to further readout electronics. Together with the Swiss company Dyconex [6] several cable prototypes based on different design layouts have been developed and characterised.

[1] *New results from Run IIa Searches from CDF and DØ*,
talks presented by S. Rolli (CDF) and G. Brooijmans (DØ) at the XXXVIIIth Rencontres de Moriond, Electroweak Interactions and Unified Theories, Les Arcs, France, March 15-22, 2003.

[2] The DØ Run IIb silicon detector collaboration: *DØ Run IIb silicon detector upgrade, Technical Design Report*, http://d0server1.fnal.gov/projects/run2b/Silicon/www/smt2b/smt2b.html.

[3] A. Dedes, H. Dreiner and U. Nierste, Phys.Rev.Lett.**87**, 251804, 2001.

[4] F. Abe et al. [CDF Collaboration], Phys.Rev.D **57**, 3811 (1998).

[5] A. Bean et al., *Silicon Sensor Quality Assurance for the DØ RunIIb Silicon Detector: Procedures and Equipment*, internal DØ publication, DØ-note 4120
http://www.physik.unizh.ch/ lehnerf/dzero/run2b.html

[6] Dyconex advanced circuit technologies, Zurich, Switzerland

11 Particle Physics with CMS

C. Amsler, A. Dorokhov, C. Hörmann, K. Prokofiev, H. Pruys, C. Regenfus,
P. Robmann, T. Speer, and S. Steiner

in collaboration with:
ETH-Zürich, Paul Scherrer Institut (PSI), Universität Basel and the CMS Collaboration.

We participate in the CMS experiment at the Large Hadron Collider (LHC) where we concentrate on physics involving the b-quark, e.g. b-quark production associated with the formation of Higgs bosons, t-quark decays, and spectroscopy of B mesons. The most interesting events at LHC will contain one or several b-jets originating from the decay of B mesons, with typical mean free paths of a few mm. To allow for efficient tagging of B mesons among the large background of light quark and gluon jets, the detection system has to follow particles towards the primary vertex. The silicon pixel detector we are developing is the closest detector to the interaction point, located only 4 cm from the beam-beam interaction point. The extremely high particle flux near the primary vertex ($\sim$ 1000 particles every 25 ns) requires the innermost tracking layers to be composed of pixel devices delivering 3D coordinates with high resolution and no ambiguity. Furthermore, the radiation dose to the nearest detector will approach 10^6 Gy (corresponding to 6×10^{14} hadrons /cm^2) after 10 years of LHC operation. This is about 10^6 more than for detectors developed earlier for space research.

Our group contributes to the design, construction and test of the pixel sensors, the readout chips and the mechanical support structure, and we are also involved in the event reconstruction software.

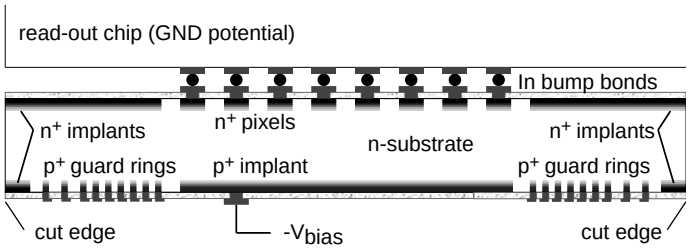

Figure 11.1: *Design of a sensor connected to the readout chip. The bias voltage is applied to the backside.*

11.1 Pixel sensors

The barrel pixel detector consists in three concentric cylindrical layers, 53 cm long with radii of 4.4, 7.3 and 10.2 cm. The layers contain some 3×10^7 silicon pixels. Coverage in the beam direction is achieved with forward/backward wheels provided by the U.S. participants. The pixel modules consist of thin, segmented sensor plates with highly integrated readout chips connected by the indium bump bonding technique. Figure 11.1 shows a sketch of the sensor/chip assembly. The pixel size was recently reduced from 150 $\times$ 150 μm^2 to 125 $\times$ 125 μm^2 and rectangular pixels of 150 $\times$ 100 μm^2 are being considered for the final design. The analogue signals are read out to determine the coordinates more accurately, using charge sharing between adjacent pixels.

For n^+ implants in n-material the pixels have to be isolated from one another. This is usually done with one or several narrow p^+-rings around each pixel (the so-called p-stop rings). To avoid excessive charging of an unbonded pixel (one with poor indium connection to the chip) leading to local

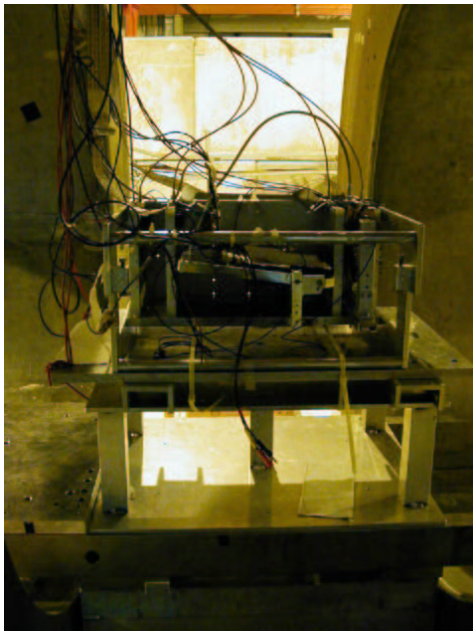

Figure 11.2: *Setup for the sensors test. The pixel detectors are located at the center of the silicon telescope. The two supraconductive coils are visible at the edges of the picture.*

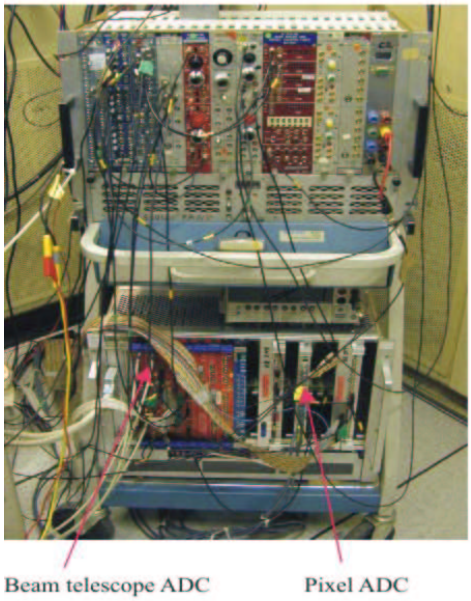

Figure 11.3: *Readout and control system.*

discharges and momentary failures of whole pixel clusters, the resistance between pixels should remain finite. A narrow resistive path between the pixels would prevent the pixels from charging up. This is accomplished by small openings in the p-rings which lead to atoll-like structures made of one or several rings surrounding each pixel (see fig. 11.6) below. More details can be found in previous annual reports, in the technical design report [1] and in a recent PhD thesis [2].

In 2002 we ordered with CiS Erfurt a batch of sensors with various atoll designs, some oxygenated (oxygen is known to reduce the acceptor concentration after type inversion and hence also the required depletion voltage). In some of the sensors the p-stop rings were missing. Instead, the p implant was not spatially defined by a mask, but sprayed over the whole wafer with moderate concentration.

A first test of this batch was performed by the Zurich group in July 2002 using 225 GeV pions from the CERN-SPS. The purpose of the test was to measure (i) the position resolution, (ii) the charge collection efficiency, and (iii) the Lorentz deflection angle in the 4 T field foreseen at CMS. The pixel detector was located at the center of our microstrip telescope [3], so that pions would traverse the detector at a grazing angle $\alpha = 15^\circ$ (fig. 11.2). Our telescope is made of 8 layers of x and y silicon microstrips (50 μm pitch size). Through charge division between neighbouring strips the telescope is capable of measuring the space coordinates of an incident charged particle with an r.m.s. resolution of 1 μm [3]. A fast trigger diode (less than 20ns rise time) provided the trigger. The silicon sensor was bump bonded to the readout chip (PSI30, DMILL/Honeywell) and was read out through VME ADC's by a LabView program. The data acquisition system is shown in fig. 11.3.

The apparatus was immersed in a longitudinal magnetic field provided by two Helmholtz coils to measure the Lorentz angle Θ_L: due to deflection in the magnetic field the charge carriers do not move along the electric field lines but drift at an angle Θ_L towards adjacent pixels. The charge deposit is therefore shared among (mostly two) adjacent pixels. The Lorentz angle can be measured by finding the coordinate z of the pixel row for which the charge collected between the main and adjacent pixels are equal (fig. 11.5). This corresponds to charge reaching the readout surface between two pixels. The coordinate Δy of the impinging track is determined by the telescope and Θ_L can be calculated from the relation tanΘ_L = Δy/z tanα. Note that for irradiated pixels after type inversion the depletion layer grows from the readout side (as shown in fig. 11.5). The depletion thickness can be determined from the length of the hit pixels along the

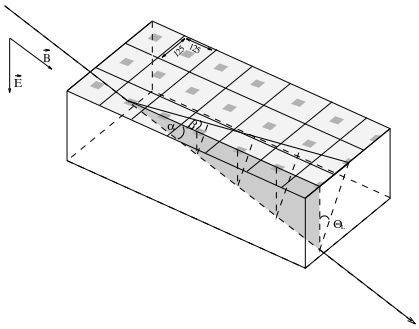

Figure 11.4: *Sketch of the pixel detector traversed by a charged particle under the grazing angle α. The Lorentz angle is denoted by Θ_L.*

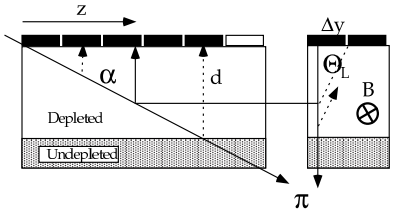

Figure 11.5: *Determination of the Lorentz angle Θ_L (see text).*

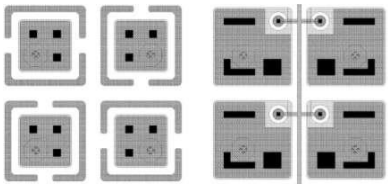

Figure 11.6: *The two pixel layouts tested in 2002: p-stop (left) and p-spray (right).*

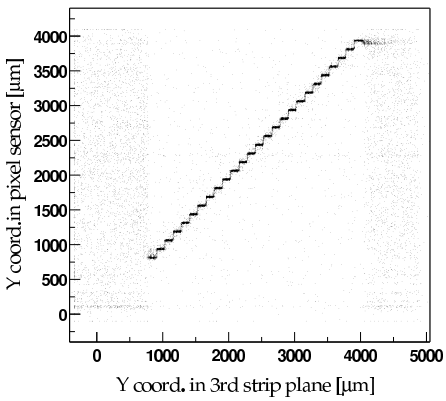

Figure 11.7: *Vertical hit coordinate in the third strip detector vs. vertical hit coordinate in the pixel sensors. The steps are due to the much smaller pitch of the microstrip detector. The dark bands left and right are due to open readout channels.*

incident direction. Similar studies were performed earlier by our group [2; 4]. However, several design parameters for the sensors have changed since then: we have now somewhat smaller pixel sizes, atoll-like p-stop rings and a different supplier. Also the pixels are now bump-bonded to a semifinal version of the readout chip.

Data were collected with two detectors made of 32 $\times$ 22 bump bonded pixels (125 $\times$ 125 μm^2), one with p-stop rings and one with p-sprays (fig. 11.6). Irradiated pixels could not be tested reliably because we could not reach the operating temperature of -10° foreseen at CMS. During two weeks of beam time we collected some 6 $\times$ 10^6 events. The analog amplitudes from the pixels had first to be corrected for common mode noise. The hit coordinates for the strips and pixels were obtained from the average hits weighted by the hit amplitudes. After the alignment, the hit position of the incident particle on the pixel sensors was known with a (moderate) precision of $\approx 5\mu$m. Figure 11.7 shows the correlation between hit coordinates in the microstrips and pixel detectors.

The charge collected by one pixel depends on the incident track. On the borders of the pixel the charge is shared between few (mostly two) pixels, hence the collected charge in the tested pixel is smaller. The average charge collected by one pixel as a function of track position can be used to calculate the lateral charge diffusion in the silicon bulk. The charge distribution is a convolution of the charge diffusion function with the size of the pixel. The average charge collected by one pixel as a function of the track position in the x and y directions on the pixel surface is shown in fig. 11.8.

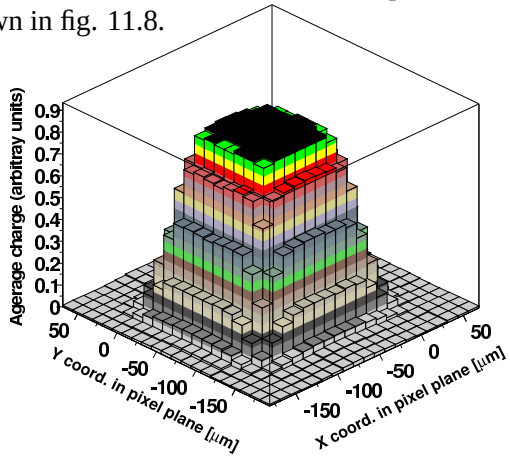

Figure 11.8: *Average collected charge by one pixel in the absence of magnetic field.*

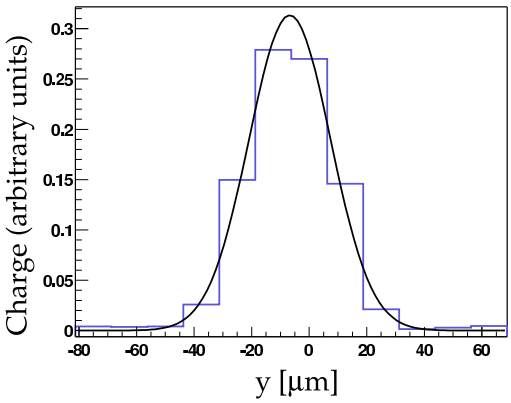

Figure 11.9: *Lateral charge distribution due to diffusion in the 280 μm thick silicon, together with gaussian fit.*

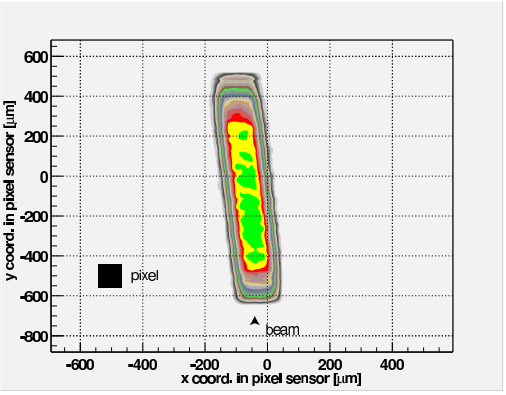

Figure 11.10: *Distribution of collected charge on the surface of the silicon sensor for grazing tracks. The y coordinate is along the beam direction.*

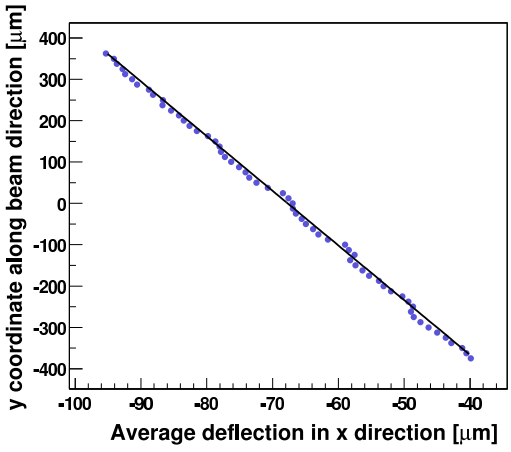

Figure 11.11: *Average deflection as a function of detected track length along the beam direction.*

The detector was oriented with its surface perpendicular to the incident beam and the magnetic field was off. The deconvoluted lateral charge distribution during the charge drift through the 280 μm thick silicon is shown in fig. 11.9, together with a gaussian fit. The lateral diffusion has an r.m.s. width of about 15 μm.

Figure 11.10 shows the distribution of charge with magnetic field. The pixel detector was oriented with its surface at a grazing angle of 15° and the field was 3 T. One can see that the charge migrates slightly to the left of the incident track. The coordinate of average energy deposit is shown in fig. 11.11 as a function of track length y. The Lorentz angle calculated for the non-irradiated sensor is about 16° at 3 T and 21° at 4 T.

Finally, we measured the position resolution of the pixel detector. In the CMS detector the tracks hitting the pixel barrel are on average perpendicular to the magnetic field. However, the field was parallel to the beam during our test. To simulate charge sharing due to the magnetic field, the detector surface was therefore tilted by an angle of 65° with respect to the beam direction to simulate the Lorentz deflection. In the vertical direction the charge was shared by several pixels while in the horizontal direction the charge was collected by single pixels (except for tracks in the border regions for which charge was collected by two adjacent pixels). The measured coordinate was obtained by weighting the pixel hits with their amplitudes. Figure 11.12 and 11.13 show the residuals between

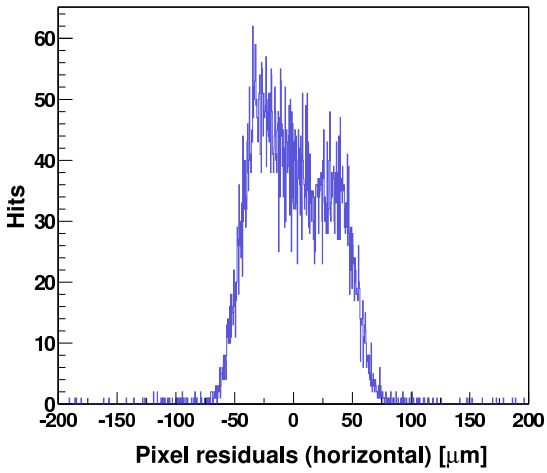

Figure 11.12: *Residuals between measured and predicted horizontal coordinates, showing the enhanced resolution obtained with charge division.*

measured and predicted hits from the telescope in the horizontal and vertical directions, respectively. In the horizontal direction the resolution is about $\sigma \simeq 34\mu$m, as expected from a box distribution for 125 μm broad pixels. In the vertical direction, however, the resolution is much better thanks to charge sharing: $\sigma \simeq 11\mu$m.
Another important aspect is the signal-to-noise ratio. The energy deposit for minimum ionizing particles was measured for perpendicular incidence. The resulting Landau distribution was compared to the (gaussian) noise distribution. We obtained a signal-to-noise ratio of 130.

[1] CMS - The Tracker Project, Technical Design Report, CERN LHCC 98-6, CMS TDR 5 (1998).

[2] R. Kaufmann, PhD Thesis, Universität Zürich, 2001.

[3] C. Amsler *et al.*, Nucl.Instr.Meth.**A 480** (2002) 501.

[4] B. Henrich and R. Kaufmann, Nucl.Instr.Meth.**A 304** (2002) 304.

[5] P. Billoir and S. Qian, Nucl.Instr.Meth.**A 311** (1992) 139.

11.2 Readout chip

During summer 2002 we also tested in a high intensity pion beam of 350 MeV/c at PSI the CMS Read Out Chip (ROC) which was designed in radiation hard DMILL technology. For that test we used the PSI43 chip, the first ROC that contained the complete functionality and the foreseen number of pixels (52 columns $\times$ 53 rows of pixels). We were able to test the chip-sensor unit under rates comparable to those expected at LHC.
In 2002 we also received our first test structures, which were processed in quarter micron technology (Deep Sub Micron, DSM). A complete redesign of the existing chip was necessary but this technology has the following advantages: DSM chips are cheaper since the process is well known and used widely by the conventional chip industry. DSM technology also offers new possibilities in designing the chip and improving its performances. There are for example five metal layers available for routing instead of only two and the smallest structure is only 0.25 μm wide, compared to 0.8 μm in DMILL. Thus

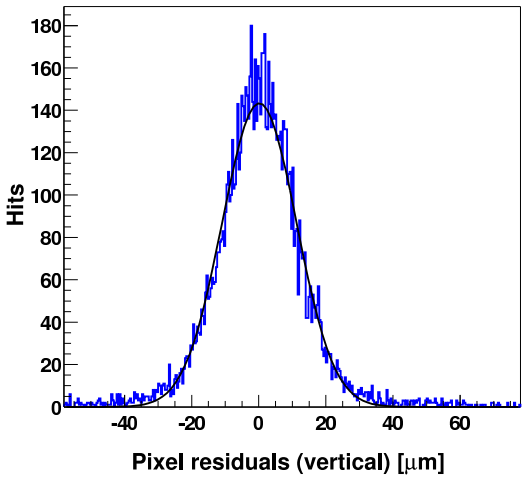

Figure 11.13: *Residuals between measured and predicted vertical coordinates, showing the enhanced resolution obtained with charge division.*

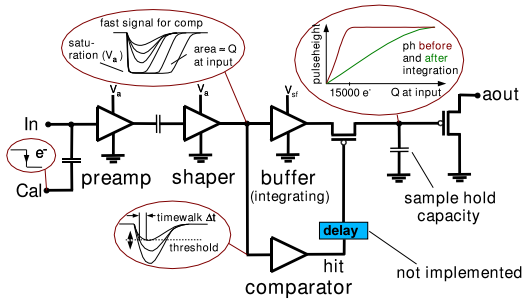

Figure 11.14: *Layout of the analog block test structure.*

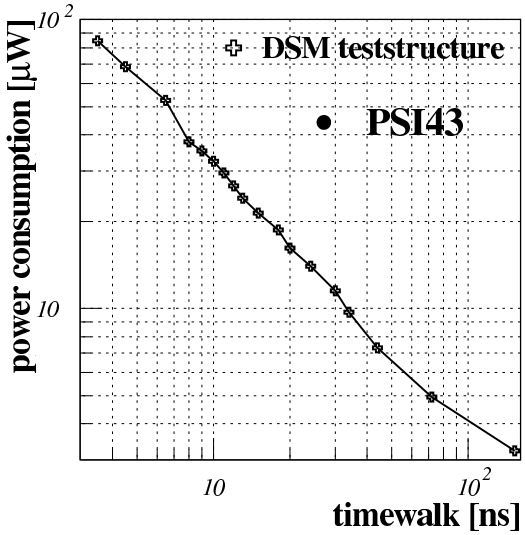

Figure 11.15: *Power consumption versus timewalk.*

we will be able to increase the number of data buffers from 24 to 32 and thereby reduce data loss. Another benefit is the low power consumption as DSM needs only half the supply voltage and half the current of DMILL. Thus, as will be shown below, the power consumption is four times lower for the same speed. We also expect a higher yield than in case of DMILL and the radiation hardness is excellent.

We have performed measurements with test structures of the analog block that were designed in DSM technology. Figure 11.14 shows the schematics of the analog block test structure.

It consists of two stages, a charge sensitive preamplifier and a shaper. Both stages have to be very fast because of the 40 MHz bunch crossing frequency at LHC. An extra amplifier integrates the signal to deal with saturated shaper output signals. These amplifier stages are followed by the sample and hold capacity and an output driver. A comparator, integrated in the analog block, generates the hit signal when the output level of the shaper is higher than the input threshold of the comparator. The hit signal is needed for storing the pulse height in the sample and hold capacity until the readout sequence is completed.

A very important measurement was power consumption versus timewalk (fig. 11.15). A low power consumption is important, because each μW/pixel leads to about 60 Watt for the entire pixel detector. As fig. 11.15 shows, power consumption decreases rapidly with timewalk. However, whenthe latter exceeds 25 ns the event is assigned to the wrong bunch crossing. For test structure A we obtained a power consumption of 14 μW for a timewalk of 25 ns. This is much smaller than for the DMILL design (40μW) advocated in the design report [1].

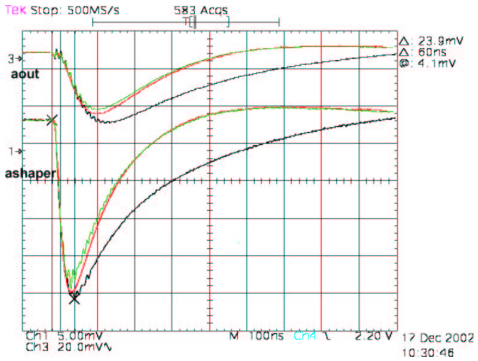

Figure 11.16: *Analog out of the shaper and aout (see also fig. 11.14) before (red) and after (black) irradiation, and after compensation (green).*

Figure 11.16 shows the output signal of the shaper and the analog output signal aout (see the layout in fig. 11.14) caused by a charge injected at the calibration input. The tests tructures were irradiated with a ^{60}Co γ-source (132 kGy) at PSI. The red curves were measured before irradiation, the black ones after radiation and the green ones after readjusting the settings for the preamp and shaper. Hence we were able to compensate for the irradiation damages, leading to an increase in gain and decay time, by readjusting the settings.

11.3 Mechanical support structure

Our group and our institute's workshop (see also the report from the mechanical workshop) are involved in the design and construction of the mechanical support structure for the detector and the service tube in beam direction. Figure 11.17 shows a sketch of a quarter of the CMS tracking system. The three layers of the pixel detector are shown, together with the 220 cm long service tube. The system has a total length of 5 m. Since the LHC beampipe will already be present during installation of the pixel detector, two vertically separated pixel half shells will be introduced on a dedicated rail system (see also fig. 11.22 below). The detector support structure (fig. 11.18) will be made of pure aluminum tubes with trapezoidal shapes to fit the geometrical constraints and a wall thickness of only 0.3 mm. Custom made, 0.24 mm thick, carbon fiber blades, which support the pixel modules, will then be glued to the tubes forming the detector segments. Four to five of these tubes will be connected

with a laser welding technique to an aluminum container which distributes the cooling fluid. Figure 11.19 shows a picture of such a welding seem taken with a microscope. Note that the width of the

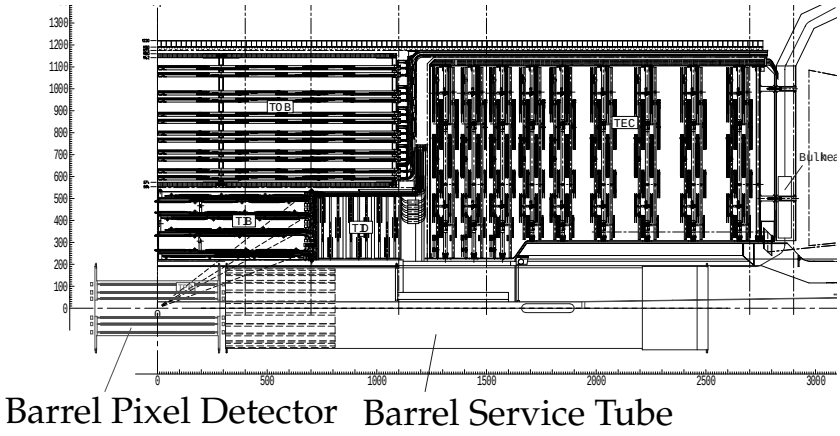

Figure 11.17: *A quarter of the CMS tracking system with the barrel pixel detector in the center and the service tube in z-direction.*

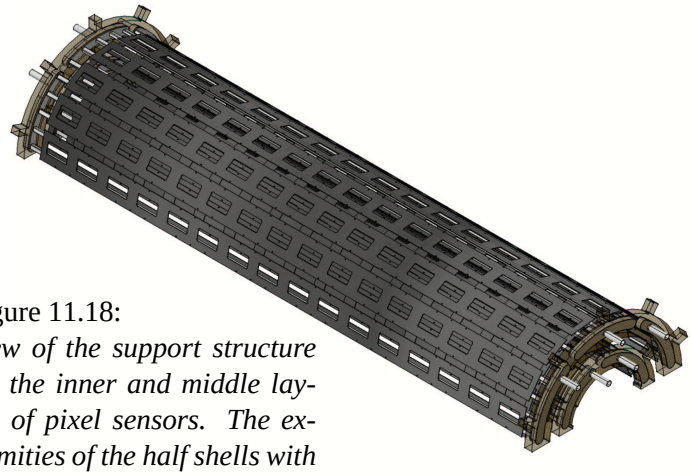

Figure 11.18:
View of the support structure for the inner and middle layers of pixel sensors. The extremities of the half shells with the embedded cooling manifolds are also shown.

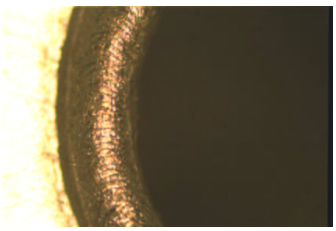

Figure 11.19: *High quality welding seem between a cooling tube (right side) and the container (left side).*

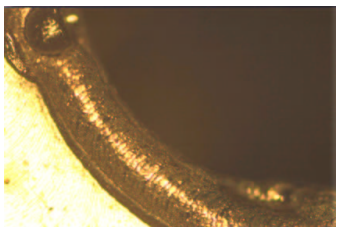

Figure 11.20: *Bad welding seem with a hole and a gap.*

seem is only about 0.3 mm. The resulting manifold will provide the necessary cooling of the detector modules to -10^{0}C with C_6F_{14}. At both ends the manifolds are embedded in a carbon fibre support frame as illustrated in fig. 11.18.
The laser welding is done in close collaboration with an external company. Tests gave promising results (fig. 11.19). However, we realized that the tool used was not precise nor massive enough. Figure 11.20 shows a problematic zone with holes and gaps. This happens when the laser beam misses the working piece or when there is an excessive gap between the parts that have to be welded. The tests indicated also that the physical and chemical properties of the different pieces have to be of the same quality. A complete detector segment was manufactured with an improved welding tool consisting of massive copper pieces supporting the segment structure during the welding process. The new tools guarantee the required precision and remove the heat during the welding process.

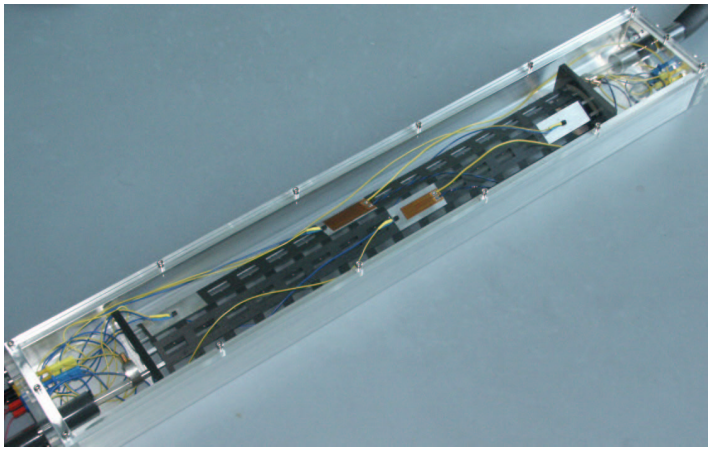

Figure 11.21: *Detector segment in its dry nitrogen container. Note the resistors to simulate the power loss and the temperature sensors mounted on the carbon fibre blades.*

The segment of the barrel pixel support structure was installed in a container and flushed with dry nitrogen for cooling tests (fig. 11.21). Mechanical survey and cooling tests will have to be performed to prove that the technique meets all requirements.

The two service tubes in $+z$ and $-z$ direction, which enclose the end cap pixel detector system (fig. 11.22), connect the barrel pixel detector to the tracking system. They transfer the power, the optical and electrical signals and the cooling fluid to the detector. To minimize multiple scattering we will use aluminum wires, which are plated with a thin copper layer for the power lines and aluminum for the cooling tubes. The motherboards which hold the optical hybrids for the analog and control links are integrated at the detector end. The power regulators are mounted at the outer ends. A honeycomb support structure is foreseen (fig. 11.23) to minimize the amount of material and to guarantee stability.

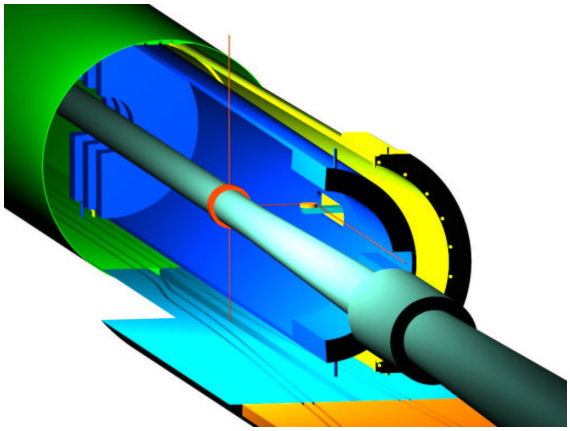

Figure 11.22: *The CMS beampipe surrounded by the pixel detector service tubes for the barrel detector (yellow) and the end cap discs (blue).*

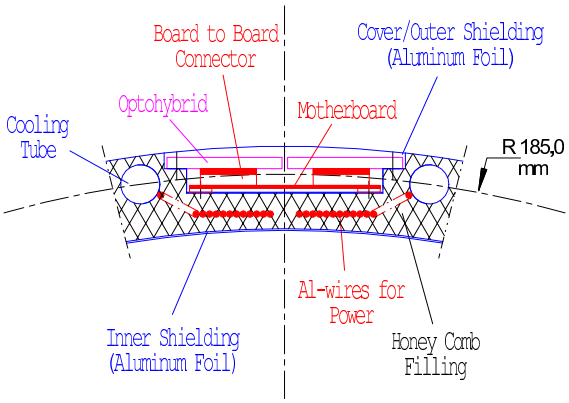

Figure 11.23: *Cross section of the service tube near the pixel detector flange, showing the motherboards which hold the optical hybrids.*

11.4 CMS event reconstruction

We are participating in the track reconstruction software and, in particular, in the vertex reconstruction techniques in the object-oriented reconstruction framework ORCA. We have implemented a single-vertex fit algorithm using the Kalman filter formalism. This algorithm is often used both in track [2] and vertex reconstruction [3].

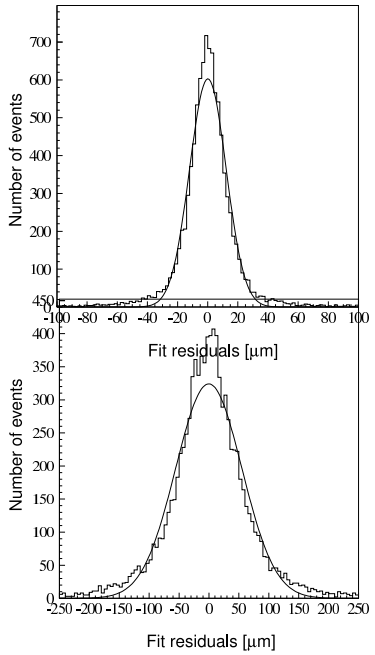

Figure 11.24: *Residuals distributions in the transverse direction for the decay vertex in $H^0 \rightarrow Z^0Z^0 \rightarrow \mu^+\mu^-\mu^+\mu^-$ (top) and in $B_s \rightarrow J/\psi\phi$ (bottom).*

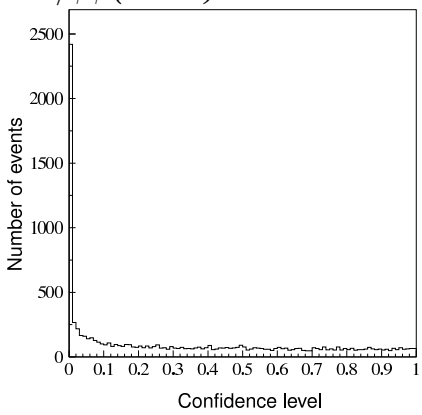

Figure 11.25: *Confidence level distribution expected for $H^0 \rightarrow Z^0Z^0 \rightarrow \mu^+\mu^-\mu^+\mu^-$.*

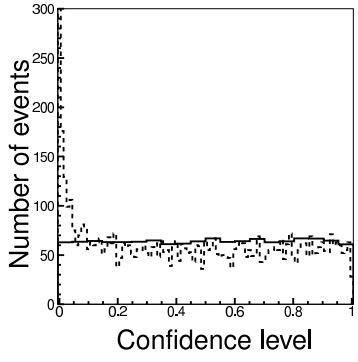

Figure 11.26: *Confidence level distribution for tracks with perfectly gaussian track parameters (full line) and tracks affected by 3% non-gaussian tails (dashed line).*

So far only a simplified version[4; 5] of a Kalman filter had been implemented. Tracks were assumed to be straight in the vertex neighbourhood. This considerably simplified the algorithm and reduced the computation time but did not allow the tracks to be refitted as emerging from a common vertex. In our improved version of the filter realistic helicoidal track models are used. Track parameters may then be recalculated with the additional vertex constraint, providing a full track-to-track covariance matrix.

The r.m.s.resolution of the reconstructed vertex in the decay $H^0 \rightarrow Z^0Z^0 \rightarrow \mu^+\mu^-\mu^+\mu^-$ is approximately 12 μm in the transverse and 19 μm in the longitudinal (z) direction. For B_s meson decays the resolutions are 55 μm and 73 μm, respectively (fig. 11.24). While no improvement is gained on the resolution, the full Kalman filter algorithm is up to four times faster than the linearized version. This is interesting in view of its possible application to the online high-level trigger.

Nevertheless, the distributions of the confidence level (fig. 11.25) show a large peak at low confidence level. This is due to the track parameters which have non-gaussian tails, as demonstrated in fig. 11.26. To alleviate this problem, we are developing a gaussian sum filter (GSF) for vertex fitting, in which the distributions of the track parameters are modelled by superpositions of gaussians describing the core and the tails. The GSF is then a weighted sum of several Kalman filters, and it can be implemented as a number of Kalman filters run in parallel.

We have started to develop a kinematic fit with additional constraints (such as masses of decaying particles, momentum and energy conservation) incorporated into the vertex fit. We are able to reconstruct intermediate particles coming from sequential decays by imposing kinematic constraints on the final state particles. For example one can reconstruct complete decay chains, such as the decays $B^- \rightarrow D^0 l^- \bar{\nu}_l$, followed by $D^0 \rightarrow K^-\pi^+$, $D^0 \rightarrow K^-\pi^+\pi^0$ or $D^0 \rightarrow K^-\pi^+\pi^-\pi^+$, where only the final longlived particles are reconstruced in the detector. This procedure can also improve the experimental resolutions.

[1] CMS - The Tracker Project, Technical Design Report, CERN LHCC 98-6, CMS TDR 5 (1998).

[2] R. Frühwirth, Nucl.Instr.Meth.**A 262** (1987) 444.

[3] R. Frühwirth, R. Kubinec, W. Mitaroff and M. Regler, Comp. Phys. Comm. **96** (1996) 189.

[4] V. Karimäki, "Effective Vertex Fitting", CMS note 1997/051.

12 Superconductivity and Magnetism

M. Angst (since December 2002), M. Bruun (since November 2002), D. Di Castro, D.G. Eshchenko (since April 2002), H. Keller, R. Khasanov, S. Kohout M. Mali, J. Roos, A. Shengelaya
M. Eremin (visiting scientist), V.A. Ivanshin (visiting scientist), B. Kochelaev (visiting scientist)
T. Schneider (Titularprofessor), and K.A. Müller (Honorarprofessor)

in collaboration with:
ETH Zürich (K. Conder, J. Karpinski), Paul Scherrer Institute (E. Morenzoni), IBM Rüschlikon Research Laboratory (J.G. Bednorz), University of Birmingham (E.M. Forgan), University of St. Andrews (S.L. Lee), University of Rome (A. Bianconi), Kazan State University (A. Dooglav, M.V. Eremin, B.I. Kochelaev), University of Belgrade (I.M. Savić), Institute of Low Temperature and Structure Research, Polish Academy of Sciences, Wroclaw (P.W. Klamut), Institute of Physics, Polish Academy of Sciences, Warsaw (R. Puzniak, A. Wisniewski), University of Tokyo (K. Kishio, T. Sasagawa, H. Takagi), Northern Illinois University, DeKalb (B. Dabrowski).

In the last year we continued our investigations on the fundamental physical properties of non-conventional superconductors (hole and electron doped cuprates and magnesium diboride). A great advantage of our approach is the combined application of complementary experimental techniques, such as muon-spin rotation (μSR), nuclear magnetic resonance (NMR), nuclear quadrupole resonance (NQR), electron paramagnetic resonance (EPR), together with bulk SQUID and torque magnetometry and resistivity, to investigate these systems. One of our main research interests concerns detailed oxygen isotope (^{16}O/^{18}O) effect (OIE) studies on various physical quantities and phenomena (critical temperature, in-plane penetration depth, charge fluctuations) in cuprate high-temperature superconductors (HTSC) in order to explore the role of the electron-phonon interaction in the basic physics of these systems. In another project, we investigated for the first time the magnetic penetration depth in an electron doped infinite layer HTSC ($Sr_{0.9}La_{0.1}CuO_2$) by μSR. Furthermore, we continued the magnetic torque studies of single-crystal magnesium diboride (MgB_2) to clarify the peculiar magnetic properties of this novel two-band superconductor. In addition, we performed a preliminary boron isotope (^{10}B/^{11}B) effect (BIE) study of the magnetic penetration depth in MgB_2 using μSR. The scientific goal of our research is to get a better understanding of the basic physical processes involved in HTSC, MgB_2 and related novel superconductors.

12.1 Studies of oxygen isotope effects in cuprates

12.1.1 Direct observation of the oxygen isotope effect on the magnetic field penetration depth in optimally doped $YBa_2Cu_3O_{7-\delta}$

There is increasing evidence that strong lattice effects are present in HTSC, which may lead to the formation of polarons (bare charge carriers accompanied by local lattice distortions) [1; 2]. One way to test this hypothesis is to demonstrate that the effective mass of the supercarriers m^* depends on the mass M of the lattice atoms. This is in contrast to conventional BCS superconductors, where m^* is independent of M. For HTSC (clean limit) the in-plane penetration depth λ_{ab} obeys the relation $\lambda_{ab}^{-2}(0) \propto n_s/m_{ab}^*$, where n_s is the superconducting charge carrier density, and m_{ab}^* is the in-plane effective mass of the supercarriers. This implies that the OIE on $\lambda_{ab}(0)$ is due to a shift in n_s and/or

m^*_{ab}, according to the relation:

$$\Delta\lambda_{ab}(0)/\lambda_{ab}(0) = 1/2\ [\Delta m^*_{ab}/m^*_{ab} - \Delta n_s/n_s]. \qquad (12.5)$$

Therefore a possible mass dependence of m^*_{ab} can be tested by investigating the isotope effect on λ_{ab}, provided that the contribution of n_s to the total isotope shift is known. Over recent years we performed detailed investigations of the OIE on $\lambda_{ab}(0)$ in underdoped $La_{2-x}Sr_xCuO_4$ by means of magnetization [3; 4] and torque magnetometry [5], as well as in underdoped $Y_{1-x}Pr_xBa_2Cu_3O_{7-\delta}$ by means of μSR [6]. As result, we found a remarkable relative isotope shift of $\Delta\lambda^{-2}_{ab}(0)/\lambda^{-2}_{ab}(0)$ of -5 to -10% in these cuprate systems.

Recently, we were able to observe a substantial OIE on $\lambda_{ab}(0)$ in an optimally doped $YBa_2Cu_3O_{7-\delta}$ film by using the novel low-energy μSR technique (LEμSR), developed at the Paul Scherrer Institute (PSI) [7]. In a LEμSR experiment slow spin-polarized muons of tunable energy between 0 and 30 keV are implanted at very small and controllable depth below the surface of a sample. This peculiarity allows to exploit all the advantages of bulk μSR in studies of local magnetic fields in thin samples, near surfaces, and as a function of depth below surfaces. Due to the random nature of the muon scattering process, LE muons do not stop at a sharp depth below the surface of the sample. The implantation depths are distributed over a nanometer scale, and the implantation depth profile $n(z)$ depends on the muon energy. This feature offers a unique possibility to measure the internal magnetic field profile $B(z)$ over some interval of distances z below the surface of a superconducting sample for a given muon energy. This so-called integral reconstruction (IR) method was recently developed by A. Suter [10]. The IR method is based on a simple approximation that links the magnetic field probability distribution $p(B)$ to the muon implantation depth distribution $n(z)$ [10]:

$$n(z)dz = p(B)dB. \qquad (12.6)$$

Integration of both sides of Eq.(12.6) gives:

$$\int_z^\infty n(\zeta)d\zeta = \int_0^{B(z)} p(\beta)d\beta, \qquad (12.7)$$

where $n(\zeta)$ is emulated and $p(\beta)$ is determined experimentally. For any given z Eq.(12.7) can be solved numerically, and the appropriate magnetic field profile $B(z)$ can be reconstructed (see Fig. 12.1).

The big advantage of the IR method in comparison with the previously used mean-value approx-

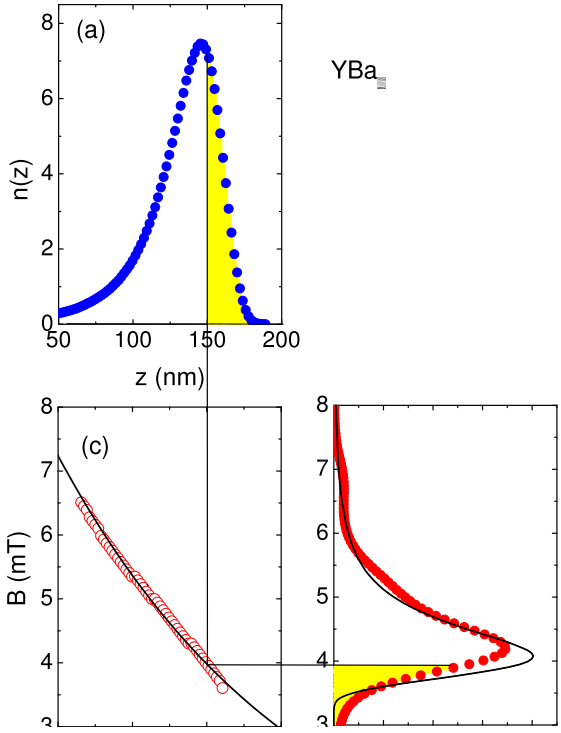

Figure 12.1: *Principle of the integral reconstruction method. (a) Calculated muon implantation depth distribution $n(z)$ using the Monte-Carlo code TRIM.SP [8]. (b) Measured probability field distribution $p(B)$ in the Meissner state, obtained from the μSR time domain spectrum by the Maximum Entropy Fourier method [9]. (c) Reconstructed field profile $B(z)$. Filled areas in (a) and (b) are equal, giving the integral equation for $B(z)$. Solid line in (c) is the best fit of Eq.(12.8) to the reconstructed $B(z)$. Solid line in (b) represents the field distribution $p(B)$ calculated for the best fit in (c) and $n(z)$ in (a).*

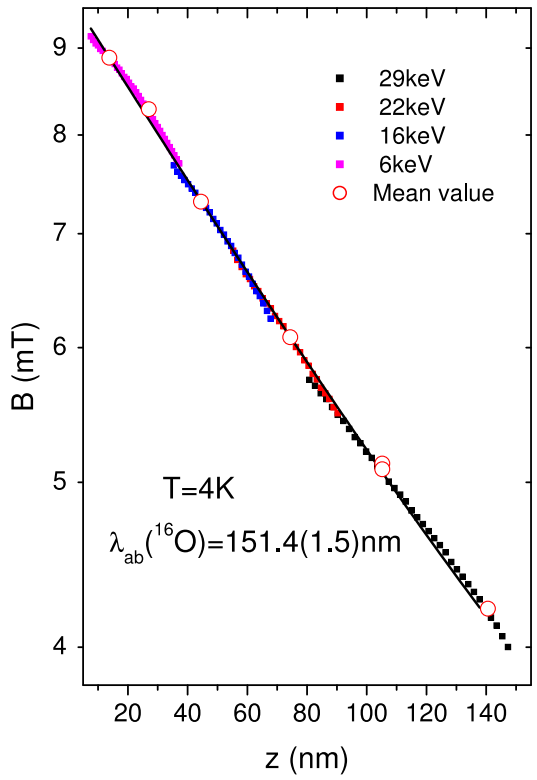

Figure 12.2: *Reconstructed magnetic field profile $B(z)$ for the ^{16}O substituted $YBa_2Cu_3O_{7-\delta}$ film measured at 4 K in the Meissner state in a magnetic field of 9.2 mT applied parallel to the surface of the film. The integral reconstruction is shown for the muon implantation energies 29, 22, 16, and 6 keV. The mean-value reconstruction is shown for implantation energies 29, 22, 16, and 6 keV (open circles). The solid curve represents the best fit by Eq.(12.8).*

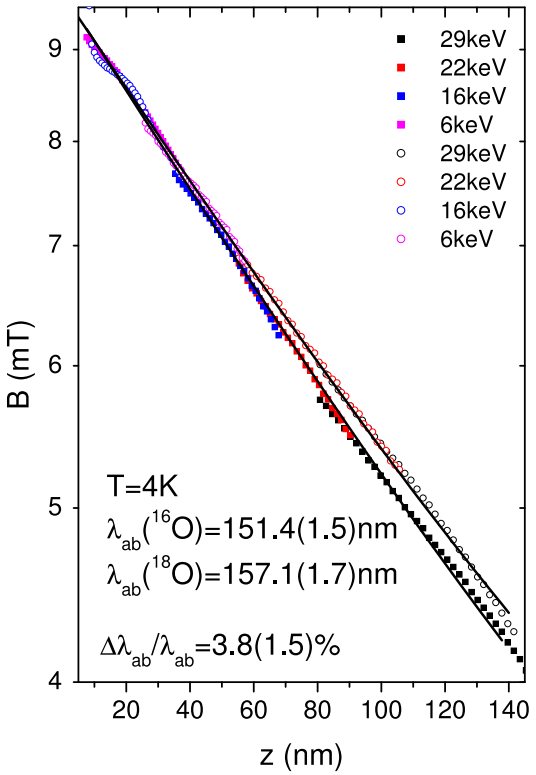

Figure 12.3: *Magnetic penetration profile of the $^{16}O/^{18}O$ substituted $YBa_2Cu_3O_{7-\delta}$ films in the Meissner state at various muon implantation energies (29, 22, 16, and 6 keV). The solid curves are fits according to Eq.(12.8).*

imation (MVA) [11] is obvious. Both methods use emulated $n(z, E)$ and a sequence of experimental μSR spectra measured at different implantation energies E. In the MVA only one point $B(z_E)$ (where z_E is the mean implantation depth for a given E) is extracted per spectrum, while in the IR method $B(z)$ can be reconstructed over a relatively wide interval of z.

We used the advantages of the IR method for the direct measurement of the oxygen isotope ($^{16}O/^{18}O$) effect on the in-plane penetration depth in an optimally doped $YBa_2Cu_3O_{7-\delta}$ film. The experiments were performed on a 600 nm thick epitaxial $YBa_2Cu_3O_{7-\delta}$ film in the Meissner state. A weak external magnetic field of 9.2 mT was applied parallel to the surface and perpendicular to the c-axis of the sample. The field profile $B(z)$ was reconstructed by the IR method for several implantation energies (from 3 to 30 keV), corresponding to implantation depths in the range 15-150 nm. The experimental field profile (Fig. 12.2) is in excellent agreement with the London theory for a slab of thickness $2t$ in the Meissner state:

$$B(z) = B_0 \frac{\cosh[(t-z)/\lambda_{ab}]}{\cosh(t/\lambda_{ab})}. \tag{12.8}$$

For the ^{16}O substituted $YBa_2Cu_3O_{7-\delta}$ film a fit of Eq.(12.8) to the reconstructed $B(z)$ yields $^{16}\lambda_{ab}(4K) = 151.4(1.5)$ nm. Note the accuracy of the IR method – the absolute value of λ_{ab} can be measured with a precision better than 1%. This means that an OIE on λ_{ab} of 1.4% or larger can easily be detected by LEμSR. Fig. 12.3 shows the field profiles determined by the IR method for $YBa_2Cu_3O_{7-\delta}$ films with two different oxygen isotopes ^{16}O and ^{18}O. It is seen that the data points for the ^{18}O sample are systematically higher than those for the ^{16}O sample, indicating that $^{16}\lambda_{ab} < {}^{18}\lambda_{ab}$. A fit with Eq.(12.8) gives $^{18}\lambda_{ab} = 157.1(1.7)$ nm. The relative oxygen isotope shift of the in-plane penetration depth was found to be $\Delta\lambda_{ab}/\lambda_{ab} = 3.8(1.5)\%$.

It was shown [3; 4; 5; 6] that the OIE on λ_{ab} arises mainly from the oxygen-mass dependence of the in-plane effective mass m^*_{ab}. The present result indicates that lattice effects even at optimal doping play an essential role in cuprate superconductors.

[1] A.S. Alexandrov and N.F. Mott, Int. J. Mod. Phys. **8**, 2075 (1994).

[2] K.A. Müller, Physica C **341-348**, 11 (2000).

[3] G.M. Zhao *et al.*, Nature (London) **385**, 236 (1997).

[4] G.M. Zhao *et al.*, J. Phys.: Condens. Matter **10**, 9055 (1998).

[5] J. Hofer *et al.*, Phys.Rev.Lett.**84**, 4192 (2000).

[6] R. Khasanov *et al.*, J. Phys. : Condens. Matter **15**, L17 (2003).

[7] E. Morenzoni *et al.*, J. Appl. Phys. **81** 3340 (1997).

[8] B.D. Rainford and G.J. Daniel, Hyperfine Interact. **87** 1129 (1994).

[9] W. Eckstein, *Computer Simulations of Ion-Solid Interactions*(Springer-Verlag, Berlin, 1992).

[10] A. Suter *et al.*, unpuplished.

[11] T.J. Jackson *et al.*, Phys. Rev. Lett. **84**, 4958 (2000).

12.1.2 Oxygen isotope effect on charge fluctuations observed by NQR at very low temperatures in $YBa_2Cu_4O_8$

It is our anticipation that knowledge of the OIE on different NMR/NQR parameters measured at plane-copper as well as at yttrium sites in $YBa_2Cu_4O_8$ will add clues to the understanding of high-T_c superconductivity. The major part of the copper hyperfine Hamiltonian comes from the interactions of the nuclear spin with its electronic environment. These hyperfine interactions are responsible for the Knight shift, the spin-lattice relaxation rate, and the unusual temperature dependence of the NQR line frequency and its linewidth [1]. Having different copper isotopes we are able to distinguish between two kinds of hyperfine interactions: the magnetic one caused by the electron spin and the quadrupolar (electric) one caused by the electron charge. This differentiation is possible because the magnetic interactions depend on the nuclear magnetic dipole moment and the quadrupolar ones on the nuclear electric quadrupole moment.

In normal conducting $YBa_2Cu_4O_8$ the plane-copper spin-lattice relaxation is predominantly of magnetic origin caused by spin fluctuations and its temperature dependence is controlled by the spin-pseudogap phenomenon [2]. In the superconducting phase this magnetic contribution to the relaxation diminishes due to the d-wave superconducting gap.

Our recent NQR measurements of the ^{63}Cu and ^{65}Cu relaxation rates in superconducting $YBa_2Cu_4O_8$ show that the reduced spin-lattice relaxation gradually changes its character by becoming progressively more quadrupolar due to yet unidentified low frequency charge fluctuations [3]. At very low

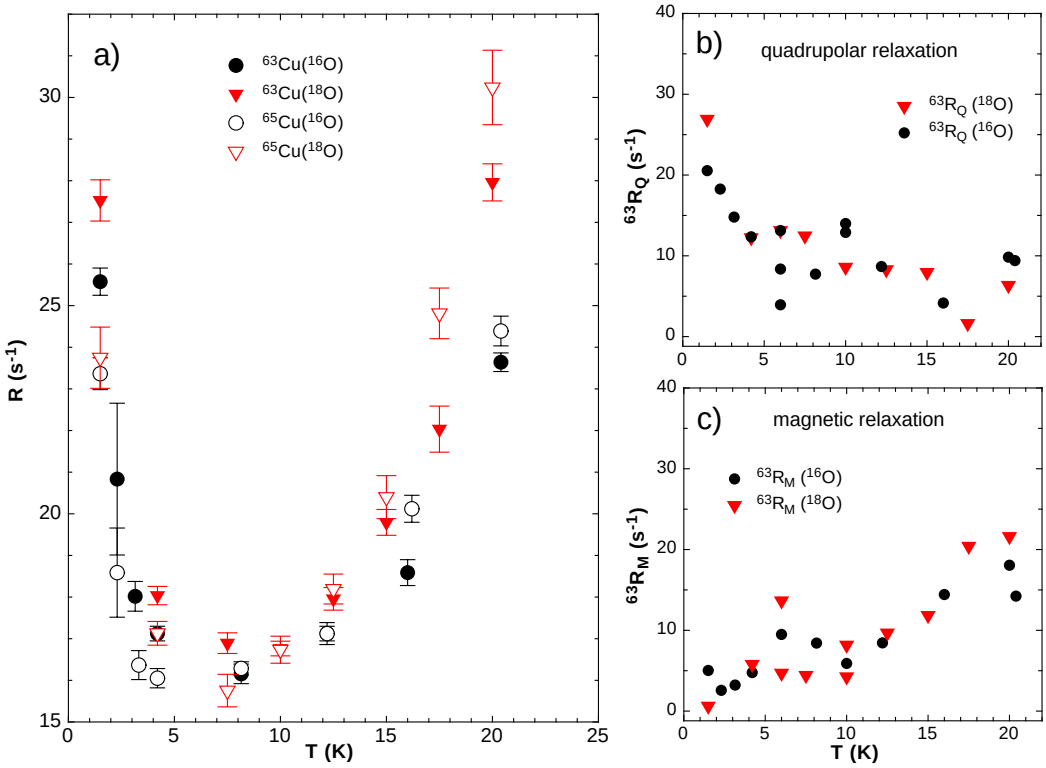

Figure 12.4: *Temperature dependence of: a) plane-^{65}Cu and ^{63}Cu spin-lattice relaxation rate R in superconducting ^{16}O and ^{18}O $YBa_2Cu_4O_8$, b) quadrupolar contribution, R_Q, and c) magnetic contribution, R_M, to R in superconducting ^{16}O and ^{18}O $YBa_2Cu_4O_8$.*

temperature the relaxation gets predominantly quadrupolar with an unexpected temperature dependence. The quadrupolar rate instead to reduce with decreasing temperature has the tendency to grow. In Figure 12.4 a) we present ^{63}Cu and ^{65}Cu relaxation rates R for ^{16}O and ^{18}O $YBa_2Cu_4O_8$ below 20 K. By inspection one notices that there is an OIE since $^{65,63}R(^{18}O)$ is always larger than the corresponding $^{65,63}R(^{16}O)$. This means that the low frequency spectral density of fluctuations at the NQR frequency is higher in the ^{18}O superconductor than in the ^{16}O superconductor. In Fig. 12.4 b) and 12.4 c) we present separately the quadrupolar (R_Q) and magnetic (R_M) contributions to ^{63}R for ^{16}O and ^{18}O exchanged $YBa_2Cu_4O_8$. One notices that for both oxygen isotopes R_M diminishes whereas R_Q grows with decreasing temperature. The separation procedure inevitably enhances the scatter of the results, so a separate OIE determination of R_M and R_Q is not possible. The completely opposite temperature behavior of R_Q and R_M is striking. While the known spin fluctuations die out, new low frequency charge fluctuations develop, which show no tendency to abate at 1.5 K, the lowest temperature we measured. The quasi particles responsible for these new charge excitations have no spin and live in the superconducting phase at 1 K and below. The question arises which type of quasiparticles this could be. At the moment we are still missing an adequate explanation for the observed quadrupolar contribution to the relaxation.

[1] M. Mali *et al.*, Phys.Rev.B **65**, 184518 (2002).

[2] F. Raffa *et al.*, Phys.Rev.Lett.**81**, 5912 (1998); M. Bankay *et al.*, Phys.Rev. B **50**, 6416 (1994).

[3] M. Mali *et al.*, Journal of Superconductivity: Incorporating Novel Magnetism **15**, 511 (2002).

12.2 μSR studies of electron-doped $Sr_{0.9}La_{0.1}CuO_2$

The high-T_c cuprate superconductors are obtained by doping holes or electrons into the antiferromagnetic (AF) insulating state. Both electron and hole-doped cuprates share a common building block, namely the copper-oxygen plane. Therefore, one would expect that the same pairing mechanism applies in both cuprate superconductors. In order to elucidate the mechanism of high-T_c superconductivity, it is very important to clarify the origin of the similarities and the differences between the hole-doped (p-type) and the electron-doped (n-type) cuprates.

The magnetic field penetration depth λ is one of the fundamental lengths of a superconductor. Detailed μSR investigations of polycrystalline cuprate superconductors have demonstrated that λ can be obtained from the muon spin depolarization rate $\sigma(T) \sim 1/\lambda^2(T)$ [1]. In contrast to p-type cuprates there is no consensus about the penetration depth value for n-type cuprates. Problems concerning the sample quality and the large dynamic relaxation due to rare-earth magnetic moments in n-type cuprates $R_{2-x}Ce_xCuO_{4-\delta}$ (R= Nd, Sm, Pr) with so-called T'-structure prevented the determination of $\sigma(0)$ using μSR [2].

There exists another class of n-type cuprates (Sr,Ln)CuO_2 (Ln=La, Sm, Nd, Gd) with the so-called infinite-layer structure (ILS). The n-type ILS superconductors have several merits. First, they have the simplest crystal structure among all HTSC consisting of an infinite stacking of CuO_2 planes and (Sr, Ln) layers. The charge reservoir block of the rock-salt type or fluorite type in HTSC does not exist in the infinite-layer structure. Second, their oxygen content is stoichiometric without vacancies or interstitial oxygen. Third, n-type ILS have much higher T_c ($\simeq$ 43 K) compared to the n-type cuprates with T'-structure ($T_c \simeq$ 25 K). Recently, we studied the penetration depth in high-quality $Sr_{0.9}La_{0.1}CuO_2$ ILS using the transverse-field (TF) μSR technique. Fig. 12.5 shows the temperature dependence of the TF-μSR depolarization rate σ at B_{ext}=0.6 T.

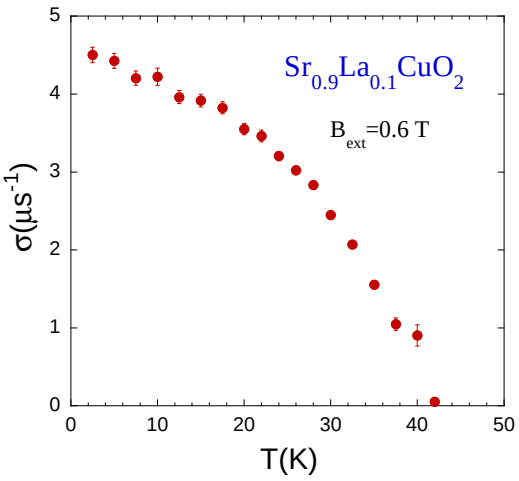

Figure 12.5: *Temperature dependence of the μSR depolarization rate σ of $Sr_{0.9}La_{0.1}CuO_2$.*

We confirmed microscopically that this compound is a bulk superconductor. Because of the absence of magnetic rare-earth ions, it was possible to measure the penetration depth in a n-type HTSC for the first time using μSR. We obtained the value $\lambda_{ab}(0)$=1170(12) Å . The zero-temperature depolarization rate $\sigma(0)$=4.6(1) μs^{-1} is more than four times larger than expected from the Uemura plot. This shows that the n-type ILS does not follow the Uemura relation established in p-type HTSC [3].

[1] See, e.g. H. Keller, in *Materials and Crystallographic Aspects of HTc-Superconductivity*, edited by E. Kaldis (Kluwer Academic Publishers, 1994), p.265; J.E. Sonier *et al.*, Rev. Mod. Phys. **72**, 769 (2000).

[2] G.M. Luke *et al.*, Phys.Rev.B **42**, 7981 (1990).

[3] Y.J. Uemura *et al.*, Phys.Rev.Lett.**62**, 2317 (1989).

12.3 Studies of magnesium diboride

12.3.1 μSR investigations of Boron isotope effect

Soon after the discovery of the novel superconductor MgB_2 [1] the isotope shift on T_c was investigated in detail [2; 3]. Whereas the boron-isotope ($^{10}B/^{11}B$) exponent was found to be $\alpha_B \simeq 0.28(2)$ [2; 3], only a small magnesium-isotope ($^{24}Mg/^{26}Mg$) effect with $\alpha_{Mg} \simeq 0.02(1)$ [3] was detected. It is interesting to note that in this layered superconductor the predominant contribution to the total isotope shift on T_c arises from the B atoms in the planes where superconductivity takes place, similar to the layered cuprate HTSC [4; 5]. In the latter a substantial shift on the magnetic penetration depth λ under oxygen isotope substitution was observed [3; 4; 5; 6], indicating that lattice effects play an important role in these systems.Therefore, we recently performed a detailed study of the boron isotope effect on the magnetic penetration depth in MgB_2 in order to clarify the role of the electron-phonon interaction in this compound. The μSR technique was used to explore the local magnetic field distribution $p(B)$ in the mixed state of polycrystalline MgB_2. The muon spin depolarization rate σ, which under certain conditions (see below) is proportional to the second moment of $p(B)$, is a direct measure of the magnetic penetration depth λ. The muon spin-depolarization rate was studied as a function of temperature and magnetic field. The results for the natural abundant boron sample MgB_2 are in good agreement with previous μSR results [6; 7]. Here we report the μSR results on $Mg^{11}B_2$ and $Mg^{10}B_2$ samples. In Fig. 12.6 the low-temperature field dependence of σ for the $Mg^{11}B_2$ sample indicates the presence of pinning induced distortion of the vortex lattice at low magnetic fields. At higher fields ($B \geq 0.4$ T) σ was found to be nearly field independent, as expected for an ideal vortex lattice. Only in this case σ is a direct measure of the magnetic penetration depth λ.

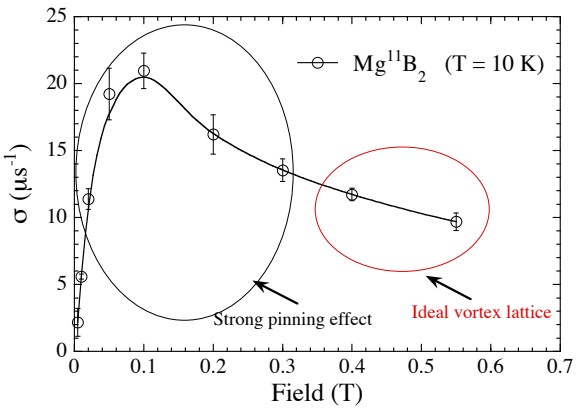

Figure 12.6: *Magnetic field dependence of the muon-spin depolarization rate σ for $Mg^{11}B_2$. The regions with strong and weak pinning induced distortion of the vortex lattice are indicated with black and red circles, respectively.*

The temperature dependence of σ for the $Mg^{10}B_2$ and $Mg^{11}B_2$ samples, measured at high fields (B = 0.4 T), reflecting $\lambda^{-2}(T)$, is shown in Fig. 12.7. A clear shift in T_c of ΔT_c = 0.9(1)K is visible , in agreement with previous results [2; 3]. However, at low temperature the two curves merge. The μSR data were fitted to the two gap equation [6], yielding the following $\sigma(0)$ values of the two isotope samples: $\sigma(0)^{^{10}B}$=13.26(14)μs^{-1} and $\sigma(0)^{^{11}B}$=13.18(27)μs^{-1}. The relative isotope shift is very small with a rather large relative error: $\Delta\sigma(0)/\sigma(0) = -0.6(2.2)\%$. From this result we estimate the upper limit of the boron isotope effect on the magnetic penetration depth to be

$$\mid \Delta\sigma(0)/\sigma(0) \mid = \mid \Delta\lambda^{-2}(0)/\lambda^{-2}(0) \mid < 3\%. \tag{12.9}$$

Considering that MgB_2 is close to the clean limit [8; 9; 10], the relation $\lambda_{ab}^{-2}(0) \propto n_s/m^*$ holds, where n_s and m^* denote the density and effective mass of the superconducting charge carriers, respectively. According to Eq.(12.5) an isotope shift on λ_{ab} then should be due to a shift in n_s and/or m^*. We can assume that the isotope substitution does not affect the superfluid density, for the fol-

lowing reasons: (i) With changing the isotope we are changing only the mass of the nuclei, and not directly the charge carrier density. (ii) The x-ray diffraction measurements, performed before the μSR experiments, showed that within experimental error, there is no difference in the lattice parameters between the two isotope samples. So, there are at least no changes in the conducting bands due to structural modifications. Thus we can conclude that Eq.(12.9) sets an upper limit for a possible isotope effect on the charge carrier effective mass in MgB_2. This conclusion may be interpreted as a confirmation for MgB_2 to be a conventional phonon-mediated superconductor. However, further theoretical calculations are needed in order to estimate what kind of contribution to the total isotope effect may arise from each one of the two effective masses in a two-gap superconductor such as MgB_2.

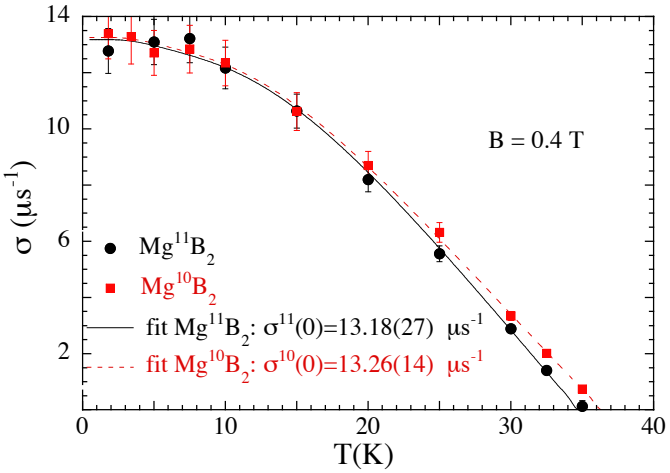

Figure 12.7: *Temperature dependence of the muon-spin depolarization rate for the two Boron isotope substituted MgB_2 samples. A clear shift of the two curves is present close to T_c, but at low temperatures they merge together.*

[1] J. Nagamatsu *et al.*, Nature (London) **410**, 63 (2001).
[2] S. L. Bud'ko *et al.*, Phys.Rev.Lett.**86**, 1877 (2001).
[3] D. G. Hinks *et al.*, Nature **411**, 457 (2001).
[4] D. Zech *et al.*, Nature (London) **371**, 681 (1994).
[5] G.M. Zhao *et al.*, J. Phys.: Condens. Matter **13**, R569 (2001).
[6] Ch. Niedermayer *et al.*, Phys.Rev.B **65**, 094512 (2002).
[7] K. Ohishi *et al.*, J. Phys. Soc. Jpn. **72**, 29 (2003).
[8] A. V. Sologubenko *et al.*, Phys.Rev.B. **65**, 180505 (2002).
[9] F. Bouquet *et al.*, Phys.Rev.Lett.**89**, 257001 (2002).
[10] A. V. Sologubenko *et al.*, Phys.Rev.B. **66**, 014504 (2002).

12.3.2 Magnetometry measurements

The anisotropic Ginzburg-Landau theory (AGLT) is very successful in describing most of the magnetic properties of the cuprate superconductors. However, for MgB_2 various deviations were observed. A refinement of the AGLT is needed, because MgB_2 is a two-gap-superconductor. We compared our torque magnetometry results with recent theoretical predictions of deviations from the AGLT.

In a torque experiment a single crystal is exposed to an external magnetic field, and the mechanical torque it experiences is measured (see section 12.4.1) as a function of time, temperature, magnetic field strength, and the angle enclosed by the field and a characteristic sample direction. Figure 12.8 shows an angle dependent measurement. It was suggested that the anisotropy (i.e. the ratio of a quantity along two perpendicular directions) of the two main superconducting properties – the penetration depth λ and the coherence length ξ (resp. the upper critical field H_{c2}) – might be different in two-gap-superconductors such as MgB_2. Based on this, Kogan [1] predicted a sign change of the torque for low temperatures. The dashed line in Fig. 12.8 illustrates this sign change for field directions close to the boron layers ($\theta = 90°$). Such a feature is not visible in the experimental data (Fig. 12.8). This discrepancy suggests that the difference between the two anisotropies cannot be as large as currently assumed. The theory might be reconciled with our results by working out explicitly the influence of the magnetic field strength on the anisotropy.

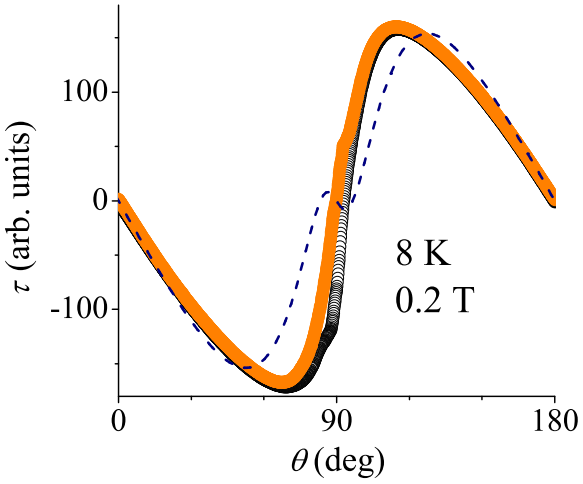

Figure 12.8: *Angle dependent torque measurement at low temperature in a low magnetic field.*

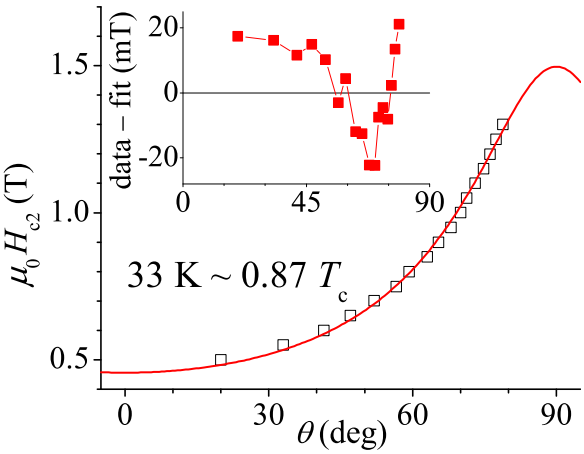

Figure 12.9: *Measured $H_{c2}(\theta)$ and a best fit of the AGLT to the data. The inset shows the difference between the data and the fit.*

A different deviation from the AGLT occurs in the angle dependence of the upper critical field $H_{c2}(\theta)$ (see Fig. 12.9). These systematic deviations can be very well approached by the recent theoretical work of Golubov and Koshelev [2]. Both the shape and the magnitude of the calculated deviations look very similar to our data.

[1] V. G. Kogan, Phys.Rev.Lett.**89**, 237005 (2002).

[2] A. A. Golubov and E. A. Koshelev, cond-mat/0303237.

12.4 New developments in instrumentation

12.4.1 Micro-torque sensors

Torque magnetometry is an excellent tool for performing highly sensitive measurements of magnetic properties of anisotropic superconductors, such as the cuprates or magnesium diboride. In a torque experiment a sample is mounted on an appropriate cantilever. By applying an external magnetic field, the sample experiences a torque which causes the sensor to be deflected in a characteristic way.

We are using two different readout schemes to measure this deflection. In the capacitive technique a capacitance change, caused by the displacement of a flexible electrode, is measured. In the piezoresistive technique, on the other hand, specifically formed piezoresistors are fabricated on the bending structures of the sensor. The stress caused by a torque changes their resistance. Careful placement of the electrodes and the readout leads of a capacitive torque sensor (see Fig. 12.10) allowed us to reach sensitivities comparable to those reported for the much more expensive piezoresistive sensors. The piezoresistive torque sensors developed by our group [1; 2; 3] have noise levels of the order of 10^{-14} Nm, whereas test measurements using the new capacitive torque sensor with a piece of magnetic tape had standard deviations of the torque as low as $3 \cdot 10^{-14}$ Nm. In an attempt to further increase the sensitivity of the piezoresistive technique, a new design of sensors was recently developed, shown in figure 12.11. Unfortunately, due to delays in the fabrication of the sensors, no results can be reported so far. But elasticity calculations suggest that the sensitivity is increased by a factor of about 2 compared to the previous devices [1; 2; 3]. This geometry allows for a choice of sensitivity by tuning the leg length l and the platform width b (a larger ratio l/b results in a higher sensitivity).

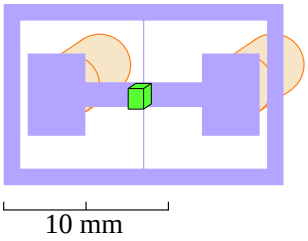

Figure 12.10: *Schematic of a capacitive torque sensor with a mounted sample (green cube). The capacitance difference between the active (purple) and the two excitation electrodes (orange) is measured.*

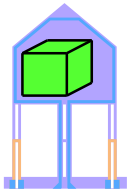

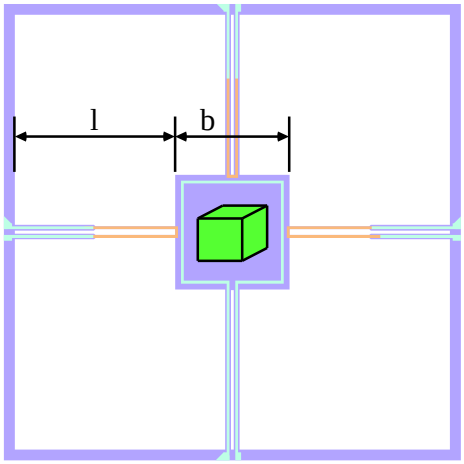

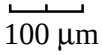

Figure 12.11: *Comparison of the existing design described in [1; 2; 3] (left) and our new squared design (right) with a mounted sample (green cube). Both sensors feature a metallic loop for calibration purposes. Piezoresistive parts are marked orange, the blue paths denote metallic conductors. The sensitivity depends on the ratio l/b.*

[1] C. Rossel *et al.*, J. Appl. Phys. **79** (11), 8166 (1996).
[2] M. Willemin *et al.*, J. Appl. Phys. **83** (3), 1163 (1998).
[3] C. Rossel *et al.*, Rev. Sci. Instrum. **69** (9), 3203 (1998).

12.4.2 Developments of LEμSR and the new μE4 surface muon beam

In the year 2002 the construction of the new surface muon beam line for LEμSR at the Paul Scherrer Institute (PSI) entered the phase of detail work with construction and manufacturing of the mechan-

ical elements, detailed specification and purchase order of the magnetic quadrupoles, dipoles and solenoids of the corresponding power supplies and design of the new area layout including shielding and support infrastructure. The main motivation for this beam is to increase the intensity of low energy muons, which is directly proportional to the flux of incoming surface muons over a 30×30 mm^2 area.

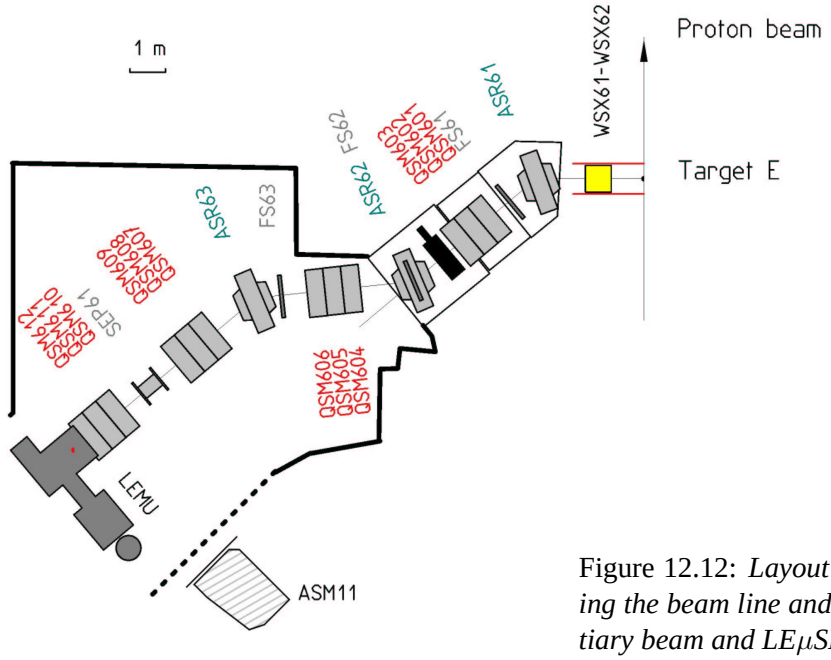

Figure 12.12: *Layout of the new μE4 area, showing the beam line and the position of the LEM tertiary beam and LEμSR spectrometer (LEMU).*

Furthermore, we started detailed work to upgrade the LEμSR apparatus. The main purpose of it is twofold. Firstly, an adaptation to the different beam conditions (larger phase space and intensity with respect to the presently used πE3). The second goal is to improve the operation and reliability of this delicate apparatus in view of an increasing number of experiments and users in the future. The first condition requires a new moderator and injection chamber with large acceptance, which have been designed and the construction of a segmented fast muon counter able to cope with rates in excess of 10^8 cps.

In order to comply with the semi-dedicated character of the new beam line a major mechanical rebuild of the entire apparatus has been initiated. The LEμSR apparatus (tertiary beam line and μSR spectrometer) will be rebuilt on a new single multipurpose platform, which will allow to move the LEμSR apparatus in and out of the area in a reasonable time.

13 Surface Physics

T. Greber, M. Hengsberger, J. Wider, H. J. Neff, F. Baumberger, M. Hoesch, W. Auwärter, M. Muntwiler, A. Tamai, A. Dolocan, M. Barry, T. Gresch, W. Deichmann, J. Osterwalder

Artificial nanostructures, exemplified e.g. by ultrathin films, quantum wires or quantum dots, are of enormous scientific and technological interest. Their electronic and magnetic properties are dominated by size- and shape dependent quantum effects and can thus be tailored to fulfil any particular need. Their diameter in at least one dimension does not exceed a few atomic layers, and therefore they consist to a large extent of interfaces and surfaces.

In the surface physics laboratory we prepare clean surfaces, ultrathin films and nanostructures under ultrahigh vacuum (UHV) conditions and characterize their surface and interface structures at atomic resolution. Their electronic and magnetic properties are studied in detail. In order to measure the geometric arrangement of the atoms within the first few monolayers of the surface we apply predominantly electron-based techniques such as x-ray photoelectron diffraction (XPD), medium-energy electron diffraction (MEED), low-energy electron diffraction (LEED), and more recently also scanning-tunneling microscopy (STM). Angle-resolved photoemission spectroscopy (ARPES) gives us a detailed picture of the electronic band structure of such systems. Specifically, our experimental setup permits to directly map sections through the Fermi surface, which describes the electronic degrees of freedom relevant for transport properties, magnetic interactions and phase transitions. An important asset of such experiments is that the same probe (photoemission) gives us structural, electronic and magnetic information, and we can therefore study the interplay between these different degrees of freedom on the same sample.

The research carried out during the last year can be grouped into four topics:

- *Clean metal surfaces and surface states*
  The close-packed (111) surfaces of several face-centred-cubic metals (e.g. Au, Ag, Cu, Ni) exhibit so-called Shockley surface states that propagate almost freely within the surface plane, and which have wave functions that decay exponentially both into the vacuum and into the bulk of the crystal. They thus exemplify a two-dimensional gas of nearly-free electrons (2DEG), which manifests itself in parabolic energy dispersion relations. We have continued to study the responses of these 2DEG to various internal or external perturbations. The Shockley state on Ni(111) is particularly difficult to study because it is just marginally occupied and extremely susceptible to surface contamination. On the other hand, it is a most interesting case because it sits on a ferromagnetic substrate. In Section 13.1 high resolution spectra are presented and the temperature dependence of the binding energy is discussed.
  On Au(111), a splitting of this same Shockley state has been explained in terms of the spin-orbit interaction. With our new COmplete PHotoEmission Experiment (COPHEE), which is now set up at the Swiss Light Source (SLS) in Villigen, we were able to reproduce this splitting (Section 13.2) and to establish for the first time the detailed spin structure in which the electron spin is coupled to the two-dimensional electron momentum.
  Vicinal Cu(111) surfaces expose (111)-oriented terraces separated by a roughly regular array of monoatomic steps; therefore they represent lateral nanostructures that can be easily prepared. For the Shockley state this regular step lattice represents a periodic repulsive potential. On Cu(443) the coherent motion of the electrons in this lattice leads to the formation of an energy gap at the Fermi energy (Section 13.3).
  Photoemission spectra from clean crystal surfaces contain not only signals from such surface states, but also strong emission from bulk states that exhibit dispersion in all three dimensions.

For this highly surface-sensitive technique, the question arises whether these bulk states correspond to the Bloch states of the sample volume that extend to infinity in all three dimensions. Our experiments at the SPring-8 synchrotron in Japan, where we measured such bulk states on Ni(111) at higher photon energies, indicate that the normal low-energy ARPES experiments probe bulk-like states that feel the presence of the surface (Section 13.4).

- *Ultrathin films*
  The preparation of well-defined monolayer-thick films permits us to study the structural, electronic and magnetic properties at an interface between two different materials. In the nanosciences, such knowledge is essential for the understanding of how nanoscale structures and devices function. In the case of a single lead layer on Cu(111), the film takes the role of a so-called surfactant, i.e. it promotes the layer-by-layer growth of other transition metals while the lead keeps floating on top of the growing film. In Section 13.5 it is tried to rationalize the surfactant effect with features in the detailed electronic structure of the film.
  Nickel monolayers on Cu(001) represent building blocks for new magnetic devices based on the spin-filter effect and oscillatory exchange coupling. In Section 13.6 it is shown how the Fermi surface of nickel evolves as a function of film thickness, and also how the magnetic state of the film transforms from paramagnetic to ferromagnetic.
  Lastly, we have continued to study single monolayers of hexagonal boron nitride on Ni(111) that provide a well-defined model case for an insulating monolayer on top of a ferromagnetic substrate. In Section 13.7 it is shown that linear defects in the film can be correlated to the occurrence of two different structural domains, and how the detailed structure at the domain boundaries can be inferred from combined STM and XPD measurements.

- *Adsorbed molecules*
  Molecular monolayers offer a highly interesting route to prepare functionalized surfaces. Chemists provide molecules with suitable chemical anchors and with the desired functional groups that are to be exposed at the surface. We are working on methods that can measure the bonding geometry of the molecules on the substrate, and we study the electronic properties of molecular layers that have a high degree of self-organized crystalline order within the layer. As a first example, Section 13.8 presents STM and XPD data from C_{60} monolayers on a stepped Cu(221) surface. The steps have a two-fold function: they align the molecules in one-dimensional chains, and they lock the individual molecules into a single, well-defined orientation.
  In Section 13.9 the adsorption geometry of cysteine, a small amino acid, is investigated by a new generation XPD experiment that makes use of the high-brightness tuneable synchrotron radiation of the SLS. The XPD patterns display directly the chiral character of the molecule when single enantiomers are adsorbed.

- *Time-resolved electron diffraction*
  The experimental setup for our picosecond time-resolved electron diffraction experiment has been completed with the installation of the laser pulse amplifier. First tests have been carried out for pump-probe experiments in which a sample is excited by a laser pump pulse and probed, after a defined delay, by a low-energy electron pulse to monitor ultrafast structural changes at the sample surface. These tests have brought forward various new experimental difficulties that need to be overcome. In Section 13.10 some of these problems and their solutions are described.
  Finally, Section 13.11 reports the development and testing of a laser pulse autocorrelator, which is an important diagnostic device for characterizing the temporal width and the coherence time of the pulses.

13.1 Temperature dependence of the Shockley surface state on Ni(111)

in collaboration with:
G. Grad and P. Blaha, Institut für Physikalische und Theoretische Chemie, TU Wien

The Shockley surface state on Ni(111) is partially occupied and exchange split [1]. This is particularly interesting with respect to the question on how these electrons that do not propagate in the bulk and that have predominant sp-character do couple to the underlying exchange split band structure. Density functional calculations predict a very small exchange splitting of 23 meV and an energy upshift of 143 meV for majority and 120 meV for minority electrons in going from the ferromagnetic to the paramagnetic state [2]. Figure 13.1 shows angular resolved photoemission data of the Shockley surface state and its temperature dependence. Our instrument exposes photoemission from band states up to $5k_BT$ above the Fermi level. The binding energy of the surface state at the $\bar{\Gamma}$-point of the surface reciprocal lattice, i.e. at normal emission, is 45$\pm$5 meV at room temperature. We do not see an exchange splitting in these spin-integrated experiments. At room temperature the exchange splitting would therefore have to be greater than 130 meV or less than 60 meV. The upper bound is given by the limitation of our photoemission experiment to $5k_BT$ above the Fermi level and the lower value is estimated from the peak width that might contain unresolved spin up and spin down components. For the temperature dependence, we find a strong increase of the energy of the surface state at $\bar{\Gamma}$ up to the Curie temperature of Ni (631 K). This increase is in fair agreement with the theoretical prediction. The drop of the increase rate coincides within the accuracy of the experiment with the Curie temperature that was inferred from the temperature dependence of a simultaneously measured bulk band. The center of gravity of the surface state peak at $\bar{\Gamma}$ crosses the Fermi level at $365 \pm 30K$. In the paramagnetic phase the temperature coefficient for the binding energy change is reduced by a factor of 9 and is close to corresponding values on noble metal surfaces [3].

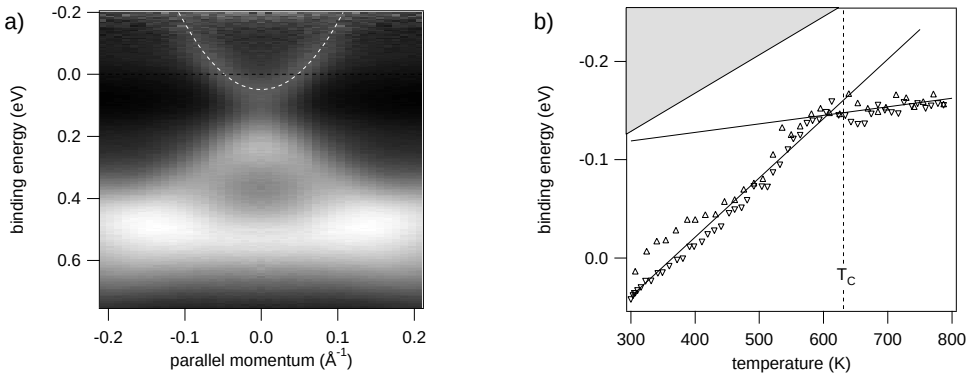

Figure 13.1: *$He\ I\alpha$ excited angular resolved photoemission data from Ni(111).*
a) Polar scan around normal emission at room temperature. The Fermi level (horizontal line) and the Shockley surface state (parabola) are emphasized with dashed lines.
b) Temperature dependence of the surface state binding energy at $\bar{\Gamma}$, i.e. at the bottom of the parabola. Triangles indicate data recorded during temperature rise ($\triangle$) and fall ($\triangledown$), respectively. The dark area $(E_F - E) > 5k_BT$ is not accessible in our photoemission experiment.

[1] M. Donath, F. Passek, V. Dose, Phys. Rev. Lett. **70** (1993) 2802.
[2] G. Grad and P. Blaha, work in progress.
[3] R. Paniago, R. Matzdorf, G. Meister and A. Goldmann, Surf. Sci. **336** (1995) 113.

13.2 Spin and angular resolved photoemission of the surface state on Au(111)

in collaboration with: V.N. Petrov, St. Petersburg Technical University, Russia and L. Patthey, M. Shi and M. Falub, Swiss Light Source, Paul Scherrer Institut, 5232 Villigen, Switzerland

The (111) surface of gold accommodates a Shockley-type surface state as well. In this case, the two-dimensional quasi-free electron gas is subject to a strong spin-orbit splitting proportional to the in-plane momentum of the electrons [1; 2]. In momentum space this results in a shift of the parabolic dispersions for spin-up and spin-down electrons.

In the beginning of 2003 the spin-resolved photoemission spectrometer COPHEE ("the COmplete PHotoEmission Experiment") was installed at the Surface and Interface Spectroscopy (SIS) beamline at the Swiss synchrotron Light Source (SLS). A first beam-time was devoted to spin-resolved measurements of the surface state on Au(111). In addition, the spin-integrating channeltron detector of COPHEE was used to investigate the performance of the spectrometer in conjunction with synchrotron radiation. Figure 13.2 shows the measured dispersion and Fermi surface of the surface state on Au(111). The splitting is nicely resolved in both data sets. The identification of the spin character

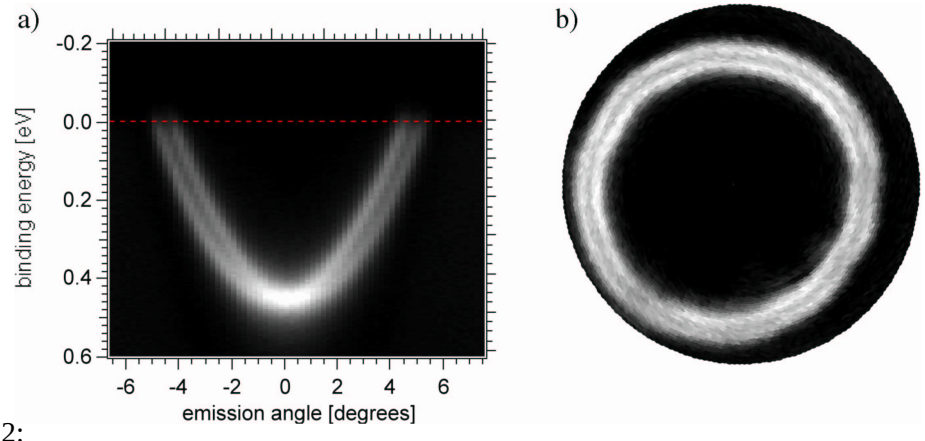

Figure 13.2:
a) Photoemission dispersion map of the surface state on Au(111). The dataset consists of photoemission spectra taken at various emission angles at a photon energy of $h\nu$=21.1 eV.
b) Fermi-surface map of this same surface state. The angular distribution of photoelectrons emitted from slightly below the Fermi edge into a small cone around normal emission (7° opening angle) is shown in a linear grey-scale in parallel projection. The sample was cooled using liquid nitrogen during the acquisition of both data sets.

of the two subbands is a direct probe of the spin-orbit interaction theory that has been inferred to describe the measured band splitting [1; 2]. Figure 13.3 shows spin-resolved photoemission spectra of the surface state on Au(111) at normal emission and positive and negative emission angles. At normal emission, no splitting is observed and the spin-up and spin-down spectra coincide. For off-normal emission, the splitting reveals itself by the presence of distinct spin-up and spin-down peaks that are shifted with respect to each other. A spin-resolved Fermi surface map (not shown) furthermore confirms the detailed spin structure that had been proposed, with in-plane spin vectors rotating tangentially along the Fermi surface contours, and with no out-of-plane component.

[1] S. LaShell, B.A. MacDougall, E. Jensen, Phys. Rev. Lett. **77** (1996) 3419.
[2] G. Nicolay, F. Reinert, S. Hüfner, P. Blaha, Phys. Rev. B **65** (2001) 33407.

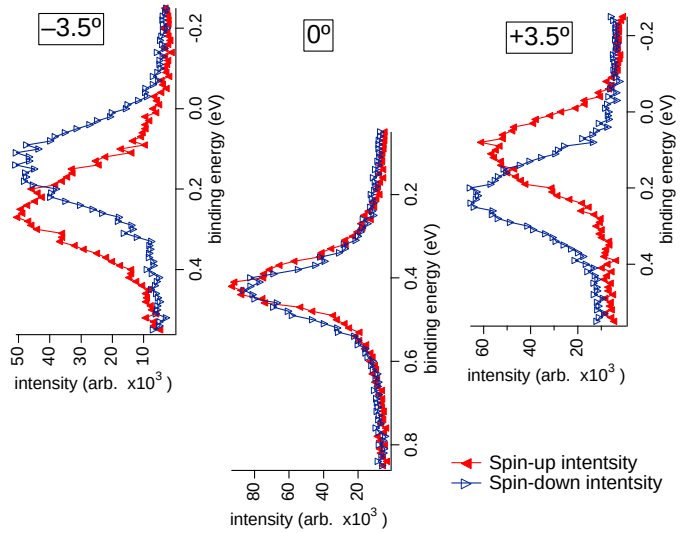

Figure 13.3: *Spin-resolved photoemission spectra of the surface state on Au(111) at different polar emission angles. The spectrometer resolution was relaxed for the acquisition of these data sets to allow for the reduced sensitivity associated with spin analysis and corresponding longer integration times. Each data set was recorded in less than two hours.*

13.3 Observation of a step induced gap in the Fermi surface of vicinal Cu(443)

in collaboration with:
J. Krempasky, M. Shi and L. Patthey, Swiss Light Source, Paul Scherrer Institut, Villigen

On vicinal Cu(111) surfaces, the Shockley surface state interacts with the steps that separate the subsequent (111) terraces. The step lattice acts like a periodic repulsive potential that confines the surface state [1; 2; 3]. Correspondingly its maximum binding energy decreases with increasing step density. The surface state is metallic and there is a critical step-step separation ℓ which is equal to the half of the Fermi wave length. At this shape resonance the formation of a gap is expected. This should cause an anisotropy of the electron transport at the surface and, more importantly, give a direct measure for the energy gain of the system due to the ordered step lattice. At room temperature this critical length is best met for Cu(443) ($\ell = 16.3$Å). In the framework of the pilot project *Surface-bulk coupling on vicinal Cu(111)* at the Swiss light source (SLS) we were able to observe for the first time a gap on the Fermi surface of the Shockley surface state resonance.

Fig. 13.4 shows the dispersion plots along the polar emission angle measured for two fixed azimuthal angles: one in the direction perpendicular to the steps (Fig. 13.4(a)) and the other in a plane rotated away by an angle of 18° (Fig. 13.4(b)). The confinement occurs between the steps, and the gap at the Fermi level is seen at $\overline{\Gamma}_{00}$ and $\overline{\Gamma}_{10}$ in Fig.13.4(a). This becomes particularly clear in comparing the data to those in Fig.13.4(b) where, for an azimuthal direction off the step normal, the Shockley surface state band crosses the Fermi level in the second surface Brillouin zone.

[1] O.Sánchez, J.M. García, P. Segovia, J. Alvarez, A.L. Vázquez de Parga, J.E. Ortega, M. Prietsch and R. Miranda, Phys.Rev.B **52**, 7894 (1995).

[2] J.E. Ortega, S. Speller, A.R. Bachmann, A. Mascaraque, E.G. Michel, A. Närmann, A. Mugarza, A. Rubio and F.J. Himpsel Phys.Rev.Lett.**84**, 6110 (2000).

[3] F. Baumberger, T. Greber and J. Osterwalder, Phys.Rev.B **64** (2001) 195411.

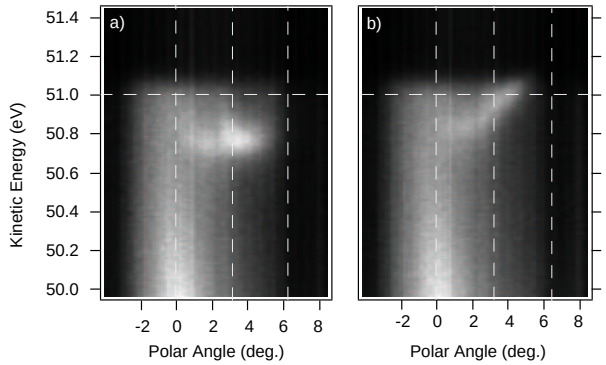

Figure 13.4: *Angular resolved photoemission ($h\nu$=55.5 eV) dispersion plots from the Shockley surface state of Cu(443) (raw data). a) Cut perpendicular to the steps. Clearly, a gap at $\overline{\Gamma}_{00}$ and $\overline{\Gamma}_{10}$ may be observed. The vertical dashed lines indicate projections of planes parallel to the steps which contain $\overline{\Gamma}_{00}$, $\overline{\Gamma}_{10}$ and $\overline{\Gamma}_{20}$, repectively. b) Cut 18° off the direction perpendicular to the steps. A band crossing the Fermi level (horizontal dashed line) in the second surface Brillouin zone is visible. The photoemission data were recorded with the Scienta SES-2002 analyzer in scanning the energy in the angle-dispersive mode. All data were measured at room temperature.*

13.4 Bulk-sensitive band mapping on Ni(111) using high-energy ARPES

in collaboration with:
A. Yamasaki, A. Sekiyama, S. Suga, Osaka University, Japan, and T. Muro, SPring-8, Hyogo, Japan

Photoemission spectroscopy is intrinsically surface sensitive due to the strong interaction of the excited photoelectrons with matter, leading to inelastic mean free paths λ_i of the order of a few atomic layers. This is particularly true for the low photon energies in the range of 20 to 100 eV typically used in ARPES experiments. It has thus been questioned as to how far photoemission can really probe true bulk states [1]. This question has been addressed by comparing ARPES data from Ni(111) measured at low photon energy ($h\nu$ = 21.22 eV), where λ_i is of the order of 6 Å, to higher energy data where λ_i lies between 10 and 20 Å. Such high-energy ARPES experiments at energy and momentum resolutions adequate for band mapping can be performed at beamline BL25U of the SPring-8 synchrotron in Japan.

The experimental ARPES data for three energies, i.e. $h\nu$=21.22 eV, 270 eV, and 497 eV are presented in Fig. 13.5. In the low-energy data (Fig. 13.5a) both the minority (lower binding energy) and majority (higher binding energy) version of the *d* band centered at 1.2 Å^{-1} are exposed [2], though with a far smaller exchange splitting between the two as compared to the density functional theoretical (DFT) curves that are given as red and blue solid lines. In the higher energy data (Figs. 13.5b and c) the same spin-split *d* band pair is observed, with Fermi level crossings at nearly the same $k_{||}$ values for all energies. At these higher energies, the bands can be followed out to higher parallel momenta. The DFT band structure calculations provide an excellent description of the measured band dispersion as far as Fermi level crossings and the general dispersion behaviour are concerned. Regarding the exact band widths and group velocities, however, one notes that the width of the minority *d* band is strongly reduced in the low-energy measurement, while the two high-energy data show a band width that is close to the DFT value. There is also a gradual increase of the exchange splitting between minority and majority *d* bands with photon energy, yet the DFT value of 0.83 eV is not reached at the highest photon energy.

This different behaviour, and the fact that the data obtained with higher-energy photons, and thus

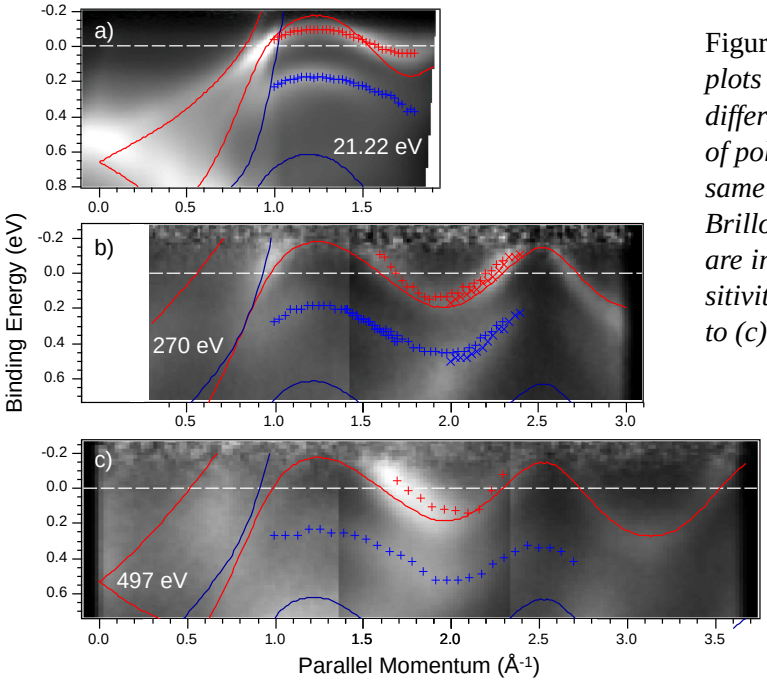

Figure 13.5: *Photoemission dispersion plots from clean Ni(111) measured at different photon energies as a function of polar angle with the goal to probe the same electronic states in different bulk Brillouin zones. The photon energies $h\nu$ are indicated in the figure, the bulk sensitivity increases in going from panel (a) to (c). Red and blue solid lines give minority and majority bands, respectively, as calculated within density functional theory. Red and blue markers indicate measured energy values within some bands as quantified from individual spectra.*

more bulk penetrating photoelectrons, are far better described by the DFT calculations, leads us to the conclusions that ARPES data measured at the typical photon energies of below 100 eV probe bulk bands that are strongly affected by the presence of the surface.

[1] S. Suga, A. Sekiyama, J. Electron Spectrosc. Relat. Phenom. **124**, 81 (2002).

[2] T. Greber, T. J. Kreutz, J. Osterwalder, Phys. Rev. Lett. **79**, 4465 (1997).

13.5 The electronic structure of a surfactant layer: Pb/Cu(111)

Monolayers of Pb promote very efficiently the layer by layer growth of epitaxial films on Cu(111) [1]. For this role as a surfactant the Pb layer must have the properties of a highly elastic skin which is only weakly coupled to the substrate. In order to step beyond the phenomenological understanding of surfactants in terms of lower surface free energy we have investigated the electronic structure of one compact layer of Pb on Cu(111) forming an incommensurate quasi (4×4) structure [2]. Angular resolved photoemission data have been compared with density functional (DFT) calculations [3].

In the Cu(111) Fermi surface map shown in Fig.13.6(a), we readily identify direct transition lines, which are characteristic for the Cu bulk Fermi surface. The contours are well reproduced by a spherical cut through the calculated bulk Fermi surface (Fig.13.6(c)). The most intense circular feature centered at $\bar{\Gamma}$ is due to the free electron like Shockley surface state, which is not reproduced in the bulk calculation. In the data from the lead covered surface (Fig.13.6(b)), the surface state is either quenched or pushed above the Fermi level. Instead, bright features appear in a sixfold symmetric arrangement in the second Brillouin zones of the overlayer 1×1–periodicity. Besides the remaining intensity from the Cu bulk Fermi surface, we observe a weak regular hexagon centered at $\bar{\Gamma}$ with its sides parallel to the surface Brillouin zone and measuring about half its linear dimension. Both features are surprisingly well reproduced in the calculated Fermi surface of a free standing Pb layer (Fig.13.6(d)). This striking similarity shows that adsorbate and substrate electronic systems are

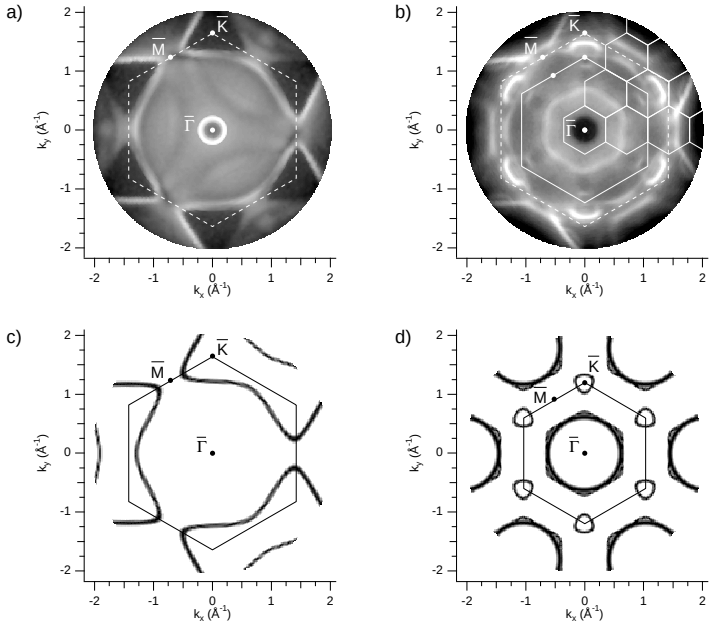

Figure 13.6: *He Iα excited Fermi surface maps of clean Cu(111) (a) and (4×4) Pb/Cu(111) (b). The photoemission intensity is shown on a logarithmic gray scale as a function of the two momentum components in the surface plane. Surface Brillouin zones constructed for the Cu (dashed) and Pb (solid line) periodicities are overlayed. The smaller hexagons in (b) show the nominal Brillouin zones. (c) Cu–bulk Fermi surface, calculated on the spherical k–space contour, defined by the energy of a free-electron-like final state. (d) Fermi surface, as obtained from a density functional calculation for a free-standing planar Pb layer.*

largely decoupled. The reason appears to be the lattice mismatch of ≈33%, which translates into a serious mismatch of the Brillouin zones, relevant inside the Cu(111) surface and inside the Pb layer. The dominant periodicity in the experimental Fermi surface map is clearly the Pb (1×1)–structure. The periodicity of the substrate is not reflected in the adlayer band structure and thus fullfills a requirement for a surfactant, i.e. contributes only weakly to the potential felt by the electrons in the Pb film.

[1] J. Camarero, T. Graf, J.J. de Miguel, R. Miranda, W. Kuch, M. Zharnikov, A. Dittschar, C.M. Schneider, J. Kirschner, Phys. Rev. Lett. **76** (1996) 4428.

[2] S. Müller, J.E. Prieto, C. Rath, L. Hammer, R. Miranda, K. Heinz, J. Phys. Cond. Matter **13** (2001) 1793.

[3] F. Baumberger, A. Tamai, M. Muntwiler, T. Greber, J. Osterwalder, Surf. Sci., in press.

13.6 Fermi-surface mapping on ultrathin films of Ni/Cu(001)

in collaboration with: V.N. Petrov, St. Petersburg Technical University, Russia

Ultrathin films of Ni on Cu(001) have recently attracted a lot of interest, because of their rich magnetic behaviour. At very low film thickness the electronic structure of the films is interesting by itself because the electronic states observed in photoelectron spectroscopy clearly derive from nickel but despite the low film thickness they show behaviour very similar to three-dimensional bulk nickel [1]. One study even reports a bulk-like Fermi surface down to the ultimate limit of a monolayer [2]. Tri-layers of Ni/Cu/Ni also show a giant magneto-resistance effect, which depends on the thickness of the Cu spacer layer and the Ni films. Information on the Fermi surface in such layered systems can improve our understanding of both the electrical transport and the origin of magnetic coupling between the layers.

Ni films were evaporated at room temperature from an electron-beam heated rod onto a clean Cu(001) surface. A slight re-annealing to 420 K after deposition helped to improve the film crystallinity while interdiffusion could be kept low. Fig. 13.7 shows the measured Fermi surface maps for a 2.4 ML

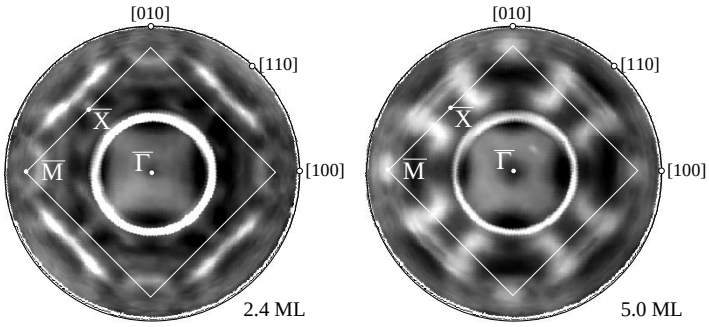

Figure 13.7: *Fermi surface maps of ultrathin films of Ni/Cu(001) measured by angle resolved photoelectron spectroscopy at a photon energy $h\nu$=21.22 eV. Both maps were taken at a sample temperature of T=150 K. The different contours observed at thicknesses of 2.4 ML and 5.0 ML are discussed in the text. The bright rings are an artefact of photons scattered into the analyzer. Figure from [3].*

thick and a 5.0 ML thick film. Both data sets were acquired at a sample temperature of T=150 K. The prominent ring feature in the center of these maps is an artifact caused by parasitic electrons that are excited when the light is directly reflected off the sample into the electron analyser. The thickness dependence of the Curie temperature leads to a paramagnetic state in the 2.4 ML thick film and a ferromagnetic state in the 5.0 ML thick film. The paramagnetic-to-ferromagnetic transition shows up in these data by the opening of an exchange splitting of the straight sp-band Fermi surface contours outside the $\overline{X}$-point as seen in the map for the 5.0 ML thick film. Otherwise, these features as well as the cushion shape in the centre of the plot are not changing much. More drastic changes are seen in the other contours, namely the d-band features around the $\overline{M}$-point, which change from a ring at 2.4 ML to a blot in the thicker film, or the line feature inside of the $\overline{X}$-point, which disappears at higher film thickness and is replaced by an entirely different structure. A comparison to band structure calculations reveals that the Fermi surface observed in the 5.0 ML thick film is indeed very similar to the one of bulk nickel, while a two-dimensional confinement is observed in the 2.4 ML thick film. This transition is, however, only observed for the electronic states derived from the Ni *d*-band, while the less localized *sp*-electrons exhibit a bulk-like Fermi surface at all film thicknesses.

[1] C. Pampuch, O.Rader, R. KlŁsges, C. Carbone, Phys.Rev.B **63** (2001) 153 409.

[2] G.J. Mankey, K. Subramanian, R.L. Stockbauer, R.L. Kurz, Phys.Rev.Lett.**78** (1997) 1146.

[3] M. Hoesch, PhD thesis, Univ. Zürich 2002.

13.7 Hexagonal boron nitride on Ni(111): defects and two-domain monolayers

A single monolayer of hexagonal boron nitride ($h-$BN) on Ni(111) forms an atomically sharp interface and can be used as a model substrate with low surface energy [1; 2; 3]. In this context line defects that we discovered in the nearly perfect $h-$BN monolayers play an important role. They influence e.g. the growth behaviour of metals on $h-$BN/Ni(111) [4]. Experiments combining scanning tunnelling microscopy (STM) and photoelectron diffraction (XPD) on the very same surface give an explanation for these defect lines in terms of a stacking fault. They appear on boundaries between different $h-$BN domains. Besides the original domain that dominates well prepared $h-$BN monolayers, the appearance of a second minority domain is triggered by impurities.
Fig. 13.8 illustrates these findings on the basis of two sub-monolayer preparations (P_1, P_2) yielding

$h-$BN islands on Ni(111). The XPD pattern in Fig. 13.8a) (P_1) reflects the well known original domain, with N atoms on top of the outermost Ni atoms and B atoms stacked on fcc sites (N,B)=(*top*,*fcc*) [2; 3]. The STM images in the conductivity mode (Fig. 13.8b) are dominated by triangular $h-$BN islands pointing in the $[\bar{1}\bar{1}2]$ direction. With respect to the B atoms the islands terminate with B-type steps (i.e. (111) nanofacets). In order to satisfy bond saturation we expect island rims with hydrogen saturated nitrogen chains. Fig. 13.8c) shows the resulting structural model. Preparation P_2 results in a diffraction pattern (Fig. 13.8d)) and in triangle directions (Fig. 13.8e)) rotated by 60° relative to the original ones. Fig. 13.8f) displays the model for this second domain with N atoms on top and B atoms on hcp sites (N,B)=(*top*,*hcp*). Here the boron atoms are hcp stacked and the islands terminate as well with B-type steps. Based on the structural models for the two domains (Fig. 13.8c) and f)) and the fact

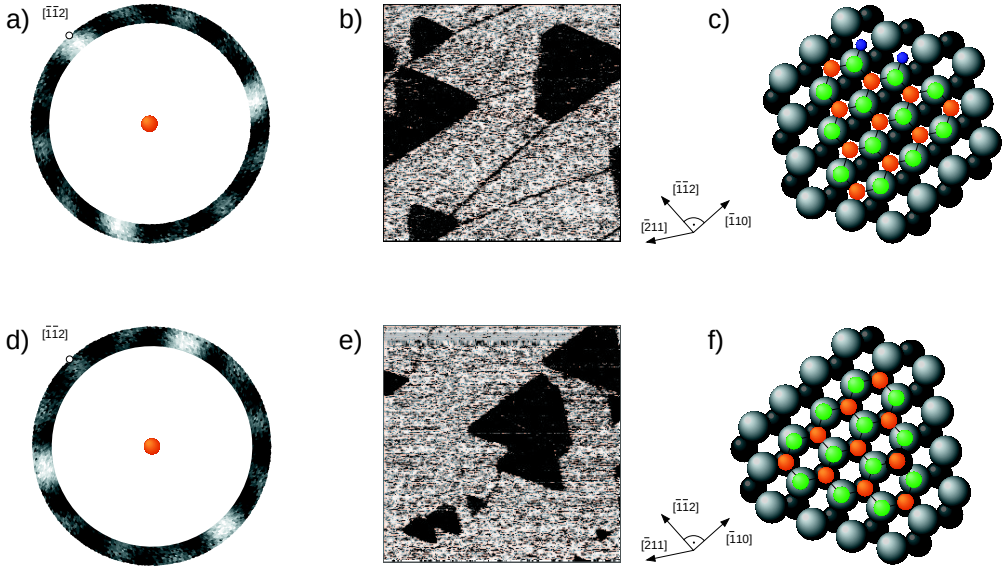

Figure 13.8: *XPD and STM results on $h-$BN islands partially covering the Ni substrate for preparation P_1 (a-c) and P_2 (d-e):*
a) Si $K\alpha$ excited B 1s XPD pattern. The three-fold maxima coincide with the $[\bar{1}\bar{1}2]$ directions.
b) a corresponding conductivity image (0.4μm×0.4μm, I=1 nA, V=-0.8 V). The $h-$BN triangles (black) point towards $[\bar{1}\bar{1}2]$ (the dark lines represent steps which induce a slight contrast).
*c) Top view of a model representing the island structure in b): the configuration is (N,B)=(*top,fcc*).*
d) Si $K\alpha$ excited B 1s XPD pattern. The main maxima point towards the $[\bar{2}11]$ direction.
e) a corresponding conductivity image (0.4μm×0.4μm, I=3 nA, V=-0.6 V). The $h-$BN triangles (black) are oriented towards $[\bar{2}11]$.
*f) Top view of a model representing the island structure in e): the configuration is (N,B)=(*top,hcp*).*

that line defects are found whenever two opposite triangles collide (not shown), an intuitive explanation for the defect lines is given: due to the different registry to the substrate, the two domains can not grow together and a linear imperfection (domain boundary) appears in between the fcc and the hcp domain. It is interesting to note that the second domain (i.e. (N,B)=(*top*,*hcp*)) which more likely appears on poorly prepared sample surfaces, was predicted by DFT calculations to be energetically only slightly less favourable (9 meV/BN unit) than the original (N,B)=(*top*,*fcc*) domain [5].

[1] A. Nagashima, N. Tejima, Y. Gamou, T. Kawai, and C. Oshima, Phys. Rev. B **51** (1995) 4606.
[2] W. Auwärter, T.J. Kreutz, T. Greber, J. Osterwalder , Surf. Sci. **429** (1999) 229 .

[3] M. Muntwiler, W. Auwärter, F. Baumberger, M. Hoesch, T. Greber, J. Osterwalder , Surf. Sci. **472** (2000) 125.

[4] W. Auwärter, M. Muntwiler, T. Greber, J. Osterwalder, Surf. Sci. **511** (2002) 379.

[5] G.B. Grad, P. Blaha, K. Schwarz, W. Auwärter, and T. Greber, submitted.

13.8 Adsorption and self-organization of C_{60} molecules on Cu(221)

Since the discovery of C_{60}, many studies have been performed in order to understand the basic properties of this complex molecule and to develop possible applications. An important issue concerns the fabrication of low-dimensional systems, where intriguing phenomena have been observed, such as Fermi gap opening in the C_{60} monolayer on Ag(100) [1] or superconductivity at alkali metal doped C_{60} surfaces at low temperature [2]. Depending on the substrate, single layers of C_{60} molecules have been found in different geometrical arrangements and different bonding and charge states. On Cu(111), C_{60} molecules form an ordered monolayer system, and photoelectron diffraction experiments showed that the molecules are adsorbed with a $6-$ring towards the surface, in two azimuthally equivalent orientations [3].

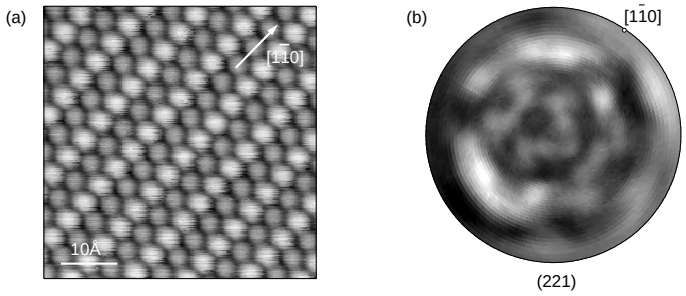

Figure 13.9: *One monolayer of C_{60} adsorbed on Cu(221). (a) Room temperature STM image showing alternating bright and dim rows of C_{60} molecules running along the step direction $[1\bar{1}0]$. (b) Experimental C1s XPD pattern (Mg Kα, $E_{kin} = 970eV$). The diffraction intensities are shown in stereographic projection and on a linear grey scale with maximum intensity corresponding to white.*

In order to orient these molecules and to align them into one-dimensional chains, we investigate C_{60} on vicinal surfaces. One monolayer of C_{60} on Cu(221) forms a quasi-hexagonal close$-$packed arrangement slightly relaxed in the direction perpendicular to the steps as we conclude from the LEED pattern. STM images show that C_{60} and Cu(221) self-organize into well ordered one-dimensional structures. The images indicate large terraces on which the molecules align themselves in parallel rows (Fig.13.9a)). On each terrace the rows have a regular modulation of the brightness. The unit cell contains two C_{60} molecules: a molecule that appears bright and a molecule that appears dim. This contrast can be explained in terms of different coordination to the substrate. From the XPD data in Fig.13.9(b) it can be concluded that at least in one of the two types of chains, the molecules have a single well-defined orientation.

[1] C. Cepek, I. Vobornik, A. Goldoni, E. Magnano, G. Selavggi, J. Kröger, G. Panaccione, G. Rossi, M. Sancrotti, Phys.Rev.Lett.**86** (2001) 3100.

[2] R. Hesper, L.H. Tjeng, A. Heeres, G.A. Sawatzky, Phys.Rev.Lett.**85** (2000) 1970.

[3] R. Fasel, P. Aebi, R.G. Agostino, D. Naumovic, J. Osterwalder, A. Santaniello, L. Schlapbach, Phys.Rev.Lett.**76** (1996) 4733.

13.9 Cysteine on Cu(110) studied with X-ray photoelectron diffraction

in collaboration with:
C. Quitmann, Swiss Light Source, Paul Scherrer Institut, 5232 Villigen, Switzerland

In the emerging field of nanotechnology, the adsorption of large molecules on surfaces plays a vital role in areas such as molecular electronics, nanodevices, and molecular recognition [1; 2]. A key piece of information that forms the starting point of any understanding of adsorbate-surface interactions is the local bonding geometry. For molecules larger than a few atoms the determination of the adsorption geometry is by no means a trivial task. Most of the traditional methods fail in the case of molecules with more than four atoms. Angle scanned X-ray photoelectron diffraction (XPD) has the potential for structural investigations of more complex systems, as was demonstrated e.g. in the case of heptahelicene adsorbed on copper surfaces [3]. With the advent of third-generation synchrotrons, a new class of XPD experiments have become possible. If the coverage of the adsorbate under investigation is in the submonolayer range, it is crucial to choose a suitable photon energy to have a high photoemission cross-section on the one hand and to optimize the signal to background ratio on the other hand.

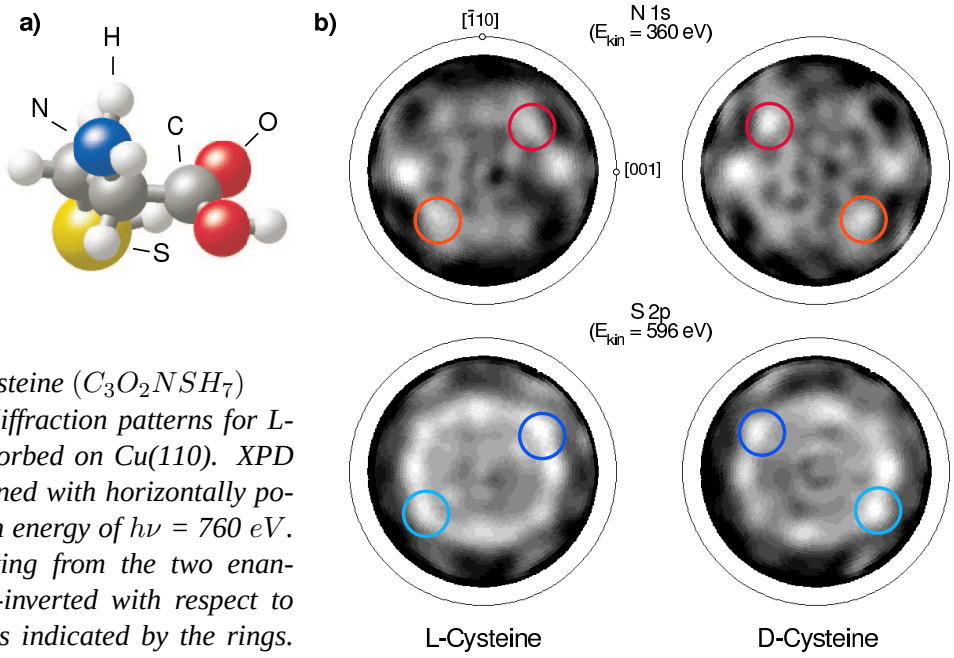

Figure 13.10: *a) Cysteine* $(C_3O_2NSH_7)$ *b) N 1s and S 2p diffraction patterns for L- and D-cysteine adsorbed on Cu(110). XPD patterns were obtained with horizontally polarized light with an energy of* $h\nu$ *= 760* eV*. The patterns resulting from the two enantiomers are mirror-inverted with respect to each other, which is indicated by the rings. The mirror plane is (001).*

During the last year we installed an endstation to perform angle resolved photoemission experiments at the Surface and Interface Microscopy (SIM) beamline at the SLS. In first experiments we deposited cysteine (Fig. 13.10(a)), a small amino-acid, onto a copper surface to study the adsorption geometry and the intramolecular rearrangement upon adsorption. We adsorbed a submonolayer of either D- or L-cysteine on a clean Cu(110) sample. In Fig. 13.10 the N 1s and S 2p XPD patterns are presented. All the patterns show clear forward scattering features (bright spots) with C_2 symmetry. They are mirror-inverted for opposite enantiomers. The chirality of the molecule is thus reflected in the patterns. The strongest forward scattering spots in the N 1s patterns correspond to scattering along the N-C axis. From the position of this spot the bonding angle of the N-C axis and the angle between this axis and the copper rows of the (110) surface can be directly determined. It is concluded that the molecules are adsorbed in two distinct azimuthal orientations. The structure will be retrieved by

comparing the experimental data to a set of scattering calculations in a trial and error approach.

[1] C. Joachim, J.K. Gimzewski, A. Aviram, Nature **408**, 541 (2000).

[2] F. Moresco et al., Phys. Rev. Lett. **86**, 672 (2001).

[3] R. Fasel, A. Cossy, K.-H. Ernst, F. Baumberger, T. Greber, J. Osterwalder, J. Chem. Phys. **115**, 1020 (2001).

13.10 Time-resolved electron diffraction

Real-time measurements of electron and atom dynamics on solid surfaces with picosecond time resolution are carried out in the so-called pump-probe mode: A strong first laser pulse puts the system under investigation into a specific state. In the simplest case the pump pulse is absorbed leading to a transient temperature rise in the surface. From this initial state the system evolves and is probed by a second time-delayed pulse (probe). The probe signal as function of delay time yields finally information about the evolution of the system.

Since several years we are to realize an experiment in which low-energy electrons are used as a time-resolved structure sensitive probe. The intensity of diffraction spots in patterns obtained from samples surfaces is then recorded as function of delay time. The experimental setup has been completed in April 2002 with the installation of a regenerative pulse amplifier (RegA) and an optic-parametric amplifier (OPA). The system purchased (Coherent Inc.) was chosen because of its high pulse repetition rate (250 kHz) and sufficient pulse energy (4 μJ). The OPA converts the high-intensity pulses of the RegA into tunable light pulses, the frequency of which covers almost the whole visible range from 450 nm to 750 nm. Meanwhile, the whole experiment was fully automated: delay stage and the CCD camera used to take the diffraction images are controlled by a host computer, and several analog voltages can be measured simultaneously. The program further allows autocorrelation experiments or voltage charts to be measured [1].

In order to acquire experience, the first pump-probe experiments were carried out using an electron gun designed for operation at medium and high energies (more than 1 keV)[2]. This gun has the advantage of producing a rather high electron current allowing optical filters, scattering geometry, detector settings, and other important parameters to be optimized. As start experiment, the transient temperature rise of the lattice after absorption of the pump pulse is to be recorded as a function of time. For this purpose, the LEED spot intensity is used as an ultra-fast thermometer (see e.g. Ref. [3]). A rise in temperature results in a decrease in spot intensity due to the Debye-Waller effect. The thermometer can be calibrated in a static experiment by measuring the spot intensity for various temperatures. Such a calibration curve is depicted in Fig. 13.11. In the inset, raw data are shown as example for a typical LEED pattern as obtained with the high-energy electron gun from Ge(111). Faint spots of the c(2x8) surface reconstruction are visible between the principal diffraction spots emphasizing the high quality of these images.

Despite the excellent signal-to-background ratio of these images, all attempts to record time-resolved data failed so far for several reasons : 1.) Spatial overlap to within a few micrometers is difficult to obtain and to maintain for electrons and photons on a distance of meters. This problem could partially be solved by attaching a channeltron detector with pinhole close to the sample position. 2.) Temporal overlap, *i.e.* the delay "zero" for which electrons and photons arrive at the same time on the sample, has to be determined in advance based on ray-tracing calculations. Since, in this gun, the electrons are slow and the path length of 0.5 m is very large, the uncertainty of these calculations is quite

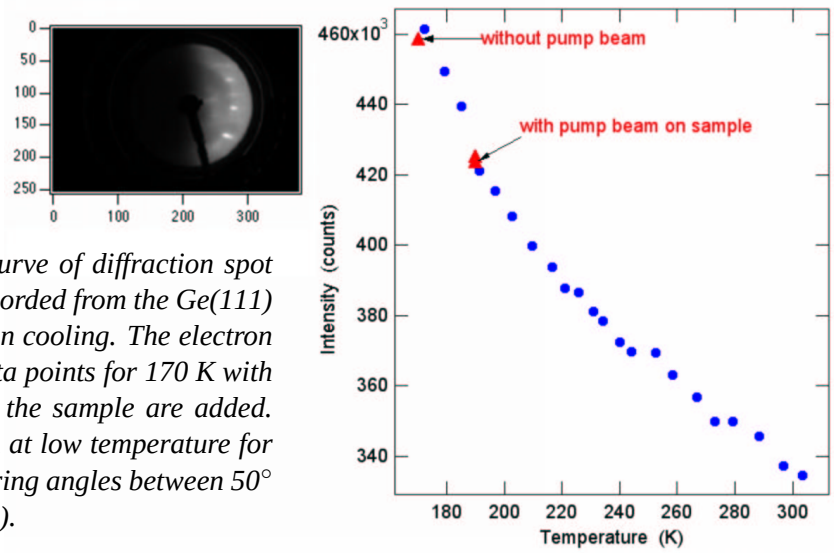

Figure 13.11: *Calibration curve of diffraction spot intensity vs. temperature, recorded from the Ge(111) surface during liquid nitrogen cooling. The electron energy was 200 eV; some data points for 170 K with and without pump beam on the sample are added. Inset : typical LEED pattern at low temperature for normal incidence and scattering angles between 50° and 90° (cut-off of the image).*

large. Again, by means of the channeltron detector this uncertainty could be reduced to smaller than 1 ns, which is within the range of the delay stage used here. 3.) Temporal broadening of the electron pulses, caused by the initial velocity distribution and path length differences. The velocity distribution is determined by the work function of the photocathode and the photon energy. The photon energy, which can be tuned by means of the OPA was set close to half the work function of the cathode , leading to 0.3 eV spread in energy for the two-photon-photoemission current. Nevertheless, due to the long flight time, this results in a temporal broadening of the order of 100 ps. Space charge may lead to similar broadening. However, this latter effect was found to become important for photocurrents higher than 100 pA at 250 kHz repetition rate, thus 2'000 photoelectrons per pulse. During pump-probe experiments, the photocurrent employed was held below 20 pA by reducing the probe light intensity. Some of the time dependent curves taken from Ge(111), pumped with 800 nm light and a fluence of about 10 mJ/cm^2, showed the expected signal but were not reproducible.

Finally, the OPA turned out to be often instable on the time scale of several hours, rendering the data analysis difficult. High harmonic generation (like the third harmonic at 266 nm, for instance) is much more stable than parametric amplification. In collaboration with P. Hamm and J. Helbing from the Physical Chemistry Institute, a setup for third harmonic generation from 800 nm light was mounted, based on frequency doubling in a type-I BBO crystal and subsequent sum frequency generation in a type-II BBO crystal. Due to the high photon energy, however, absorption in lens and window materials becomes important, and this project was postponed.

After these preliminary experiments, the actual gun designed for low-energy electrons [4; 5] was mounted. It is expected to provide electron pulses with a temporal spread of the order of 5 ps. However, the low current output of this gun (a few fA at 250 kHz repetition rate) necessitates operation of the two-stage microchannel plate LEED detector at highest amplification level and the subtraction of dark reference images taken under the same conditions but without electrons. Typical CCD exposure times are of the order of ten minutes per image. Nevertheless, the first measurements are already promising. One curve, recorded from Ag(111) using 800 nm pump light at a fluence of 20 mJ/cm^2, is shown in Fig. 13.12 beside a typical image after subtraction of the dark image. Unfortunately, it was impossible to take advantage of the resonant surface plasmon absorption at 400 nm for the pump pulse [6], because stray light of these high-energy photons (3.15 eV) was found to produce strong background in the LEED detector. The step, which is seen in Figs. 13.12(b) and (c) close to the expected time "zero" is likely due to purely instrumental intensity fluctuations and thus not the result of a real thermal effect in the sample surface. Nevertheless, we hope that we will be able to record

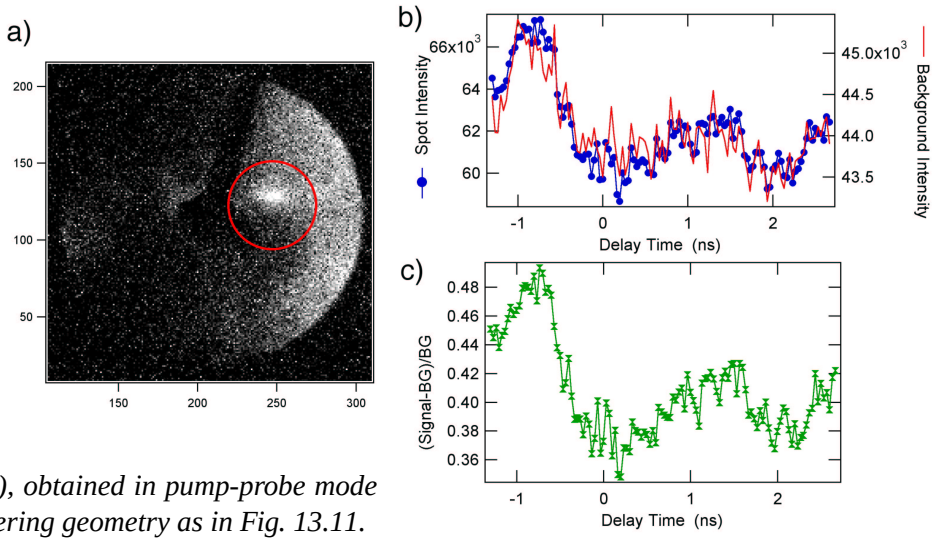

Figure 13.12:
Results from Ag(111), obtained in pump-probe mode using a similar scattering geometry as in Fig. 13.11.
a) One image from this series of 121 images after subtraction of a reference dark image; the LEED spot is highlightened by a red circle.
b) Spot (blue) and background (red) intensities
c) the normalized difference signal-background as function of delay time. The width of the step seen in all curves in (b) and (c) close to delay zero is about 200-250 ps. Since the background behaves in the same way, this step is probably due to fluctuations in the laser power and/or gun current.

time-resolved LEED images with picosecond resolution in near future.

[1] M. Barry, *Vorbereitende Arbeiten für zeitaufgelöste LEED-Experimente*, Diplomarbeit, Universität Zürich, 2002.

[2] M. Aeschlimann, E. Hull, C.A. Schuttenmaer, J. Cao, Y. Gao, D.A. Mantell, and H.E. Elsayed-Ali in *Time-resolved electron and x-ray diffraction*, P.M. Rentzepis (Ed.), Proc. SPIE **2521**, 103 (1995).

[3] X. Zeng, H.E. Elsayed-Ali, Phys. Rev. B **64**, 085410 (2001).

[4] R. Karrer, *Bau einer Elektronenkanone für zeitaufgelöste Beugung mit langsamen Elektronen*, Diplomarbeit, Universität Zürich, 2000.

[5] R. Karrer, H.J. Neff, M. Hengsberger, T. Greber, and J. Osterwalder, Rev. Sci. Instrum. **72**, 4404 (2001).

[6] J. Lehmann, M. Merschdorf, W. Pfeiffer, A. Thon, S. Voll, and G. Gerber, Phys.Rev.Lett.**85**, 2921 (2000).

13.11 Measurement of femtosecond pulses - autocorrelation

For any study of ultrafast processes by means of femtosecond laser systems, tools are needed for characterising the pulse shape, spectrum, and temporal width. Since the temporal width is of the order of a few tens of femtoseconds, too fast for any electronic device, reliable results about the width can only be obtained by correlation experiments. In this type of experiment, a pulse of comparable or even smaller width is used to measure the quantity of interest. If the two pulses originate from one single pulse by beam splitting, one speaks of autocorrelation. After the beamsplitter, both fractional pulses travel different path lengths such that one is delayed with respect to the other. At the end both

are brought back together in a non-linear process and the second-order signal is measured, like the second harmonic intensity obtained in a frequency-doubling crystal, for instance. The second-order yield depends on the product of the pulse intensities in contrast to a linear process, the output of which depends on the sum (see e.g. Ref. [1]). The second-order signal is therefore directly proportional to the autocorrelation function.

For this purpose, an autocorrelator was to be built which had the following specifications : low cost, smallest number of optical elements (for reasons of pulse broadening and alignment), and a fast scan rate such that it allows optical paths and pulse compression stages to be optimized for smallest temporal chirp. Further requirements would be the possible operation over a large range in wavelength (400-800 nm), and the possibility to measure the coherence time. The latter is given by Fourier transforming the frequency spectrum of the pulses and corresponds to the minimum pulse duration, which can be achieved for a given setup. The final autocorrelator design was based on a Michelson-Morley interferometer comprising one beamsplitter and two mirrors. This setup can easily be extended by using two further mirrors and a lens to a confocal arrangement for background suppression [1]. In one of the two branches, the mirror position and thereby the optical delay are moved by a piezocrystal, simply controlled by an analog voltage.

Initially, two-photon-photoemission from the photocathode of a photomultiplier tube (PMT) should be used as second-order signal. The PMT (Hamamatsu) is optimised for operation in the visible light range with a fairly sharp cut-off between 650 and 700 nm. Using this PMT, the setup was tested with 800 nm light. In the next step, the PMT should be replaced by a so-called solar-blind PMT having its cut-off wavelength in the ultraviolet. Thereby, a strong non-linear response is to be expected for the whole wavelength range of interest. The advantage of using a PMT are its fast response time and high quantum efficiency allowing for high scan rates on one hand and an amplified strong signal output on the other hand. Finally, it turned out that despite the sharp cut-off the linear response is still sufficiently strong at 800 nm to mask the second-order 2PPE signal.

The output, shown in Fig. 13.13 (a) and (b) represents therefore the interference pattern of the two pulses. The width of this pattern corresponds to the coherence length (and time) of the pulses, found to be 40 fs after deconvolution of the fitted Gaussian shape (full width at half maximum 56 fs). From an independent measurement of the pulse spectrum (Gaussian shape of 25 nm width at 795 nm central wavelength), 37 fs are obtained in good agreement with the value found here. The pulse duration at the output of the laser oscillator was measured to be 64 fs with a commercial autocorrelator.

It has to be noted that the ratio of linear to second-order response of the PMT depends critically on experimental parameters like light intensity and PMT voltage. However, no conclusive results have been obtained by optimising the output signal. Two-quanta photodiodes or solar-blind PMTs could be used in order to circumvent this problem. To this end, the true autocorrelation curve was measured, as shown in Fig. 13.13c, by introducing a frequency-doubling β-bariumborate (BBO) crystal in front of the detector and by removing the remnant fundamental light by appropriate filters. The curve was best fitted by assuming $(\mathrm{sech})^2$-pulse shape yielding 135 fs for the pulse duration after deconvolution. This value compares favourably to the value of 140 fs obtained with a commercial autocorrelator after an arrangement of filters and mirrors similar to the one used here.

[1] W. Demtröder, *Laser Spectroscopy, Basic Concepts and Instrumentation*, 2nd edition, pp 622-629, Springer (Berlin, Heidelberg, New York), 1998.

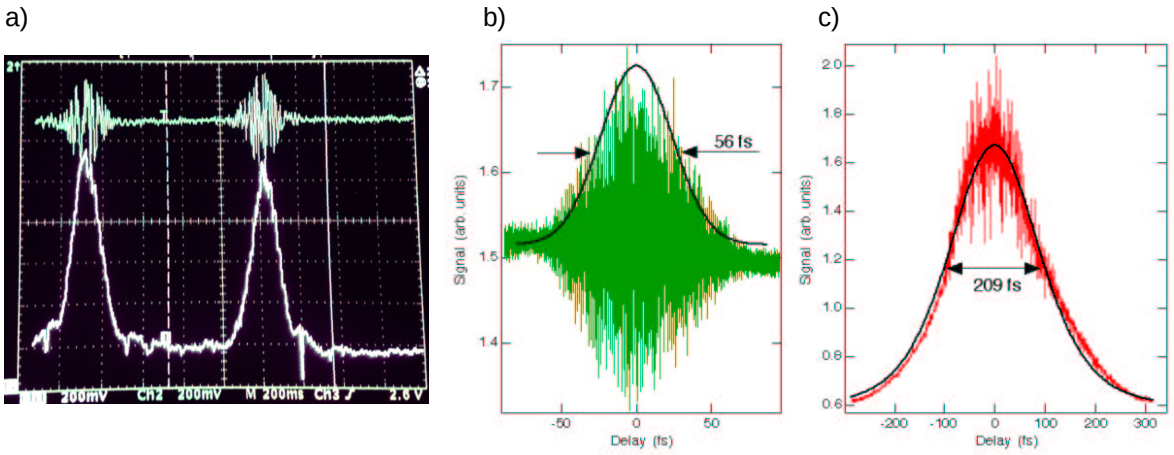

Figure 13.13: *Typical signals from the autocorrelator :*
a) Single shot measurements of the coherence length, recorded by means of an oscilloscope and a peak detector; the scanning rate was 0.33 Hz. The upper green curve are raw data from the PMT, the white curve underneath it is the envelope function as output from the peak detector.
b) Computer controlled measurement of the coherence length. The black line shows a Gaussian fitted to the envelope yielding the width of 56 fs.
c) Autocorrelation experiment recorded using a BBO crystal for frequency doubling. The autocorrelation width is found to be 209 fs. Note the obtained signal-to-background of 2:1 as theoretically expected for this setup.

14 Physics of Biological Systems

Tatiana Latychevskaja (until December 2002), Cornel Andreoli, Conrad Escher,
Hans-Werner Fink, Michael Krüger (since February 2003),
Hiroshi Okamoto (since February 2002) and Thomas Rusterholz (since September 2002)

in collaboration with:
Clondiag Chip Technologies (Germany), Orsay Physics (France), National Center of Competence in Research (NCCR) Nano-Scale Science, CNRS Marseille (France) and the Bio-Chemistry Institute of the University of Zurich

In the past year the new laboratory has become available and the installation and operation of most of the scientific equipment was celebrated in October 2002. The overall goal of our efforts is directed towards an understanding of the unique properties of objects with nanometer-scale dimensions with a special emphasis on biological systems. The high brightness and coherence of our electron source in combination with high phase contrast in scattering off biological molecules and the lack of radiation damage are key issues that make us believe that LEEPS - Low Energy Electron Point Source - microscopy has the potential of becoming a novel tool for structural biology on a level of individual molecules. Our recently completed laboratory environment with its mechanical damping platforms and ac-magnetic field compensation has been designed in such a way as to preserve the coherence of the low energy electron wave fronts used for imaging.

Apart from the imaging aspects needed for structural information, the LEEPS technique also allows to mechanically and electronically manipulate individual objects at the nanometer scale. This possibility of in-situ imaging and manipulation makes it possible to also address issues related to the electrical conductivity in molecules or other mesosopic systems.

In order to be able to control single molecules already in the liquid phase we adopted the technique of optical fluorescent video microscopy in the frame of Conrad Escher's diploma thesis that was completed in early 2002. Meanwhile, video microscopy has become a powerful tool for us, not only for controlling single molecules in the liquid environment, but also for developing strategies to interface them to silicon structures. This is currently pursuit in a close collaboration with Clondiag Chip technologies, a biotechnology company in Jena.

14.1 Low energy electron point source - LEEPS- microcopy

The key to the LEEPS technology is a coherent electron source of atomic dimension that emits low energy electrons. This allows performing holography in a lens-less setup with the advantages of absence of lens aberrations and high contrast due to the low energy of the electrons. The lack of radiation damage, also due to the low kinetic energy, makes this technique particular appealing for applications in molecular biology. The latter is pursued in the frame of our involvement in the National Center of Competence in Research (NCCR) Nano-Scale Science. In collaboration with Andreas Plckthun's group of the Biochemistry Institute at the University of Zurich, techniques for preparing individual proteins to be investigated by low energy electron holography shall be developed.

An important issue, not only for structural biology, is the ultimate resolution that can be achieved. Preliminary holograms of carbon nanotubes and fibers, taken in late 2002, indicate already a significantly improved interference resolution as evident from the increased number of fringes in the holograms. A detailed distance calibration and a quantitative evaluation of the data are currently in progress. A state of the art CCD detection system has made it possible to gather holograms with a

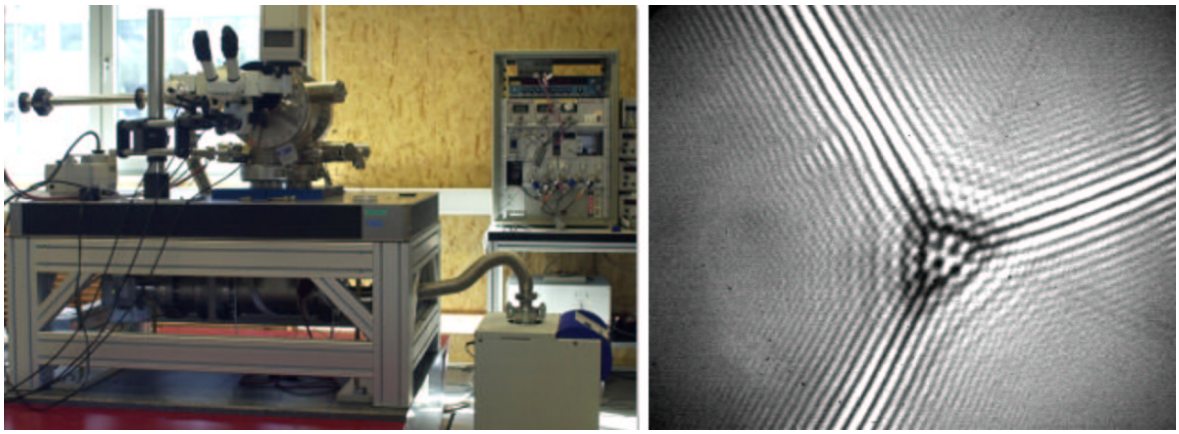

Figure 14.1: *Room temperature LEEPS microscope (left) and holograms of carbon nanotubes taken with 100 eV electrons.*

continuous variation of the kinetic energy by a factor of three. This is an important aspect to eliminate the twin image problem in the numerical reconstruction process and a prerequisite for reaching 3-dimensional real space information.

14.2 Low temperature LEEPS microscopy

Once optimal protection of the coherent wave front is achieved and routinely implemented, intrinsic thermal vibrations will still be present. To freeze in the vibrational modes of molecules, Hiroshi Okamoto has initiated a cryogenic temperature LEEPS microscope project. He started the design and building of a low temperature system in February 2002. Meanwhile, all mechanical and electronic parts, built by our machine- respectively electronic-shop, are completed. Since channel-plates do not operate at low temperature, a new spatial detector for low energy electrons is being developed in the frame of the diploma thesis of Thomas Rusterholz. The testing and assembly of all parts of the low temperature LEEPS are in progress and first results are hoped to show up soon.

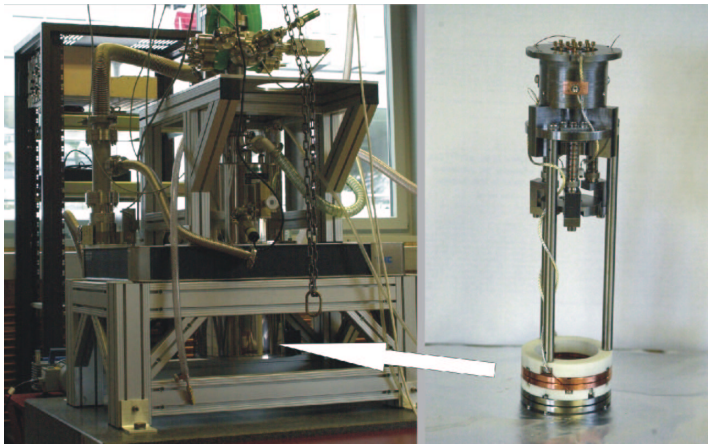

Figure 14.2:
Low temperature (2.5K) LEEPS microscope - Hiroshi Okamoto.

The scientific benefit of a low temperature holographic microscope is not just related to aspects of ultimate resolution. It is also expected to provide new insight into single electron quantum effects since individual elementary charges, respectively their surrounding electric field, can be visualized by coherent low energy electron wave fronts. Thus, at low enough temperature, the dynamics of individual charge transfer processes in single electron devices could be made visible.

14.3 Numerical hologram reconstruction

The second step in holography is concerned with the retrieval of the 3-dimensional shape of the object. Back-propagating the waves from the holographic record, which contains amplitude and phase information, does this. However, back propagating implies replacing the time (t) by (-t) which can -fortunately- not be achieved in real life, but by the use of a computer.

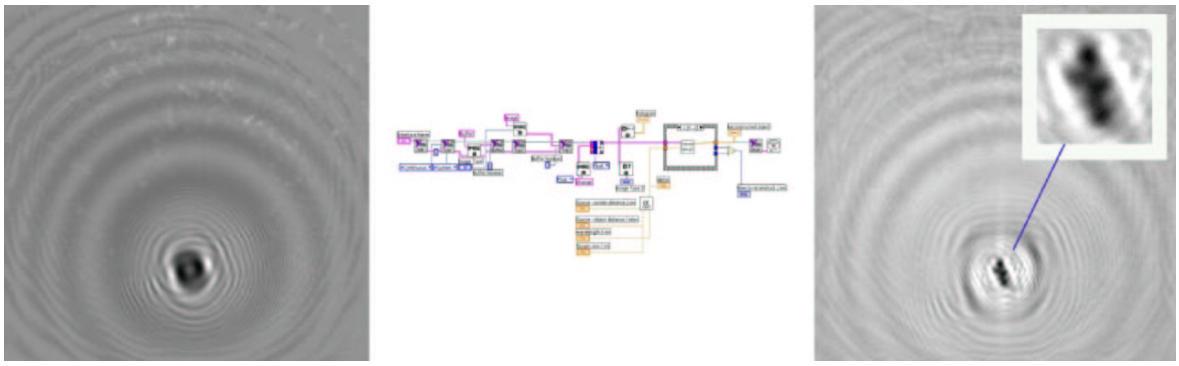

Figure 14.3: *Numerical on-line hologram reconstruction tested here with green Laser light and a sample consisting of 1-micron diameter Latex spheres on a glass plate. The hologram is shown at left. Data acquisition from a CCD system and the numerical reconstruction takes about three seconds before the reconstruction, shown at right is being displayed - Tatiana Latychevskaia.*

Tatiana Latychevskaia has started to work on a project concerning the numerical reconstruction of holograms. The goal is to reach a fast on-line reconstruction routine based on a numerical solution of the Fresnel Kirchhoff Integral. The numerical methods were tested with an optical set-up and it appears that the essential requirements for a fast on-line reconstruction routine can be met.

14.4 Field ion microcopy (FIM)

Atomically sharp tips, which we employ as electron point sources, are shaped by field ion microscopy techniques. Field evaporation is used to create the desired structures by removing one atom at a time in a controlled fashion. A Field Ion Microscope has been completed and became operational in fall of 2002.
At present, the FIM serves mainly as a tool to characterize our electron sources. Its design however is such as to be able to also carry out correlation experiments on a high phase space density ensemble of free electrons to explore their fermion statistics. This project has been pursuit for one year, unfortunately with no success. Thus, it has been stopped in summer 2002.

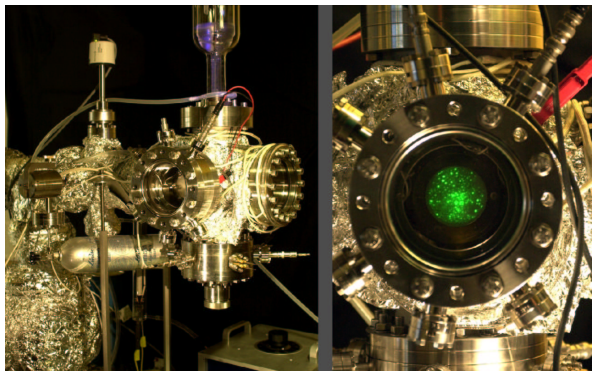

Figure 14.4: *Liquid nitrogen cooled Field Ion Microscope, designed and built by Cornel Andreoli. At right, a helium field ion image of a tungsten tip is shown with atomic resolution.*

14.5 Polymer dynamics

The possibility to control biological molecules in their natural liquid environment appears to be highly desirable for a number of our research goals including the open questions in regards to DNA conductivity. In the course of these efforts some basic questions in polymer physics are also being addressed. The theory of polymer physics, as put forth by Gilles de Gennes, predicts that a coil to stretch transition plays an important role in understanding the properties of these interesting materials. To actually observe this transition and to quantitatively measure its kinetics and energetics on an individual molecular level is an experimental challenge. In Fig.14.5 an experiment of this sort is illustrated. A single DNA molecule, a biopolymer, has been anchored to a surface at one end. Under ordinary thermal conditions, the Brownian agitation drives the system to assume its equilibrium state, a configuration of minimal free energy. In the case of a DNA this configuration is a random coil, the accepted model for this highly flexible polymer. By employing an external force, in our case realized by an electric field, a stretched DNA configuration can be arranged. This is a situation that would hardly ever be observed under equilibrium conditions. By switching off the electric field, the equilibrium situation is re-established almost instantaneously, considering the time-scales relevant for the molecular dynamics. Thus, the stretched polymer configuration evolves again towards its equilibrium configuration, the random coil. By using video microscopy it became possible to measure the relaxation time of a single DNA molecule. Further experiments for improving the data statistics to be carried out at various temperatures should reveal quantitative values for the random coil free energy, that is believed to be made up mainly of an entropy term.

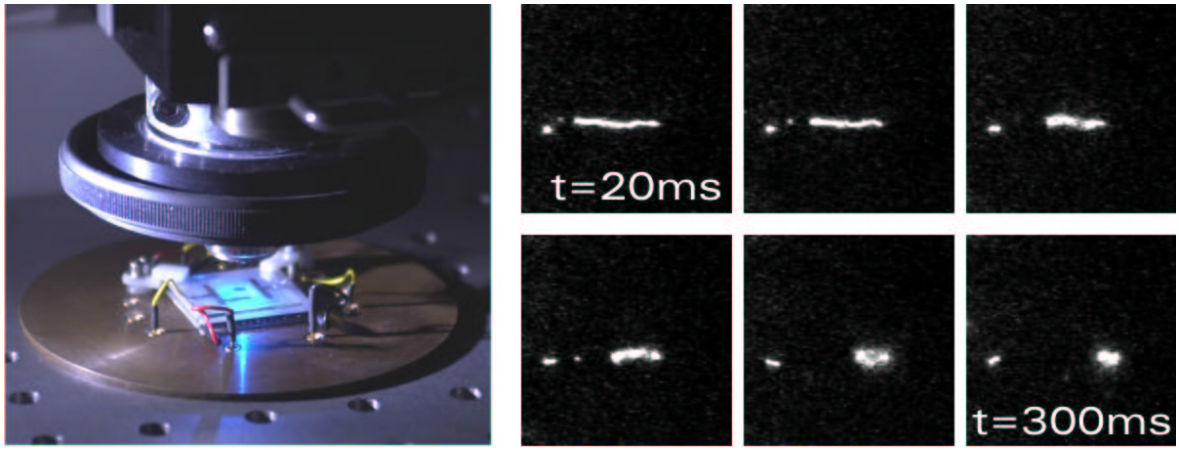

Figure 14.5: *Objective lens and cooling stage of a modified commercial fluorescent microscope are shown at left. The sequence at right shows a single DNA molecule, anchored to a surface at its right end and stretched by an electric field to its contour length of 16 micron. Once the external force is switched of, the molecule assumes its equilibrium configuration. As evident from the above sequence, it is possible to observe the transition from the stretched configuration to the random coil structure at 5 C and thus measure quantitatively the polymer relaxation time - Conrad Escher.*

14.6 Interfacing molecules to micro- and nano-structures

For combining molecules with silicon structures, an understanding of the liquid solid interface is needed. We employ a commercial ESEM microscope, modified by Cornel Andreoli to allow for sample cooling and electrical contacts to the samples, to investigate wet samples.

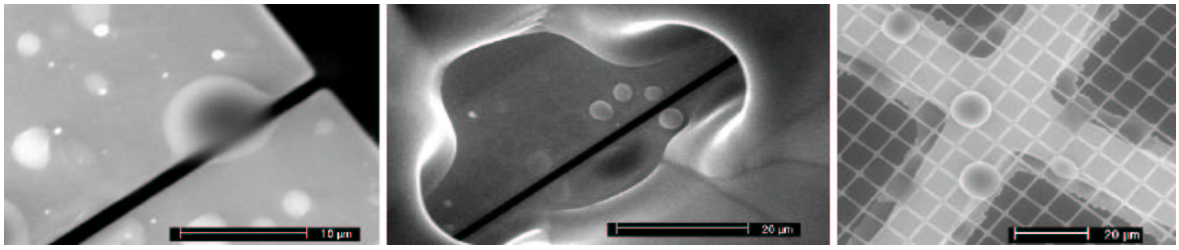

Figure 14.6: *Wetting behaviour of a slit-structure in a silicon nitride membrane, provided by Condiag chip technologies. At right: condensation of water on a micro-machined carbon grit (Quantifoil GmbH).*

The same scanning electron microscope is also used for creating sub-micron structures of freestanding objects. An example of which is shown in Fig.14.7. Gap structures of the order of 10 nm can be produced in this way.

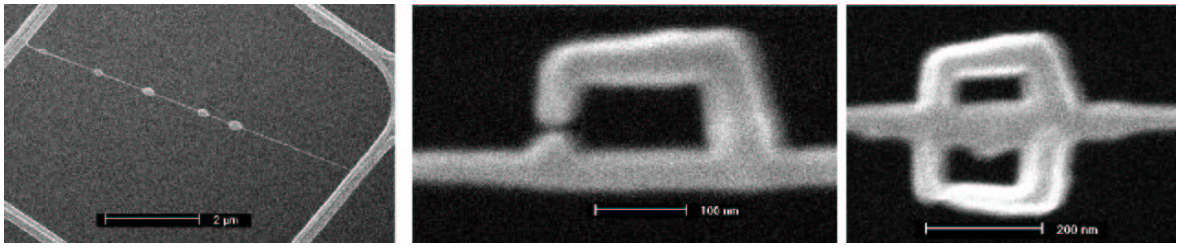

Figure 14.7: *In-situ growth of amorphous carbon structures onto a free-standing carbon single-wall nanotubes rope. Left: About 8 micron long carbon nanotube-rope, as stretched over a grid, and subsequent writing of a structure onto it.*

15 Computer Assisted Physics

C. Bersier, T. Mayer (since Aug. 02), P. F. Meier, E. Olbrich, S. Renold, and E. Stoll

In this report, we want to concentrate on the following research topics:

- Interpretation of the properties of high temperature superconductivity materials using spin-polarized *ab initio* calculations
- Non-linear dynamical study with particular reference to time series analysis of electroencephalograms in collaboration with two groups of the Medical Faculty

We selectively report on the charge distribution in La_2CuO_4 before and after doping (15.1.1), on the calculation of copper chemical shifts in cuprates and re-examination of Knight shift data (15.1.2), and on results of time series analysis of sleep EEG (15.2).

15.1 Electronic structure of high-T_c materials

15.1.1 Charge distribution in $La_{2-x}Sr_xCuO_4$

The parent compounds of high-T_c materials are insulators. This has been rationalized within an ionic model where the state of each atom is described by a formal valence which has an integer value. Thus, for example in La_2CuO_4 these ionic charges are La^{3+}, Cu^{2+}, and O^{2-}, respectively. Upon doping, i.e. when some La^{3+} are substituted by Ba^{2+} or Sr^{2+}, the substance becomes metallic and superconducts below the critical temperature T_c. In the ionic model the missing electrons that are introduced by doping are attributed to the planar oxygens which become O^{1-}. In the terminology of holes it is said that the intrinsic holes are on the coppers and the extrinsic holes due to doping go to the oxygens.

This view, however, is too simplistic. We therefore have performed a detailed analysis of the charge distribution in undoped and doped La_2CuO_4.

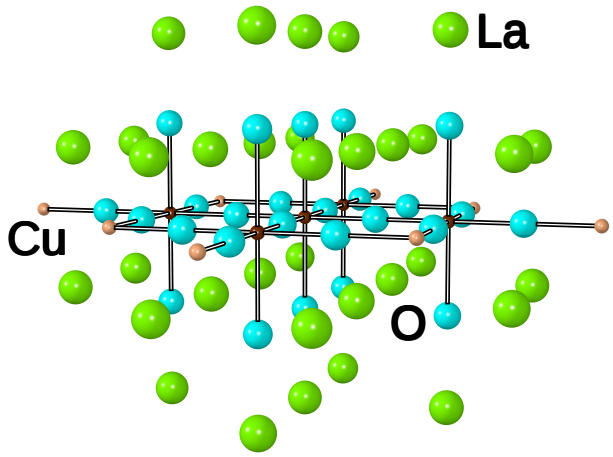

Figure 15.1: *The Cu_5O_{26}/Cu_8La_{34} cluster.*

The results are obtained for the cluster Cu_5O_{26}/Cu_8La_{34} (see Fig. 15.1) which comprises five unpaired electrons calculated with spin multiplicity M=4 which qualitatively corresponds to four spin-down electrons distributed on the four exterior coppers of the cluster and one spin-up electron on the central

copper atom, coinciding with the model of long-range antiferromagnetism observed for La_2CuO_4. The nuclear positions were fixed according to the tetragonal crystal structure. There are five Cu atoms and 26 oxygen atoms in the cluster but for the analysis of charges we select only those atoms at the center of the cluster for consideration. Those atoms close to the periphery of the cluster are not accounted for since these will include effects expected from the cluster edge.

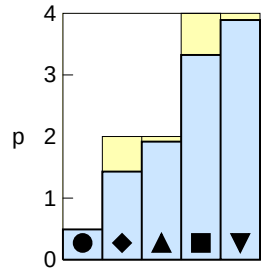

Figure 15.2: *Partial Mulliken populations (tinted blue) of the atomic orbitals for La_2CuO_4: Black symbols denote $4s$ (circles), $3d_{x^2-y^2}$ (diamonds), and $3d_{3z^2-r^2}$ (triangles up), $2 \times p(O_p(2p_\parallel))$ for the planar oxygens (squares), and $2 \times p(O_a(2p_\parallel))$ for the apical oxygens (triangles down). The yellow tinted areas denote the missing charge against the simple ionic model.*

For La_2CuO_4, the Mulliken populations p of the relevant orbitals are $p(3d_{x^2-y^2}) = 1.43$, $p(3d_{3z^2-r^2}) = 1.92$, $p(O_p(2p_\parallel)) = 1.66$, and $p(O_a(2p_\parallel)) = 1.95$ where $O_p(2p_\parallel)$ denotes the atomic orbital (AO) of the planar oxygen pointing towards the two copper neighbors and $O_a(2p_\parallel)$ is the AO of the apical oxygen directed along the z-axis. Note that all other copper $3d$ and oxygen $2p$ orbitals are effectively doubly occupied. These populations are shown in Fig. 15.2. They correspond to an "intrinsic hole content" of about 1.43, which, however, is compensated by the occupancy of the copper $4s$ orbital by $p(4s) = 0.49$.

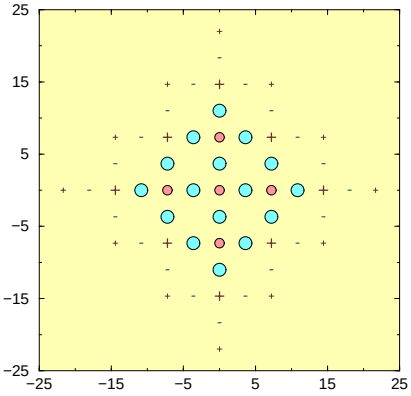

Figure 15.3: *Illustration of the peripheral charge method representing the five copper atoms (red circles), the 16 planar oxygen atoms (blue circles), and additional point charges (+ and − signs). The additional plus signs (brown) are at the locations of copper atoms and the minus signs (blue) at the locations of oxygen atoms. We have tried to indicate the relative magnitude of each charge by the size of the + and - sign symbols.*

Doping is simulated in two ways, firstly by removing an electron from the undoped cluster and changing the multiplicity from M=4 to M=3 and secondly (see Fig. 15.3) by placing additional point charges around the periphery of the cluster (the peripheral charge method).

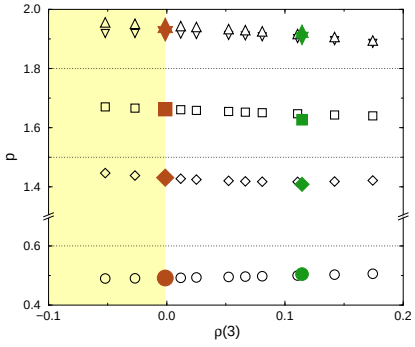

Figure 15.4: *Partial Mulliken populations of the atomic orbitals versus charge $\rho(3)$ for La_2CuO_4: $3d_{3z^2-r^2}$ (triangles down) and $2p_z$ ($O_a(2p_\parallel)$) for the apical oxygens (triangles up), $3d_{x^2-y^2}$ (diamonds) and $2p_\sigma$ ($O_p(2p_\parallel)$) for the planar oxygens (squares), and $4s$ (circles). Empty symbols refer to calculations with the peripheral charge method. The yellow area denotes an electron doped region not accessible by experiments. (The horizontal dotted lines are included to assist visibility.)*

The main interest in this dual treatment of doped clusters is to determine whether the choice of spin state crucially affects the charge distribution. In Fig. 15.4 we present the changes in the partial Mulliken populations as calculated by the peripheral charge method to simulate doping (empty symbols). The quantity $\rho(3)$ is given by $\rho(3) = \rho(\mathrm{Cu}) + 2\rho(\mathrm{O}_p) + 2\rho(\mathrm{O}_a) + 6$ and is interpreted as an approximate estimate of the number of extrinsic holes. It should be zero for the stoichiometric compound. The filled symbols in Fig. 15.4 for $\rho(3) = 0$ and $\rho(3) = 0.12$ refer to calculations on the stoichiometric cluster before and after removal of a single electron respectively. The correspondence of the two methods is surprisingly good if it is remembered that there is no spin state change in the peripheral charge method, that is all symbols refer to the M=4 spin state, whereas the filled symbols for $\rho(3) = 0.12$ refer to the M=3 spin state. Thus, the frequently used simplistic model of doping which solely removes electronic charge from the planar oxygen orbitals ($O_p(2p_{\|})$ is not entirely supported here since these results show that the apical oxygen p orbitals are affected to a similar extent. However the redistribution of charge in the copper orbitals is very significant. It has to be noted that these results are obtained with fixed nuclear positions. A change in the charges, however, invariably will lead to a change in bond lengths. To account for this effect requires extensive calculations which currently are under way.

Electric field gradients (EFG) depend sensitively on the aspherical charge distributions around the target nucleus. Experiments [1; 2] show that in $La_{2-x}Sr_xCuO_4$ the nuclear quadrupole frequency at the copper increases with increasing doping concentration x with a slope of approximately $0.8x$. This variation is partly due to a change in the lattice constant a as has been shown in Ref. [3] where $\mathrm{d}a/\mathrm{d}x \sim -0.2$ Å was estimated. The influence of the size of the lattice constant on the EFG values has been investigated in Ref. [4]. In the following the results for the calculated EFG values have been corrected for this change in a.

Figure 15.5: *Electric field gradients for the central Cu nucleus in La_2CuO_4. The dotted curve denotes ${}^{\mathrm{I}}V_{zz}$, the dashed curve is the sum ${}^{\mathrm{I}}V_{zz}+{}^{\mathrm{II}}V_{zz}$ and the full curve (with diamonds) $V_{zz} = {}^{\mathrm{I}}V_{zz}+{}^{\mathrm{II}}V_{zz}+{}^{\mathrm{III}}V_{zz}+W_{zz}$. Curves refer to calculations with the peripheral charge method and squares refer to calculations without additional point charges. Stars are experimental data [1]. The yellow area denotes an electron doped region not accessible by experiments.*

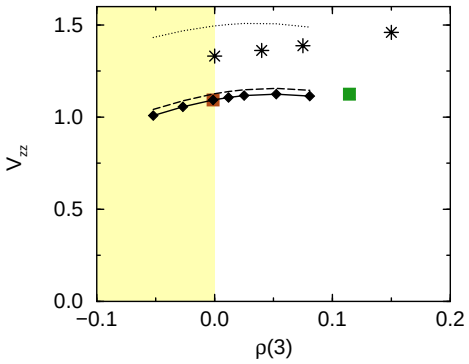

In Fig. 15.5 we represent the main EFG component V_{zz} at the copper as obtained from the simulated doping calculations. The filled squares denote the values obtained without point charges for M = 4 and, at $\rho(3) = 0.12$, for one electron removed and M = 3. The diamonds denote the results obtained with the peripheral charge method, using filled diamonds to emphasize the linear response region. Experimental data [1] for the copper quadrupole frequencies are represented by stars. For La_2CuO_4, the theoretical value is about 15 % smaller than the experiment which in view of the extreme sensitivity of the EFG on the partial occupations is still considered as a good agreement. (A redistribution of Δp of 0.02 electrons from the $3d_{3z^2-r^2}$ to the $3d_{x^2-y^2}$ AO suffices to explain this difference.) The slope of the increase of the calculated EFG with doping, however, reproduces the data astonishingly well for small doping concentrations where the peripheral charge method should be applicable.

A partitioning of the contributions to the EFG tensor V_{ij} of the target nucleus is given in the following

way

$$V_{ij} = {}^{\mathrm{I}}V_{ij} + {}^{\mathrm{II}}V_{ij} + {}^{\mathrm{III}}V_{ij} + W_{ij} \tag{15.10}$$

where the "on-site" term (I) accounts for contributions from basis functions centered at the target nucleus, the term labelled II contains mixed on-site and off-site contributions, and III and W contain purely off-site contributions (see Ref. [5] for further details). In Fig. 15.5 the contribution I is indicated by the dotted line. It is evident that the changes of the total value (full curve) are dominated by the contribution I, i.e. the changes in the partial occupations of the on-site copper orbitals. The dashed line represents the summed contributions from I and II. The difference between the dashed and the full curve thus is the "lattice contribution" ${}^{\mathrm{III}}V_{ij} + W_{ij}$ which is small and not modified upon doping. This result is of particular relevance for the interpretation of NQR data since changes in the nuclear quadrupole frequencies are often analysed in terms of changes in the "lattice contributions". The ab-initio calculations, however, demonstrate [5] that these "lattice contributions" are marginal.

15.1.2 Re-examination of NMR shifts in cuprates

In collaboration with the Department of Physical Chemistry of the University of Geneva we have extended our previous cluster calculations in La_2CuO_4 to calculate and understand the chemical shifts [6]. Chemical shielding tensors have been notoriously difficult properties to calculate with accuracy in the past but recent developments of several state-of-the-art quantum chemical methods have proved encouraging. This has enabled us to monitor the influence of the cluster size, the quality of the basis set used for the description of the atomic orbitals, and the type of gauge invariance on the calculated shielding contributions. These investigations have been used for a critical review of copper Knight shift data in cuprates.

The chemical shielding σ is a measure of the local magnetic field δH at a nucleus produced by the electronic currents under the influence of a homogeneous external magnetic field H_{ext}, i.e. $\sigma = -\Delta H / H_{ext}$. For the determination of the chemical shielding the electronic ground state is calculated and then perturbation theory is used for the induced current density and the magnetic field ΔH.

The electronic ground state is obtained self-consistently using spin-polarized density functional theory for clusters of different sizes with different basis sets formed as linear combinations of atomic orbitals into molecular orbitals (LCAO-MO). Given the ground state the chemical shielding tensor is calculated perturbation theoretically with different standard quantum chemical schemes which differ essentially in the way they choose the gauge for the magnetic field.

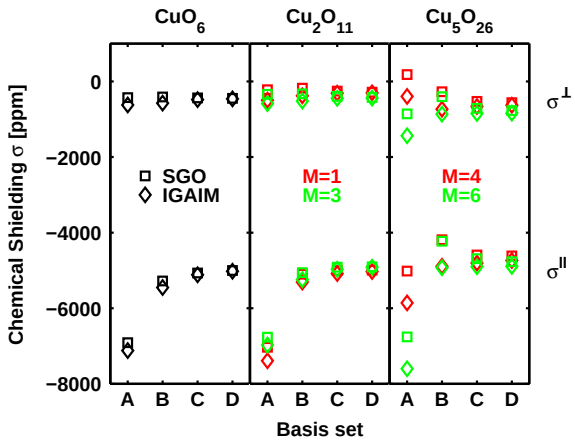

Figure 15.6: *The plot summarizes the results for the in-plane component, $\sigma^{\perp}$, (upper part) and the component parallel to the c-axis, $\sigma^{\parallel}$, (lower part) of the chemical shielding at the copper nucleus in La_2CuO_4. The left (middle, right) panel displays the results in the smallest (intermediate, largest) cluster as a function of basis set quality. The squares and the diamonds distinguish between results obtained with two different quantum chemical schemes. For the two larger clusters, calculations with different electronic spin states (multiplicity M) have been performed. They are distinguished with red and green colors.*

The calculations for the shielding constant at the copper nucleus in La_2CuO_4 [6] are summarized in Fig. 15.6. Both components, $\sigma^{\parallel}$ and $\sigma^{\perp}$, are given for clusters containing one, two, and five copper atoms (named CuO_6, Cu_2O_{11} and Cu_5O_{26}) as a function of basis set size for two different schemes and different spin states (see figure caption). It is seen that for large basis sets (C and D) the shielding become independent on all these parameters and we conclude with the following theoretical values: $\sigma^{\parallel} = -(4800 \pm 300)$ ppm and $\sigma^{\perp} = -(600 \pm 300)$ ppm.

To compare the obtained shielding constants in La_2CuO_4 to experiments one has to take into account that the measured Knight shifts are in fact differences of resonance frequencies between a target and a reference substance which - in the case of copper NMR - is the monovalent copper in CuCl. We have therefore repeated the calculations for a cluster representing CuCl.

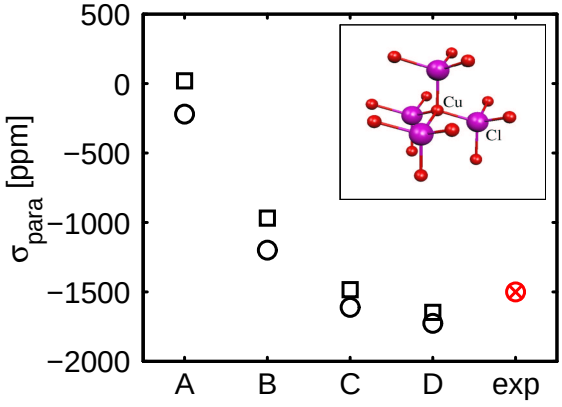

Figure 15.7: *Paramagnetic part of the shielding constant at the copper nucleus in the reference substance CuCl as a function of basis set size with quality increasing from A to D. On the right, the experimental result [7] is indicated in red. The inset shows the used cluster.*

In Fig. 15.7 the paramagnetic part of the isotropic component of the shielding tensor is given as a function of the basis set for two schemes, SGO and IGAIM. It is seen that for increasing basis set quality the results become independent on the schemes and converge to a value of $\sigma_{para} = -1700$ ppm. Its absolute value is comparable to the diamagnetic shielding of $\sigma_{dia} = 2400$ ppm.

First, we were quite surprised to get such a substantial paramagnetic contribution to the shielding constant but we then figured out that in 1978 already, NMR chemists compared the shielding of copper in the free copper ion (with - by symmetry - no paramagnetic contribution) to those in various copper compounds and found a paramagnetic shielding in CuCl of $\sigma_{para} = -1500$ ppm [7]. Thus, our theoretical result is in good agreement with the experimental value.

This result has serious consequences. The experimental data for cuprates have been explained using a perturbation theoretical formula for the paramagnetic shielding. If the reference substance itself has a substantial paramagnetic contribution to the shielding constant this formula must not be applied to the measured shifts. For a correct comparison between theory and experiment the experimental chemical shifts have to be corrected for the paramagnetic shielding of the reference substance.

We therefore suggest to use a new terminology in NMR, the paramagnetic field modification $\overline{K}_L(t) = -\sigma_{para}(t) = K_L(t-r) - \sigma_{para}(r)$, being the magnetic shift of the target with respect to the reference substance $(t-r)$ corrected for the paramagnetic shielding of the reference substance (r). This quantity has the important advantage that it is independent of the reference substance. For further details, see [6].

The Knight shift is the relative difference of the resonance frequencies of a particular nuclear magnetic moment in the target substance and in an arbitrary reference substance. It can be divided into a temperature independent chemical shift arising from the non-itinerant electrons and a spin shift arising from the electrons in the conduction band. It is assumed that the spin contribution in the superconducting state gradually vanishes as temperature is decreased due to more and more electrons

being bound in Cooper pairs. Hence, the chemical shift is identified as the magnetic shift at lowest temperatures. The connection to the shielding is as follows: the chemical shift is the difference between the shielding in the reference and the target substance.

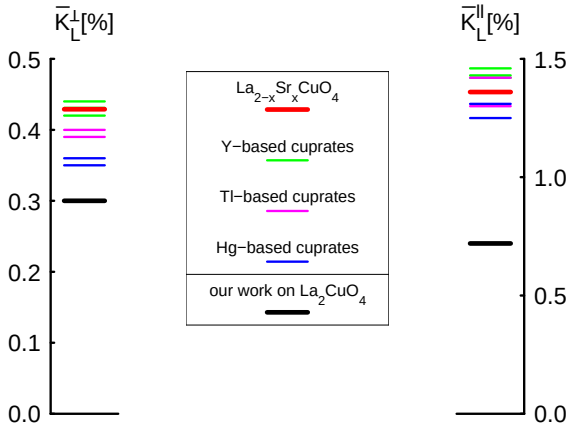

Figure 15.8: *A comparison between theoretical values in La_2CuO_4 (black) and experimental values in $La_{2-x}Sr_xCuO_4$ (red) and in various other high temperature superconducting cuprates. The left (right) side shows the paramagnetic field modification for the applied field in the plane (along the c-axis).*

In Fig. 15.8 the theoretical values for the paramagnetic field modifications (black) are compared to values extracted from experiments in the La-compound (red) and in other high-temperature superconducting cuprates. For the perpendicular component of the paramagnetic field modification the theoretical values are smaller but still in reasonable agreement with experiment. However, for the component parallel to the crystallographic c-axis there is a large discrepancy between theory and experiment. We presently investigate various explanations for this disagreement. First, we note that Zheng, *et al.*, have measured the copper magnetic shifts both in $YBa_2Cu_4O_8$[8] and in $TlSr_2CaCu_2O_{6.8}$[9] and found that they are unexpectedly appreciably field dependent and decrease with decreasing magnetic field. A correct comparison of theory and experiment, however, requires the extrapolation to zero field. Second, we emphasize that impurities in the sample lead to a non-vanishing spin contribution to the magnetic shifts even at lowest temperatures.

15.2 Time series analysis of EEG

In the previous year we continued our research on nonlinear time series analysis of EEG, which is conducted in collaboration with the institute of pharmacology and toxicology and the neurological clinic. As a next step in unravelling the character of the dynamics of the EEG we focused our research on the relationship between nonlinearity and nonstationarity. By performing a surrogate data analysis one can test, how likely the time series under study was produced by a linear system. However, if the null hypothesis is rejected this can be not only due to nonlinearity but also due to nonstationarity. We studied the question, whether the nonlinear signatures observed in the human sleep EEG previously [10] are due to a stationary nonlinear dynamics or rather are caused by nonstationary linear dynamics.

We found, that short segments of human sleep EEG with a duration ≤ 1 s are well described by linear models such as autoregressive (AR)-models and show no significant nonlinearity, while the rejection of the linearity hypothesis for longer segments can be explained by the temporal dynamics of the coefficients of these linear models. It turned out that the magnitude of their variations depends on the sleep stages. They are strongest in light sleep and less strong in slow wave and non-REM sleep.

Studying the dynamics of the coefficients of the AR-models allows to define oscillatory events, because the dynamics of an AR(p)-model is composed of m relaxators and n harmonic oscillators with $p = m + 2n$. The frequencies f_k and the damping coefficients γ_k are related to the complex poles

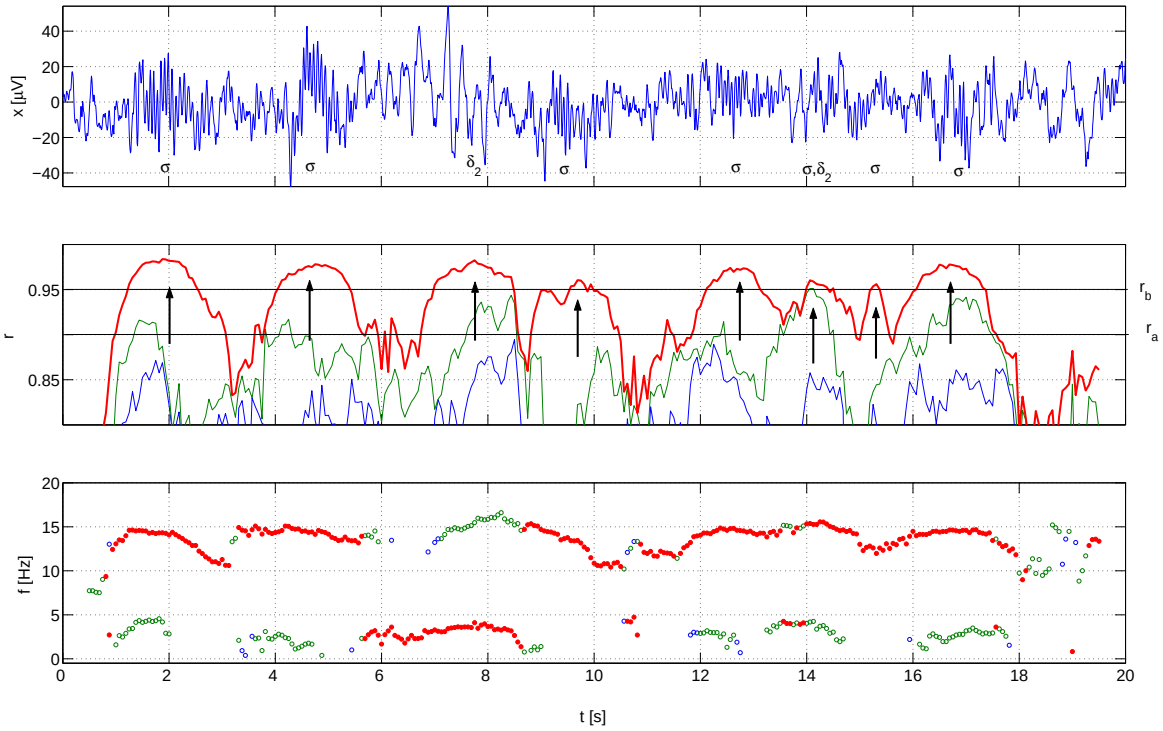

Figure 15.9: *EEG data (upper panel) with oscillatory events marked by arrows, σ-spindles and δ_2-fast delta waves. The time course of r_k and the corresponding frequencies f_k are shown in the lower panels. The pole with lowest damping is indicated by the bold red line and filled circles, the poles with the second and third lowest damping by the green and blue lines and circles, respectively.*

$z_k = r_k \exp(i\phi_k)$ of the AR-model by $f_k = (2\pi\Delta)^{-1}\phi_k$ and $\gamma_k = -\Delta^{-1} \ln r_k$ with Δ denoting the sampling time. An oscillatory event is detected, whenever the absolute value of a pole exceeds a predefined threshold r_a as illustrated in Fig. 15.9. In the shown segment both sleep spindles (marked by σ) and fast delta waves (denoted as δ_2) were detected. It turned out that this algorithm is a reliable detector for sleep spindles and, furthermore, also for alpha waves, as well as for fast and slow delta waves. Because the algorithm is model based and not a pattern recognition algorithm, it might help to identify the dynamical processes leading to the occurrence of spindles or other oscillatory events in the sleep EEG.

[1] T. Imai, C. P. Slichter, K. Yoshimura, and K. Kosuge, Phys.Rev.Lett.**70**, 1002 (1993).

[2] S. Ohsugi, Y. Kitaoka, K. Ishida, G. Zheng, and K. Asayama, J. Phys. Soc. Jpn. **63**, 700 (1993).

[3] R. L. Martin, Phys.Rev.Lett.**75**, 744 (1995).

[4] S. Renold and P. F. Meier, J. of Superconductivity, in print.

[5] E. P. Stoll, T. A. Claxton, and P. F. Meier, Phys.Rev.B, **65**, 064532 (2002).

[6] S. Renold, T. Heine, J. Weber, and P. F. Meier, Phys.Rev.B **67**, 024501 (2003).

[7] O. Lutz, H. Oehler, and P. Kroneck, *Z. Phys. A*, **288**, 17 (1978).

[8] G.-q. Zheng, W. G. Clark, Y. Kitaoka, K. Asayama, Y. Kodama, P. Kuhns, and W. G. Moulton, Phys.Rev.B **60**, R9947 (1999).

[9] G.-q. Zheng, H. Ozaki, Y. Kitaoka, P. Kuhns, A. P. Reyes, and W. G. Moulton, Phys.Rev.Lett.**88**, 077003 (2002).

[10] Y. Shen, E. Olbrich, P. Achermann, and P. F. Meier, *Clin. Neurophysiol.*, **114**, 199-209 (2003).

16 Mechanical Workshop

K. Bösiger, B. Schmid, B. Lussi (since May 2002), M. Schaffner, Y. Steiger (left the workshop in June 2002), P. Treier, B. Wachter, Ramon Caro (apprentice) and A. Rochat (apprentice)

The modern infrastructure of our mechanical workshop helps us solve demanding problems both for the in-house projects presented in this report and for some projects from other institutes of our university. Over 30 institutes again made use of the metal and other technical material supply stores maintained by the shop[4]. A small fraction of our activities was devoted to special designs, modifications and small series for outside companies. This work is charged and provides some income.

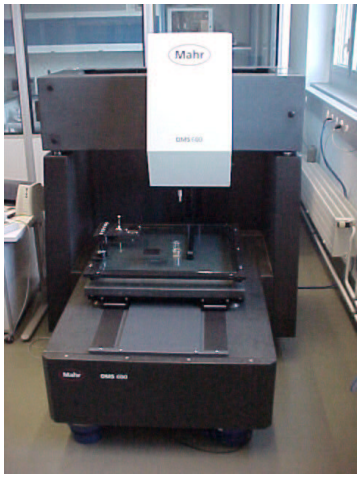

Figure 16.1: *The new coordinate measuring system in the air-conditioned clean room of the institute.*

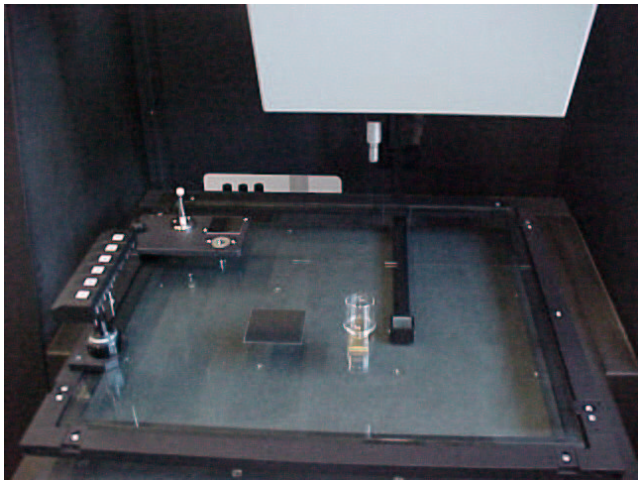

Figure 16.2: *Detailed view of the glass surveying table with two measuring samples.*

Last year the workshop equipment was supplemented by a MAHR OMS 600 coordinate measuring system from which many projects may benefit enormously. The instrument allows precise ($1.5\,\mu$m) mechanical and optical (with a video and a laser system) surveying of mechanical parts with dimensions up to $650 \times 600 \times 300$ mm^3.

A selection of our projects is listed below:

- *CMS pixel detector (Group Amsler, see Section 11)*
  For the production of the support structure for the CMS pixel detector all the necessary tools were produced. Additional laser welding tests were performed in close collaboration with an outside company. Some modifications and better tools for the welding process led to nice results. A full support structure segment is now being prepared for cooling and stability tests.

- *LHCb inner tracking detector (Group Straumann, see Section 9)*
  Cooling balconies made of different materials were manufactured to study the specific characteristics. In addition test stands and other small parts were produced.

- *Surface Physics (Group Osterwalder, see Section 13)*
  For this group the priorities were repair and maintenance work.

[4]For a catalogue see http://www.physik.unizh.ch/groups/ werkstatt/dienstleistung.html

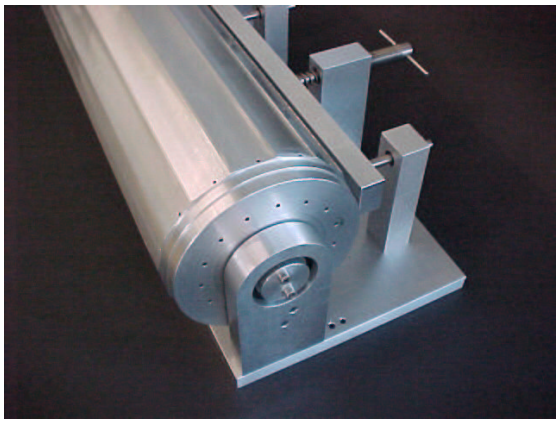

Tool used to produce the support structure for the middle layer of the CMS pixel detector.

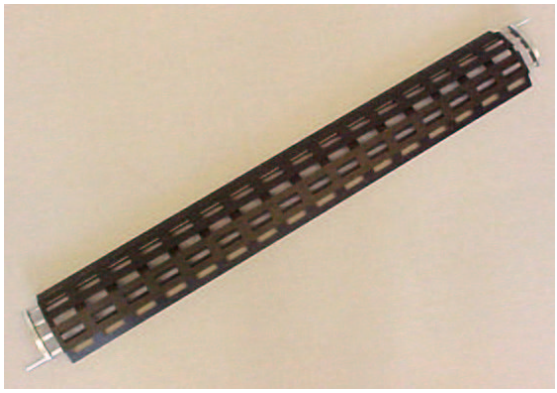

Completed segment of the pixel detector support structure.

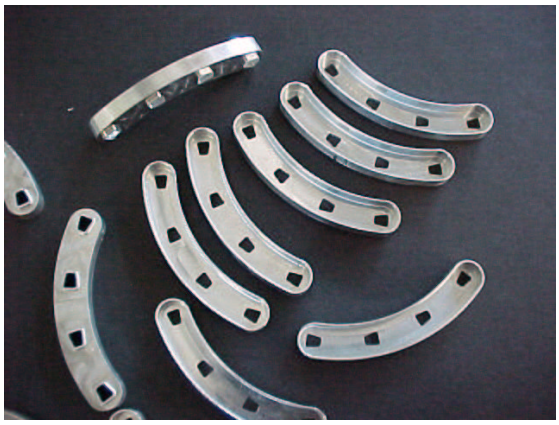

Open aluminum cooling containers after the difficult machining.

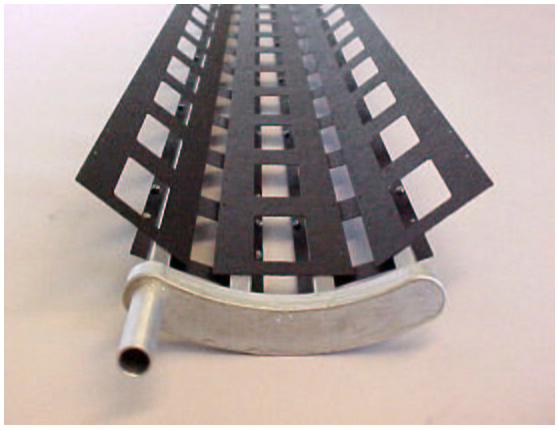

End view of the support and cooling structure. The aluminum parts are connected by laser welding.

Figure 16.3: *Pictures from the CMS pixel project.*

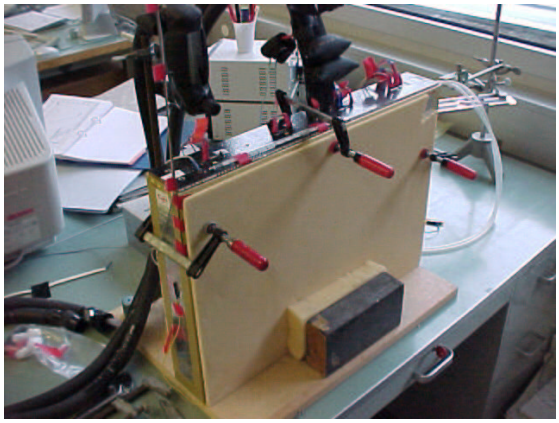

Isolating detector box made out of polyurethane during the cooling test.

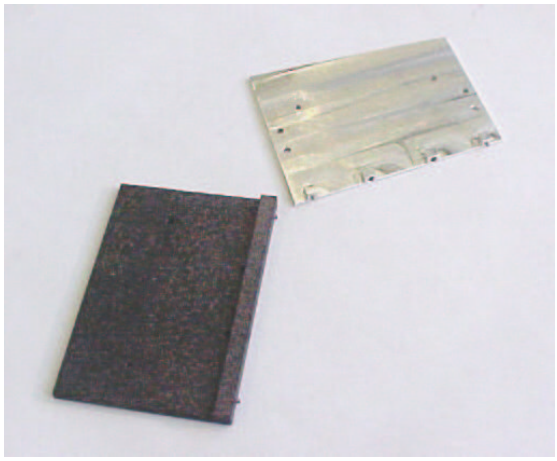

Two cooling balcony prototypes made out of aluminum and carbon fiber composite.

Figure 16.4: *Pictures from parts of the LHCb inner tracker.*

- *Physics of Biological Systems (Group Fink, see Section 14)*
  Different structures for the experiments and test stands were manufactured.

- *Rack for the CPU cluster of the institute for theoretical physics*
  A rack was designed and built which carries the 144 dual processor motherboards with all the necessary power supplies and hard disks. The quadratic tower which contains the full equipment has a side length of 1.70 m and a height of 1.85 m.

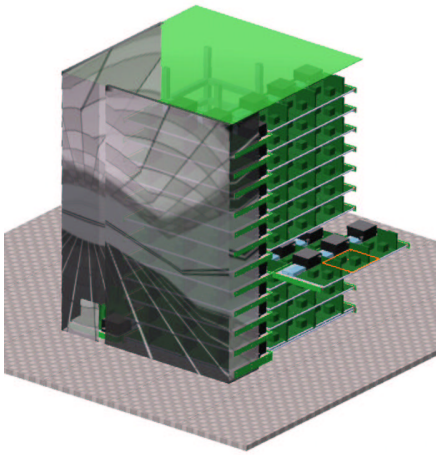

Isometric view of the rack for the computer cluster.

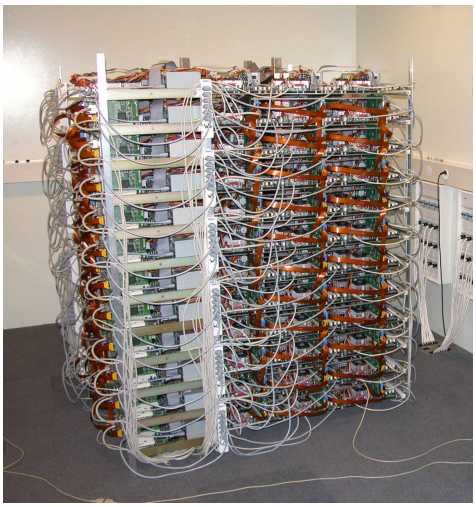

The rack after the installation of all nodes. The rack will be covered to guarantee proper cooling.

Figure 16.5: *Pictures of the computer rack.*

- *Apprentice exam work*
  The candidates produce workpieces that will be used eventually, such as a circular saw with diamond blade to be used in the workshop afterwards. For the instructors this means more preparation work although it allows more flexibility as well. During the early stages of the projects the apprentices participate in discussions and preparations. They now do the exam work in the home workshop which has the advantage that the work is done in their familiar environment with well known equipment. The time for the production of the parts varies between 24 and 120 hours. The exam is completed with an oral presentation followed by a discussion with the examinator.

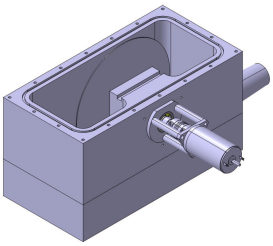

Housing for the circular saw with sawing table removed.

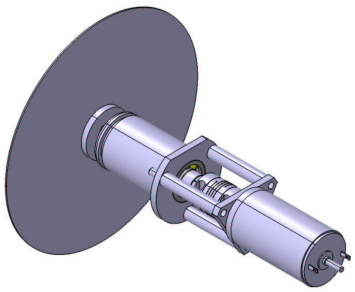

Motor and drive for the diamond saw.

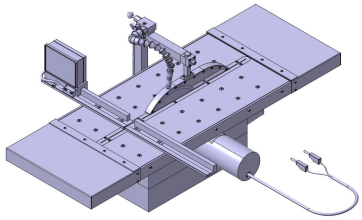

View of the completed circular saw.

Figure 16.6: *Pictures from the apprentice examination work.*

17 Electronics Workshop

W. Fässler, H.P. Meyer, P. Soland, K. Szeker

All research groups presented in this report require the electronics workshop for maintenance and repair of their electronic equipment. If necessary the repair in the official service centers is organized. Besides modifications to existing modules and construction of simple circuitry for the various laboratories the main effort went into the following three projects:

- We designed and manufactured trigger modules for the H1 CIP upgrade (Group Straumann and Truöl, see Section 6.2.2) and the LHCb experiment (Group Straumann, see Section 9). We were also involved in the production of the new series of CIP readout electronics.
- For the laboratory of Physics of Biological Systems (Group Fink, see Sec.14) we designed and built several modules which are used to control the experiments. Some of them are shown below.
- Another interesting project in which the electronics workshop is engaged is the replacement of equipment used for demonstration experiments in the lecture halls. In close collaboration with L. Pauli and J. Seiler who are responsible for the preparation of these experiments we are about to replace the ancient equipment with a computer controled system with associated interface electronics. This new system is very flexible and the experiments and the measured data can be presented in a more transparent fashion.

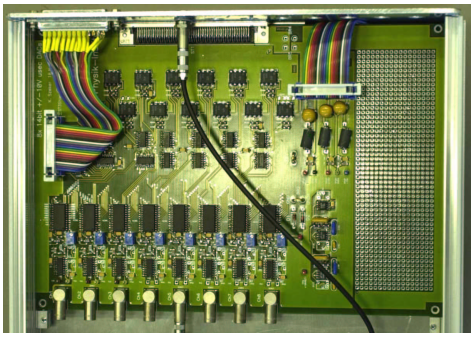

Digital to analog converter (8 $\times$ 14 bit) used for the piezo drive in the Physics of Biological Systems laboratory.

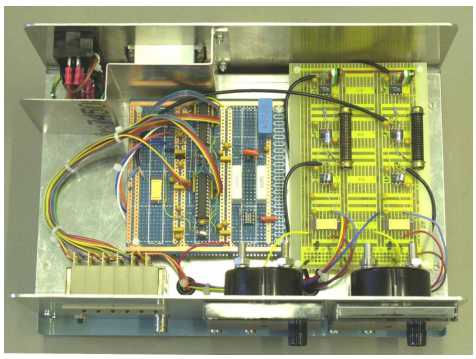

Digital to analog converter module which adds a programmable offset voltage in the range of ± 10 V to a given input level.

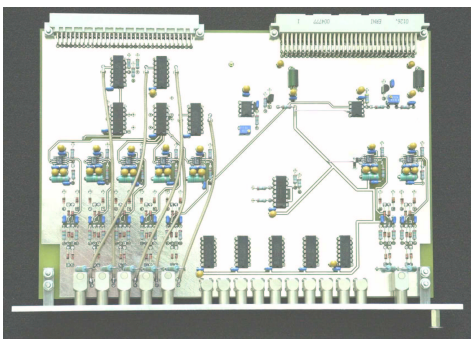

STC trigger card for the H1 experiment.

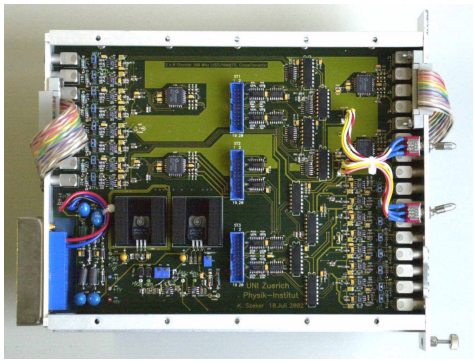

LVDS, TTL and NIM signal cross converter module.

Figure 17.1: *Some modules produced in the electronic workshop*

18 Publications

18.1 Research group of Prof. C. Amsler

Articles

- *A new measurement of the $\bar{\nu}_e e^-$ elastic cross section at very low energy*
  C. Amsler et al. (MUNU collaboration), Phys.Lett.B 545 (2002) 57.
- *Sub MeV particles detection and identification in the MUNU detector*
  M. Avenier et al. (MUNU collaboration), Nucl.Instr.Meth.A 482 (2002) 408.
- *Production and detection of cold antihydrogen atoms*
  M. Amoretti et al. (ATHENA collaboration), Nature 419 (2002) 456.
- *Non-$q\bar{q}$ mesons*
  C. Amsler, Phys.Rev.D 66 (2002) 010001-754.
- *The η(1440), f_1(1420), and f_1(1510)*
  M. Aguilar-Benitez, C. Amsler and A. Masoni, Phys.Rev.D 66 (2002) 010001-493.
- *Comment on "Protonium annihilation into $\pi^0\pi^0$ at rest in a liquid hydrogen target"*
  C. Amsler et al. (Crystal Barrel collaboration), Phys.Rev.D 66 (2002) 058101.
- *Further evidence for a large glue component in the $f_0(1500)$ meson*
  C. Amsler, Phys.Lett.B 541 (2002) 22.
- *Review of Particle Physics*
  K. Hagiwara et al. (Particle Data Group), Phys.Rev.D 66 (2002) 010001.
- *Particle data booklet*
  K. Hagiwara et al. (Particle Data Group), AIP pub. 72 (2002).
- *Upgrade of the ATHENA Detector with Avalanche Photodiodes and Quantum Efficiency Measurements at Cryogenic Temperatures*
  A. Glauser, Diplomarbeit, Universität Zürich, 2003.
- *A high resolution silicon beam telescope*
  C. Amsler et al., Nucl.Instr.Meth.A 480 (2002) 501.
- *Temperature dependence of pure CsI: scintillation light yield and decay time*
  C. Amsler et al., Nucl.Instr.Meth.A 480 (2002) 494.
- *Meson Resonances in Proton-Antiproton Annihilation*
  C. Amsler, Proc. Int. Conf. on the Structure and Interactions of the Photon (PHOTON 2001), Ascona, World Scientific (2001) 253.
- *The Atlas and CMS trackers*
  T. Speer, Proc. 5th Int. Conf. on Hyperons, Charm and Beauty Hadrons, Vancouver (2002), Nucl.Phys.B (Proc. Suppl.) 115 (2003) 318 .
- *Tracking in CMS : software framework and tracker performance*
  A.I. Khanov, M. Lenzi, T. Todorov, T. Speer, P. Vanlaer and M. Winkler, Nucl.Instr.Meth.A 478 (2002) 460.

Articles in press

- *Annihilation at rest of antiprotons and protons into neutral particles*
  C. Amsler et al. (Crystal Barrel Collaboration), Phys.Lett.B.

- *Positron plasma diagnostics and temperature control for antihydrogen production*
  M. Amoretti et al. (ATHENA collaboration), Phys.Rev.Lett.

- *Light exotic mesons*
  C. Amsler, Proc. Quark Confinement and the Hadron Spectrum V, Gargnano, 2002, World Scientific.

- *A cryogenic silicon microstrip and pure-CsI detector for detection of antihydrogen annihilations*
  C. Regenfus, Proc. Int. Workshop (Vertex 2001), Brunnen, Nucl.Instr.Meth.A.

- *Detection of antihydrogen annihilations with a cryogenic pure-CsI detector*
  C. Regenfus, C .Amsler, A. Glauser, D. Grögler, D. Lindelf, H. Pruys, Proc. of "New developments in photodetection", Beaune 2002, Nucl.Instr.Meth.A.

- *Development of APD readout for pure-CsI crystals at cryogenic temperatures*
  A. Glauser, Proc. of "New developments in photodetection", Beaune 2002, Nucl.Instr.Meth.A.

- *New Developments in Vertex Reconstruction for CMS*
  R. Frühwirth, K. Prokofiev, T. Speer, P. Vanlaer and W. Waltenberger, Nucl.Instr.Meth.A.

Invited lectures

- C. Amsler: *New results in proton-antiproton annihilation and the status of glueballs*
  Seminar, Università di Genova, 19.4.02.

- C. Amsler: *The spectrum of light quark-antiquark mesons*
  Università degli Studi di Pavia, 17.4, 18.4 and 23.4.02.

- C. Amsler: *New results in proton-antiproton annihilation and the status of glueballs*
  Seminar, Helsinki University, 27.8.02.

- C. Amsler: *Light exotic mesons*
  Invited talk, Quark Confinement and the Hadron Spectrum V, Gargnano, 12.9.02.

- C. Amsler: *Experimental evidence for a large glue content in the $f_0(1500)$ meson*
  Invited talk, Aspects of confinement and nonperturbative QCD, ECT* Center, Trento, 14.3.03.

- C. Amsler: *Glueballs and other exotic mesons*
  Seminar, Universität Basel, 16.01.03.

- O. Link: *The MUNU experiment*
  Contributed talk, Workshop on large TPC for low energy rare event detection, 5.12.02.

- N. Madsen: *First production of cold antihydrogen*
  Seminar, Center for Ultracold Atoms, MIT, Cambridge, USA, 15.10.02.

- C. Regenfus: *Detection of antihydrogen atoms in the ATHENA experiment with a cold Si-μ-strip and pure CsI detector*
  Seminar, PSI, 26.4.02.

- C. Regenfus: *First production and detection of cold antihydrogen*
  Seminar, Universität Basel, 31.10.02.

- C. Regenfus: *Production of cold antihydrogen atoms in large quantities*
  Plenary talk, Frühjahrstagung der DPG, Aachen, 13.03.03.

- T. Speer: *The ATLAS and CMS Trackers*
  Invited talk, 5th Int. Conf. on Hyperons, Charm and Beauty Hadrons, Vancouver, 28.06.03.

ATHENA Collaboration (2002)

M. Amoretti, C. Amsler, G. Bonomi, A. Bouchta, P. Bowe, C. Carraro, C. L. Cesar, M. Charlton, M. J. T. Collier, M. Doser, V. Filippini, K. S. Fine, A. Fontana, M. C. Fujiwara, R. Funakoshi, P. Genova, J. S. Hangst, R. S. Hayano, M. H. Holzscheiter, L. V. Joergensen, V. Lagomarsino, R. Landua, D. Lindelöf, E. Lodi Rizzini, M. Macri, N. Madsen, G. Manuzio, M. Marchesotti, P. Montagna, H. Pruys, C. Regenfus, P. Riedler, J. Rochet, A. Rotondi, G. Rouleau, G. Testera, A. Variola, T. L. Watson, D. P. van der Werf

MUNU Collaboration (2002)

C. Amsler, M. Avenier, C. Broggini, J. Busto, C. Cernac, Z. Daraktchieva, G. Gervasio, P. Jeanneret, G. Jonkmans, D.H. Koang, J. Lamblin, D. Lebrun, O. Link, F. Ould-Saada, G. Puglierin, A. Stutz, A. Tadsen, J.L. Vuilleumier

CRYSTAL BARREL Collaboration (2002)

C. Amsler, C. A. Baker, B. M. Barnett, C. J. Batty, M. Benayoun, P. Blüm, K. Braune, D. V. Bugg, T. Case, V. Credé, K. M. Crowe, M. Doser, W. Dünnweber, D. Engelhardt,M. A. Faessler, R. P. Haddock, F. H. Heinsius, M. Heinzelmann, N. P. Hessey, P. Hidas, D. Jamnik, H. Kalinowsky, P. Kammel, J. Kisiel, E. Klempt, H. Koch, M. Kunze, U. Kurilla, R. Landua, H. Matthäy, C. A. Meyer, F. Meyer-Wildhagen, R. Ouared, K. Peters, B. Pick, M. Ratajczak, C. Regenfus, J. Reinnarth, W. Roethel, A. Sarantsev, S. Spanier, U. Strohbusch, M. Suffert, J. S. Suh, U. Thoma, I. Uman, S. Wallis-Plachner, D. Walther, U. Wiedner, K. Wittmack, and B. S. Zou

PARTICLE DATA Group (2002)

K. Hagiwara, K. Hikasa, K. Nakamura, M. Tanabashi, M. Aguilar-Benitez, C. Amsler, R.M. Barnett, P.R. Burchat, C.D. Carone, C. Caso, G. Conforto, O. Dahl, M. Doser, S. Eidelman, J.L. Feng, L. Gibbons, M. Goodman, C. Grab, D.E. Groom, A. Gurtu, K.G. Hayes, J.J. Hernandez-Rey, K. Honscheid, C. Kolda, M.L. Mangano, D.M. Manley, A.V. Manohar, J. March-Russell, A. Masoni, R. Miquel, K. Mönig, H. Murayama, S. Navas, K.A. Olive, L. Pape, C. Patrignani, A. Piepke, M. Roos, J. Terning, N.A. Törnqvist, T.G. Trippe, P. Vogel, C.G. Wohl, R.L. Workman, W.-M. Yao

18.2 Research group of Prof. H. Keller

Articles

- *Oxygen isotope effect of the plane-copper NQR frequency in* $YBa_2Cu_4O_8$
  M. Mali, J. Roos, H. Keller, J. Karpinski, K. Conder, Phys.Rev.B **65**, 184518-1-6 (2002).

- *Temperature and field dependence of the anisotropy of* MgB_2
  M. Angst, R. Puzniak, A. Wisniewski, J. Jun, S.M. Kazakov, J. Karpinski, J. Roos, H. Keller, Phys.Rev.Lett.**88**, 167004-1-4 (2002).

- *Competition between anisotropy and superconductivity in organic and cuprate superconductors*
  T. Schneider, Europhys. Lett. **60**, 141-147 (2002).

- *On the magnetic and superconducting properties of* $Ru_{1-x}Sr_2RECu_{2+x}O_{8-\delta}$*, RE=Gd, Eu, compounds*
  P.W. Klamut, B. Dabrowski, S.M. Mini, S. Kolesnik, M. Maxwell, A. Shengelaya, R. Khasanov, H. Keller, I. Savic, C. Sulkowski, M. Matusiak, A. Wisniewski, R. Puzniak, and I. Fita, J. Appl. Phys. **91**, 7134-7136 (2002).

- *Superconductivity and Magnetism in Pure and Substituted* $RuSr_2GdCu_2O_8$
  B. Dabrowski, P.W. Klamut, M. Maxwell, S.M. Mini, S. Kolesnik, J. Mais, A. Shengelaya, R. Khasanov, H. Keller, C. Sulkowski, D. Wlosewicz, M. Matusiak, J. Supercond. **15**, 439-445 (2002).

- *Clues obtained from the oxygen isotope effect on NMR/NQR parameters Observed in* $YBa_2Cu_4O_8$
  M. Mali, J. Roos, H. Keller, A.V. Dooglav, Y.A. Sakhratov, A.V. Savinkov, J. Supercond. **15**, 511-515 (2002).

- *Vortex motion in type-II superconductors probed by muon spin rotation and small-angle neutron scattering*
  D. Charalambous, P.G. Kealey, E.M. Forgan, T.M. Riseman, M.W. Long, C. Goupil, R. Khasanov, D. Fort, P.J.C. King, S.L. Lee, and F. Ogrin, Phys.Rev.B**66**, 054506-1-4, (2002).

- *On the macroscopic* s- *and* d-*wave symmetry in cuprate superconductors*
  K.A. Müller, Philosophical Magazine **82**, 279-288 (2002).

- *High-temperature superconductors: Results and relations*
  K.A. Müller, Appl. Phys. **A** 74 [Suppl.], S1641S1644 (2002).

- *Implantation studies of keV positive muons in thin metallic layers*
  E. Morenzoni, H. Glöckler, T. Prokscha, R. Khasanov, H. Luetkens, M. Birke, E.M. Forgan, Ch. Niedermayer, and M. Pleines, Nucl.Instr.Meth.B**192**, 254 266 (2002).

- *Oxygen stoichiometry and isotope effect in* $La_{1-x}Ca_xMnO_{3+\delta}$
  K. Conder, Guo-meng Zhao, R. Khasanov, Phys.Rev.B**66**, 212409-1-4 (2002).

- *Oxygen-isotope effects on local structure distortions and transport properties of epitacial thin films of* $Nd_{067}Sr_{033}MnO_3$
  R.P. Sharma, Guo-meng Zhao, D.J. Kang, M. Robson, H. Keller, H.D. Drew, T. Venkatesan, Phys.Rev.B **66**, 214411-1-4 (2002).

- *Superparamagnetism in Heterogeneous AgFe thin films - A Low Engergy SR Study*
  T.J. Jackson, E.M. Forgan, T.M. Riseman, H. Glückler, E. Morenzoni, T. Prokscha, H.P. Weber, Ch. Niedermayer, M. Pleines, G. Schatz, J. Litterst, H. Luetkens, H. Keller, R. Khasonov, T.S. Rong, C. Binns, Hyperfine Interactions **136/137**, 403-408 (2002).

- *Influence of Impurities on Short Range Electron Transport in GaAs*
  D.G. Eshchenko, V.G. Storchak, J.H. Brewer, and R.L. Lichti, Phys.Rev.Lett.**89**, 226601 (2002).

- *Excess electron transport and delayed muonium formation in condensed rare gases*
  D.G. Eshchenko, V.G. Storchak, J.H. Brewer, G.D. Morris, S.P. Cottrell, and S.F.J. Cox, Phys.Rev.B **66**, 035105 (2002).

- *Anisotropy of the superconducting state properties and phase diagram of* $\mathrm{MgB_2}$ *by torque magnetometry on single crystals*
  M. Angst, R. Puzniak, A. Wisniewski, J. Roos, H. Keller, P. Miranović, J. Jun, S.M. Kazakov, J. Karpinski, Physica C **385**, 143-153 (2003).

- *The oxygen-isotope effect on the in-plane penetration depth in underdoped* $\mathrm{Y}_{1-x}Pr_xBa_2Cu_3O_{7-\delta}$ *as revealed by muon-spin rotation*
  R. Khasanov, A. Shengelaya, K. Conder, E. Morenzoni, I.M. Savić, and H. Keller, J. Physics: Condens. Matter, **15**, L17-L23 (2003).

- *Unconventional isotope effects in cuprate high-temperature superconductors*
  H. Keller, Physica B **326**, 283-288 (2003).

- *Low energy muons as probes of thin films and near surface regions*
  E. Morenzoni, R. Khasonov, H. Luetkens, T. Prokscha, A. Suter, N. Garifianov, H. Glückler, M. Birke, E.M. Forgan, H. Keller, J. Litterst, Ch. Niedermayer, G. Nieuwenhuys, Physica B **326**, 196-204 (2003).

- *Universal properties of cuprate superconductors*
  T. Schneider, Physica B **326**, 289295 (2003).

- MgB_2 *single crystals: high pressure growth and physical properties*
  J. Karpinski, M. Angst, J. Jun, S.M. Kazakov, R. Puzniak, A. Wisniewski, J. Roos, H. Keller, L. Degiorgi, M. R. Eskildsen, L. Vinnikov and A. Mironov, Supercond. Sci. Technol. **16**, 221-230 (2003).

Articles in press

- *Relationship between the isotope effects on transition temperature, specific heat and penetration depths*
  T. Schneider, Phys. Rev. B.

- *Three-Spin-Polarons and Their Elastic Interaction in Cuprates*
  B.I. Kochelaev, A.M. Safina, A. Shengelaya, H. Keller, K.A. Müller, and K. Conder, Mod. Phys. Lett. B.

Conference reports

- *Anisotropic phase diagram of MgB_2 by torque magnetometry (poster)*
  M. Angst, D. Di Castro, S. Kohout, J. Roos, H. Keller, J. Jun, S. M. Kazakov, J. Karpinski, R. Puzniak, and A. Wisniewski, Annual meeting of the Swiss Physical Society, Basel, 20-21 Mrch, 2003.

- *Study of the boron isotope effect on the magnetic penetration depth in MgB_2 superconductor by μSR experiment*
  D. Di Castro, R. Khasanov, D. Eschenko, A. Shenghelaya, I.M. Savic, K. Conder, S. Kazakov, J. Karpinski, M. Angst, J. Roos, and H. Keller, Annual meeting of the Swiss Physical Society, Basel, 20-21 March, 2003.

- *New Nanotorque Sensors for Magnetometry*
  S. Kohout, D. Di Castro, M. Angst, H. Keller, Annual meeting of the Swiss Physical Society, Basel, 20-21 March, 2003.

Invited lectures

- M. Angst: *Anisotropy and phase diagram of MgB_2 by torque magnetometry*
  Seminar über Festkörperphysik, Forschungszentrum Karlsruhe und Universität Karlsruhe, Germany, 25 November, 2002.

- D. Eshchenko:
  Muonium Formation and End-of-Track Processes in Insulators and Semiconductors
  Laboratory for Muon Spin Spectroscopy; Seminar; PSI Villigen, Switzerland, 23 January, 2002.

- D. Eshchenko: *Muonium Ionization in CdS; a Cascade Approach*
  XXXVI Annual Winter School on Nuclear and Particle Physics of the St.Petersburg Institute of Nuclear Physics, Repino, Russia, 26 February - 2 March, 2002.

- D. Eshchenko: *Diamagnetizm of a Weakly Bound State in Semiconductors*
  XXXVI Annual Winter School on Nuclear and Particle Physics of the St.Petersburg Institute of Nuclear Physics, Repino, Russia, 26 February - 2 March, 2002.

- H. Keller: *Unconventional isotope effects in high-temperature cuprate superconductors*
  Tbilisi State University, Tbilisi, Georgia, 17 September, 2002.

- H. Keller: *Unconventional isotope effects in high-temperature cuprate superconductors*
  Anorganisch-chemisches Institut, Universität Zürich, 20 December, 2002.

- H. Keller: *Unconventional isotope effects in high-temperature cuprate superconductors*
  9th International Conference on Muon Spin Rotation, Relaxation and Resonances, Williamsburg (VA), U.S.A., 6 June, 2002.

- T. Schneider: *Universal properties of cuprates superconductors*
  Institut fur Festköperphysik, KFA Karlsruhe, 31 January, 2002.

- T. Schneider: *Quantum phase transitions in cuprates superconductors*
  Physics Department, University Neuchatel, 17 May, 2002.

- T. Schneider: *Universal properties of cuprates superconductors*
  Laboratorium fur Festkörperphysik, ETH, Zürich, 23 May, 2002.

- T. Schneider: *Universal properties of cuprates superconductors*
  9th International Conference on Muon Spin Rotation, Relaxation and Resonances, Williamsburg (VA), U.S.A., 5 June, 2002.

- A. Shengelaya: *Recent Results of EPR studies of* $La_{2-x}Sr_xCuO_4$
  International Conference on Low Energy Electrodynamics in Solids (LEES), Montauk NY, USA, 13 October, 2002.

- M. Mali: *Pseudogap in cuprate superconductors measured by NMR/NQR*
  Workshop on *Gaps and pseudogaps in cuprates"*, Physik-Institut, Universität Zürich, 11 December, 2002.

18.3 Research group of Prof. P. F. Meier

Articles

- *Electric field gradients from first-principles and point-ion calculations*
  E. P. Stoll, T. A. Claxton, and P. F. Meier, Phys.Rev.B **65**, 064532 (2002).

- *Comparison of the Electronic Structures of* La_2CuO_4, $Sr_2CuO_2Cl_2$, *and* $Sr_2CuO_2F_2$
  C. Bersier, E. P. Stoll, P. F. Meier, and T.A. Claxton, J. Supercond. Inc. Nov. Magn. **15**, 403-408 (2002).

- *Muon sites and hyperfine fields in* La_2CuO_4
  H.U. Suter, E. P. Stoll, and P. F. Meier, Physica B: Condensed Matter, **326**, 329-332 (2003).

- *Nuclear magnetic resonance chemical shifts and paramagnetic field modifications in* La_2CuO_4
  S. Renold, T. Heine, J. Weber, and P. F. Meier, Phys.Rev.B **67**, 024501 (2003).

- *Dimensional complexity and spectral properties of the human sleep EEG*
  Y. Shen, E. Olbrich, P. Achermann, and P. F. Meier, Clin. Neurophysiol., **114**, 199-209 (2003).

Articles in press

- *Influence of Lattice Parameter Scaling on Local Electronic and Magnetic Properties in* La_2CuO_4
  S. Renold and P. F. Meier, J. of Superconductivity, In Press, (2003).

- *Dynamics of human sleep EEG*
  E. Olbrich, P. Achermann and P. F. Meier, Neurocomputing, In Press, (2003).

- *Charge Distribution in* $La_{2-x}Sr_xCuO_4$
  E. P. Stoll, P. F. Meier, and T. A. Claxton, Int. J. of Mod. Physics B, In Press, (2003).

Diploma and PhD theses

- *Time Series Analysis of the Human Electroencephalogram*
  Y. Shen, Dissertation, Universität Zürich, 2002.

- *Modellrechnungen zu MNR-Experimenten an Kuprat-Supraleitern*
  T. Mayer, Diplomarbeit, Universität Zürich, 2002.

- *Temperature Dependence of NMR Relaxation Rates in Cuprates Interpreted by Spin Correlations in Heisenberg Systems*
  A. Höchner, Diplomarbeit, Universität Zürich, 2002.

Invited lectures

- E. P. Stoll: *Electric field gradients from first-principles and point-ion calculations*
  SPG Tagung, Lausanne, 28.02.02.

- E. Olbrich: *Dynamics of human sleep EEG*
  Seminar, Max-Planck-Institut für Physik komplexer Systeme, Dresden, 27.03.02.

- E. P. Stoll: *"Stripes", Perkolation, Fraktale – Konsequenzen für HTSC-Theorien*
  Seminar für Experimentalphysik, Universität Zürich, 13.06.02.

- P.F. Meier: *Time Series Analysis of Electroencephalograms*
  Kolloquium, MPI München, 12.12.02.

- P.F. Meier: *Charge Distribution in Undoped and Doped La_2CuO_4*
  Internat. Conference on Superconductors, New^{3}SC, SanDiego, USA, 20.01.03.

18.4 Research group of Prof. J. Osterwalder

Articles

- *The Fermi surface in a magnetic metal-insulator interface*
  T. Greber, W. Auwärter, M. Hoesch, G. Grad, P. Blaha, J. Osterwalder, Surf. Rev. Lett. 9 (2002) 1243-1250.

- *Reduction of the magnetic moment at the h-BN/Ni(111) interface*
  T. Greber, W. Auwärter, G. Grad, P. Blaha, J. Osterwalder, Proceedings of the *Conference on Atomic Level Characterization (ALC'01)*, Nara, Japan, (Nara-Ken New Public Hall 2002), 235-240.

- *Spin-polarized Fermi surface mapping*
  M. Hoesch, T. Greber, V. N. Petrov, M. Muntwiler, M. Hengsberger, W. Auwärter, J. Osterwalder, J. Electron Spectrosc. Relat. Phenom. 124 (2002) 263-279.

- *Co on h-BN/Ni(111): from island to island-chain formation and Co intercalation*
  W. Auwärter, M. Muntwiler, T. Greber, J. Osterwalder, Surf. Sci. 511 (2002) 379-386.

- *Tailoring confining barriers for surface states by step decoration: CO/vicinal Cu(111)*
  F. Baumberger, T. Greber, B. Delley, J. Osterwalder, Phys.Rev.Lett.88, 237601 (2002).
- *Quenching of majority-channel quasiparticle excitations in cobalt*
  S. Monastra, F. Manghi, C. A. Rozzi, C. Arcangeli, E. Wetli, H.-J. Neff, T. Greber, J. Osterwalder, Phys.Rev.Lett.88, 236402 (2002).

Articles in press

- *XPS/AES structural effects: diffraction*
  J. Osterwalder, Book chapter in *Surface Analysis by Electron Spectroscopy*, D. Briggs and J. Grant, eds., Surface Spectra Ltd and IM Publications (2003).
- *The electronic structure of a surfactant layer: Pb/Cu(111)*
  F. Baumberger, A. Tamai, M. Muntwiler, T. Greber, J. Osterwalder, Surf. Sci. (2003).
- *Optical recognition of atomic steps on surfaces*
  F. Baumberger, Th. Herrmann, A. Kara, S. Stolbov, N. Esser, T. S. Rahman, J. Osterwalder, W. Richter, T. Greber, Phys. Rev. Lett. (2003).

Diploma and PhD theses

- *Electronic surface states in lateral super-structures*
  Felix Baumberger, Ph. D. Thesis, Physik-Institut, Universität Zürich, 2002.
- *Spin-resolved Fermi surface mapping*
  Moritz Hoesch, Ph. D. Thesis, Physik-Institut, Universität Zürich, 2002.
- *One monolayer of hexagonal boron nitride on Ni(111): an atomically sharp interface*
  Wilhelm Auwärter, Ph. D. Thesis, Physik-Institut, Universität Zürich, 2002.
- *Vorbereitende Arbeiten für zeitaufgelöste LEED-Experimente*
  Michael K. Barry, Diploma Thesis, Physik-Institut, Universität Zürich, 2002.

Contributed conference presentations

- *Spin-polarized Fermi surface mapping*
  M. Hoesch, SPG Jahrestagung, EPF Lausanne, 1.3.02.
- *Observation of electron standing waves normal to the surface*
  T. Greber, Symposium on Surface Science 2003, St. Christoph, Austria, 6.3.02.
- *Surface states in lateral super-structures*
  F. Baumberger (Poster), Symposium on Surface Science 2003, St. Christoph, Austria, 6.3.02.
- *Realization of a time-resolved low-energy electron diffraction experiment*
  M. Hengsberger (Poster), 9th Workshop on Desorption Induced by Electronic Transitions, Aussois, France, 4.6.02.

- *The electronic structure of a surfactant layer: Pb/Cu(111)*
  M. Muntwiler, Nano-7 and 21st European Conference on Surface Science, Malmö, Sweden, 26.6.02.

- *An instrument for spin-resolved Fermi surface mapping*
  M. Hoesch (Poster Award), Nano-7 and 21st European Conference on Surface Science, Malmö, Sweden, 26.6.02.

- *Electronic Surface States in Lateral Super-Structures*
  T. Greber (Poster), Workshop on Low-Dimensional Structures, Universität Marburg, 2.7.02.

- *Optical recognition of atomic steps on surfaces*
  T. Greber, SPG Jahrestagung, Universität Basel, 21.3.03.

- *Direct determination of the adsorption geometry of large molecules*
  J. Wider, SPG Jahrestagung, Universität Basel, 21.3.03.

Invited lectures

- M. Hoesch: *COPHEE, the complete photoemission experiment*
  Surface Science Seminar at EMPA Dübendorf, 16.5.02.

- J. Osterwalder: *6 Hours of Lecture on Photoemission Spectroscopy*
  ICTP School on Synchrotron Radiation, Trieste, Italy, 20.-24.5.02.

- J. Osterwalder: *Grenzflächen von Band-Ferromagneten untersucht mit winkelaufgelöster Photoemission*
  Kolloquium, FB Physik, TU Braunschweig, 18.6.02.

- J. Osterwalder: *Aus dem Bilderbuch der Photoemission: Grenzflächen von Band-Ferromagneten*
  Kolloquium, Physikalisches Institut, Universität Münster, 13.11.02.

- F. Baumberger: *Surface electronic structure of stepped Cu(111): super-lattice states and charge asymmetries at low coordinated sites*
  Surface Science Seminar at EMPA Dübendorf, 4.12.02.

- T. Greber: *Investigating an atomically sharp spintronic junction with angular resolved photoemission and scanning tunneling spectroscopy: h-BN/Ni(111)*
  294th WE Heraeus Seminar on Frontiers in Nanomagnetism, Bad Honnef, 8.1.03.

- T. Greber: *The next 23 years: functional films and surfaces*
  ITS, EPF Lausanne, 16.1.03.

- J. Osterwalder: *Angle-resolved photoemission: measuring electronic bands at high resolution in energy, momentum and spin*
  19th SAOG Meeting, Fribourg, 24.1.03.

18.5 Research group of Prof. U. Straumann, (for H1 publications see Sec.18.6)

Articles

- *Determination of the Gravitational Constant with a Beam Balance*
  St. Schlamminger, E. Holzschuh, W. Kündig, Phys.Rev.Lett.**89** (2002) 161102.

- *Studies of Aging and HV Breakdown Problems during Development and Operation of MSGC and GEM Detectors for the Inner Tracking System of HERA-B*
  Y. Bagaturia, O. Baruth, H.B. Dreis, F. Eisele, I. Gorbunov, S. Gradl, W. Gradl, S. Hausmann, M. Hildebrandt, T. Hott, S. Keller, C. Krauss, B. Lomonosov, M. Negodaev, C. Richter, P. Robmann, B. Schmidt, U. Straumann, P. Truöl, S. Visbeck, T. Walter, C. Werner, U. Werthenbach, G. Zech, T. Zeuner, and M. Ziegler, hep-ex/0204011, Nucl.Instr.Meth.**A490** (2002), 223 - 242.

- *Purity Monitoring System for the H1 Liquid Argon Calorimeter*
  H1 Calorimeter Group, E. Barrelet et al., Nucl.Instr.Meth.**A490** (2002) 204-222.

- *Search for the production of single sleptons through R-Parity Violation in $p\overline{p}$ collisions at $\sqrt{s}$=1.8 TeV*
  DØ-Collaboration, V. M. Abazov *et al.*, Phys.Rev.Lett.**89** (2002) 261801.

- *$t\bar{t}$ production cross section in $p\overline{p}$ collisions at$\sqrt{s}$ = 1.8 TeV*
  DØ-Collaboration, V. M. Abazov *et al.*, Phys.Rev.D **67** (2003) 012004.

- *Search for mSUGRA in single-electron events with jets and large missing transverse energy in $p\overline{p}$ collisions at $\sqrt{s}$ = 1.8 TeV*
  DØ-Collaboration, V. M. Abazov *et al.*, Phys.Rev.D **66** (2002) 112001.

- *Improved W boson mass measurement with the D0 detector*
  DØ-Collaboration, V. M. Abazov *et al.*, Phys.Rev.D **66** (2002) 012001.

- *A direct measurement of W boson decay width*
  DØ-Collaboration, V. M. Abazov *et al.*, Phys.Rev.D **66** (2002) 032008.

- *Search for R-parity violating supersymmetry in dimuon and four-jets channel*
  DØ-Collaboration, V. M. Abazov *et al.*, Phys.Rev.Lett.**89** (2002) 171801.

- *Search for leptoquark pairs decaying to nu nu + jets in $p\overline{p}$ collisions at $\sqrt{s}$ = 1.8 TeV*
  DØ-Collaboration, V. M. Abazov *et al.*, Phys.Rev.Lett.**88** (2002) 191801.

- *The inclusive jet cross-section in $p\overline{p}$ collisions at $\sqrt{s}$ = 1.8 TeV using the k(T) algorithm*
  DØ-Collaboration, V. M. Abazov *et al.*, Phys.Lett.B **525** (2002) 211.

- *Subjet multiplicity of gluon and quark jets reconstructed with the k(T) algorithm in $p\overline{p}$ collisions*
  DØ-Collaboration, V. M. Abazov *et al.*, Phys.Rev.D **65** (2002) 052008.

- *Hard single diffraction in $\overline{p}p$ collisions at $\sqrt{s}$ = 630 GeV and 1800 GeV*
  DØ-Collaboration, V. M. Abazov *et al.*, Phys.Lett.B **531** (2002) 52.

- *A precise measurement of the direct CP violating parameter Re(ϵ'/ϵ)*
  the NA48 Collaboration, Eur.Phys.J.22, 231-254.

- *Precise measurement of the decay* $\mathrm{K_L} \to \pi^0\gamma\gamma$
  the NA48 Collaboration, Phys.Lett.536, 229-240.

- *A Measurement of the K_S Lifetime*
  the NA48 Collaboration, Phys.Lett.537, 28-40.

Articles in press

- *The CIP2k First Level Trigger System at the H1 experiment at HERA*
  M. Urban, J. Becker, S. Schmitt and U. Straumann, IEEE Trans. Nucl. Sci. **50**, No. 4 (2003).
- *Multiple Jet Production at low transverse energies in $p\overline{p}$ collisions at $\sqrt{s}$= 1.8 TeV*
  DØ-Collaboration, V. M. Abazov *et al.*, FERMILAB-PUB-02-153-E, hep-ex/0207046, July 2002, submitted to Phys.Rev.D.
- *Investigation of $\mathrm{K_S} \to \pi^+\pi^-e^+e^-$ decays*
  the NA48 Collaboration, to be submitted to Eur.Phys.J.

Diploma and PhD theses

- *Determination of the Gravitational Constant Using a Beam Balance*
  Stephan Schlamminger, PhD Thesis, Physik-Institut, Universität Zürich, 2002.
- *A Silicon Inner Tracker for the LHCb Experiment*
  Phillip Sievers, PhD Thesis, Physik-Institut, Universität Zürich, 2002.

Conference reports

- M. Urban, J. Becker, S. Schmitt and U. Straumann: *The CIP2k First Level Trigger System at the H1 experiment at HERA*
  Proceedings of the 2002 IEEE NSS/MIC, Norfolk, Virginia, USA, Nov. 10-16, 2002.
- J. Becker, H. Cramer, M. Hildebrandt, K. Müller, S. Schmitt, U. Straumann, M. Urban and N. Werner: *A First Level Trigger Susbsystem CIP2k for the H1 experiment at HERA*
  8th topical seminar on innovative particle and radiation detectors, Siena, Italy, 21 to 24 October 2002.
- P. Sievers: *Performance tests of large pitch silicon strip sensors for the LHCb Inner Tracker*
  Poster Session at the 9th European Symposium on Semiconductor Detectors, June 23 - 27, 2002, Schloss Elmau, Germany, LHCb public note 2002-044, to be published in Nucl.Instr.Meth.A.
- St. Schlamminger, E. Holzschuh, W. Kündig: *A Beam Balance Experiment to Determine the Gravitational Constant*
  Conference Digest, to be published in Conference on Precision Electromagnetic Measurements, 2002.
- J. Blocki and F. Lehner: *The thermal properties of Silicon Detectors used in high energy physics*
  ANSYS 2002 Conference, April 22-24, 2002, Pittsburgh, Pennsylvania, USA.
- Peter Fierlinger: *Giant Absorption Cross Sections of Gadolinium on UCN*
  Annual Meeting of the SPS, Basel 20.-21.3.03.

- Peter Fierlinger: *Giant Absorption Cross Sections of Gadolinium on UCN*
  DPG Frühjahrstagung, Tübingen 17.-21.3.03.

Invited lectures

- F. Lehner: *The Status of LHCb and its Inner Tracker detector*
  Experimental Particle Physics Seminar at Kansas State University, March 10, 2003, Manhatten, Kansas, USA.

- Phillip Sievers: *The LHCb Silicon Inner Tracker*
  High Energy Physics Seminar, UCLA Los Angeles, 29.01.2003.

- F. Lehner on behalf of the LHCb Silicon Tracker Collaboration: *The LHCb Inner Tracker technical design*
  61st open LHCC session, November 27, 2002, CERN, Geneva, Switzerland.

- F. Lehner on behalf of the LHCb Silicon Tracker Collaboration: *The LHCb Silicon Tracker*
  11th International Workshop on Vertex Detectors 'Vertex 2002', November 3-8, 2002, Kailua Kona, Hawaii, USA, to be published in Nucl.Instr.Meth..

- Achim Vollhardt: *Development of the Inner Tracker Detector Electronics for LHCb*
  8th Workshop on Electronics for LHC Experiments, September 9 - 13, 2002, Colmar, France, LHCb public note LHCb-2002-068.

- U. Straumann: *Experimental Methods in Deep Inelastic Scattering at the HERA Collider*
  Graduiertenkolleg Tübingen – Basel, Basel, 5. Juli 2002.

- Nicole Werner: *Structure function measurements at HERA and the determination of α_s and the parton distributions*
  XXXVIIIth Rencontres de Moriond: to QCD and High Energy Hadronic Interactions, Les Arcs F (March 2003), 22. 3. 2003

Notes and technical design reports

- *Silicon Sensor Quality Assurance for the DØ RunIIb Silicon Detector: Procedures and Equipment*
  Frank Lehner, DØ-note 4120, March 2003.

- *Tracking Performance and Robustness Tests*
  Matthew Needham, LHCb note 2003-020.

- *Silicon Tracker simulation performance*
  Matthew Needham, LHCb note 2003-015.

- *LHCb Inner Tracker: Technical Design Report*
  LHCb Collaboration, CERN/LHCC 2002-029, November 2002.

- *The liquid cooling system of the LHCb Inner Tracker: Design constraints and considerations*
  F. Lehner and M. Stodulski, LHCb-2002-066.

- *Alignment Tolerances for the Inner Tracker*
  F. Lehner and O. Steinkamp, LHCb Note 2002-064.

- *The LHCb Inner Tracker data readout system*
  A. Vollhardt, LHCb public note 2002-062.

- *The LHCb Inner Tracker cooling balcony and plate: Design and Material Selection Studies*
  K. Bösiger et al., LHCb-2002-061.

- *Design, Construction and Thermal Measurements on a Detector Box for the LHCb Inner Tracker*
  K. Bösiger et al., LHCb-2002-059.

- *Test Beam Results of Multi-Geometry Prototype Sensors for the LHCb Inner Tracker*
  M. Agari, C. Bauer, B. Carron, S. Heule, S. Jimenez-Otero, F. Lehner, A. Ludwig, V. Pugatch, M. Schmelling, P. Sievers, O. Steinkamp, U. Straumann, M.T. Tran, A. Vollhardt, H. Voss, LHCb Note 2002-058.

- *Layout and R&D for an All-Silicon TT Station*
  O. Steinkamp, LHCb Note 2002-056.

- *Momentum resolution studies for the inner tracker*
  Matthew Needham, LHCb note 2002-043.

- *Description and evaluation of multi-geometry silicon prototype sensors for the LHCb Inner Tracker*
  F.Lehner, P.Sievers, O.Steinkamp, U.Straumann, A.Vollhardt, M.Ziegler, LHCb public note 2002-038, July 2002.

- *Inner and Outer tracker occupancies in the light LHCb detector*
  Matthew Needham, LHCb note 2002-032.

- *New data model, digitization and reconstruction algorithms for the inner tracker*
  Matthew Needham, LHCb note 2002-030.

18.6 H1 Publications by the groups of Straumann and Truöl

Articles

- *Measurement of Dijet Electroproduction at Small Jet Separation*
  H1-Collab., C. Adloff *et al.*, hep-ex/0111006, Eur.Phys.J.**C24** (2002), 33 - 41.

- *Measurement of Dijet Cross Sections in Photoproduction at HERA*
  H1-Collab., C. Adloff *et al.*, hep-ex/0201006, Eur.Phys.J.**C25** (2002), 13 - 23.

- *Energy Flow and Rapidity Gaps between Jets in Photoproduction at HERA*
  H1-Collab., C. Adloff *et al.*, hep-ex/0203011, Eur.Phys.J.**C24** (2002), 517 - 527.

- *A Measurement of the t Dependence of the Helicity Structure of Diffractive ρ Meson Electroproduction at HERA*
  H1-Collab., C. Adloff *et al.*, hep-ex/0203022, Phys.Lett.**B539** (2002), 25 - 39.

- *Inelastic Photoproduction of J/Ψ Mesons at HERA*
  H1-Collab., C. Adloff *et al.*, hep-ex/0205064, Eur.Phys.J.**C25** (2002), 25 - 39.

- *Inelastic Leptoproduction of J/Ψ Mesons at HERA*
  H1-Collab., C. Adloff *et al.*, hep-ex/0205065, Eur.Phys.J.**C25** (2002), 41 - 53.

- *Search for QCD Instanton-Induced Processes in Deep-Inelastic Scattering at HERA*
  H1-Collab., C. Adloff *et al.*, hep-ex/0205078, Eur.Phys.J.**C25** (2002), 495 - 509.

- *Diffractive Photoproduction of $\Psi(2S)$ Mesons at HERA*
  H1-Collab., C. Adloff *et al.*, hep-ex/0205107, Phys.Lett.**B541** (2002), 251 - 264.

- *Measurement of Inclusive Jet Cross Sections in Deep-Inelastic ep Scattering at HERA*
  H1-Collab., C. Adloff *et al.*, hep-ex/0206029, Phys.Lett.**B542** (2002), 193 - 206.

- *Search for Odderon-induced Contributions to Exclusive π^0 Photoproduction at HERA*
  H1-Collab., C. Adloff *et al.*, hep-ex/0206073, Phys.Lett.**B544** (2002), 35 - 43.

- *Search for Excited Electrons at HERA*
  H1-Collab., C. Adloff *et al.*, hep-ex/0207038, Phys.Lett.**B548** (2002), 35 - 44.

- *Compact Front End Electronics and Bidirectional 3.3 GBPS Optical Datalink for fast Proportional Chamber Readout*
  S. Lüders, R. Baldinger, D. Baumeister, K. Bösiger, R. Eichler, M. Feuerstack-Raible, C. Grab, S. Löchner, B. Meier, P. Robmann, B.A. Schmid, U. Stange, S. Steiner, U. Straumann, S. Streuli, K. Szeker, and P. Truöl, hep-ex/0107064, Nucl.Instr.Meth.**A484** (2002) 515 - 527.

Articles in print

- *Isolated Electrons and Muons in Events with Missing Transverse Momentum at HERA*
  H1-Collab., C. Adloff *et al.*, V. Andreev *et al.*, hep-ex/0301030, Phys.Lett.**B**.

- *Measurement of Inclusive Jet Cross Sections in Photoproduction at HERA*
  H1-Collab., C. Adloff *et al.*, hep-ex/0302034, Eur.Phys.J.**C**.

- *Measurement and QCD Analysis of Neutral and Charged Current Cross Sections at HERA*
  H1-Collaboration, C. Adloff *et al.*, hep-ex/0304003, submitted to Eur.Phys.J.**C** (2003)

H1-collaboration (2003)

A. Aktas, V. Andreev, T. Anthonis, A. Asmone, A. Babaev, S. Backovic, J. Bähr,P. Baranov, E. Barrelet, W. Bartel, S. Baumgartner, J. Becker, M. Beckingham, O. Behnke, O. Behrendt, A. Belousov, Ch. Berger, T. Berndt, J.C. Bizot, J. Böhme, M.O. Boenig, V. Boudry, J. Bracinik, W. Braunschweig, V. Brisson, H.-B. Bröker, D.P. Brown, D. Bruncko, F.W. Büsser, A. Bunyatyan, G. Buschhorn, L. Bystritskaya, A.J. Campbell, S. Caron, F. Cassol-Brunner, V. Chekelian, D. Clarke, C. Collard, J.G. Contreras, Y.R. Coppens, J.A. Coughlan, M.-C. Cousinou, B.E. Cox, G. Cozzika, J. Cvach, J.B. Dainton, W.D. Dau, K. Daum, B. Delcourt, N. Delerue, R. Demirchyan, A. De Roeck, E.A. De Wolf, C. Diaconu, J. Dingfelder, V. Dodonov, J.D. Dowell, A. Dubak, C. Duprel, G. Eckerlin, V. Efremenko, S. Egli, R. Eichler, F. Eisele, M. Ellerbrock, E. Elsen, M. Erdmann, W. Erdmann, P.J.W. Faulkner, L. Favart, A. Fedotov, R. Felst, J. Ferencei, M. Fleischer, P. Fleischmann, Y.H. Fleming, G. Flucke, G. Flügge, A. Fomenko, I. Foresti, J. Formánek, G. Franke, G. Frising,

E. Gabathuler, K. Gabathuler, J. Garvey, J. Gassner, J. Gayler, R. Gerhards, C. Gerlich, S. Ghazaryan, L. Goerlich, N. Gogitidze, S. Gorbounov, C. Grab, V. Grabski, H. Grässler, T. Greenshaw, M. Gregori, G. Grindhammer, D. Haidt, L. Hajduk, J. Haller, G. Heinzelmann, R.C.W. Henderson, H. Henschel, O. Henshaw, R. Heremans, G. Herrera, I. Herynek, M. Hildebrandt, K.H. Hiller, J. Hladký, P. Höting, D. Hoffmann, R. Horisberger, A. Hovhannisyan, M. Ibbotson, M. Jacquet, L. Janauschek, X. Janssen, V. Jemanov, L. Jönsson, C. Johnson, D.P. Johnson, H. Jung, D. Kant, M. Kapichine, M. Karlsson, J. Katzy, F. Keil, N. Keller, J. Kennedy, I.R. Kenyon, C. Kiesling, M. Klein, C. Kleinwort, T. Kluge, G. Knies, B. Koblitz, S.D. Kolya, V. Korbel, P. Kostka, R. Koutouev, A. Kropivnitskaya, J. Kroseberg, J. Kueckens, T. Kuhr, M.P.J. Landon, W. Lange, T. Laštovička, P. Laycock, A. Lebedev, B. Leißner, R. Lemrani, V. Lendermann, S. Levonian, B. List, E. Lobodzinska, N. Loktionova, R. Lopez-Fernandez, V. Lubimov, H. Lueders, S. Lüders, D. Lüke, L. Lytkin, A. Makankine, N. Malden, E. Malinovski, S. Mangano, P. Marage, J. Marks, R. Marshall, H.U. Martyn, J. Martyniak, S.J. Maxfield, D. Meer, A. Mehta, K. Meier, A.B. Meyer, H. Meyer, J. Meyer, S. Michine, S. Mikocki, D. Milstead, F. Moreau, A. Morozov, J.V. Morris, K. Müller, P. Murín, V. Nagovizin, B. Naroska, J. Naumann, Th. Naumann, P.R. Newman, F. Niebergall, C. Niebuhr, D. Nikitin, G. Nowak, M. Nozicka, B. Olivier, J.E. Olsson, D. Ozerov, C. Pascaud, G.D. Patel, M. Peez, E. Perez, A. Petrukhin, D. Pitzl, R. Pöschl, B. Povh, N. Raicevic, J. Rauschenberger, P. Reimer, B. Reisert, C. Risler, E. Rizvi, P. Robmann, R. Roosen, A. Rostovtsev, S. Rusakov, K. Rybicki, D.P.C. Sankey, E. Sauvan, S. Schätzel, J. Scheins, F.P. Schilling, P. Schleper, D. Schmidt, S. Schmidt, S. Schmitt, M. Schneider, L. Schoeffel, A. Schöning, V. Schröder, H.C. Schultz-Coulon, C. Schwanenberger, K. Sedlák, F. Sefkow, I. Sheviakov, L.N. Shtarkov, Y. Sirois, T. Sloan, P. Smirnov, Y. Soloviev, D. South, V. Spaskov, A. Specka, H. Spitzer, R. Stamen, B. Stella, J. Stiewe, I. Strauch, U. Straumann, G. Thompson, P.D. Thompson, F. Tomasz, D. Traynor, P. Truöl, G. Tsipolitis, I. Tsurin, J. Turnau, J.E. Turney, E. Tzamariudaki, A. Uraev, M. Urban, A. Usik, S. Valkár, A. Valkárová, C. Vallée, P. Van Mechelen, A. Vargas Trevino, S. Vassiliev, Y. Vazdik, C. Veelken, A. Vest, A. Vichnevski, V. Volchinski, K. Wacker, J. Wagner, B. Waugh, G. Weber, R. Weber, D. Wegener, C. Werner, N. Werner, M. Wessels, B. Wessling, M. Winde, G.G. Winter, Ch. Wissing, E.E. Woehrling, E. Wünsch, J. Žáček, J. Zálešák, Z. Zhang, A. Zhokin, F. Zomer, and M. zur Nedden

18.7 Research group of Prof. P. Truöl, (for H1 publications see Sec.18.6)

18.7.1 Articles

- *A Large Acceptance, High Resolution Detector for Rare K^+-decay Experiments*
  E865-Collaboration, R. Appel *et al.*, Nucl.Instr.Meth.**A479** (2002), 349 - 406.

- *Experimental Study of the Radiative Decays $K^+ \to \mu^+\nu_\mu e^+e^-$ and $K^+ \to e^+\nu_e e^+e^-$*
  E865-Collaboration, A.A. Poblaguev *et al.*, hep-ex/0204006, Phys.Rev.Lett.**89** (2002), 061803-1 - 061803-4.

- *Measurement of the $\bar{b}b$ Production Cross Section at HERA in 920 GeV Proton-Nucleus Collisions*
  HERA-B Collaboration, I. Abt *et al.*, hep-ex/0205106, Eur.Phys.J.**C26** (2003), 345 - 355.

- *Studies of Aging and HV Breakdown Problems during Development and Operation of MSGC and GEM Detectors for the Inner Tracking System of HERA-B*
  Y. Bagaturia, O. Baruth, H.B. Dreis, F. Eisele, I. Gorbunov, S. Gradl, W. Gradl, S. Hausmann, M. Hildebrandt, T. Hott, S. Keller, C. Krauss, B. Lomonosov, M. Negodaev, C. Richter, P. Robmann, B. Schmidt, U. Straumann, P. Truöl, S. Visbeck, T. Walter, C. Werner, U. Werthenbach, G. Zech, T. Zeuner, and M. Ziegler, hep-ex/0204011, Nucl.Instr.Meth.**A490** (2002), 223 - 242.

- *Testing lepton flavour conservation*
  A. van der Schaaf, Proceedings of the Intern. Conf. on CP Violation (KAON 2001), eds. F. Constantini, G. Isidori and M. Sozzi, Pisa, Italy, June 12 - 17, 2001, Frascati Physics Series, Vol. XXVI, ISBN 88-86409-33-8.

Articles in print

- *High Statistics Measurement of K_{e4} Decay Properties*
  E865-Collaboration, S. Pislak *et al.*, hep-ex/0301040, Physical Review **D** (2003).
- *J/Ψ Production via χ_c Decays in 920 GeV pA Interactions*
  HERA-B Collaboration, I. Abt *et al.*, DESY 02-187, hep-ex/0211033, Phys.Lett.**B**.
- *Inclusive V^0 Production Cross Section from 920 GeV Fixed Target Proton-Nucleus Collisions*
  HERA-B Collaboration, I. Abt *et al.*, hep-ex/0212040, Eur.Phys.J.**C**.
- *WG2 Summary part 2: rare muon decays*
  A. van der Schaaf, Proceedings of the 3rd Intern. Workshop on *Neutrino Factories based on Muon Storage Rings* (NuFACT'01), May 24 - 30 2001, Tsukuba, Japan, to appear in Nucl.Instr.Meth.A.
- *μe Conversion experiments: status and prospects*
  A. van der Schaaf, Proceedings of the 3rd Intern. Workshop on *Neutrino Factories based on Muon Storage Rings* (NuFACT'01), May 24 - 30 2001, Tsukuba, Japan, to appear in Nucl.Instr.Meth.A.
- *Open Heavy Flavor Production at HERA*
  J. Kroseberg, Proc. Lake Louise Winter Institute on Fundamental Interactions, Lake Louise, Alberta, Canada (2002), hep-ex/0206042.
- *Beauty in ep collisions*
  J. Kroseberg, Proc. Int. Conf. on the Structure and Interactions of the Photon (Photon03), Frascati I (April 2003).

Lectures

- P. Truöl: *From biomolecules to quarks and gluons: the research program in experimental physics at the University of Zürich*
  Vilnius Gediminas Technical University, Vilnius, Lithuania, 25.03.2002.
- P. Truöl: *From biomolecules to quarks and gluons: the research program in experimental physics at the University of Zürich*
  Kaunas University of Technology, Kaunas, Lithuania, 26.03.2002.
- A. van der Schaaf: *Physics with Intense Muon Beams: Status and Prospects*
  Plenary talk, 3rd Intern. Workshop on *Neutrino Factories based on Muon Storage Rings* (NuFACT'02), July 1 - 6 2002, London, Proceedings in print (J. Phys. G.).
- A. van der Schaaf: *Search for μe Conversion with SINDRUM II*
  Parallel session, 3rd Intern. Workshop on *Neutrino Factories based on Muon Storage Rings* (NuFACT'02), July 1 - 6 2002, London, Proceedings in print (J. Phys. G.).

- A. van der Schaaf: *Experiments on Charged Lepton Flavour Violation*
  Proceedings of the PSI Summer School *Exploring the Limits of the Standard Model*, eds. R. Rosenfelder and M. Spira, August 18 - 24 2002, Zuoz, Switzerland, PSI Proceedings 03-02, ISSN 1019-6447.

- A. van der Schaaf: *μe Conversion Experiment*
  4th Workshop on Neutrino Oscillations and their Origin (NOON2003), February 10-14 2003, to be published by World Scientific.

- J. Kroseberg: *B Production at HERA*
  seminar Santa Cruz Institute for Particle Physics, 21.01.03.

- J. Kroseberg: *B Production at HERA*
  seminar UCLA Physics Department, 22.01.03.

PhD theses

- *A Measurement of Beauty Production in High-Energy Positron-Proton Scattering*
  Jürgen Kroseberg, PhD Thesis, Universität Zürich, 2002.

The HERA-B Collaboration

I. Abt, A. Abyzov, M. Adams, H. Albrecht, V. Amaral, A. Amorim, S. J. Aplin, A. Arefiev, I. Ariño, M. Atiya, V. Aushev, Y. Bagaturia, R. Baghshetsyan, V. Balagura, M. Bargiotti, S. Barsuk, O. Barsukova, V. Bassetti, J. Bastos, C. Bauer, Th. S. Bauer, M. Beck, A. Belkov, Ar. Belkov, I. Belotelov, I. Belyaev, K. Berkhan, A. Bertin, B. Bobchenko, M. Böcker, A. Bogatyrev, G. Bohm, C. Borgmeier, M. Bräuer, D. Broemmelsiek, M. Bruinsma, M. Bruschi, P. Buchholz, M. Buchler, T. Buran, M. Capeáns, M. Capponi, J. Carvalho, J. Chamanina, B. X. Chen, R. Chistov, M. Chmeissani, A. Christensen, P. Conde, C. Cruse, M. Dam, K. M. Danielsen, M. Danilov, S. De Castro, H. Deckers, K. Dehmelt, H. Deppe, B. Dolgoshein, X. Dong, H. B. Dreis, M. Dressel, D. Dujmic, R. Eckmann, V. Egorytchev, K. Ehret, V. Eiges, F. Eisele, D. Emeliyanov, S. Erhan, S. Essenov, L. Fabbri, P. Faccioli, W. Fallot-Burghardt, M. Feuerstack-Raible, J. Flammer, H. Fleckenstein, B. Fominykh, S. Fourletov, T. Fuljahn, M. Funcke, D. Galli, A. Garcia, Ll. Garrido, D. Gascon, A. Gellrich, K. E. K. Gerndt, B. Giacobbe, J. Gläß, T. Glebe, D. Goloubkov, A. Golutvin, I. Golutvin, I. Gorbounov, A. Gorišek, O. Gouchtchine, D. C. Goulart, S. Gradl, W. Gradl, Yu. Guilitsky, T. Hamacher, J. D. Hansen, R. Harr, C. Hast, S. Hausmann, J. M. Hernández, M. Hildebrandt, A. Hölscher, K. Höpfner, W. Hofmann, M. Hohlmann, T. Hott, W. Hulsbergen, U. Husemann, O. Igonkina, M. Ispiryan, S. İşsever, H. Itterbeck, J. Ivarsson, T. Jagla, Y. Jia, C. Jiang, A. Kaoukher, H. Kapitza, S. Karabekyan, P. Karchin, N. Karpenko, Z. Ke, S. Keller, F. Khasanov, H. Kim, Yu. Kiryushin, I. Kisel, F. Klefenz, K. T. Knöpfle, V. Kochetkov, H. Kolanoski, S. Korpar, C. Krauss, P. Kreuzer, P. Križan, D. Krücker, T. Kvaratskheliia, A. Lange, A. Lanyov, K. Lau, G. Leffers, I. Legrand, B. Lewendel, Y. Q. Liu, T. Lohse, R. Loke, B. Lomonosov, J. Lüdemann, R. Männer, R. Mankel, U. Marconi, S. Masciocchi, I. Massa, I. Matchikhilian, G. Medin, M. Medinnis, M. Mevius, A. Michetti, Yu. Mikhailov, R. Miquel, R. Mizuk, A. Mohapatra, A. Moshkin, B. Moshous, R. Muresan, S. Nam, M. Negodaev, I. Négri, M. Nörenberg, S. Nowak, M. T. Núñez Pardo de Vera, T. Oest, A. Oliveira, M. Ouchrif, F. Ould-Saada, C. Padilla, P. Pakhlov, Yu.Pavlenko, D. Peralta, R. Pernack, T. Perschke, R. Pestotnik, B. AA. Petersen, M. Piccinini, M. A. Pleier, M. Poli,

V. Popov, A. Pose, D. Pose, I. Potashnikova, V. Pugatch, Y. Pylypchenko, J. Pyrlik, S. Ramachandran, F. Ratnikov, K. Reeves, D. Reßing, K. Riechmann, J. Rieling, M. Rietz, I. Riu, P. Robmann, J. Rosen, Ch. Rothe, W. Ruckstuhl, V. Rusinov, V. Rybnikov, D. Ryzhikov, F. Saadi-Lüdemann, D. Samtleben, F. Sánchez, M. Sang, V. Saveliev, A. Sbrizzi, S. Schaller, P. Schlein, M. Schmelling, B. Schmidt, S. Schmidt, W. Schmidt-Parzefall, A. Schreiner, H. Schröder, H.D. Schultz, U. Schwanke, A. J. Schwartz, A. S. Schwarz, B. Schwenninger, B. Schwingenheuer, R. Schwitters, F. Sciacca, S. Semenov, N. Semprini-Cesari, E. Sexauer, L. Seybold, J. Shiu, S. Shuvalov, I. Siccama, D. Škrk, L. Sözüer, A. Soldatov, S. Solunin, A. Somov, S. Somov, V. Souvorov, M. Spahn, J. Spengler, R. Spighi, A. Spiridonov, S. Spratte, A. Stanovnik, M. Starič, R. StDenis, C. Stegmann, S. Steinbeck, O. Steinkamp, D. Stieler, U. Straumann, F. Sun, H. Sun, M. Symalla, S. Takach, N. Tesch, H. Thurn, I. Tikhomirov, M. Titov, U. Trunk, P. Truöl, I. Tsakov, U. Uwer, V. Vagnoni, C. van Eldik, R. van Staa, Yu. Vassiliev, M. Villa, A. Vitale, I. Vukotic, G. Wagner, W. Wagner, H. Wahlberg, A. H. Walenta, M. Walter, T. Walter, J. J. Wang, Y. M. Wang, R. Wanke, D. Wegener, U. Werthenbach, P. J. Weyers, H. Wolters, R. Wurth, A. Wurz, S. Xella-Hansen, J. Yang, Yu. Zaitsev, M. Zavertyaev, G. Zech, T. Zeuner, A. Zhelezov, Z. Zheng, Z. Zhu, R. Zimmermann, T. Živko, A. Zoccoli, J. Zweizig